GKSS FORSCHUNGSZENTRUM in der HELMHOLTZ-GEMEINSCHAFT

GeNF – Experimental Report 2004

GeNF

Geesthacht Neutron Facility



Editors:

A. Schreyer
J. Vollbrandt
R. Willumeit

GKSS 2005/7

ISSN 0344-9629

HELMHOLTZ GEMEINSCHAFT GKSS ist Mitglied der Hermann von Helmholtz-Gemeinschaft Deutscher Forschungszentren e.V.

GKSS 2005/7

GeNF – Experimental Report 2004

Editors:

A. Schreyer
J. Vollbrandt
R. Willumeit

(Institute for Materials Research)

GKSS-Forschungszentrum Geesthacht GmbH • Geesthacht • 2005

Die Berichte der GKSS werden kostenlos abgegeben.
The delivery of the GKSS reports is free of charge.

Anforderungen/Requests:

GKSS-Forschungszentrum Geesthacht GmbH
Bibliothek/Library
Postfach 11 60
D-21494 Geesthacht
Germany
Fax.: (49) 04152/871717

Als Manuskript vervielfältigt.
Für diesen Bericht behalten wir uns alle Rechte vor.

ISSN 0344-9629

GKSS-Forschungszentrum Geesthacht GmbH · Telefon (04152)87-0
Max-Planck-Straße · D-21502 Geesthacht / Postfach 11 60 · D-21494 Geesthacht

GKSS 2005/7

GenF – Experimental Report 2004

Andreas Schreyer, Jürgen Vollbrandt, Regine Willumeit (Editors)

240 Seiten mit 188 Abbildungen und 16 Tabellen

Abstract

At the Geesthacht Neutron Facility GeNF about 180 experiments were performed in 2004 by GKSS and by or for external users, partners or contractors. In most cases the measurements were performed and analysed in cooperation by the guests and by the GKSS staff or by the permanent external user group staff. The activities, which are based on a proposal procedure and on the in house R&D program, are reported in 58 contributions in the present annual experimental report for the year 2004. The contributions may contain one or also several combined experiments.

During 2004 the GKSS research reactor FRG-1 achieved an operation time of 228 days at the full 5 MW reactor power providing a neutron flux of ca. $1{,}4 \cdot 10^{14}$ thermal neutrons / cm^2s. The cold neutron source was available during the complete operation time.

The focus of the in house R&D work at GeNF instruments was the characterisation of metal alloys, the analysis of stresses in welds and technical structures at ARES, FSS, DCD and SANS-2, the structural investigation of hydrogen containing substances such as polymers, colloids and biological macromolecules at SANS-1 as well as the characterisation of magnetic thin films at PNR, POLDI and RÖDI. The thorough upgrade of the reflectomer TOREMA to the instrument NeRo was nearly completed. It now offers new measurement possibilities on actual standards.

In appendices the progress of the project REFSANS at FRM-II is reported as well as the experimental activities of the young GKSS outstation HARWI-II at DESY.

Jahresbericht 2004 über die Experimente an GeNF

Zusammenfassung

An der Geesthachter Neutronenforschungseinrichtung GeNF wurden von GKSS und von oder für externe Nutzer, Partner oder Auftraggeber etwa 180 Experimente in 2004 durchgeführt. In den meisten Fällen wurden die Messungen gemeinschaftlich von den Gastwissenschaftlern und GKSS-Personal vorgenommen und ausgewertet. Die Experimente, die in der Regel über das Antragsverfahren und über das GKSS-eigene F&E-Programm abgewickelt wurden, werden in diesem Jahresbericht in Form von 58 Experimentierberichten dargestellt. Dabei können die Berichte einzelne Experimente oder auch mehrere zusammengefasst beschreiben.

Während 2004 erreichte der Forschungsreaktor FRG-1 228 Volllasttage bei 5 MW und bei einem Fluss von $1{,}4 \cdot 10^{14}$ thermischen Neutronen je cm^2 und s. Die kalte Neutronenquelle war während der gesamten Betriebszeit verfügbar.

Der Schwerpunkt der GKSS-eigenen Forschungsarbeiten lag in 2004 im Bereich der Charakterisierung von Metalllegierungen, der Analyse von Eigenspannungen in Schweißverbindungen und technischen Strukturen an ARES, FSS, DCD und SANS-2, im Bereich der Strukturanalyse von wasserstoffhaltigen Substanzen wie Polymere, Kolloide und Biomolekülen an der SANS-1 sowie im Bereich der Charakterisierung magnetischer Schichtstrukturen an PNR, POLDI und RÖDI. Der gründliche Umbau des Reflektometers TOREMA zum neuen Instrument NeRo wurde weitgehend abgeschlossen. NeRo bietet nun erweiterte Messmöglichkeiten auf neustem Standard.

In Anhängen wird auch über den Fortschritt des Projekts REFSANS am FRM-II sowie über die experimentellen Arbeiten der neuen GKSS-Außenstation HARWII bei DESY berichtet.

Manuscript received / Manuskripteingang in TDB: 8. August 2005

CONTENTS

Preface

– GeNF Operation
– Operation of FRG-1
– GeNF Instruments (overview)

SANS-1 **19**

M. Kiselev
Origin of sucrose penetration into the DMPC lipid membrane 21

G. Milkereit, S. Gerber, V. Vill
Micellar structure of a sugar based bolaamphiphile in pure solution and destabilizing effects in mixtures of glycolipids 23

L. A. Prado, K. Schulte, R. Willumeit, S. P. Nunes
Analysis of the microstructure of swollen sulphonated (block) naphtalenic copolyimides by SANS 25

M. V. Avdeev, L. Vekas
Nuclear and magnetic structures of ferrofluids on organic non-polar carriers by small-angle scattering of polarized neutrons 27

A. Paschke
SANS-study of the size distribution of model-chylomicrons 29

E. A. Kraynova, M. V. Avdeev
Structure of carbon from cellulose-based solid houshold wastes by SANS 31

N. Rozhkova, M. V. Avdeev
Nanostructure of shungites by small-angle neutron scattering 33

S. V. Grigoriev, G. P. Kopitsa
The study of the orbital part of the magnetic scattering amplitude in the heavy-fermion compound $CeRu_2Si_2$ by means of SAPNS 35

G. Milkereit, V. Vill
How thermotropic properties influence the formation of lyotropic aggregates near the critical micelle concentration 39

J. Zbytovská
Influence of Ceramides on the DMPC Membrane Structure Studied via Small Angle Neutron Scattering 41

R. Traiphol
Aggregation of MEH-PPV polymer in solution studied by SANS 43

M. Almgren
Demixing in Micellar Solutions Containing CTAC and a Partially Fluorinated Cationic Surfactant 45

G. Milkereit, V. Vill
Influence of methylation of the alkyl chain on the micelle formation of glycolipids 47

A. Dedinaite, M. Bergström, J. S. Pedersen
Association between chitosan and oppositely charged surfactants 49

P. Claesson, A. Dedinaite, R. Makuska
Association between a graft comb polyelectrolyte and oppositely charged surfactants 51

M. Harms, C. C. Müller-Goymann, T. Paepenmüller
Structure of ISCOMs 55

A. Timchenko, I. Serdyuk, O. Selivanova
Studies of multifunctional ribosomal protein S1 from Thermus thermophilus at different ionic conditions in solution by neutron and X-ray small-angle scattering 57

A. Triolo, C. M. Gordon
Aggregative behaviour of Room Temperature Ionic Liquids in Water 61

M. Kiselev
Structural investigation of mixed dipalmitoylphosphatidylcholine/ceramide 6 vesicles 63

J. Zbytovská
Influence of Cholesterol on the Structure of SC Model Lipid Membrane Studied via Small Angle Neutron Scattering 65

G. Milkereit, V. Vill
"Hydrophobic" effect of ethyl branching on the micellar structure of a long chain neoglycolipid" 67

T. Asakawa
Segregated domains of fluorocarbon and hydrocarbon surfactants in vesicles revealed by SANS 69

A. Heins, H. Stöckmann
Determination of particle size in several micellar solutions dependent on antioxidants added 71

E. Kettler, W. Richtering
Investigations on Structure Changes and Length Scales in Copolymer/SDS mixtures 73

SANS-2 **75**

E. Grossman, R. Verker, N. Eliaz
Characterisation of the Effect of Space Debris Impact on Polymer Foils by SANS and USANS 77

R. Kampmann, M. Marmotti, M. Haese-Seiller, V. Kudryashov
2D-multi-wire neutron detector for REFSANS at FRM-II: Performance of the final detector and its prototype 79

M. Bischof
Precipitation kinetics of a tool steel containing carbides and intermetallic phases 83

A. Michels, O. Moze, K. Suzuki
Dipole-field controlled spin disorder in a nanocomposite ferromagnet 87

S.V. Grigoriev, A. I. Okorokov, N. Grigorieva
The study of new magnetic nanocomposites based on mesoporous silica with embedded Fe-particles by SAPNS: technology 89

A. I. Okorokov, S.V. Grigoriev
The study of the static and dynamic spin chirality in the reentrant spin-glass system $Fe_{40}Ni_{40}Mn_{20}$ by means of small angle scattering of polarized neutrons 91

A.I. Okorokov, S.V. Grigoriev, P. Böni, R. Georgii
Study of the mosaic of the spin spiral structure of MnSi 93

T. Klassen, M. Dornheim, A. Schreyer, P. K. Pranzas
Investigation of structural changes of nanocrystalline Mg/MgH_2 during absorption and desorption of hydrogen 95

M. Bischof
Characterisation of particles in dispersoide strengthened tantalum 99

R. Ivanova, C. M. Papadakis, T Bonné
Aggregation behavior of poly(2-oxazoline)-based A-B-C triblock copolymers in aqueous solution 103

T. A. Tyson, Y. Qin
Spin structure probed by SANS in $Bi_{0.125}Ca_{0.875}MnO_3$ 107

D. Lamago, R. Georgii, P. Böni
Reinvestigation of magnetic critical phenomena in MnSi 111

S.V. Grigoriev, A. N. Pirogov, A. I. Okorokov
SANS study of the magnetic structure of YMn_6Sn_6 compound 113

S.V. Grigoriev, I.V. Golosovsky
The study of magnetic nanocomposites based on porous glasses with embedded Fe_3O_4-particles by SAPNS 115

M. Wolff, H. Zabel, V. Leiner
Crystallisation of polymer micelles at solid interfaces 117

G. P. Gordeev, L. A. Axelrod, S.V. Grigoriev, I. M. Lasebnik, V. N. Zabenkin
The search of the static spin chirality in the spin-glass like system $(Pd_{0.984}Fe_{0.016})_{0.95}Mn_{0.05}$ by small angle scattering of polarised neutrons 121

DCD **125**

T. Klassen, M. Dornheim, A. Schreyer, P. K. Pranzas
Investigation of structural changes of nanocrystalline Mg/MgH_2 during absorption and desorption of hydrogen 127

V. Ryukhtin, P. Stepanek,
USANS investigations of organized nanostructures of diblock copolymers in immiscible solvents 131

PNR **133**

D. W. Schubert, F. Faupel, J. Kranzow, J. Kruse
Feasibility study – Complementarity of neutron reflection and PALS for soft matter interface investigations 135

R. Georgii, R. Kampmann
High resolution 2D-multi-wire neutron detector for MIRA at FRM-II 137

ARES **141**

U. Cihak, W. Marketz
Residual Stress in IN718 Turbine Discs 143

W. V. Vaidya, M. Kocak
Residual stresses in laser beam welded Al sheets 147

FSS **151**

G. Bokuchava
Application of Rietveld profile refinement at FSS 153

H. G. Priesmeyer
Software development and experimental test of the Neutron Activation Calculator (NAC) 157

H. G. Priesmeyer
The diffraction-thermal expansion constants (CTE) of copper 159

N. Hort
Investigation of Residual Stresses in Cast AZ 91 161

J. Göken
Investigation the Elastic Constants of AZ 31 163

H. G. Priesmeyer
Positron annihilation experiments 165

TEX-2 **169**

W. Strotzki, N. Scherbaum
Global textures of ECAP deformed Al alloy 5109 171

M. Y. Zheng, W. M. Gan, S. W. Xu, K. Wu, H.-G. Brokmeier
Texture Measurements of ECAE Processed Mg-Zn-Y-Zr Alloy and Hot Compressed SiCw/AZ91 Composite 173

A. Pyzalla, M. Stempniewicz
Bone fossilization and Sauropod Texture 177

L. Wondraczek, H. Palkowski, H.-G. Brokmeier
Texture analysis of cast stripped Mg-AZ31 179

Y. Estrin, H.S. Kim
Title Equal Channel Angular Pressing of Mg and Mg Alloys 181

M. Mattei, F. Cifelli
Tectonic fabric in “undeformed” clays: comparison between AMS and neutron diffractometry data 183

L. Wagner, M. Kocan, H. Rack
Fatigue performance of metastable beta titanium alloys:
effects of microstructure and surface finish 185

POLDI **187**

V. Dangendorf, H. Friedrich
Thermal Neutron Imaging with ^{6}Li-foil converters coupled to Gas Electron Multipliers (GEMs) 189

F. Jeanneau
Neutron imaging with a Micromegas detector 191

M. Luszik-Bhadra, R. Böttger, H. Friedrich, M. Reginatto, F. d’Errico, Q. Chau, T. Lahye, A. Fiechtner, R. Tanner, F. Vanhavere
Determination of personal dosemeter responses within the EC project EVIDOS 195

M. Bode, D. Lott, A. Schreyer
Neutron diffraction study on EuSe 197

A. Schreyer, D. Lott
Polarized Neutron Diffraction on a Dy/Y Superlattice 201

Appendix I **207**

REFSANS Progress Report

R. Kampmann, M. Haese-Seiller, V. Kudryashov, C. Daniel, B. Nickel, J. Rädler, A. Schreyer, E. Sackmann
Status of the Horizontal Reflectometer REFSANS at FRM-II 209

Appendix II **213**

Reports of experiments carried out at HASYLAB/DESY by GKSS personel – GKSS outstation HARWI-II at DESY – as responsible experimenters in support of external users

F. Beckmann, T. Lippmann, J. Metge, R.V. Martins, T. Dose and A. Schreyer
High-energy beamline HARWI-II

H.-A. Crostack, J. Nellesen, H. Blum, T. Rauscher, F. Beckmann, G. Fischer
Analysis of the material behaviour of the MMCAI/TiN by microtomography

R. Verker, P. K. Pranzas, F. Beckmann, T. Donath, A. Schreyer, N. Eliaz and E. Grossman
Characterisation of the Effect of Simulated Space Debris on Polymers Using X-ray Microtomography

J. Fischer, J. Nellesen, H.-A. Crostack, T. Donath, F. Beckmann and F. Witte
Determination of in-vivo corrosion rates of degradable implants by SR-microtomography

P. Lehmann, A. Kaestner, F. Beckmann and H. Flühler
Geometric properties of layered sands and their relevance for water distribution

T. Walther, H. Thömen, T. Donath, F. Beckmann
Microstructure of Medium Density Fiberboard (MDF)

O. Brunke, S. Odenbach and F. Beckmann
Using synchrotron μCT to analyse the development process of metallic foams

R. Zettler, J. F. dos Santos, T. Donath, F. Beckmann, T. Lippmann, D. Lohwasser and A. Schreyer
Validation of Marker Material Flow in 4 mm Thick Friction Stir Welded Al 2024-T351 as reported by Computed Microtomography using Standard Metallographic Techniques

J. Fischer, U. Dietz, P. Thurner, F. Beckmann and B. Müller
Visualization of capillaries in the myocardium using synchrotron radiation based microtomography

T. Lippmann, W. Morgenroth, A. Kirfel
Electron Density Distribution in Co-Olivine, CO_2SiO_4, from D3 and BW5 Data

M. Nickel, E. Bullinger, H. M. Reiswig, T. Donath and F. Beckmann
Functional Micromorphology of Sponges (Porifera)

R. Bernhardt, T. Douglas, T. Beleites, M. Neudert, M. Ney, D. Scharnweber, F. Beckmann, Th. Zahnert, H. Worch
High Resolution 3D-Analysis of the Middle Ear Stapes with Footplate using Synchrotron Radiation Microcomputed Tomography (SRμCT)

Preface

GeNF Operation

The Geesthacht Neutron Facility (GeNF) is operated as an open facility for external users for about 2/3 of the available beam time and it is used for GKSS in house research within its materials science programme for the remaining 1/3. The external users come either from national and international scientific research institutions, universities and industry, or they own and operate experiments at GeNF as permanent external partners.

The beam time allocations for GeNF instruments are established on the base of a proposal procedure which can react in a flexible and fast way on new proposals. Proposals can be submitted at any time. In 2004 about 180 experiments were performed at GeNF by or for external users, partners or contractors as well as for the in house research programmes. A part of these activities – mainly the part of external use based on proposals – is reported in the present annual experimental report for the year 2004. In many cases several experiments are concentrated in one experimental report.

Operation of FRG-1

In 2004 the FRG-1 was operated routinely interrupted by the two planned major shut downs in January/February and in July. The total operation time was to 228 days at its full 5 MW power providing a neutron flux of ca. $1{,}4 \cdot 10^{14}$ thermal neutrons / cm^2 s. The cold neutron source was always available during FRG operation.

GeNF Instruments

The current set of instruments at GeNF is shown in Fig. A and listed in table A. The available sample environment is listed in table B.

In 2004 the installation of the modern experiment control hardware and software based on LabView was continued for NeRo and SANS-2. The thorough upgrade of former TOREMA to state of the art neutron reflectometer NeRo was nearly completed. The POLDI experiment was transferred from PTB to GKSS but still with the option, that PTB will use the modified instrument for neutron dosimetry purposes since PTB has qualified it as thermal neutron reference field.

The focus of the GKSS in-house research at GeNF is the investigation of metal alloys, the analysis of stresses in welds and technical structures at ARES, FSS, DCD and SANS-2, the structural investigation of hydrogen containing substances such as polymers, colloids and biological macromolecules at SANS-1 as well as the characterisation of magnetic and polymer thin films at PNR, POLDI and RÖDI.

Also in 2004 a major issue of activities concerning instrument improvements are focussed on the setup of the GKSS high-energy synchrotron beamline HARWI-II at DESY. For details see the report in appendix II.

Geesthacht Neutron Facility (GeNF)

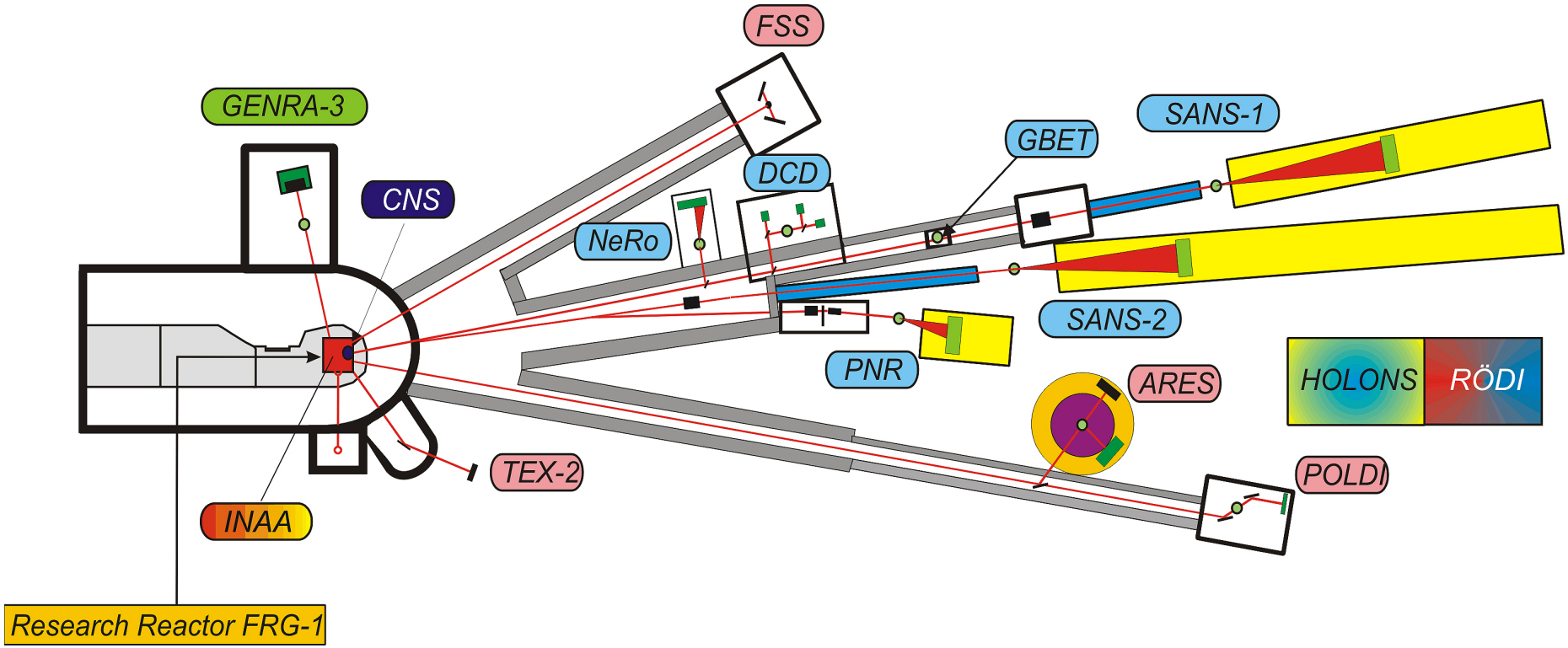


Figure A: **Arrangement of the Instruments at GeNF.**

Table A: List of GeNF Instruments

Instrument	Short Instrument Description /Main Tasks	Characteristic Data	Operator / Local Contact
SANS-1	Small Angle Neutron Scattering using cold non-polarised/polarised neutrons primarily to investigate molecular biology, colloids and polymers	$\Phi_{max} = 6 \cdot 10^5$ cm^{-2} s^{-1} (coll.2 m,λ=0.8nm) $\Delta\lambda/\lambda = 0.1$ ($\lambda = 0.85$ nm) Particle sizes: 2 - 80 nm 2-D position-sens. ^{3}He- detector	GKSS / Regine Willumeit Vasyl Haramus
SANS-2	Small Angle Neutron Scattering using cold non-polarised/polarised neutrons to characterise precipitates, clusters, interfaces, grain sizes, magnetic structures etc. in materials (metals, polymers, colloids a.o.)	$\Phi_{max} = 2 \cdot 10^7$ cm^{-2} s^{-1} (coll.1 m,λ=0.5nm) $\Delta\lambda/\lambda = 0.1$ Particle sizes: 1 - 100 nm 2-D position-sens. ^{3}He- detector	GKSS / Helmut Eckerlebe P. Klaus Pranzas
DCD	Double Crystal Diffractometer for ultra small angle neutron scattering (USANS) using non-polarised cold neutrons to characterise large creep pores, fatigue and sintering cavities, precipitates, voids, bubbles, etc. in materials	$\Phi \approx 0.5 \cdot 10^3$ cm^{-2} s^{-1} $\Delta\lambda/\lambda = 1 \cdot 10^{-5}$ ($\lambda = 0.443$ nm) Particle sizes: 30 nm - 24 μm 3 x ^{3}He- detectors	GKSS / P. Klaus Pranzas
ARES	Diffractometer for the Analysis of REsidual Stresses in specimens with technical sizes (up to 100 kg) using thermal non-polarised neutrons	$\Phi \approx 3 \cdot 10^5$ cm^{-2} s^{-1} (perfect Si-Monochr.) $\Delta d/d \approx 4 \cdot 10^{-3}$ take-off angle: 57° - 120° 2-D position-sens. ^{3}He- detector	GKSS / Peter Staron
FSS	Time of flight Fourier Strain Spectrometer to investigate residual stresses in specimens with technical sizes using thermal neutrons	$\Phi = 5.5 \cdot 10^6$ cm^{-2} s^{-1} timing res. ca. $4 \cdot 10^{-3}$ ($\lambda = 0.1$ - 0.4 nm) Analyser: 2 x 3072 TOF channels 2 detector banks (90° & 270°)	CAU - Universität Kiel / Hans-Georg Priesmeyer
NeRo	Neutronen Reflectometer to study magnetic and other surfaces, layers, thin films and membranes using cold non-polarised/polarised neutrons with high resolution	$\Phi = 5 \cdot 10^4$ cm^{-2} s^{-1} (standard collimation) $\Delta\lambda/\lambda = 0.02$ ($\lambda = 0.435$ nm) 2-D position-sens. ^{3}He- detector, ^{3}He-pencil counter	GKSS / Dieter Lott
PNR	Polarised Neutron Reflectometer to study magnetic and other surfaces, layers, thin films and membranes using cold non-polarised/polarised neutrons at high fluxes	$\Phi_{nonpol} = 1 \cdot 10^5$ cm^{-2} s^{-1} $\Phi_{nonpol} / \Phi_{pol} = 3 / 1$ $\Delta\lambda/\lambda = 0.05$ ($\lambda \geq 0.635$ nm) 2-D position-sens. ^{3}He- detector	GKSS / Danica Solina

Table A: List of GeNF Instruments (continued)

Instrument	Short Instrument Description /Main Tasks	Characteristic Data	Operator / Local Contact
RÖDI	X-ray (RÖntgen) DIffractometer to investigate residual stresses, textures and thin films	Seifert XRD 3003 PTS Heavy load goniometer	GKSS / Peter Staron
TEX-2	Four circle neutron TEXture diffractometer to characterise textures in metallic, ceramic and geologic materials using thermal non-polarised neutrons	$\Phi = 0.3 - 2 \cdot 10^6$ cm^{-2} s^{-1} take-off angle: 17° - 57° (in 10°-steps) λ-range: 0.08 – 0.27 nm ^{3}He-single detect., 38° JULIOS-PSD 2-D position-sens. ^{3}He- detector	TUC - Technische Universität Clausthal / Heinz-Günter Brokmeier
POLDI	POLarised DIffractometer; 3-D depolarisation analysis is used to investigate magnetic properties and correlations in magnetic materials; additional time of flight option in non-polarised mode	$\Phi_{max} = 0.8 \cdot 10^5$ cm^{-2} s^{-1} (polarized) take-off angle: 10° < 2 Θ_M < 65° λ-range: 0.1 nm - 0.36 nm ^{3}He-single detector	GKSS / Dieter Lott
HOLONS	HOLOgraphy and Neutron Scattering to investigate the properties in functional materials of photonics (e.g. photopolymers and photorefractive crystals) and to study light-induced changes simultaneously by light and neutron diffraction	holographic setup in SANS-2: angular resol.≤ 0.01°; angul.setting acc = 0.001° lasers (excitation & diffract.): Ar^+-laser (single&multi line mode: 25 W /visible, 5.5 W / UV), HeNe-lasers (green, red)	Universities of Vienna and Osnabrück / Romano Rupp
GENRA-3	GEesthacht Neutron RAdiography facility for non-destructive analysis of materials by static and dynamic imaging	Φ_{therm} / $\Phi_{epi} = 1.4 \cdot 10^6$ / $8 \cdot 10^3$ [cm^{-2} s^{-1}] image: 15 x 15 to 45 x 45 cm^2 max. size of specimen: 100 x 200 cm^2	GKSS / Jürgen Vollbrandt
GBET	Geesthachter Boron- capture (Einfang) Therapy originally designed to study cell cultures in tumours with enriched boron; now available as a cold neutron irradiation facility	$\Phi = 1.6 \cdot 10^8$ cm^{-2} s^{-1} (λ_m= 0.6 nm) irrad. area : 30 x 40 mm^2 E_m = 2.3 meV	GKSS / Hans-Ulrich Ruhnau
ICI	In Core Irradiation - service for industry and others, different core positions, pneumatic dispatch system available	Φ_{therm} = 2 to $8 \cdot 10^{13}$ cm^{-2} s^{-1} Φ_{fast} = 0.02 to 0.06 Φ_{therm} max. sample size: 40 mm∅ x 100 mm	GKSS / Wolfgang Knop

Table B: GeNF Sample Environment

Instrument	Cryostat	Magnets	Temp. Conditioning	Other Devices
SANS-1	^{3}He / ^{4}He – Cryostat: horizontal dilution-refrigerator with NMR sample coil and microwave source: T-range: 120 mK - RT; NMR: 106 and 16 MHz; Microwave: tunable: 68 to 74 GHz sample dimension: 2,8 x 17 x 19 mm^3 (optimum design for NMR coil), NMR is made for ^{1}H and ^{2}H resonance in 2.5 Tesla continuous wave mode;	2.5 Tesla magnet	heater up to 80 °C	
SANS-2	refrigerator cryostat Model Leybold RGD 210, temp.-range: 12 - 475 K flexible operation in various instruments	• **B-E 25**: up to 2 Tesla with closed cycle refrigerator (T: 8 - 300 K) • **B-E 15**: up to 1.5 Tesla with closed cycle refrigerator (T: 8 - 300 K) • **B-E 10**: up to 1 Tesla with closed cycle refrigerator (T: 8 - 300 K), alternative furnace (T: 300 - 900 K), usable for polarised neutrons • **superconducting magnet:** up to 5 Tesla with closed cycle refrigerator (T: 8 - 300 K) usable for polarised neutrons	heater (electric) / cooler (thermostat liquid circuit): T-range: -30 - 400 °C vacuum or inert gas atmosphere	- sample container for big samples - lasers;
DCD	refrigerator cryostat Model Leybold RGD 210, temp.-range: 12 - 475 K flexible operation in various instruments			
ARES	refrigerator cryostat Model Leybold RGD 210, temp.-range: 12 - 475 K flexible operation in various instruments			

Table B: GeNF Sample Environment (continued)

Instrument	Cryostat	Magnets	Temp. Conditioning	Other Devices
FSS	refrigerator cryostat Model Leybold RGD 210, temp.-range: 12 - 475 K flexible operation in various instruments		heater (up to 1000 °C)	- stress rig max. force: 30 t
PNR	refrigerator cryostat Model Leybold RGD 210, temp.-range: 12 - 475 K flexible operation in various instruments	• **electro magnet:** up to 0.9 Tesla • **superconducting magnet:** up to 5 Tesla with closed cycle refrigerator (T: 8 - 300 K) usable for polarised neutrons	• heater / cooler (thermostat liquid circuit): T-range: -30 - 250 °C	
NeRo	refrigerator cryostat Model Leybold RGD 210, temp.-range: 12 - 475 K flexible operation in various instruments	• **electro magnet:** up to 0.9 Tesla	• 2 x vacuum furnaces: T-range: RT - 200 °C - one especially. for annealing purposes under PC control • heater / cooler (thermostat liquid circuit): T-range: -30 - 250 °C	
TEX-2			mirror furnace up to 2000 °C	- loading device: tension up to 1.5 t, compression up to 2.0 t - sophisticated set of sample holders
POLDI	- refrigerator T > 10 K	DC magnetic field < 160 A/cm pulsed field < 6.5 kA/cm		

GKSS FORSCHUNGSZENTRUM in der HELMHOLTZ-GEMEINSCHAFT	EXPERIMENTAL REPORT	GeNF SANS-1
Small-angle scattering instrument SANS-1		

Short Instrument Description:

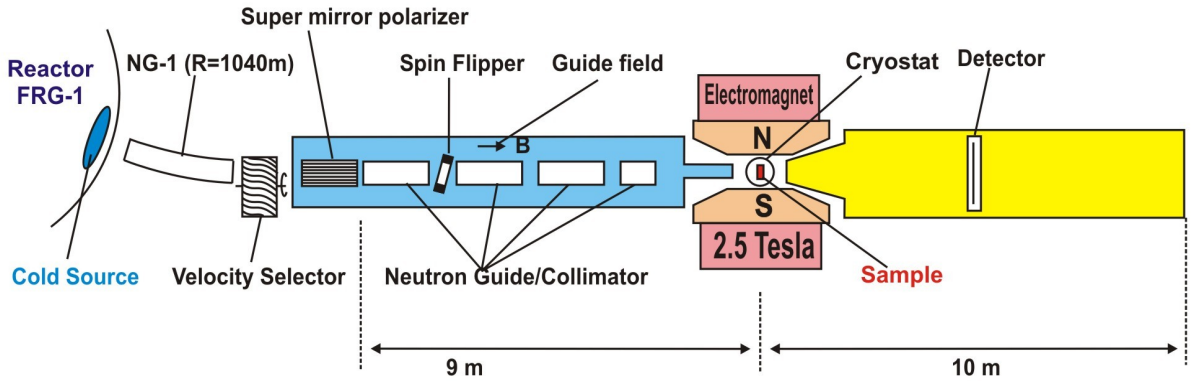
The small angle neutron scattering instrument SANS-1 using cold non-polarised/polarised neutrons serves primarily to investigate molecular biology, colloids and polymers.

Local Contact:

Dr. Regine Willumeit
Phone/Fax : +49 (0)4152 87 – 1291 / +49 (0)4152 87 – 1356
e-mail: regine.willumeit@gkss.de

Dr. Vasyl Haramus
Phone/Fax : +49 (0)4152 87 – 1290 / +49 (0)4152 87 – 1356
e-mail: vasyl.haramus@gkss.de

Schematic view of SANS-1:



Instrument Details:

Beamline:	Beamline 8 - NG-1, radius of curvature R = 1040 m, cross section 3 x 4 cm^2, cold neutrons
Monochromator	helical slot selector
Wavelength range behind polariser and selector:	$\geq$ 0.45 nm;
Wavelength resolution	$\Delta\lambda / \lambda$= 0.1 (λ= 0.85 nm)
Length L of collimation:	1 m, 3 m, 5 m, 7 m, 9 m
Flux at specimen:	Φ = 0.04 - $6 \cdot 10^5$ cm^{-2} s^{-1} see table

Instrument Details (continued)**:**

Range of momentum transfer:	$0.05 \leq Q \leq 3$ nm^{-1}
Distance sample to detector:	0.7 m $\leq$ d $\leq$ 9m
Detector: active area: effective pixel size: background:	2-dim position-sensitive ^{3}He-counter 55 **x** 55 cm^2 0.7 x 0.7 cm^2 1 cps
Polarized target station:	dilution refrigerator (120 mK) 2.5 T C-shaped electro-magnet microwave emitter (68 - 74 GHz) NMR circuit for protons and deuterons selective nuclear spin depolarisation
Other sample environment	thermostat (5 °C to +200 °C) automatic sample change

Flux of polarized cold neutrons at the sample position:

length of collimator [m]	**1**	**3**	**5**	**7**	**9**
Φ **[**10^3 n cm^{-2} s^{-1}**]** (λ= 0.85 nm)	**600**	**360**	**120**	**72**	**40**

GKSS FORSCHUNGSZENTRUM in der HELMHOLTZ-GEMEINSCHAFT	**EXPERIMENTAL REPORT**	**GeNF SANS-1**

Origin of sucrose penetration into the DMPC lipid membrane

Principal Proposer:	**Mikhail Kiselev [1,2]**
Co-Proposers:	[1]Martin- Luther University Halle-Wittenberg, Halle, Germany [2]Frank Laboratory of Neutron Physics, JINR, Dubna, Russia
Experimental Team:	**Denis Matveev[2], Reinhard Neubert[2]**
User Group Leader:	**Reinhard Neubert[2]**

Date(s) of Experiment:	March 2004

Objectives

Disaccharides posses well known bioprotection properties. Sucrose and trehalose stabilize the membrane and protein during a drying. Bioprotection properties of the disaccharides based by the replacement of water molecules near the membrane (protein) surface are commonly believed [1]. In this respect the important question is possibility of sucrose penetration inside the membrane. The next question will be the sugar influence on the quantity of the water molecules inside the membrane.

Experiment

For the case of the unilamellar vesicle with diameter about 500Å, the quantity of water molecules inside of the DMPC membrane and the water distribution function across the membrane have been calculated from SANS experiment [2]. Raman spectroscopy study of sucrose and trehalose influence on the dimyristoylphosphatidylcholine (DMPC) membrane structure shows that both disaccharides have no influence on the hydrocarbon chain conformation and, probably, have no penetration in the region of hydrocarbon chains [3]. Molecular dynamic simulations support this experimental result [4]. Simulations of the phospholipid structure in the disaccharide solutions demonstrate the preferable location of disaccharide molecules near the membrane surface and the absence of any changes of the membrane structure [4]. The Influence of trehalose on the DMPC membrane thickness was detected by SANS [5]. Two reasons can exist for the decrease of the DMPC membrane thickness under the trehalose influence. First reason is the penetration of the trehalose molecules into the polar head group region. The location of trehalose molecules in the polar head group region will increase the DMPC surface area. The increase in the value of A results mainly in the decrease of the membrane thickness d. Other reason is a presence of surface active molecules in the commercial available trehalose. The purpose of present experiment was to check the influence of surface active impurities on the DMPC-sucrose interaction. Sucrose of 99% purity from Avanti was used for the preparation of 20% solution in D_2O with addition of 0.02% sodium azide. The 20% aqueous sucrose solution was cleaned in the Langmur trough [5]. The solution demonstrates an absence of the impurities after two cleaning procedure. DMPC unilamellar vesicles were prepared from 1% (w/w) multilamellar DMPC dispersions in pure D_2O and D_2O with 20% sucrose by extrusion through pores of 500Å diameter. The obtained unilamellar vesicular population was characterized via SANS technique.

Achievements and Main Results

Fig. 1 demonstrates the measured macroscopic cross section of vesicles at T=30^{o}C. As seen from the position of first minimum, the average vesicle radius decreases from the value of 260Å to the value of 210Å under sucrose influence. Fig. 2 demonstrates Kratky-Porod plot for the calculation of the membrane thickness in the Guinier approximation. The decrease of line slope reflects the decrease in the value of membrane thickness. Guinier

approximation gives value of membrane thickness d=43Å±0.8Å in D_2O. Membrane thickness decreases to the value of 37.8±0.8Å under sucrose influence. Guinier approximation gives underestimated value of membrane thickness, but describes well the relative change in the membrane thickness [2]. Obtained experimental result supports the penetration of the disaccharide molecules into the region of polar head group described in [5] for the case of trehalose.

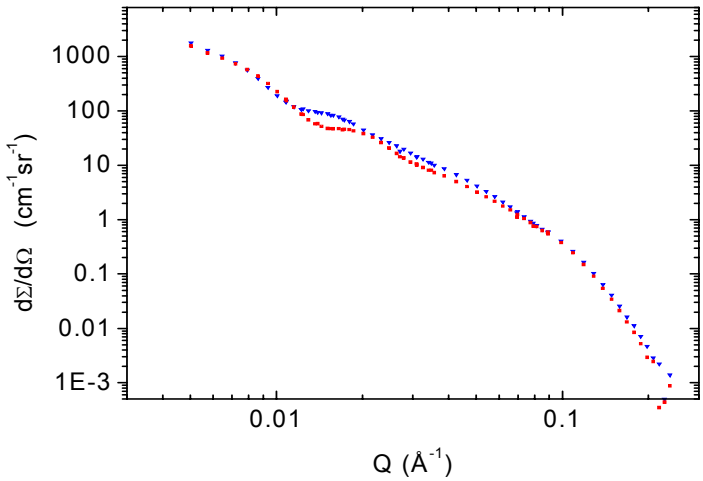


Fig. 1. SANS curves at T=30°C. DMPC unilamellar vesicles in D_2O (blue curve) and in 20% sucrose solution (red curve).

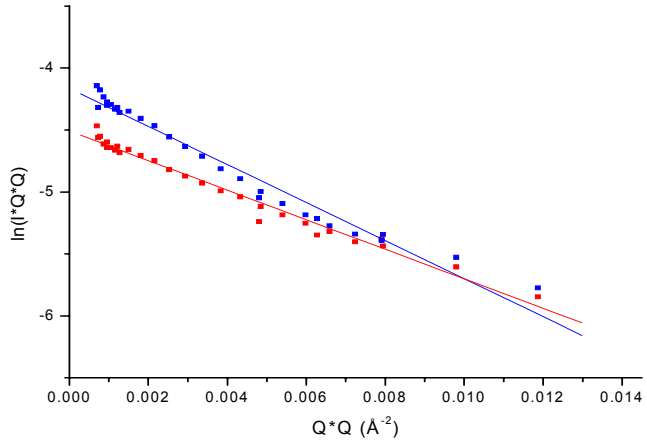


Fig. 2. Kratky Porod plot of the scattering curves from unilamellar DMPC vesicles in D_2O (blue) and in 20% sucrose solution (red).

References:

[1] J.H. Crowe, L.M. Crowe, J.F. Carpenter, A.S. Rudolph, C.A. Wistrom, B.J. Spargo, T.J. Anchordogy. Biochim. Biophys. Acta 947 (1988) 367-384

[2] M.A. Kiselev, E.V. Zemlyanaya, A. Vinod. Crystallography report 49 (2004) s131-s136.

[3] M.A. Kiselev, S. Wartewig, M. Janich, P. Lesieur, A.M. Kiselev, M. Ollivon, R. Neubert. Chemistry and Physics of Lipids 123 (2003) 31-44

[4] A.K. Sum, R. Faller, J.J. de Pablo. Biophys. J. 85 (2003) 2830-2844.

[5] M.A. Kiselev, J. Zbytovska, D. Matveev, S. Wartewig, I.V. Gapienko, J. Perez, P. Lesieur, A. Hoell, R. Neubert. Colloids and Surfaces A (2004) accepted.

GKSS FORSCHUNGSZENTRUM in der HELMHOLTZ-GEMEINSCHAFT	**EXPERIMENTAL REPORT**	**GeNF SANS-1**

Micellar structure of a sugar based bolaamphiphile in pure solution and destabilizing effects in mixtures of glycolipids

Proposer:	**Götz Milkereit**[1], Inst. of Organic Chemistry, University of Hamburg, Martin-Luther-King-Platz 6, 20146 Hamburg
Co-Proposers:	**Sven Gerber**[1], **Volkmar Vill,**[1]
Experimental Team:	**Regine Willumeit,** [2] **Vasyl Haramus**[2], [2]GKSS
User Group Leader:	**Volkmar Vill,**[1]
Date(s) of Experiment:	March 2004

Objectives

Bolaamphiphiles are special lipids where the non polar part of the lipids is connected on both ends of the chain to polar head groups. Until now only very little data are available on the physical properties of bolaamphiphiles [1], and especially data for the sugar based ones can hardly be found. We have synthesized a new bolaamphiphile with two disaccharide head groups, linked to an alkyl chain consisting of 12 carbon atoms (Fig. 1). The lyotropic properties of the pure compound and of mixtures with octyl-β-D-glucopyranoside (Fig. 1) were investigated using small-angle neutron scattering and surface tension measurements.

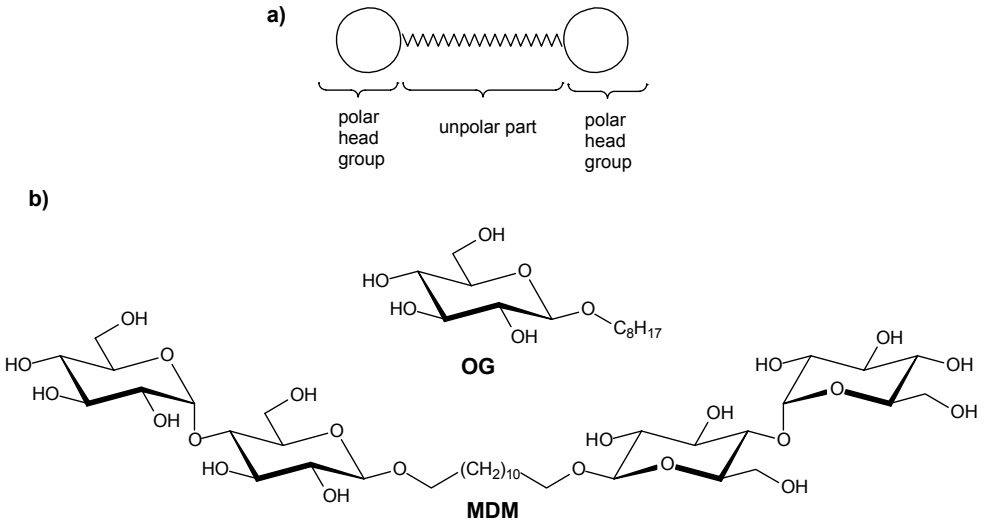


Figure 1: *a) Principal structure of bolaamphiphiles; b) investigated compounds: Octyl-β-D-glucopyranoside (**OG**); 1,12-bis-[4''-O-(α-D-glucopyranosyl)-β-D-glucopyranosyl]-dodecane (**MDM**).*

Experiment

SANS data were collected for following solutions: **OG** in D_2O (0.01 g/mL; 34.2 mM); **MDM** in D_2O (0.01 g/mL; 11.8 mM); the mixture of **OG**(0.01 g/mL, 34.2 mM**)** and of **MDM** (0.001 g/mL; 1.18 mM) in D_2O at 25 °C (Figure 2).

The scattering intensities of **OG** and **MDM** solutions are very different. **OG** solution represents the typical scattering for anisotropic aggregates (short rod-like aggregates) which were observed earlier [2]. In the case of **MDM** solution we have observed strong scattering in the lower *q* region which points on the presence of very large aggregates but also there is a significant scattering at the higher *q* range which points on the presence of smaller aggregates, too. It looks that there are the populations of aggregates with different size. The

scattering curve of the mixed solution is similar to curve of pure **OG**, as it should be expected because of the very small molar fraction of added **MDM**, but despite this, the curve is lower than that of the pure **OG** solution. This can point on a decreasing of the micelles on the addition of the mixture component **MDM**. The interaction between surfactants leads to a decreasing of the micellar size, which is in agreement with the CMC observation.
Figure 2 shows a reasonable agreement between experimental data and model fits. The values of the fit parameters show that micelles become smaller upon addition of **MDM** to the solution i.e., length of micelles decreases from L=74±4 Å for the pure **OG** solution to L=63±3 Å for the **OG-MDM** mixture. The radius of cross section does not change R=12±1 Å.
As reported by Caponetti et al. [3], the size of micelles formed by bolaform (non-carbohydrate surfactant) can be reduced upon the addition of salt, in our case, we reduced the size of micelles formed by normal alkyl glucoside by the addition of a bolaamphiphile.

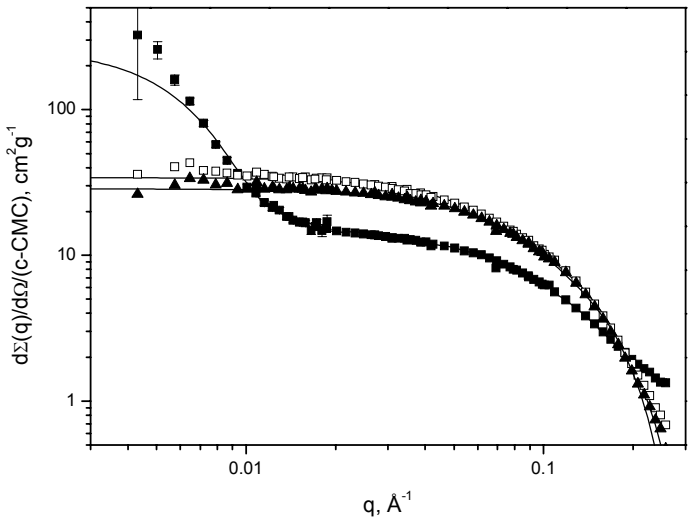


Figure 2: *SANS data of solutions of pure 1,12-bis-[4''-O-(α-D-glucopyranosyl)-β-D-glucopyranosyl]-dodecane 0.01 g/mL (filled squares), pure Octyl-β-D-glucopyranoside 0.01 g/mL (empty squares) and mixture of OG (0.01 g/mL) with 0.001 g/mL of MDM in D_2O, T=25 °C. Solid lines are fits by IFT (**MDM**) and cylindrical model (**OG** and mixture).*

Achievements and Main Results

A new carbohydrate based bolaamphiphile (**MDM**) has been synthesized and described by surface tension and small angle neutron scattering. **MDM** shows quite low CMC values and population of supramolecular aggregates with different length scales (small r~15 Å and large r~350 Å). The interaction of **MDM** with octyl glucoside (**OG**) is antagonistic which is confirmed by a higher mixture CMC compare to the ideal mixing expectation (value of parameter β is positive) and a decreasing of length of **OG** micelles upon addition of small amount of **MDM** to the solution (from 74 to 63 Å). The results were unexpected, because due to the very similar chemical structure of the investigated compounds (**OG**: one gluco-headgroup, **MDM**: two glucobased-headgroups) normally a increasing of the size of micelles would be expected. The biological relevance of this effect is under investigation.

References

[1] I. Isjizuka, T. Yamakawa, Glycolipids. In: Wiegandt, H. (Ed.), New Comprehensive Biochemistry, vol. 10. Elsevier, (1985).
[2] L.-Z. He, V.M. Garamus, B. Niemeyer, H. Helmholz, R. Wilumeit, *J. Mol. Liq.*, 89 (2000), 239.
[3] E. Caponetti, D. Chillura-Martino, C. La Messa, R. Muzzalupo, L. Pedone, *J. Phys.Chem. B*, 108 (2004), 1214.

GKSS FORSCHUNGSZENTRUM in der HELMHOLTZ-GEMEINSCHAFT	EXPERIMENTAL REPORT	GeNF SANS-1

Analysis of the microstructure of swollen sulphonated (block) naphtalenic copolyimides by SANS.

Proposer:	**Luis Antonio S. de Almeida Prado,** [1]Technical University Hamburg-Harburg, Polymer Composites, Hamburg, Germany
Co-Proposers:	**Karl Schulte,[1] Regine Willumeit[2], Suzana P. Nunes[2],** [2]GKSS
Experimental Team:	**Yolanda Álvarez-Gallego[2], Vasyl Haramus[2]**
User Group Leader:	**Suzana P. Nunes**
Date(s) of Experiment:	02-15 April 2004

Objectives

The aim of these small angle neutron scattering experiments is the analysis of sulphonated (block) naphtalenic copolyimides in the swollen state, using D_2O for the selective enhancement of the scattering produced by the ionic $–SO_3H$ groups.

Experiment

Sulphonated naphtalenic polyimides are potential candidates for membranes for direct-methanol fuel-cells (DMFC), due to their good chemical, thermal and mechanical stabilities. It is well known that block copolyimides can exhibit facilitated proton-transport, which is strongly required for a good performance of the DMFC. Systematic researches on synthesis and properties of sulphonated copolyimides have been currently done in GKSS. Two kinds of polyimides were analyzed: (1) Copolyimides prepared from the reaction between the benzidinedisulfonic acid (BDSA), diaminobenzimidazole (DABI) and 1,4,5,8-Naphthalenetetracarboxylic acid dianhydride (NTDA) and (2) copolymers synthesized from NTDA, diamino-diphenyl ether (DDE) and sulphonated DABI (sDABI).

These polymers were obtained as orange or red thin films with thickness around 80 μm. The membranes were kept in deuterium oxide for three days in order to attain the highest swelling. As the D_2O is highly hydrophilic, it should be absorved preferentially in the ionic domains, therefore the scattering produced by ionic clusters, expected to be present in the sulphonated polyimides [1,2], will be enhanced on account of the higher cross-section of deuterium to neutrons. In this case, the investigation of the micro-structure of the polyimides in the swollen state would be possible, and information concerning the phase separation between the ionic groups and the non-ionic polyimide matrix can be obtained.

The membranes were cut into small pieces and placed in quartz cuvettes filled with D_2O. In order to increase the scattering intensity, many stacks of the membrane were stacked in the cuvette. The composition of the membranes under analysis is displayed in Table 1.

Table 1. Composition, Ionic Exchange Capacity (IEC), Block Length (BL) and position of the ionomer peak q of the sulphonated copolyimides.

Polyimide	IEC	BL[a]	q ($Å^{-1}$)[b]
NTDA/BDSA:DABI	1,94	1	No peak
100/50/50		9	No peak
NTDA/sDABI:DDE	1.54	1	No peak
100/79/21		3	0.02
		9	No peak

Achievements and Main Results

Only the polyimide derived from sDABI, DDE and NTDA having a block constituted by 9 repeating units bearing sulphonic groups (see Figure 1) showed a peak. The same membranes were characterized by anomalous small-angle X-ray scattering and showed peaks associated to separation between the ionic groups and the polyimide matrix (except by the NTDA/BDSA:DABI statistical copolymer). For the polyimides containing sDABI, the ionomer peak is observed at q 0.2 $Å^{-1}$ in the ASAXS curves (see Figure 1). As all these membranes have the same composition, and all of them exhibited phase separation (attested by ASAXS), a similar behaviour for all these membranes should be observed by SANS. It seems that the block copolymers with larger block lengths absorbs different amounts of water, as a consequence of the different molecular architecture. The difference between the position of the ionomer peak in the swollen and the dry membrane reflects the micro-structural changes caused by the absorption of water. These groups are expected to grow and separated as the membrane swells.

Both ASAXS and SANS curves of this NTDA/sDABI:DDE membrane should be fitted according to the existing models for ionomers.

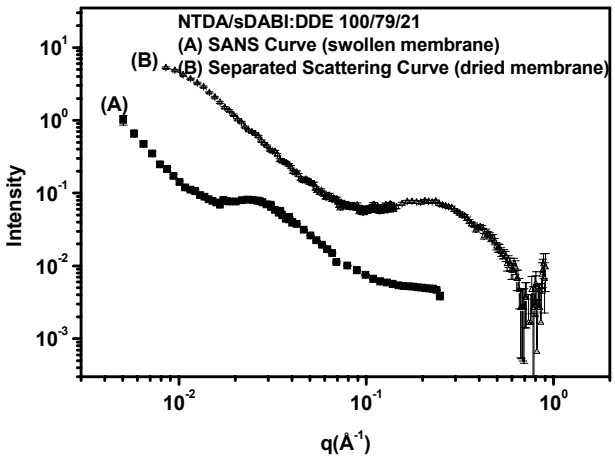


Figure 1 (A) SANS spectra of the swollen polyimide membrane; (B) separated scattering curve produced by the $–SO_3Rb$ groups.

References

[1] Piroux, F.; Espuche, E.; Mercier, R.; Pinéri, M.; Gebel, G. J. Membrane Sci. 2002, 209, 241.

[2] Blachot, J. F.; Diat, O.; Putaux, J. L.; Rollet, A. L.; Rubatat, L.; Vallois, C.; Muller, M.; Gebel, G. J. Membrane Sci. 2003, 214, 31.

GKSS FORSCHUNGSZENTRUM in der HELMHOLTZ-GEMEINSCHAFT	EXPERIMENTAL REPORT	GeNF SANS-1

Nuclear and magnetic structures of ferrofluids on organic non-polar carriers by small-angle scattering of polarized neutrons

Principal Proposer:	**Mikhail V. Avdeev**[1]
Co-Proposers:	[1] Frank Laboratory of Neutron Physics, JINR, Dubna, Russia **Ladislau Vekas**[2], [2]Center of Fundamental and Advanced Technical Research, Romanian Academy of Sciences, Timisoara, Romania
Experimental Team:	**Doina Bica**[2], **M.Balasoiu**[1,3], **Vasyl M. Haramus**[4] [3]Institute of Space Sciences, Bucharest, Romania [4]GKSS Research Centre, Germany
User Group Leader:	**Ladislau Vekas**[2]
Date(s) of Experiment:	15-30 April 2004

Objectives

Our recent SANS applications for studying ferrofluids (fine dispersions of magnetic materials in liquids) revealed [1,2] some interesting features in the structural organization of the highly stable system magnetite/oleic acid/benzene. Its stability is explained by a special structure of oleic acid ($C_{17}H_{33}COOH$) [3]. The double bond between C-atoms in the middle of the surfactant molecule results in additional "hardness" of the stabilizing shell around magnetite particles. It was shown [1,2] that the nuclear scattering from this ferrofluid is described well by the spherical core-shell model, and no significant effects of aggregation and interparticle interaction were observed for the magnetite concentration up to 5 vol. %. The aim of the current experiments was to follow changes in the structure of the considered ferrofluid when the surfactant or/and carrier are changed. For this purpose dispersions of magnetite in non-polar organic carriers D-benzene and D-cyclohexane stabilized with oleic (OA), stearic (SA) and myristic (MA) acids were prepared in the same way [3, 4]. Stearic acid ($C_{17}H_{35}COOH$) contains the same number of carbon atoms as oleic acid, but no peculiarity mentioned above takes place. Myristic acid ($C_{13}H_{27}COOH$) is significantly shorter than oleic acid.

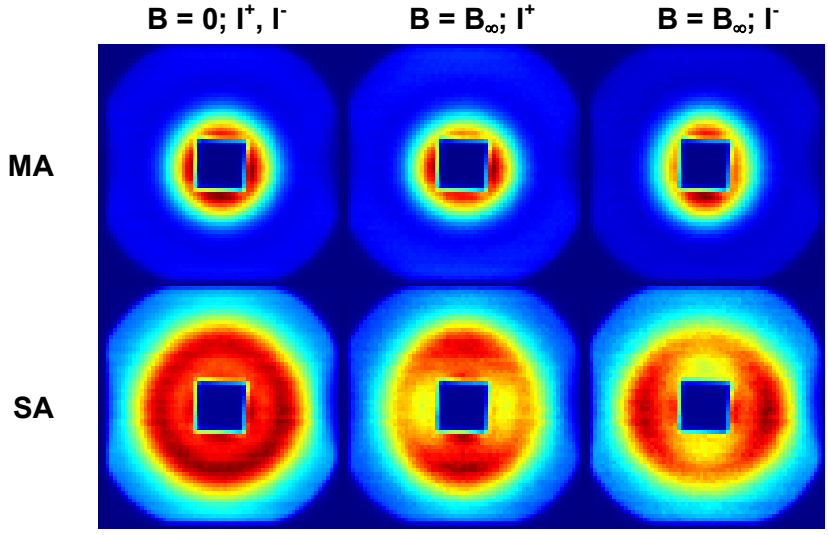


Fig. 1. 2D scattering patterns obtained for ferrofluids based on d-cyclohexane and stabilized with myristic (MA) and stearic (SA) acids. Volume fraction of magnetite in both samples is 2.8 %. Sample-detector distance is 1.8 m.

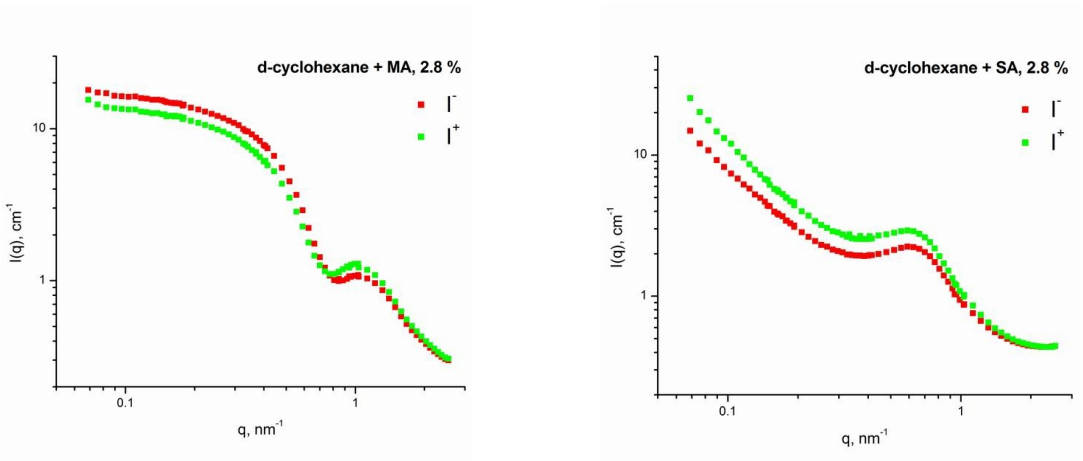


Fig. 2. Radially averaged scattering curves for two polarization states of the incident neutron beam. Samples are under saturation.

Experiment

Polarized neutron scattering was used to characterize the nuclear and magnetic structures of ferrofluids. In Fig.1 one can see examples of the obtained 2D detector images for neutron beams with two polarization states, which are along (I^-) and opposite (I^+) to the direction of the applied magnetic field (B = 2.5 T). The samples are saturated in this field. In the absence of a magnetic field both kinds of patterns are isotropic, while, when the field is turned on, specific anisotropy different for two polarization states appears. The difference is determined by interference between nuclear and magnetic scattering from the particles in ferrofluids. To follow this difference in the whole *q*-range covered the scattering patterns are averaged over the radial angle at the detector. Results are presented in Fig.2.

Achievements and Main Results

Several important conclusions can be made from the preliminary treatment. Structures of ferrofluids based on the two studied organic carriers are close, while the use of different surfactants results in significant structural differences. Despite the shorter length of the surfactant, ferrofluids with MA are as highly stable in the magnetic field as ferrofluids with OA. However, the scattering reflects the presence of significantly smaller particles in these systems, which means that the surfactant regulates the size distribution function of the stabilized particles during the preparation procedure. The stabilized size is determined not only by the length of the surfactant but also by its adsorption properties [4]. As concerns the magnetic structure, qualitatively, their peculiarities in ferrofluids with MA are similar to those obtained for ferrofluids with OA. The stability of ferrofluids with SA is worse in comparison with ferrofluids containing other two surfactants. This is reflected in the structural organization of the systems, namely in the appearance of aggregates. This makes these fluids close to polar ferrofluids. Nevertheless, peculiarities of the particles composing aggregates are observed in the SANS curves and can be analyzed quantitatively.

[1] V.L.Aksenov, M.V.Avdeev, M.Balasoiu, L.Rosta, Gy.Török, L.Vékás, D.Bica, V.M.Garamus, J.Kohlbrecher, *Appl. Phys. A* 74 (2002) s943.

[2] M.V.Avdeev, M.Balasoiu, V.L.Aksenov, V.M.Garamus, J.Kohlbrecher, D.Bica, L.Vékás, *J. Mag. Mag. Mater.* 270 (2004) 371.

[3] L.Vekas, D.Bica, M.Rasa, O.Balau, I.Potencz, D.Gheorghe, In *Micro and nanstrucutures*, Eds.D.Dascalu et al., Ed. Academiei Romane (2001) 127.

[4] M.Balasoiu, M.V.Avdeev, A.I.Kuklin, V.L.Aksenov, D.Bica, L.Vékás, D.Hasegan, Gy.Török, L.Rosta, V.Garamus, J.Kohlbrecher, *Magnetic hydrodynamics*, submitted (2004).

GKSS FORSCHUNGSZENTRUM in der HELMHOLTZ-GEMEINSCHAFT	EXPERIMENTAL REPORT	GeNF SANS-1

SANS-study of the size distribution of model-chylomicrons

Principal Proposer:	**Angelika Paschke**[1] [1]Universität Hamburg, Inst. f. Biochemie und Lebensmittelchemie, Hamburg
Experimental Team:	**Iris Oppermann**[1]**, Sabine Eichweber**[1]**, Götz Milkereit**[2] [2]Inst. of Organic Chemistry, University of Hamburg, Hamburg
User Group Leader:	**Götz Milkereit**
Date(s) of Experiment:	15-20 April 2004

Objectives:
Chylomicrons are lipoprotein complexes which carry dietary cholesterol and triglycerides from the small intestine to adipose tissue, liver and muscle cell after food ingestion. Model chylomicrons were produced in order to validate a method to separate the chylomicron-fraction into triglycerides and phospholipids using solid phase extraction. The size of these models had to be determined to verify the analogy with the real particles.

Experiment
Three different concentrations of chylomicrons in solution were measured (c_1 = 11.48 x 10^{-3} g/mL, c_2 = 8.6 x 10^{-4} g/mL, c_3 = 1.1 x 10^{-4} g/mL), model chylomicrons were prepared in D_2O. The shape of the curves did not change with increasing concentration, no concentration dependence was observed in this concentration range. The scattering curve indicated the formation of different aggregates in solution. Different models were applied to fit experimental data in the *q* range of 0.07 to 0.25 Å^{-1} and 0.005 to 0.05 Å^{-1}. The scattering curve together with the model-fits is shown in figure 1.

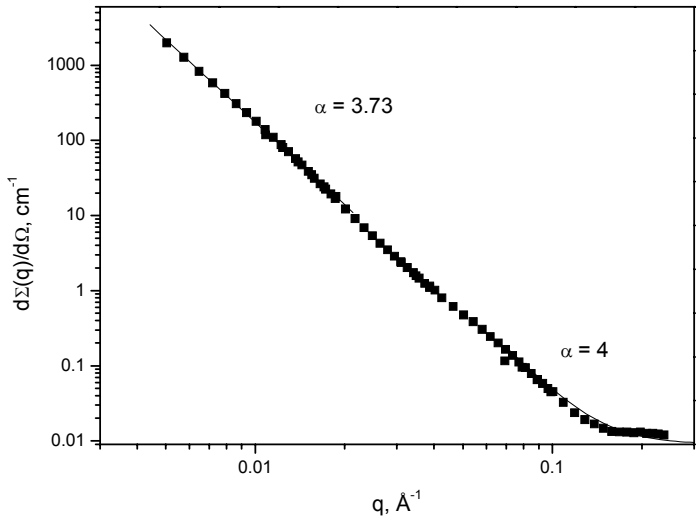


Figure 1: Scattering curve (filled squares) together with the model fits (solid line) for different parts of the scattering vector *q*: α = 4 for *q* = 0.07 - 0.25 Å^{-1} and α = 3.73 for *q* = 0.005 - 0.05 Å^{-1} (c_1 = 11.48 x 10^{-3} g/mL).

The q-range from 0.07 to 0.25 Å^{-1} was analysed by the power law
$\frac{d\Sigma(q)}{d\Omega} \sim A \cdot q^{-\alpha}$.
The obtained value of α = 4 points on a sharp and smooth surface of smaller-primary aggregates (analysis of large q interval). From the obtained Porod-paramter the surface and diameter of the aggregates were calculated [1]. The scattering at the low q-range is connected with formation of aggregates with polydispersity in the size distribution of the formed aggregates. The diameter of the smallest aggregates in this part of the scattering curve was estimated to be *d* ~ 100 nm (see also table 1). Additional Static and dynamic light scattering experiments (data not shown) showed that the main size distribution of the model-chylomicrons was in the range of d = 100 to 200 nm. Thus it can be excluded that the scattering at the low q-range belongs to the formation of aggregates with fractal surface [2].

Achievements and Main Results

The main size distribution of natural chylomicrons from human blood was estimated to be in the range of d ~110 nm (data not shown). The obtained diameter of the model-chylomicrons shows similar sizes (43 nm to 200 nm). It can therefore be concluded that the method for the preparation of the model-chylomicrons is suitable and will give reliable results on further experiments.

Table 1: Results from SANS analysis

	q = 0.07 - 0.25 Å^{-1}	**q = 0.005 - 0.05 Å^{-1}**
α	4	3.73
Surface *S*	1.60 x 10^4 cm^2/cm^3	
Diameter of Aggregates	43.0 nm (± 0.4)	> 100 nm

References

[1] Feigin, L.A., Svergun, D.I., *Structure Analysis by Small-angle X-ray and Neutron Scattering*, Plenum Press, New York, **1987**.

[2] Schmidt, P.W., In: *The Fractal Approach to heterogenous Chemistry*, D. Avnier (Ed.), Wiley & Sons, Chichester, **1989**, 67-79.

GKSS FORSCHUNGSZENTRUM in der HELMHOLTZ-GEMEINSCHAFT	EXPERIMENTAL REPORT	GeNF SANS-1

Structure of carbon from cellulose-based solid houshold wastes by SANS

Principal Proposer:	**Ekaterina A. Kraynova**[1]
	[1] Department of the Technique of Biospere Protection, D.Mendeleev University of Chemical Technology, Moscow, Russia
Co-Proposers:	**Mikhail V. Avdeev**[2], [2]Frank Laboratory of Neutron Physics, Joint Institute for Nuclear Research, Dubna, Russia
Experimental Team:	**Anatoly I. Rodionov**[1], **Vasyl Haramus**[3]
	[3] GKSS
User Group Leader:	**Mikhail V. Avdeev**[2]

Date(s) of Experiment:	April 2004

Objectives

Effective methods for utilizing household solid wastes are of current interest. The reported experiment was made in the frame of the study of technical carbon obtained as a result of special treatment of the mentioned type of wastes. This carbon is comparatively cheap, and there are prospects for its use in different industrial applications [1, 2]. The base of the treatment is the chemical reaction of cellulose and starch (which compose up to 80 % of the considered wastes) with the concentrated sulphuric acid. The remained acid is neutralized (e.g. sodium hydrocarbonate) or extracted from the system using water. As a result of the following drying, finely dispersed carbon is formed. Despite the fact that the reaction is well known, yet no systematic study of the resulting carbon has been made. The tasks of our study are to determine the composition and the size of structural units of the obtained form of carbon, as well as its pore structure in the scale interval of 1-100 nm. First, samples obtained from household solid wastes were probed by small-angle neutron scattering to clarify possibilities of the method with respect to the structural features of carbon, as well as the sensitivity of the scattering to different ways of preparation.

Experiment

Initially, a probe of cellulose containing household solid wastes (cardboard 38.0 w. %; food wastes 40.0 w. %; wood 3.0 w. %; leather and rubber 2.5 w. %; textiles 6.0 w. %; bones 2.0 w. %; polymeric materials 5.5 w. %; ferrous and non-ferrous metals 3.0 w. %) with cellulose content of about 50 w. % was treated with concentrated sulphuric acid. Then, the remains of sulphuric acid were removed in two ways. In the first case (sample 1) the extraction with distilled water was used. After drying in the air the sample looked like peat (pH about 6.5). In the second case (sample 2) the acid was neutralized with $NaHCO_3$. After drying in the air the sample was a homogeneous mixture of carbon-like material and crystallites of Na_2SO_4 with mass ratio 1:1 (pH about 7.5).

SANS curves for samples 1 and 2 and their preliminary treatment are shown in Figs.1-3. One can see that the way of removing sulphuric acid from the samples strongly affects the nanostructure of the obtained carbon material. For the sample 1 several structural levels are reflected in the scattering curve. Two characteristic radii, R, can be distinguished according to the rule $R \sim 2\pi / q$. They are $R \sim 15$ and 40 nm (corresponding peculiarities in the curve are marked in Fig.2). The scattering from the two corresponding levels are well described by a power law revealing fractal-type structures with mass fractal dimensions of 2.5 and 1.7,

respectively (Fig.2). The behavior of the curve at smallest *q*-values allows one to conclude about the more structural level with the characteristic radius $R > 60$ nm. The last estimate corresponds to the minimal *q*-value covered in the experiment. In contrast, in the case of sample 2 no size-effects are seen in the scattering curve (Fig. 3). The curve is fitted well by the power-law scattering corresponding to the mass fractal with the dimension of 2.5. The coincidence of this value with the fractal dimension of the first structural level of sample 1 (Fig.2) points to a common origin of the samples. So, water ablution of the initial sample results in appearance of smaller inhomogeneities in the material in comparison with the neutralization of sulphuric acid.

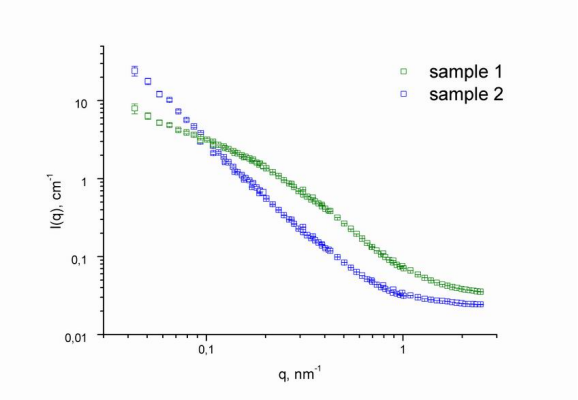


Fig. 1. Experimental scattering curves for samples 1 and 2.

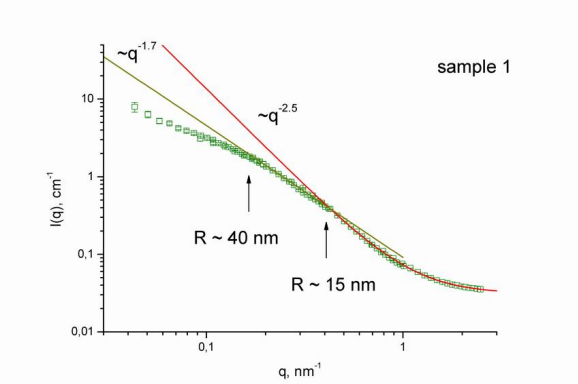


Fig. 2. Power-law treatment of the scattering curve for sample 1. Obtained exponents correspond to mass fractals with dimensions of 2.5 and 1.7. Arrows point to scattering peculiarities by which the characteristic size of levels' units are estimated.

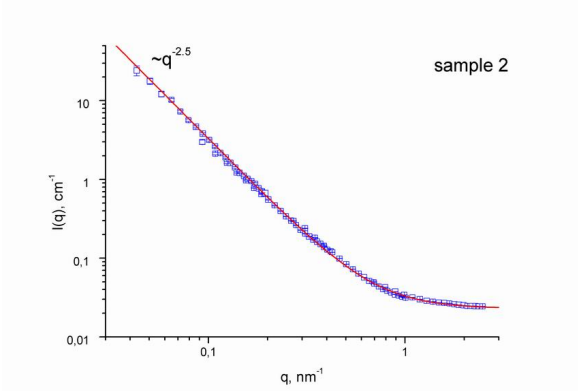


Fig. 3. Power-law treatment of the scattering curve for sample 2. Obtianed exponent corresponds to mass fractals with dimension of 2.5. No size-effects are observed.

Achievements and Main Results

The conclusion is that the nanostructure of the discussed carbon powders is sensitive to the way of treatment of the wastes, which can be effectively studied by the SANS method. Further investigations of the effect of the preparation procedure on the structural parameters of the materials obtained from the wastes, as well as investigations of the correlation between their absorption properties and structural characteristics are planned. For this purpose systems modelling the wastes will be used.

References:

[1] E.A.Kraynova, In *Uspekhi khimii i khimicheskoy technologii* Proc. RChTU V.XVII, N.12, RChTU: Moscow, p.47 (In Russian).

[2] Rodionov A.I., Klushin V.N., Sister V.G. "Technological processes of ecological safety" Kaluga, 2003 (In Russian)

GKSS FORSCHUNGSZENTRUM in der HELMHOLTZ-GEMEINSCHAFT	EXPERIMENTAL REPORT	GeNF SANS-1

Nanostructure of shungites by small-angle neutron scattering

Principal Proposer:	**Natalia N. Rozhkova**[1]
Co-Proposers:	[1]Institute of Geology, Karelian Research Center of Russian Academy of Sciences, Petrozavodsk, Russia **Mikhail V. Avdeev**[2], [2]Frank Laboratory of Neutron Physics, JINR, Dubna, Russia
Experimental Team:	**Vasyl Haramus**[3], [3] GKSS
User Group Leader:	**Mikhail V. Avdeev**[2]
Date(s) of Experiment:	April - May 2004

Objectives

In recent years, shungites attract much attention due to prospects of their use in different industrial and medical applications [1]. Shungite is a carbon-rich rock of Precambrian age, which is widespread over Russian Karelia. The general task is to distinguish the most effective ways to employ shungites. In this connection, the knowledge about the structure of this rock and its modifications is of great importance to realize the task. Previous investigations [1-2] including SAXS and SANS experiments with samples from various deposits showed that the structure of shungites has a common two-level organization in the scale interval 1-1000 nm, while the details depend on the origin. The first level (characteristic size > 100 nm) corresponds to fullerene-like hollow globules. Structural units of the second level (characteristic size 6 – 20 nm) are to be clarified.

Experiment

In the reported small-angle neutron scattering experiments we pursued two goals. The first one was to exclude from the SANS signal the scattering contribution corresponding to open porosity in shungites. For this purpose the shungite from the Maksovo deposit was chosen. This type has developed inner surface (BET value 180-240 m m/g) and high ratio between open and closed porosity (3:1). The contrast matching was used basing on the fact that the scattering length densities of carbon and heavy water are close. The scattering experiments were followed by the absorption of heavy water by the powder for two weeks. The comparison of the scattering curves from the initial powder sample and the D_2O absorbed powder during one week is presented in Fig.1. One can see that the significant qualitative changes of the scattering during absorption of D_2O take place at large q-values. After one week the scattering curve does not change significantly further, which means that the pores available for water are filled with D_2O completely and, hence, the open porosity is matched in the low curve in Fig.1. The detected changes allow one to conclude that structural features (characteristic size 6 nm, fractal dimension 2.7) reflected at large q-values correspond to the pore structure of the sample. An interesting observation is that after the matching the curve in this region can be connected with highly elongated particles producing the scattering of power-law type with exponent –1 (Fig.1). Presumably, these particles are closed pores. From the SANS curve one can estimate the limits for the characteristic cross section radius of the particles ($R < 2$ nm) and for their length ($L > 60$ nm). Elongated structures of larger size in shungites were observed previously in TEM experiments [1, 2]. The given experiment shows that smaller particles of this type are present in shungites. Their number is significant, which means that they should be taken into account when modeling the structure of shungites.

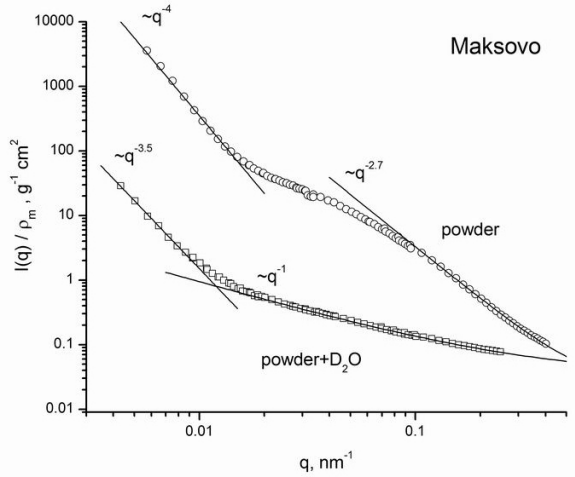


Fig. 1. Comparison of the scattering curves for initial powder of shungite and for the same sample after absorption of heavy water during one week. Changes in the scattering are due to matching of open porosity. The curves are calibrated on the bulk density of the powder. The upper curve (powder) is taken from [4].

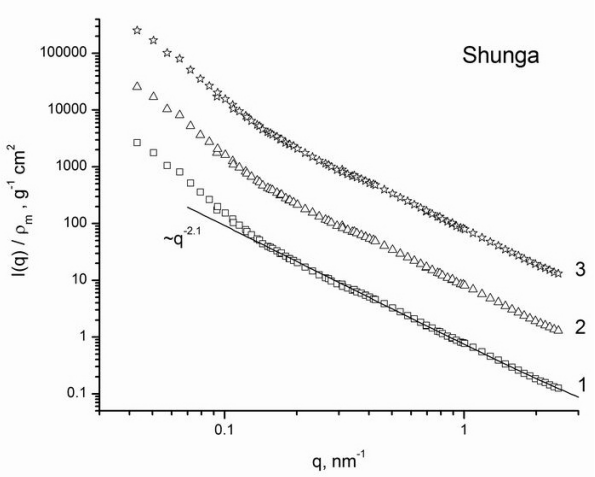


Fig. 2. Scattering curves for: (1) initial powder; (2) particles dispersed in water with ultrasound (22 kHz, 400 W), the curve is multiplied by 10; (3) the same, but with other frequency (44 kHz), the curve is multiplied by 100. No significant changes in the scattering are observed.

The second goal concerns aqueous dispersions of shungites. Basing on a specific interaction of shungites with organic solvents and water [1], the method to produce stable aqueous dispersions of shungites is under development. It is close to the solvent substitution method used for obtaining fullerene dispersions in water [3], when fullerenes are transferred from an organic solution into an aqueous phase with the help of the high power ultrasonic treatment. Such dispersions are highly stable (several months), however, the stabilization mechanism is unclear at the moment. The produced shungite dispersions are less stable (several days), nevertheless they can be used as well to obtain SANS curves. The task of our work is to disjoint the structural units of shungites, put them into water and apply the contrast variation technique with mixtures of light/heavy water to obtain information about the inner structure of the units.

Achievements and Main Results

At present, we are successful in design of stable dispersions with the shungite content ~1 mg/ml. However, no reliable SANS signals from these systems were detected, which means that the characteristic size of the particles is rather high to be resolved in SANS experiments. This is testified by the scattering from powders of shungite particles extracted from the dispersions. Examples of SANS curves for these powders based on shungite from the Shunga deposit are shown in Fig.2. Compared to the initial sample, no significant changes in the nanostructure of the shungite take place after it was dispersed in water with different parameters of the treatment.

The work is performed under ISTC project #2769.

[1] N.N.Rozhkova, *In Perspectives of Fullerene Nanotechnology*, Ed.E.Osawa, Dordrecht: Kluwer Academic Pub. (2002) 237

[2] V.V.Kovalevski, P.R.Buseck, J.M.Cowley, *Carbon* 39 (2001) 243

[3] M.V.Avdeev, A.A.Khokhryakov, T.V.Tropin, G.V.Andrievsky, V.K.Klochkov, L.I.Derevyanchenko, L.Rosta, V.M.Garamus, V.B.Priezzhev, M.V.Korobov, V.L.Aksenov, *Langmuir*, *20* (2004) 4363

GKSS FORSCHUNGSZENTRUM in der HELMHOLTZ-GEMEINSCHAFT	**EXPERIMENTAL REPORT**	**GeNF SANS-1**

The study of the orbital part of the magnetic scattering amplitude in the heavy-fermion compound $CeRu_2Si_2$ by means of SAPNS

Proposer:	**S.V. Grigoriev[1],** [1]Petersburg Nuclear Physics Institute, Peterburg, Russia
Co-Proposers:	**G.P. Kopitsa[1]**
Experimental Team:	**V.M. Haramus[2]**, [2]GKSS
User Group Leader:	**S.V. Grigoriev[1]**
Date(s) of Experiment:	3 – 12 May 2004

Objectives.
The proposal was aimed to observe and to investigate the orbital part of the magnetic scattering amplitude in heavy-fermion substances at low temperatures ((1 K) by small angle polarized neutron scattering (SAPNS). A good example of such systems is a family of compounds CeRu2(Si1-xGex)2 [1,2]. The single crystal CeRu2Si2 was used.

Experiment
1. Theoretical background. The theoretical studies [3 - 5] have shown that the orbital part of the magnetic scattering amplitude contains the term, which is singular at q (0 and gives rise the small-angle neutron scattering on the conduction electrons in metals:

$$F_{\sin g} = -i \cdot r \frac{\sigma[q \times p]}{q^2} \quad , \qquad (1)$$

where $r = |\gamma| e^2/mc^2 = 5.4 \cdot 10^{-13}$ cm and $\gamma = -1.91$ is the neutron *g*-factor; ***q*** is the momentum transfer and ***p*** is the electron momentum. It was also shown [3 – 5] that in metals the scattering cross section is proportional to $(m/M)^2$, where *m* is the effective mass of the electrons (carriers) and *M* is the mass of the neutron. For ordinary metals this factor is of order 10^{-5} - 10^{-6} and the neutron-electron scattering is negligibly small. However for some heavy-fermion substances $m \sim 100 m_e$ [2] and $(m/M)^2 \sim 10^{-2}$. In such cases the neutron-carrier scattering could be observed if one takes into account that the static cross section $d\Sigma(\vartheta)/d\Omega$ is proportional to ϑ^{-1} for $2E\vartheta >> T$ and $T/(\vartheta^2 E)$ for $T >> 2E\vartheta$, where $\vartheta << 1$ is the scattering angle and *E* is the neutron energy. The crossover from one regime to another is observed at $q_c = k \cdot \sin(T/2E)$. The presence of the magnetic field *H* results in the appearance of the additional term in the orbital part of the magnetic scattering amplitude [6,7]:

$$F_H \propto \frac{\sigma[q \times [H \times q]]}{q^4} \propto \frac{\sigma(Hq^2 - (Hq)q)}{q^4} \propto \frac{\sigma H_\perp}{q^2} \quad . \qquad (2)$$

In this case the static cross section $d\Sigma(\vartheta)/d\Omega$ of the neutron-carrier scattering becomes proportional to ϑ^{-2} for $2E\vartheta >> T$ and $T/(\vartheta^2 E)^2$ for $T >> 2E\vartheta$. Moreover, as it can be seen from Eq.(2), this scattering is anisotropic and could be observed at ***q*** that are perpendicular to the magnetic field ***H***.

2. Sample. The intermetallic system $CeRu_2Si_2$, which crystallizes in a body-centered tetragonal structure (the $ThCr_2Si_2$ structure) with lattice parameters $a = b = 4.197$ Å and $c = 9.797$ Å [1], is an archetypal heavy-fermion compound with a large value of the linear coefficient of the specific heat $\gamma = C/T \approx 350$ mJ/K^2 mol below $T \approx 1$ K [8,9]. According to data of the dHvA

experiments [10,11], in this compound the effective mass of quasi-particles foot up to ≈ $200m_e$. The large single crystal ($V \cong 0.4$ cm^3) used for our SAPNS measurements was grown in a three-arc furnace using the Czochralski method [1].

3. Experimental Technique. The SAPNS experiments were performed at the SANS-1, which operates in near point geometry and initial polarization $P_0 \approx 0.98$. In the present experiment the wavelengths $\lambda_1 = 8.1$ and $\lambda_2 = 10.5$ Å were used. The range of momentum transfer $1.5 \cdot 10^{-2} < q < 2 \cdot 10^{-1}$ Å^{-1} was obtained using three sample-to-detector distances (0.7 — 4.5 m). The scattered neutrons were detected by a position sensitive detector with 64x64 pixels. The sample was mounted in a criostat and the measurements were carried out at two different temperatures $T = 0.81$ K and $T = 290$ K. The external magnetic field H was changed from 0 to 1 T.

4. Data presentation. The momentum dependence of the cross section $d\Sigma(T \approx 0.8\ \text{K}, q)/d\Omega$ of SANS at H = 0 (empty circles) and H = 1T (solid circles) for two wavelengths $\lambda_1 = 8.1$ (red circles) and $\lambda_2 = 10.5$ Å (blue circles) are shown in Fig. 1. In the case of "zero" field ($H \approx 0$) the low temperature isotropic scattering in $CeRu_2Si_2$ system occurs for both wavelengths at $q \leq 0.04$ Å. This scattering is weak but statistically resolved while no scattering is observed at $q > 0.04$ Å. The applied magnetic field of $H = 1$ T results in the sharp increase of the cross section and, moreover, in appearance of the additional scattering at $q > 0.04$ Å, which has a small but clear maximum at $q \approx 0.067$ Å.

The q-dependence of the cross section $d\Sigma_H(q)/d\Omega$ for the field induced scattering is shown for both wavelengths in a log-log scale in Fig. 2. It is seen from the figure that there are two different q-range, where the cross section $d\Sigma_H(q)/d\Omega$ obeys the different scattering laws q^{-n}. The points of the crossover from one range to another are marked by the arrows in Fig. 2 and have the values $q_{c1} = 0.023$ and $q_{c2} = 0.03$ Å^{-1} for $\lambda_1 = 8.1$ and $\lambda_2 = 10.5$ Å, respectively. These values of q_c are in agreement with the estimations, which were obtained with the use of the expression $q_c = k \cdot \sin(T/2E)$ discussed above. In a small q range the scattering is well described by the law: $I(q) = A/q^4$ with $A \sim (H/E)^2$. These facts correspond well to the theoretically predicted expression (Eq.2) for the small-angle neutron-carriers scattering in the presence of the magnetic field H [6,7]. It should be noted that data presented in Fig. 1 and 2 were azimuthally averaged for a better statistics. On the other hand, as is evident from Eq.2, the field-induced part of the neutron-carrier scattering must be dependent on the direction of the magnetic field H, i.e. anisotropic.

The q-dependencies of $d\Sigma_H(q)/d\Omega$ along $\parallel$ (blue circles) and perpendicular to $\perp$ (red circles)

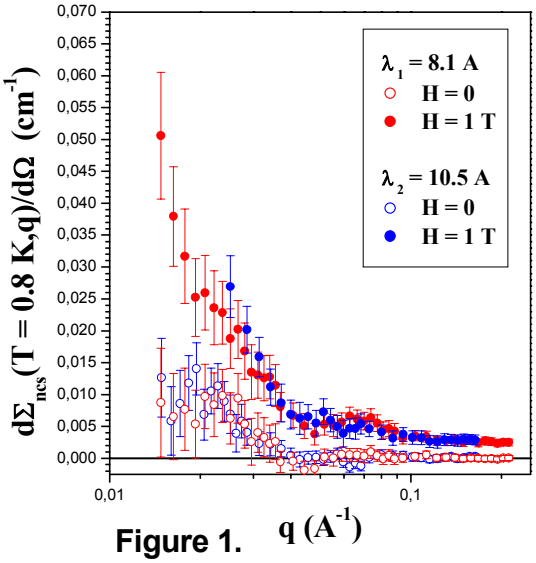


Figure 1.

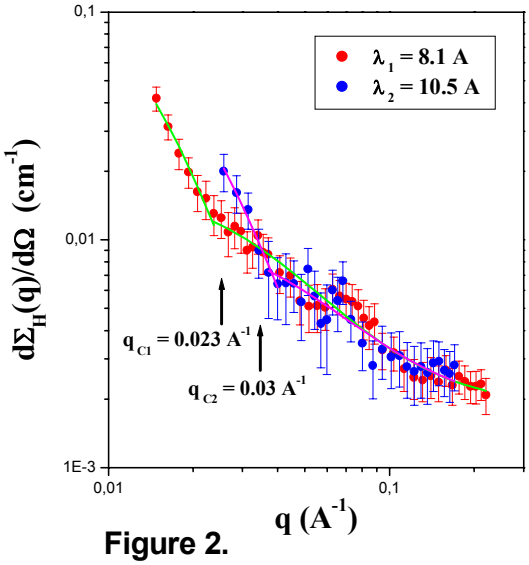


Figure 2.

the magnetic field H = 1 T are shown in Figs. 3 and 4 for the wavelengths λ_1 = 8.1 and λ_2 = 10.5 Å, respectively. It is apparently seen from these figures that in both cases the scattering becomes anisotropic at q < q_c. In this q-range the field induced scattering shows the remarkable growth at $\boldsymbol{q} \perp \boldsymbol{H}$ while at $\boldsymbol{q} \parallel \boldsymbol{H}$ it tends to zero with the decreasing q. At $q > q_c$ this scattering is isotropic.

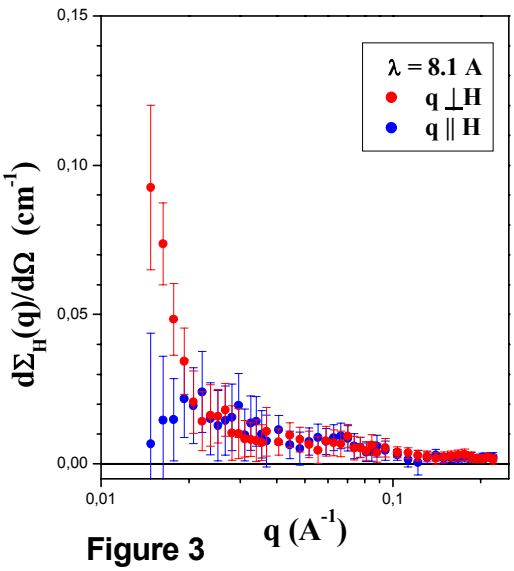


Figure 3

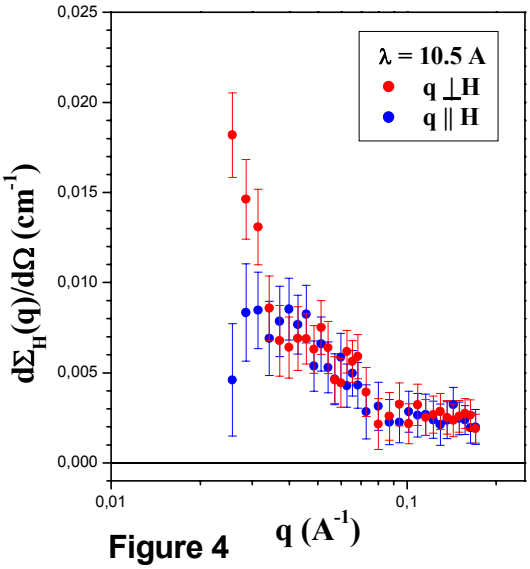


Figure 4

5. Achievements and Main Results. In the course of SAPNS experiment on the single crystal $CeRu_2Si_2$ at $T \approx 0.8$ K we found, firstly, the additional small-angle scattering at $q \leq 0.04$ Å (Fig. 1) which may be attributed to the contribution of the neutron-carrier scattering to the orbital part of the magnetic scattering amplitude in this heavy-fermion system, as predicted theoretically in [5]. Secondly, it was found that the applied magnetic field results in both the increase of the scattering at $q \leq 0.04$ Å and the appearance of the additional scattering at $q >$ 0.04 Å (Fig. 1). At small q the field-induced scattering is mostly anisotropic with respect to the magnetic field $\boldsymbol{H}$ while at large q scattering is isotropic and the crossover point is well described by $q_c = k \cdot \sin(T/2E)$.

References

[1] L. P. Regnault, W.A. Erkelens, J. Rossat-Mignod, P. Lejay and J. Flouquet, Phys. Rev B 38 , 4481 (1988).
[2] G.R. Stewart, Rev. Mod. Phys. 56, 755 (1984).
[3] R.J.Elliott, Proc.Roy.Soc. 235 A, 298 (1956).
[4] S.L.Ginzburg, S.V. Maleyev, Fiz.Tv.Tela 7, 3065(1965); Sov.Phys. Phys.Solids. 8, 2320 (1966).
[5] S.V. Maleyev, Lecture on "Polarised Neutrons and Magnetism", Gatchina (2002).
[6] R.J.Elliott, W.G. Kleppmann, J. Phys. C: Solid State Phys. 8, 2737 (1975).
[7] G.P. Kopitsa, S.V. Grigoriev, V.M. Garamus, V.V. Runov, *Neutron Scattering in the Investigations of Condensed Matter*, Workshop Proceedings (NSICM'2004), unpublished.
[8] M.J. Besnus et al., Solid State Commun 55, 779 (1985).
[9] R.A. Fisher, C. Marcenat, N.E. Phillips, P. Haen et al., J. Low Temp. Phys. 84, 49 (1991).
[10] H. Aoki, S. Ujii et al., Phys. Rev. Lett 71, 2110 (1993).
[11] S.R. Julian, F.S. Tautz et al., Physica B 199 - 200, 63 (1994).

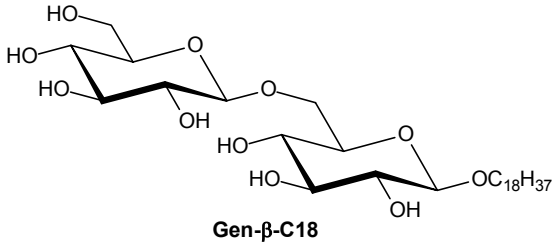
GKSS FORSCHUNGSZENTRUM in der HELMHOLTZ-GEMEINSCHAFT	**EXPERIMENTAL REPORT**	**GeNF SANS-1**

How thermotropic properties influence the formation of lyotropic aggregates near the critical micelle concentration

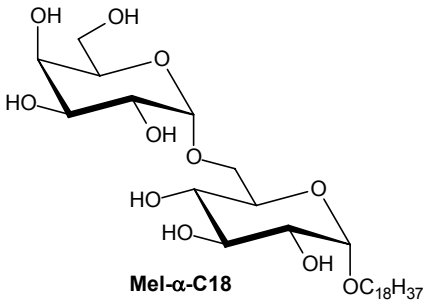
Proposer:	**Götz Milkereit[1],** [1] Inst. of Organic Chemistry, University of Hamburg, Hamburg
Co-Proposers:	**Volkmar Vill[1]**
Experimental Team:	**Vasyl Haramus[2], Regine Willumeit[2]**, [2]GKSS
User Group Leader:	**Volkmar Vill[1]**
Date(s) of Experiment:	May 2004

Objectives

In this work we investigated the lyotropic aggregation behaviour in dilute solutions of synthetic glycolipids with different molecular shapes: slightly wedge-shaped (**Gen-β-C18**) and significantly tilted (**Mel-α-C18**) (Fig. 1). We found that a complex thermotropic phase behaviour lead to the formation of complex aggregates already in dilute solution, whereas a lipid showing a simple thermotropic phase behaviour formed only small micelles in dilute solution.



Gen-β-C18



Mel-α-C18

Figure 1: *Chemical structures of the investigated lipids **Gen-β-C18** and **Mel-α-C18**.*

Experiment

SANS data were collected for solutions of **Gen-β-C18** (c = 1.0 x 10^{-4}, 5.0 x 10^{-4}, 1.0 x 10^{-3} g/mL) at 25 °C and **Mel-α-C18** (c = 6.3 x 10^{-4} g/mL) at 50 °C in D_2O, this concentrations are near the CMC (CMC <1x10^{-5} g/mL).

The obtained scattering curves are very different for the two glycosides (see figure 2). Compound **Gen-β-C18** shows a significant and rapidly decreasing scattering ($d\Sigma(q)/d\Omega \sim q^{-\alpha}$, α=1-2) at the low and intermediate intervals of the scattering vector ($q < 0.1$ Å^{-1}). At large values of the scattering vector *q* a diffraction maximum ($q \approx 0.15$ Å^{-1}) can be observed. In contrast to the scattering curve of the lipid **Gen-β-C18** the scattering curve of the lipid **Mel-α-C18** shows a small and approximately constant scattering at the low and intermediate

intervals of *q*. It can be assumed that the two lipids form different aggregates in aqueous solution: i) **Gen-β-C18** forms large aggregates with well-ordered plane or disc-shaped substructures; ii) **Mel-α-C18** forms small and near spherical aggregates.

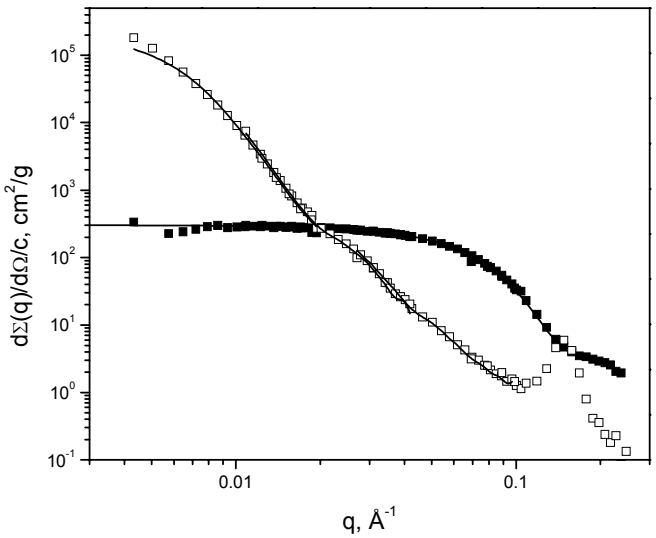


Figure 2: *Scattering curves and model fits for solutions of **Gen-β-C18** (c = 1.0 x 10^{-3} g/mL, empty symbols) and **Mel-α-C18** (c = 6.3 x 10^{-4} g/mL, filled symbols) in D2O. The curves are normalized to the concentration of the surfactant in micelles. The solid lines represent fits by the IFT method.*

Achievements and Main Results

The thermotropic properties of both compounds were already investigated [1]. **Mel-α-C18** shows only thermotropic Smectic A phase whereas **Gen-β-C18** shows thermotropic Smectic A and cubic phases. Also the lyotropic structures at a concentration of 0.1 g/mL were investigated for both compounds by small angle x-ray scattering (SAXS) [1]. At this high concentration both compounds form lamellar structures in a broad temperature range. SANS-experiments were performed at a concentration near the CMC that is about 10^2 to 10^3 times lower than the concentrations that were used for the SAXS-measurements. At this low concentration where the interaction between aggregates can be neglected a strong influence of the molecular shape on the aggregation behaviour is observed. The tilted melibioside **Mel-α-C18** is packed into spherical micelles, here the imbalance between the hydrophilic and hydrophobic moiety is large, whereas in the pure state this imbalance is small, as can be seen from the thermotropic phase behaviour. The slightly wedge- shaped gentibioside **Gen-β-C18** on the other hand is subject to the conflict between the hydrophilic and hydrophobic moiety, were the carbohydrate head favours the formation of columnar structures and the lipophilic tail favours the formation of lamellar structures. From the thermotropic properties this can be seen in the formation of a cubic phase besides the Smectic A phase. In dilute solution this effect decreases resulting in the formation of large disc-like aggregates, because a wedge-shaped structure would favour spherical or cylindrical structures and a rod-like structure the formation of bilayers. Hence large bilayer structures (discs) are formed as a tribute to the slightly tilted structure. With increasing concentration the interaction between the aggregates will be superior and besides other phases the lamellar phase with its bilayer structure dominates the lyotropic phases.

References

[1] Minden, v. H.M., Brandenburg, K., Seydel, U., Koch, M.H.J., Garamus, V.M., Willumeit, R., Vill, V., Chem. Phys. Lipids, 106 (2000) 15722

GKSS FORSCHUNGSZENTRUM in der HELMHOLTZ-GEMEINSCHAFT	EXPERIMENTAL REPORT	GeNF SANS-1

Influence of Ceramides on the DMPC Membrane Structure Studied via Small Angle Neutron Scattering

Principal Proposer:	**Jaromila Zbytovská** [1]
Co-Proposers:	[1] Institute for Pharmaceutical Technology and Biopharmacy, Martin-Luther-University Halle-Wittenberg, Halle/Saale, Germany
Experimental Team:	**V. Haramus**[2], **R. Neubert**[1], **S. Wartewig**[1], **M.A. Kiselev**[1,3]
	[2] GKSS
	[3] Frank Laboratory of Neutron Physics, JINR, Dubna, Russia
User Group Leader:	**R. Neubert**[1]
Date(s) of Experiment:	May 2004

Objectives

Ceramides are unique lipids, which abound in many special functions in biological membranes [1]. In interactions with phospholipids, they act as a messenger for apoptosis. Ceramide molecules are the most abundant lipids in mammalian skin, which are responsible for the excellent skin barrier function.

Experiment

The aim of present study was to examine an influence of ceramides on the DMPC membrane structure. Small angle neutron scattering (SANS) from unilamellar vesicles (ULVs) provides information about the vesicle size (average vesicle radius, R) and the membrane thickness (d_g) [2]. Ceramide 3 (N-stearoylphytosphingosine, Cer3) or Ceramide 6 (α-hydroxy-N-stearoylphytosphingosine, Cer6), which differ in their polar head group, have been incorporated into a DMPC matrix in the 0.14 molar concentration of ceramides. Multilamellar vesicles (MLVs) of this system have been prepared via the "thin layer method" [3]. ULVs have been produced by extrusion of the MLV-dispersion through a 500 Å filter. The final lipid concentration was 1% (w/w) in pure D_2O or 20% sucrose solution in D_2O. The measurements were carried out on the SANS1 spectrometer at 32°C at the wavelength of 8.1Å.

Achievements and Main Results

Fig. 1a shows the scattering curves from pure DMPC, DMPC/Cer3 and DMPC/Cer6 in D_2O. According to the model of separated form factors [4], a minimum typical of the average vesicle radius (q_{Rmin}) is observable in the curves. In this approach, the average vesicle radius can be calculated as $R=\pi/q_{Rmin}$. The R-values established from this experiment are summarized in table 1. It is obvious that in both D_2O and 20% sucrose solution environments, ceramides evoke an increase in the R-value compared to pure DMPC. This effect is stronger in the DMPC/Cer6 than in the DMPC/Cer3 ULVs. In all the systems, the R-values are higher in the D_2O samples than in the sucrose solution samples by about 15%. Accuracy of the q_{Rmin} is smaller in the samples with ceramides than in pure DMPC. This indicates increased polydispersity of the ULVs population in the ceramide samples. Summarizing these facts one can deduce that at 32°C, incorporation of ceramides into DMPC increases the membrane rigidity in comparison to pure DMPC.

Kratky-Porod analysis has been used for the scattering curves evaluation [5]. The membrane thickness was estimated from the absolute value of the slope of Kratky-Porod plot (Fig. 1b), so called gyration radius (R_g) as:

$$d_g^2 = 12 R_g^2$$

The values of d_g of the studied samples are shown in table 1. As in D_2O so in sucrose solution, at 32°C, the membrane thickness of DMPC/Cer ULVs is larger compared to pure DMPC. The d_g value of pure DMPC is about 35Å and of the DMPC/Cer systems about 40Å. No significant difference has been found between the two types of ceramides. The d_g values of the systems in D_2O and sucrose solution are not significantly different either.

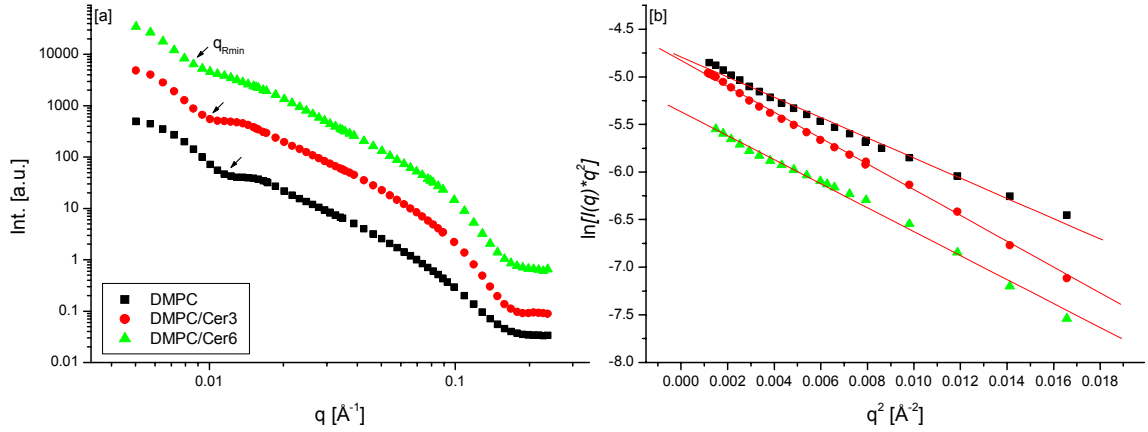


Figure 1: [a] Scattering curves from pure DMPC (black squares), DMPC/Cer3 (red circles) and DMPC/Cer6 (green triangles) ULVs measured in D_2O. [b] Kratky-Porod plot of the curves (the same legend).

Table 1: Calculated values of average vesicle radius and membrane thickness of DMPC, DMPC/Cer3 and DMPC/Cer6 ULVs.

System	D_2O		20% sucrose solution in D_2O	
	R [Å]	d_g [Å]	R [Å]	d_g [Å]
Pure DMPC	251	35.7	217	34.2
DMPC/Cer3	302	40.3	251	39.3
DMPC/Cer6	365	38.9	324	40.7

References:

[1] Krönke M., *Chem. Phys. Lipids*, **1999**, 101, 109-121.
[2] M.A. Kiselev, S. Wartewig, M. Janich, P. Lesieur, A.M. Kiselev, M. Ollivon, R. Neubert, *Chem. Phys. Lipids*, **2003**, 123, 31-44.
[3] R. R. C. New. Liposomes: a practical approach. Oxford University Press, **1990**.
[4] M. A. Kiselev, P. Lesieur, A. M. Kisselev, D. Lombardo, V. L. Aksenov, *Appl. Phys.*, **2002**, A 74, S1654-S1656.
[5] P. Balgavý, M. Dubníčková, N. Kučerka, M. A. Kiselev, S. P. Yaradaikin, D. Uhríková, *Biochim. Biophys. Acta*, **2001**, 1512, 40-52.

GKSS FORSCHUNGSZENTRUM in der HELMHOLTZ-GEMEINSCHAFT	EXPERIMENTAL REPORT	GeNF SANS-1

Aggregation of MEH-PPV polymer in solution studied by SANS

Principal Proposer:	**Rakchart Traiphol**
Co-Proposers:	Chemistry Department, Naresuan University, Phitsanulok, Thailand
Experimental Team:	Vasyl Haramus, GKSS
User Group Leader:	

Date(s) of Experiment:	May 2004

Objectives:

Conjugated polymers have attracted great attention recently. Their conjugated nature results in unique properties including high fluorescence and electrical conductive.[1-4] Therefore this type of polymers is potentially importance for many device applications such as organic light emitting diodes (OLED)[4], molecular wires[2] in molecular scale electronics, and chemical sensors[3]. The use of conjugated polymers is very promising in the field of microelectronics. However there are many steps needed to be understood in order to realize full potential of the conjugated polymers.

Experiment

To utilize conjugated polymers as a molecular wire in microelectronics, for example, it is crucial to learn how to capture polymer chains onto solid substrate in a controllable way. This normally involves dispersing polymers in solution. Then the chains are transferred onto solid substrates. The conformation of polymers in solution dictates the polymer morphology on solid substrate. Therefore one of a very important step is to understand factors affecting structure and conformation of polymers in solution. The electro-optical properties of conjugated polymers also depend on molecular conformation and the intermolecular interaction.[1] The conjugated polymers of interest in this study is methylethylhexyl-polyphenylenevinylene(MEH-PPV). This type of conjugated polymer tends to aggregate forming nanostructure in dilute solution, driven mainly by attractive π-π interaction between the conjugated backbones.[5] The close proximity between individual chains within aggregates allows an electronic communication between backbones, lowering the HOMO-LUMO energy gap. This results in the color change of polymer solution, which corresponds to the appearance of red-shift peak in UV-visible absorption spectra.[5]

This study investigated the influences of concentration, temperature and solvent quality on the aggregation of MEH-PPV in solution by using SANS. The MEH-PPV polymer was dissolved in chloroform_d solvent to the saturated concentration of about 3.6 mg/ml. However the high neutron absorption coefficient of chlorine atom in the solvent caused a relatively low transmission of neutrons from the sample, forbidding the SANS measurement. Toluene_d8 solvent, although, provided relatively low saturated concentration of about 0.4 mg/ml, the SANS profile was still able to be measured as shown in figure 1. The scattering intensity at q range larger than 0.1 $Å^{-1}$, arising mainly from the scattering of molecular length scale, was minimal due to the low polymer concentration. At smaller q range, however, the scattering intensity sharply increased, indicating the presence of large dimension aggregates. The scattering profile was fitted to the Porod's law scattering function, $I(q) = 2\pi(\Delta\rho)^2 Sq^{-4}$, where $\Delta\rho$ is neutron scattering contrast and S is total scattering interface

between the aggregates and solvent. This scattering characteristic suggests that the interface of the aggregates is extremely sharp and the aggregate dimension is also very large, allowing only the scattering from the surface of aggregates to be detected in this q range. Taking the prefactor value of q^{-4} term obtained from the fitting and neutron scattering contrast ($\Delta\rho$) between the polymer and toluene_d8 solvent, which is 4.9 x 10^{10} cm^{-2}, the surface per volume (S/V) of the aggregates is calculated to be equal to 1.95 x 10^4 cm^{-1}.

Achievements and Main Results

The rough estimation of the aggregate dimension could be obtained by making assumption that the aggregates exhibit spherical shape. Therefore the aggregate diameter calculated from this assumption and the S/V value is approximately 1.5 x 10^4 Å. To obtain more information about the morphology of the aggregates, atomic force microscopy (AFM) measurements were carried out on polymer thin films prepared by self-assembling of the same solution on silicon wafer. The aggregates on the si surface exhibited a characteristic morphology similar that of snowflake crystal. The aggregates also appeared to be two-dimensional flat with thickness of about 15 ± 5 nm. The diameters of the aggregates are approximately 4 micron, which is within the same order magnitude of the diameter estimated from SANS data.

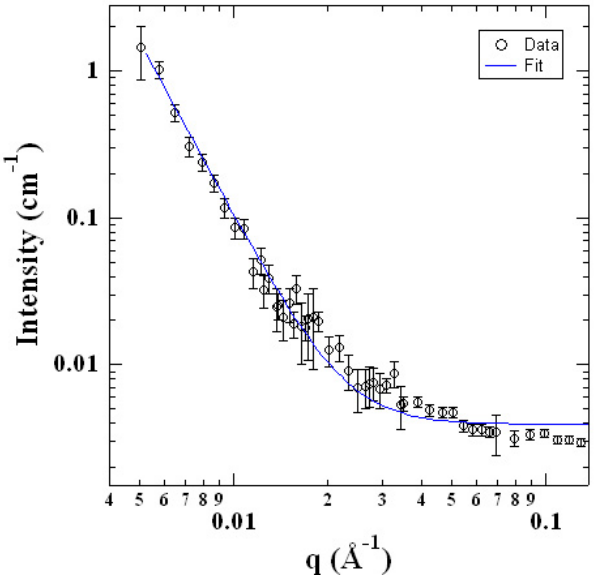


Figure 1 SANS profile of 0.4 mg/ml MEH-PPV solution in toluene_d8 measured at 25 °C. The solid line is obtained from fitting to Porod's law scattering function as described in text.

Increasing temperature to 70 °C resulted in a drastic drop of scattering intensity at low q region, indicating the dissociation of the MEH-PPV aggregates. The aggregates were also not detected when the polymer concentrations were decreased to 0.3 and 0.2 mg/ml.

References

1. Bunz, U. H. F. *Chem. Rev.* **2000**, *100*, 1605
2. Tour, J. M. *Acc. Chem. Res*. **2000**, *33*, 791
3. McQuade, D. T.; Pullen, A. E.; Swager, T. M. *Chem. Rev*. **2000**, *100*, 2537
4. Kraft, A.; Grimsdale, A. C.; Holmes, A. B. *Angew. Chem. Int. Ed*. **1998**, *37*, 402
5. Teetsov, J. A.; Vanden Bout, D. A. *J. Am. Chem. Soc.* **2001**, *123*, 3605

GKSS FORSCHUNGSZENTRUM in der HELMHOLTZ-GEMEINSCHAFT	**EXPERIMENTAL REPORT**	**GeNF SANS-1**

Demixing in Micellar Solutions Containing CTAC and a Partially Fluorinated Cationic Surfactant.

Proposer:	**Mats Almgren,** Uppsala University, Uppsala, Sweden
Experimental Team:	**Vasyl Haramus,** GKSS Research Centre
User Group Leader:	**Mats Almgren,** Uppsala University, Uppsala, Sweden
Date(s) of Experiment:	24-28 May 2004

Objetives

Mixtures of fluorocarbon and hydrocarbon surfactants in aqueous solution either assemble to form mixed micelles, or to form coexisting populations of hydrocarbon-rich and fluorocarbon-rich micelles. Only in few cases have uncontroversial evidence for a microscopic demixing it been presented. The objective was to settle whether a demixing into co-existing micelles occurs in water solutions containing both a normal cationic surfactant, CTAC, and a partially fluorinated surfactant, HFDePC, or if only mixed micelles are present.

Experiment

In SANS fluorinated surfactants and hydrogenated surfactants have quite different scattering length densities, and would seem to be ideally suited for contrast matching experiments. Attempts to utilize this method for demonstrating micellar demixing have not been successful, however, but have either shown that only mixed micelles are present or been inconclusive.[1] We have now made new series of measurements at several contrasts in order to test whether demixing occurs. First of all, we have performed measurements in water and salt(0.1 NaCl)/water solvents which gave us the possibility to make separation between internal demixing (within micelle) and external demixing (populations of different micelles). Further measurements with H_2O/D_2O variation as solvent in 0.1 NaCl/water solutions gave the magnitude of demixing and together with temperature jump above demixing T (at 60 ^oC there is 100% mixing of both surfactants) suggested the formation of two populations of fluorocarbon and hydrocarbon enriched micelles.

The cationic fluorocarbon surfactant HFDe-d-PC (N-(1,1,2,2-tetrahydroperfluorodecanyl)-pyridinium chloride), with a deuterated headgroup, was a gift from Prof. Asakawa (Kanazawa University, Japan). C_{16}TAC (cetyltrimethylammonium chloride) was prepared from the bromide salt (Serva, analytical grade) by ion exchange.

Data analysis by Indirect Fourier Transformation (IFT) was performed at q>0.02 $Å^{-1}$ where the effects of intermicellar interactions are negligible. This yields the scattering at zero angle ($d\Sigma_m(0)/d\Omega$) and the radius of gyration (R_g) without any presumptions regarding particle size and shape.

Figure 1 shows the scattering curves for solutions with salt (0.1 NaCl) and without salt in D_2O and at “match point” of mixture (35 % D_2O).

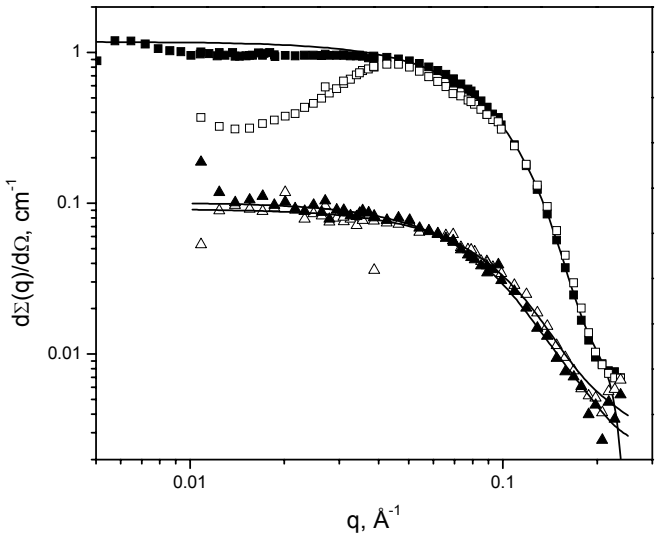


Figure 1. Scattering intensity as a function of scattering vector for samples with the same amounts of the surfactants HFDePC and CTAC (33mM surfactant *in toto*). Empty symbols are solutions without salt and filled symbols are solutions with 0.1 M NaCl, squares are solutions at D_2O and triangles are solutions at match point, solid lines are the fit by IFT.

Achievements and Main Results

The experiments show that a substantial residual scattering is retained at the solvent composition where the average scattering length density of mixed micelles would match that of the solvent. It is moreover observed that in solutions without added salt, a prominent correlation peak is present in 100% D_2O but disappears at the match point. The observations are in accord with a separation into two populations of mixed micelles of similar size but different compositions. They would not result from micelles of similar composition but inhomogeneous internal structure. Increasing the temperature from 25 to 60°C, where only mixed micelles are expected, reduces the scattered intensity at zero angle at the match point by a factor of four.

Acknowlegdement

This research project has been supported by the European Commission under the 6th Framework Programme through the Key Action: Strengthening the European Research Area, Research Infrastructures. Contract n°: RII3-CT-2003-505925'

References

[1]. See the following and references therin: Kadi, M.; Hansson, P.; Almgren, M.; Bergström, M.; Garamus, V. M. *Langmuir* 2004, *20*, 3933-3939.

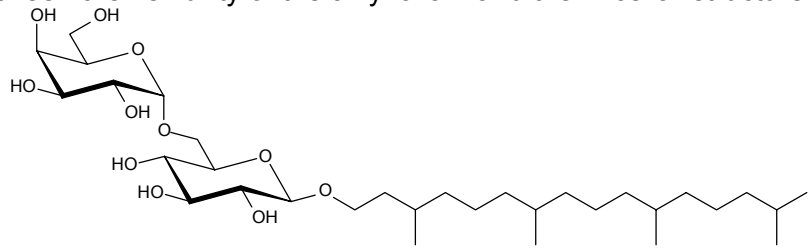
GKSS FORSCHUNGSZENTRUM in der HELMHOLTZ-GEMEINSCHAFT	**EXPERIMENTAL REPORT**	**GeNF SANS-1**

Influence of methylation of the alkyl chain on the micelle formation of glycolipids

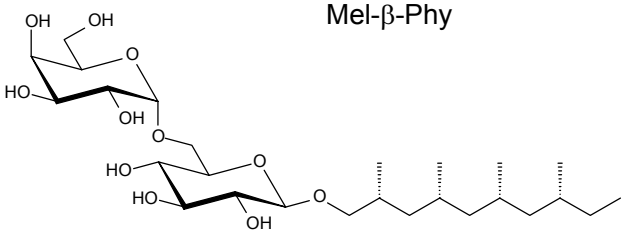
Proposer:	**Götz Milkereit[1],** Inst. of Organic Chemistry, University of Hamburg, Hamburg
Co-Proposers:	**Volkmar Vill,[1]**
Experimental Team:	**Vasyl Haramus[2], [2]GKSS**
User Group Leader:	**Volkmar Vill,[1]**
Date(s) of Experiment:	May, June 2004

Objectives

Alkyl glycosides bearing methyl branched alkyl chains, with a homogenous alternating sequence of the branching were synthesized. The isoprenoid type alcohols were obtained from plant (Phytanol), and animal source (The chiral alcohol (*2R,4R,6R,8R*)-tetramethyl-decanol was extracted from preen-glands of the domestic goose). As carbohydrate headgroup we choose the $\alpha 1 \rightarrow 6$ linked sugar melibiose consisting of a galactose and a glucose moiety. The micellar structure was investigated to give information about the relationship between the flexibility of the alkyl chain and the micellar structure (Fig. 1).



Mel-β-Phy



Mel-β-TMD

Figure 1: *Chemical structures of the investigated glycolipids: 1-O-[(2''R,4''R,6''R,8''R)-2'',4'',6'',8''-Tetramethyldecyl]-6-O-(α-D-galactopyranosyl)-β-D-glucopyranoside (**Mel-β-TMD**) and 1-O-(3'',7'',11'',15''-Tetramethylhexadecyl)-6-O-(α-D-galactopyranosyl)-β-D-glucopyranoside (**Mel-β-Phy**).*

Experiment

SANS data were collected for solutions of **Mel-β-TMD** (c = 1.0 x 10^{-3} g/mL) and **Mel-β-Phy** (c = 5.0 x 10^{-4} g/mL) in D_2O at a temperature of 50 °C for **Mel-β-Phy** and 20, 50 and 70 °C for **Mel-β-TMD** (Fig. 2). The obtained scattering curves are very different for the two glycosides. Compound **Mel-β-TMD** shows a high scattering at the lowest interval of the scattering vector ($q < 0.01$ Å^{-1}). At an intermediate q range (0.01 - 0.1 Å^{-1}) the scattering curve changes and shows a disc-like behaviour according to $d\Sigma(q)/d\Omega \sim q^{-2}$. For large values of q a diffraction

maximum (q≈0.15 Å^{-1}) is observed. In contrast the scattering curve of the lipid **Mel-β-Phy** shows a rod-like behaviour at an intermediate range of the scattering vector ($d\Sigma(q)/d\Omega \sim q^{-1}$). It can be assumed that the two lipids form different aggregate structures in aqueous solution:
- **Mel-β-TMD** forms large aggregates with partial plane or disc-shaped substructures
- **Mel-β-Phy** forms small rod-like aggregates

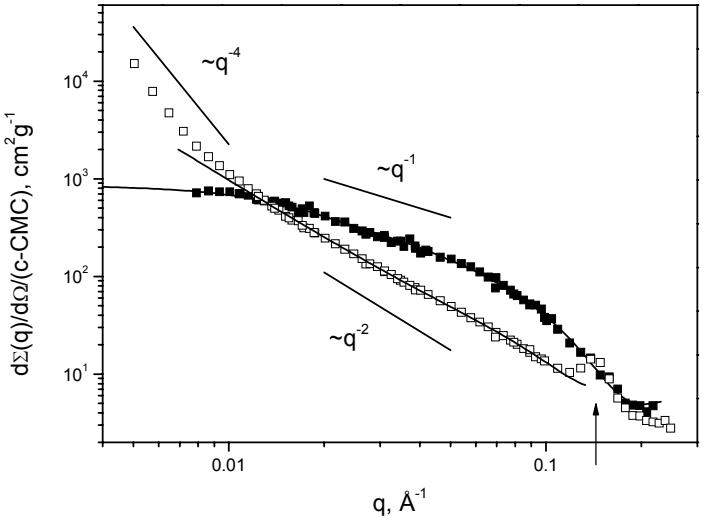


Figure 2: *Scattering curves and model fits for solutions of **Mel-β-TMD** (c = 1.0 x 10^{-3} g/mL, empty symbols) and **Mel-β-Phy** (c = 5.0 x 10^{-4} g/mL, filled symbols) in D2O, T = 50 °C. The curves are normalized to concentration of surfactant in aggregates (c-CMC). The solid lines represent fits or approximations. The arrow points on the position of the maximum in the scattering data of **Mel-β-TMD**.*

Achievements and Main Results

We found a strong dependence of the chain structure on the aggregation behaviour in water. **Mel-β-TMD** is not very good soluble in water, even above the Krafft-temperature **Mel-β-Phy** on the other hand has a greater hydrophobic moiety than **Mel-β-TMD**, but it is better soluble in water, due to the more flexible Phytanyl chain [1]. **Mel-β-Phy** forms cylindrical micelles due to the more flexible alkyl chain, whereas the less flexible TMD chain disables the formation of a large micellar solution region. Compound **Mel-β-TMD** forms disc-like aggregates/bilayers instead, of small or medium size because the stiff alkyl chain makes the formation of micelles less favorable, and gives the molecule a stiff rod-like shape.

Table 1: *Results of SANS data analysis by a model independent approach (IFT), model fitting and calculated parameter of aggregates for **Mel-β-Phy** (c = 5.0 x 10^{-4} g/mL, T = 50 °C) and **Mel-β-TMD** (c = 1.0 x 10^{-3} g/mL, T = 25, 50, 70 °C).*

	Mel-β-Phy	**Mel-β-TMD**
Micellar shape	cylindrical	bilayer/large aggregates
Radius [Å]	19.0 ± 0.4 (cross section)	~ 4000 (large aggregates)
Length [Å]	290 ± 10	--
Thickness of layer [Å]	--	39 ± 2 (bilayer)
Repeat distance between layers [Å]	--	40-50 (bilayer)
Mass per unit length [Å]	(1.4 ± 0.1) x 10^{-13}	--
Mass per surface unit [g/cm^2]	--	(8.3 ± 0.5) x 10^{-10}
Number of molecules per 1 nm of length	~ 13	--
Surface area per molecule [Å]	90	100 (bilayer)

References

[1] G. Milkereit, V.M. Garamus, J. Yamashita, M. Hato, M. Morr, V. Vill, *J. Phys. Chem. B*, in press.

GKSS FORSCHUNGSZENTRUM in der HELMHOLTZ-GEMEINSCHAFT	EXPERIMENTAL REPORT	GeNF SANS-1

Association between chitosan and oppositely charged surfactants

Proposer:	**Andra Dedinaite[1],** [1]Dept. Chemistry, KTH, Stockholm, Sweden
Co-Proposers:	**Magnus Bergström[2],** [2]Dept. Pharmacy, Uppsala University, Sweden
	Jan Skov Pedersen[3], [3]Dept. Chemistry, University of Aarhus, Denmark
Experimental Team:	**Vasyl Haramus[4],** [4]GKSS,
	Maria Lundin[1], Dept. Chemistry, KTH, Stockholm, Sweden
User Group Leader:	**Andra Dedinaite[1]**

Date(s) of Experiment:	17-21 May 2004 and 21-25 June 2004

Objectives

The main goal is the detailed understanding of the structures formed between the cationic naturally available polyelectrolyte, chitosan, and oppositely charged surfactant, sodium dodecyl sulphate (SDS). In particular, to explore how these structures can be modified when factors such as ionic strength, polylelectrolyte concentration and the molar ratio between the charged segments of the polyelectrolyte and the anionic surfactant are varied.

Experiment

The SANS-1 instrument employing a 2 mm cuvette was carried out. The q-range within 0.005 to 0.25 $Å^{-1}$ was covered. In all samples the solvent was deuterium dioxide. The surfactants used were hydrogenated (h-SDS) and deuterated (d-SDS) sodium dodecyl sulfate.

Achievements and Main Results

Small angle neutron scattering data obtained in 0.5 weight % chitosan solutions in D_2O are shown in Figure 1. The scattering intensity due to chitosan is low, however, from the slope of scattering curve in the q-range of 0.01- 0.1 $Å^{-1}$ it can be deduced that the chitosan adopts the conformation of a Gaussian chain in a theta solvent. It is known from turbidity measurements that in the presence of oppositely charged surfactant, SDS, the association between chitosan and SDS takes place. This is also reflected in SANS data: at the condition of the molar ratio between positively charged segments on the chitosan chain and the dodecyl sulphate ions being 0.5, scattering intensity is dramatically increased and a pronounced peak in scattering curve is present (Figure 1). The broad feature appears at high q-values with a peak at ≈ 0.16 - 0.17 $Å^{-1}$, corresponding to a characteristic distance of 37-39 Å. We attribute this scattering feature to the formation of a well-ordered mixed chitosan-SDS structure. A similar scattering curve is obtained in chitosan - dSDS mixtures. In D_2O solvent scattering due to dSDS is insignificant, thus only the chitosan contributes. The intensity of scattering is lower but nevertheless the scattering curve is featured by the presence of peak located at q values of about 0.18 – 0.19 A^{-1} (see Figure 1). Thus, it can be concluded that chitosan is included into the complex structure.

The experiments proved to be successful and the rigorous theoretical evaluation of the obtained results is under way.

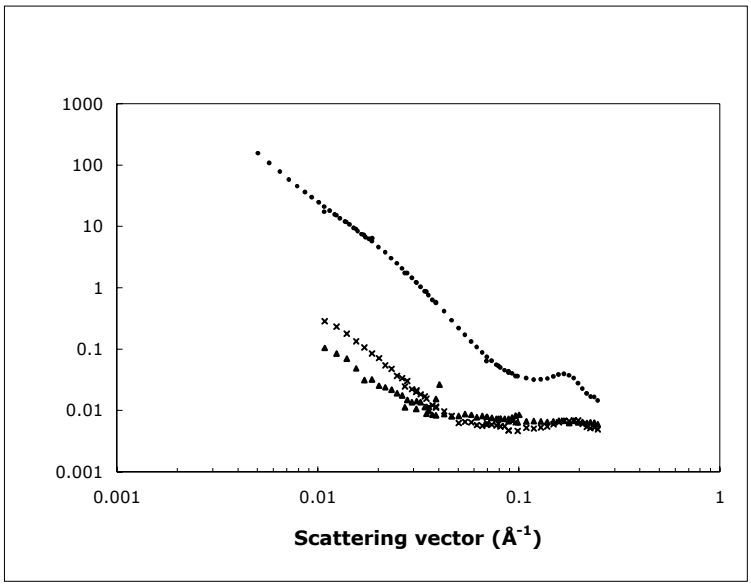


Figure 1. Scattering intensity, I(q), as a function of scattering vector, q. The concentration of chitosan is fixed at 0.5 weight %. Scattering due to chitosan without surfactant (triangles) and at the molar ratio of 0.5 between h-SDS (circles) or d-SDS (crosses) and the charged segments of chitosan.

Acknowlegdement
This research project has been supported by the European Commission under the 6th Framework Programme through the Key Action: Strengthening the European Research Area, Research Infrastructures. Contract n°: RII3-CT-2003-505925'

References
Andra Dedinaite, Maria Lundin, Vasyl Haramus, Jan Skov Pedersen, Magnus Bergström, Luis Bastardo “Solution Properties of Chitosan – SDS mixtures”
Manuscript in preparation.

GKSS FORSCHUNGSZENTRUM in der HELMHOLTZ-GEMEINSCHAFT	EXPERIMENTAL REPORT	GeNF SANS-1

Association between a graft comb polyelectrolyte and oppositely charged surfactants

Proposer:	**Per Claesson[1],** [1]Chemistry Department, KTH, Stockholm, Sweden
Co-Proposers:	**Andra Dedinaite**[1]
	Ricardas Makuska[2], [2]Dept. Polym. Chem., Vilnius Uni., Lithuania
Experimental Team:	**Iruthayaraj Joseph**[1]
User Group Leader:	**Per Claesson**[1]
Date(s) of Experiment:	21 June - 2.July 2004

Objectives

The goal of this project was to obtain a detailed understanding for the structures formed between a cationic low charge density graft comb polyelectrolyte and oppositely charged surfactants, and to understand how the grafted EO-chains influence the polyelectrolyte stiffness and association with surfactant. This is of great interest since it has been shown that such comb polyelectrolytes show benefits in various cleaning formulations also containing surfactants. Next to nothing was previously known about the association between this type of polyelectrolyte and surfactants. However, the studies carried out at GKSS have significantly improved the understanding of these systems.

Experiment

The experiments were carried out on the SANS 1 instrument employing the q-range 0.005-0.25 $Å^{-1}$. The graft polyelectrolyte, consisting of a methacrylate backbone and grafted 44-units long poly(ethylene oxide) (PEO) side-chains was specially made at Vilnius University. 98% of the segments in the polymer carry a grafted PEO-chain, and the remaining 2% of the segments carry a permanent positively charged quaternary ammonium group. This polymer will in this report be referred to as “M4”. The surfactants used were hydrogenated SDS and deuterated SDS. The solvents used were D_2O that contrast matches the dSDS, and a mixture of 82% H_2O and 18% D_2O, which contrast matches the polymer. In some cases salt was added to determine the effect of electrostatic interactions on the polymer conformation.

Achievements and Main Results

The scattering of a 0.2 wt% M4 solution in D_2O is shown in Figure 1 at three different salt concentrations. Clearly, the salt concentration does not affect the scattering curve, demonstrating that the polymer conformation is not affected by the electrostatic repulsion between the charged segments. Instead, it is the repulsion between the grafted PEO-chains that determines the solution conformation. The scattering intensity at low q-values decays as q^{-1}, demonstrating that the polymer conformation is that of a semiflexible rod. The change in slope to a q^{-4} dependence at intermediate q-values allows us to determine that the cylinder radius of the semiflexible chain is 40 Å and has a sharp interface.

The polymer conformation is also found to be insensitive to the presence of the anionic surfactant sodium dodecyl sulphate, SDS. It thus appears that the association between the polymer and the surfactant is rather limited, and the results for samples where the polymer is contrast matched suggest that the surfactant bind in monomer form to the polymer. Thus, neither does the surfactant form micelles along the polymer nor is any ordered internal

structure (e.g. hexagonal) obtained within the polymer-surfactant complex. This is strikingly different to what is observed for mixtures of polyelectrolytes without grafted sidechains and oppositely charged surfactants.
The results obtained will be reported in two manuscripts.

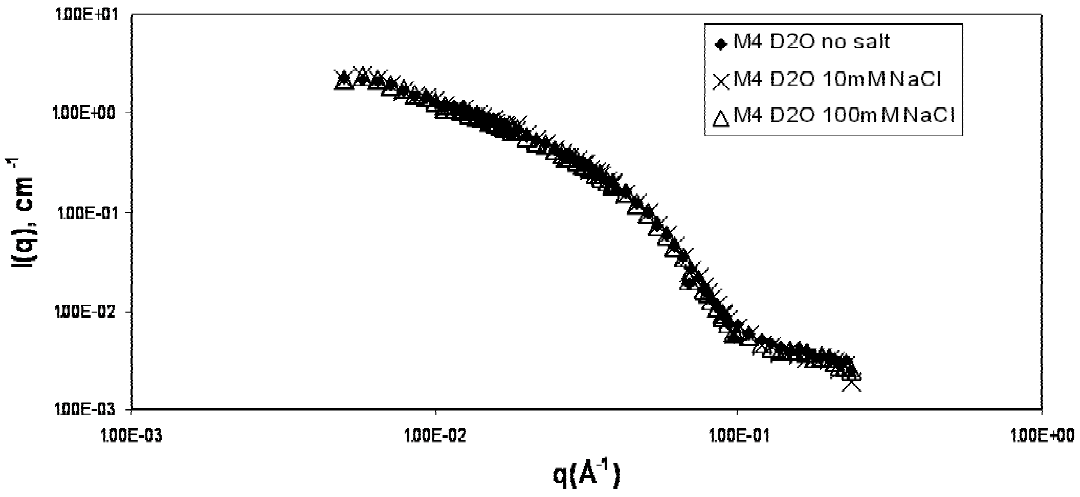


Figure 1. Scattering intensity vs. scattering vector for M4 samples (0.2%) in D_2O at different NaCl concentrations. The legends to the right show the different NaCl concentrations in the samples.

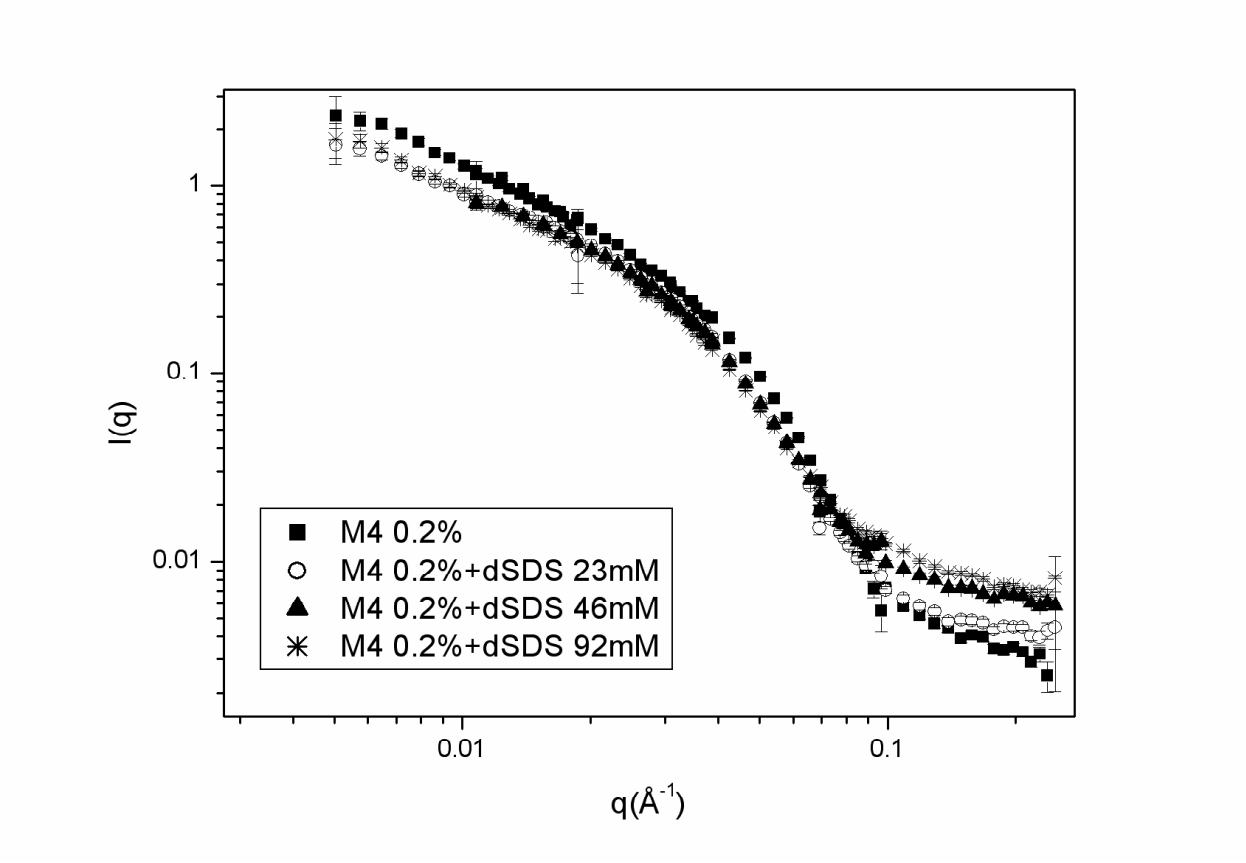


Figure 2. Scattering intensity vs. scattering vector for M4 samples in D2O at different *d*-SDS concentrations. The legends to the left show the *d*-SDS concentrations in the samples.

Acknowlegdement
This research project has been supported by the European Commission under the 6th Framework Programme through the Key Action: Strengthening the European Research Area, Research Infrastructures. Contract n°: RII3-CT-2003-505925'

References
Joseph, I., Bastardo, L., Dedinaite, A., Makuska, R. vanderWal, A., Garamus, V. M., and Claesson, P.M.
“Solution properties of a low charge density comb polyelectrolyte: Effects of added salt and anionic surfactant”
manuscript in preparation
Bastardo, L., Joseph, I., Garamus, V. M., and Claesson, P.M.
“Solution properties of a weakly cross-linked low charge density polymer: Effect of surfactant addition”
manuscript in preparation

GKSS FORSCHUNGSZENTRUM in der HELMHOLTZ-GEMEINSCHAFT	EXPERIMENTAL REPORT	GeNF SANS-1

Structure of ISCOMs

Proposer:	**M. Harms[1]**
Co-Proposers:	**C.C. Müller-Goymann[1], T. Paepenmüller**[1] [1] TU Braunschweig, Inst. f. pharm. Technologie, Braunschweig, Germany
Experimental Team:	**R. Willumeit[2], V. Haramus[2],** [2] GKSS
User Group Leader:	**C.C. Müller-Goymann[1]**
Date(s) of Experiment:	June-September 2004

Objectives

Quaternary systems consisting of saponine (Quilajasaponine A (QA)), cholesterol (Chol) and phospholipid in water or buffer form a variety of different structures, i.e. ring-like micelles, worm-like micelles and ISCOM matrices [1]. Demana at al. [2] prepared a pseudo-ternary phase diagram with coexistence of all structures in most cases. In some areas of the phase-diagram, one of the structures is predominating.

SANS experiments were performed to get a deeper insight into the different structures. Therefore four different systems with one of the structures predominating were prepared. Additionally pseudo-binary systems of different Chol / QA ratios were prepared representing worm-like micelles only.

Experiment

Samples were kept in quartz cuvettes with a path length of 2 or 5 mm at 25 ±1°C. Raw spectra were corrected for background scattering from the solvent (Tris-buffer 140 mM pH 7.4 in D_2O). The measured samples where prepared with D_2O instead of H_2O.

<u>All Structures</u>

The slope of a log-log-presentation should equal –1.0 at low h (scattering vector) in the case of stiff rodlike particles. With regard to the data obtained (Fig. 1) the existence of stiff worm-like micelles has to be excluded. Furthermore TEM micrographs reveal a helical superstructure. Hence such stiff rodlike particles are not likely to exist. The small minimum at 0.03 $Å^{-1}$ would not exist in rodlike particles as well, but might be due to periodical effects within the observed helical superstructure.

In the case of the liposomal system further deviations from theory occurred. The slope of a liposomal system should be close to -2.0. Yet a slope of -2.72 was determined. There is no explanation for this effect, yet. The small maximum at approx. 0.09 $Å^{-1}$ is due to the interlayer spacing of the multilamellar liposomes. The interlayer spacing was calculated from the Bragg equation as to approx. 70 Å.

The ISCOM system exhibits nearly the same slope as the liposomal system, this might be due to the coexistence of different structure types, i.e. liposomes.

It is also difficult to make a statement for the ring-like micelles due to the coexistence of different structures.

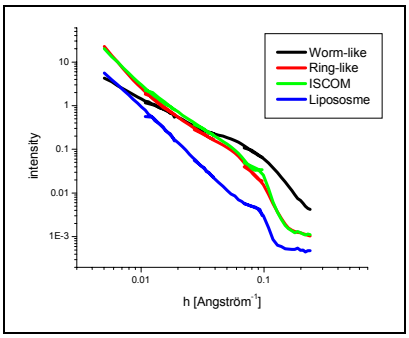


Fig. 1 Scattering data of systems with different predominant structures. Tab. 1 gives further descriptions of the composition of the systems.

Tab. 1 Composition and predominant structure of the investigated systems. Total concentration of solutes was 6.7 mg/ml. The slope was determined from the linear part of the scattering curve in a log-log presentation at low h.

Type	QA [%]	Chol [%]	DPPC [%]	Slope
Worm-like	70	30	0	-1.61
Ring-like	30	50	20	-3.11
ISCOM	30	30	40	-2.70
Liposome	0	30	70	-2.72

Worm-like micelles

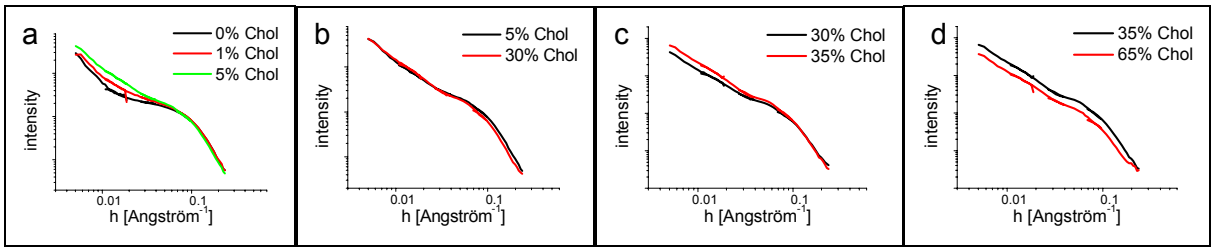


Fig. 2 Selected scattering data of pseudo-binary systems with different ratios of QA and Chol. The total solute concentration is 6.7 mg/ml.

Binary systems of QA and Chol are supposed to consist of worm-like micelles only. Marein et al. [2] have shown aqueous QA solutions to be micellar systems. In the present case an additional structure has to be concluded from the scattering data. We do not know what kind these structures are, yet.
As soon as Chol is added a change in the scattering curve can be observed Fig. 2(a). In the middle part of the curve additional scattering is detected. This effect gets more pronounced up to a content of 5% Chol. A further rise in Chol content up to 30% does not lead to additional changes in the scattering curve Fig. 2(b). An increase in scattering at small angles again takes place at 35% Chol Fig. 2(c). Further addition of Chol results in precipitation of the excess Chol [2]. Therefore the total scattering intensity decreases, while the form of the scattering curve does not change Fig. 2(d).
These data show, that Chol induces a change in the structure of the QA-micelles. QA can solubilize up to 35% of Chol, higher concentrations result in a precipitation of the excess Chol, while the ratio of QA and Chol within the micelles – and therefore the form of the micelles - is suggested to be constant.

Achievements and Main Results

A helical superstructure is most likely but cannot be proven. Data interpretation is complicated by the coexistence of different structures. Hence separation of these structures is required for further studies.

References

[1] Kersten, Spiekstra, Beuvery, Crommelin, Biochim Biophys Acta. 1062(2)(1991) 165 171
[2] Demana, Davis, Vosgeran, Rades, International Journal of Pharmaceutics 270(2004) 229

GKSS FORSCHUNGSZENTRUM in der HELMHOLTZ-GEMEINSCHAFT	EXPERIMENTAL REPORT	GeNF SANS-1

Studies of multifunctional ribosomal protein S1 from *Thermus thermophilus* at different ionic conditions in solution by neutron and X-ray small-angle scattering

Proposer:	**A. Timchenko [1]**
Co-Proposers:	**I. Serdyuk[1], O.Selivanova[1]**
	[1]Institute of Protein Research, Pushchino, Moscow Region, Russia
Experimental Team:	**V.Haramus[2], H. Kihara[3], K. Kimura[4]**
	[2]GKSS; [3]Physics Laboratory, Kansai Medical University Uyamahigashi, Hirakata Osaka 593, Japan, [4]Center of Medical Informatics, Dokkyo University School of Medicine, Tochigi, Japan
User Group Leader:	**R. Willumeit[2]**
Date(s) of Experiment:	July 2004

Objectives

Ribosomal protein S1 is the largest protein of eubacterial ribosomes with a molecular mass of 61 kDa and a length of 557 amino acid residues. It is an RNA-binding protein involved in retention of mRNA during initiation of translation and, maybe, during elongation. The most specific feature of the primary structure of the *Escherichia coli* protein S1 is the presence of six homologous amino acid repeats of about 70 amino acids long separated by spacers of 10-15 residues**.** Physical studies of isolated protein S1 from *E.coli* showed that the protein in solution manifested a highly extended, non-compact conformation with the longest dimension (23nm) of the whole ribosome[1]. At the same time our recent sedimentation and microcalorimetry data [2] have shown the compact structure of S1 *Th. th..* at low ionic strength. To study the detailed structural behaviour of this protein in solution at different ionic conditions we used SANS and SAXS techniques.

Experiment

As mentioned above, previous studies of ribosomal protein S1 from *E.coli* could show a strongly asymmetric, highly elongated shape of the protein in solution. At the same time, the highly elongated shape of the protein, with the dimension of order of the whole 30 S ribosomal subunit, did not seem to be very realistic for functioning ribosome. The electron microscopy study of the RNA-dependent RNA polymerase of Qβ-infected *E.coli* cells, where ribosomal protein S1 is included as a subunit, showed very compact, globular shape of all four subunits of the enzyme, suggesting the capability of the protein S1 to be stabilized in the compact conformation upon binding to functional surfaces. Similar situation favourable for acquiring compact conformation for protein S1 on the ribosome surface could not be excluded. Our sedimentation and microcalorimetry data support this conclusion. To study the macromolecular structure of S1 in details he we've applied the SANS and SAXS techniques.

Ribosomal protein S1 has been recently identified in *Thermus thermophilus* [2] and its gene has been expressed in *E.coli* overproducing strain BL21(DE3)pET21d-tthS1 and S1 has been successfully purified in the sufficient amounts. The protein was stored at 4°C in the precipitated form in $(NH_4)_2SO_4$. Samples for measurements were prepared by solving the precipitate either in 25 mM HEPES-NaOH (or NaOD) buffer, pH 7.5 (buffer A) or in 25 mM HEPES-NaOH (or NaOD) buffer, pH 7.5, with 100 mM NaCl (buffer B) and subsequent dialysis against the same buffers at room temperature overnight. The used protein concentrations were in the range of 0.15-1% for SAXS experiments and 1% for SANS

experiments. Synchrotron X-ray measurements were done on a small-angle camera BL-15A (Photon Factory, Tsukuba) [3].

Scattering patterns for S1 in both buffers plotted in the Guinier coordinates showed the nonlinear behaviour with the initial ordinate indicating the association of protein molecules. Thus, we can only estimate the value of radius of gyration (Rg). These values are in the range 7-11 nm to be considerably higher the expected one (about 3nm) for globular protein of 61kD. For S1 in the buffer A (without salt) the essential concentration dependence of scattering pattern is observed, and the associates correspond to trimers and higher order oligomers. For S1 in the buffer B (with salt) such dependence is weak, and the associates correspond preferentially to dimers, trimers. The more structural information we can obtain from the scattering patterns plotted in the Kratky coordinates. Fig.1 presents such plots for S1 in both buffers using light and heavy water. One can see the bell-shaped plot for S1 in the buffer B corresponding to compact particles. The value Rg estimated from the position of maximum on the Kratky plot was 2.9 nm which is expected for globular protein of 61kD. Thus, S1 particles at the moderate ionic strength in light water associates in the random order building dimers, trimers with the globular conformation of monomer inside them. Judging the Fig.1, S1 particles at the low ionic strength in light water form the globular-like high-order associates with the globular conformation of monomer inside them. The same behaviour of the Kratky plot in Fig.1 (left) was observed for SANS patterns in light water whereas in heavy water S1 particles form the fibrillar-like oligomers (see Fig.1(right)). The future model calculations will give the more detailed composition of oligomers.

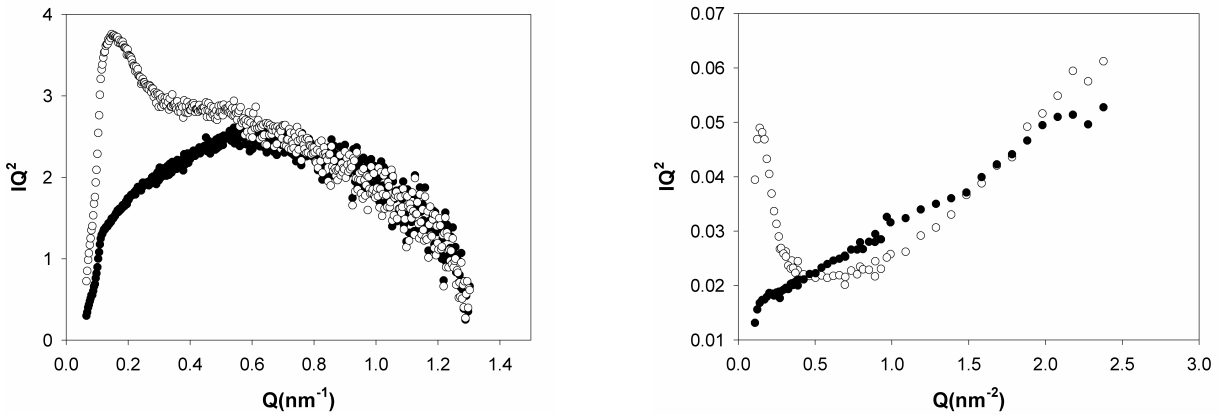


Fig.1 Left. Kratky plot of SAXS data for S1 in light water in buffer B (with salt, full circles) and in buffer A (without salt, empty circles). **Right.** Kratky plot of SANS data for S1 in heavy water in buffer B (full circles) and in buffer A (empty circles).

Achievements and Main Results

It has been shown that ribosomal protein S1 is globular at low and moderate ionic strength in light water, and form associates in solution. Probably, these associates are not stable and can dissociate into monomers under high pressure [2]. Association is maybe responsible for binding more than one molecule S1 per 30S ribosomal subunit [1]. It has been found that heavy water stimulates to form fibrillar-like associates of S1. For the detailed analysis of this process it is desirable to measure the concentration dependence of SANS patterns. Perhaps, the previous results on the high elongated shape of S1 were due to some association of protein under nonperturbed conditions. At any case molecular mass of S1 from *E.coli* in SAXS experiments [4] was evaluated to be 90kD. Further experiments on the study of interaction of S1 with native ligands may shed light on the functional meaning of association. This work was supported by the RFBR project no. 04-04-97319.

References

1. Laughrea, M. & Moore, P.B. (1977), *J.Mol.Biol.*, **112**, 399-421
2. Selivanova O.M. et al. (2003), J.Biol.Chem. , **278**(38):36311-4.
3. Amemiya Y. et al. (1983) *Nucl.Instr.Methods*, **208**, 471-477.
4. Labischinski, H. & Subramanian, A-R. (1979), *Eur.J.Biochem.*, **95**, 359-366.

GKSS FORSCHUNGSZENTRUM in der HELMHOLTZ-GEMEINSCHAFT	EXPERIMENTAL REPORT	GeNF SANS-1

Aggregative behaviour of Room Temperature Ionic Liquids in Water

Proposer:	**Alessandro Triolo** [1] Istituto per i Processi Chimico-Fisici, CNR, Messina, Italy
Co-Proposers:	**Charles M. Gordon** [2] Institut für Technische und Makromolekulare Chemie, RWTH Aachen, Germany
Experimental Team:	**Alessandro Triolo** [1]
	Vasyl Haramus [3], [3] GKSS
User Group Leader:	**Alessandro Triolo** [1]

Date(s) of Experiment:	16-24 August 2004

Objectives

Room Temperature Ionic Liquids (RTILs) are a novel class of materials that are characterised by ionic nature and low melting point. A typical representative of this class is 1-methyl-3-alkyl-imidazolium chloride [C_n-mim][Cl]. As a function of the alkyl chain length this salt can be either liquid or lead to crystalline phases at temperatures close to ambient conditions. These materials are attracting a great attention for a number of biocatalytic applications.
In this study we aim to characterise the formation of micellar aggregates when dissolving these salts in water. The SANS technique has been applied to extract morphological details at a nanoscopic spatial scale. These data have been complemented with conductivity and density data and we are in the progress of collecting light scattering data accessing similar experimental conditions.

Experiment

Aiming to create nanopools in water that are built up by green surfactants, we are presently investigating the aqueous solutions of RTILs. Such a study would provide a bridge between studies of the pure RTILs (that are already now used for biocatalysis) and aqueous solutions, the micellar aggregates being the connection betweent these two extreme situations.
We investigated a number of RTILs in aqueous (D_2O) solutions at concentrations between 0.1 and 8 % wt. at room temperature. In particular we explored the behaviour of the following RTILs: [C_n-mim][Cl] (with n=8,10,12,14,16) and [C_n-mim][Br] (with n=12,14,16).
Samples were contained in either 1 or 2mm thick cells and corrections for transmission, detector efficiency and empty cell were applied.
In Figure 1 we report the concentration dependence of the SANS patterns for the system [C_{16}-mim][Cl] in the composition range above the critical micellar concentration (that has been estimated to be approx. 0.115 % wt. from conductivity measurements).
In Figure 2 we report the effect of alkyl chain length at approximately constant surfactant concentration, in the case of the series [C_n-mim][Cl] (n=10-16), for c=2 % wt.

Achievements and Main Results

As can be expected from the ionic nature of the surfactant, a strong contribution arising from the structure factor can be found at the explored concentration regime.

While we were in the progress of developing the present set of measurements, a contribution appeared in the literature dealing with SANS investigation of much more concentrated solutions of shorter alkyl chains RTILs [Bowers, 2004].
We are presently in the progress of modelling these data sets in terms of structural models accounting for the core-shell nature of the aggregates and the electrostatic interaction between the aggregates.
Our present data set allow at present to conclude that also long chain RTILs lead to aggregative phenomena in aqueous solvent. This finding can be relevant for optimization of processing using these green materials.

References

[Bowers, 2004] J. Bowers et al., Langmuir, 20, 2191 (2004)

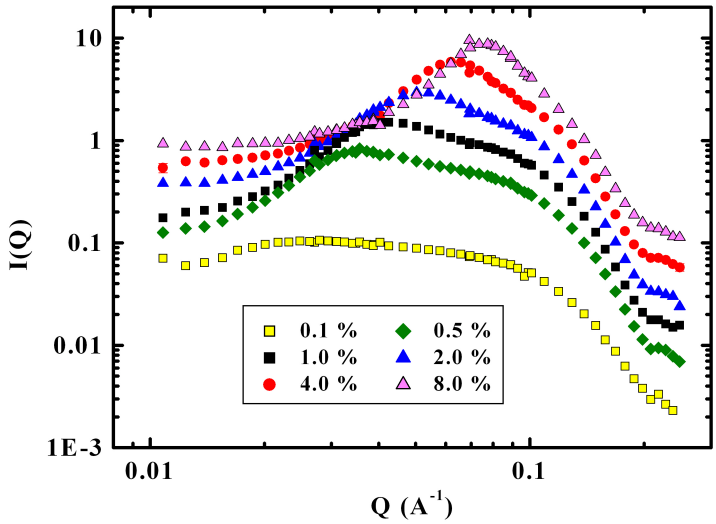


Figure 1

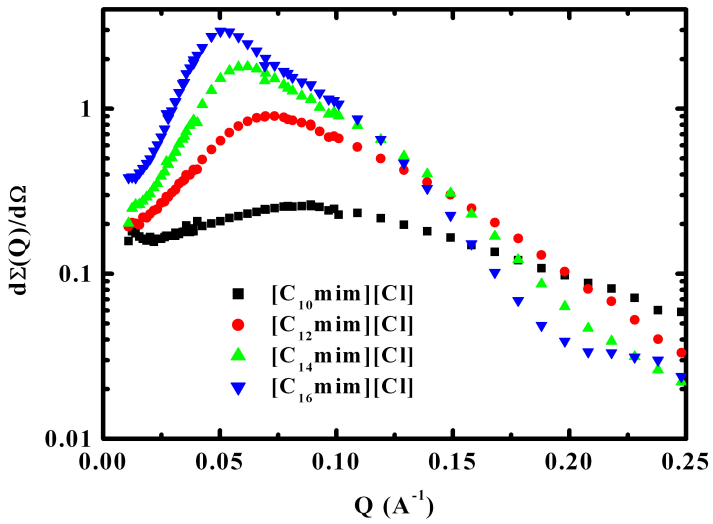


Figure 2

GKSS FORSCHUNGSZENTRUM in der HELMHOLTZ-GEMEINSCHAFT	**EXPERIMENTAL REPORT**	**GeNF SANS-1**

Structural investigation of mixed dipalmitoylphosphatidylcholine/ceramide 6 vesicles

Principal Proposer:	**Mikhail Kiselev**[1,2] [1] Martin-Luther University Halle-Wittenberg, Halle, Germany [2] Frank Laboratory of Neutron physics, JINR, Dubna, Russia
Co-Proposers:	
Experimental Team:	**Vasyl Haramus**[3], **Reinhard Neubert**[1] [3] GKSS
User Group Leader:	**Reinhard Neubert**[1]
Date(s) of Experiment:	September 2004

Objectives

Stratum corneum (SC) is the outermost layer of the mammalian skin and exhibits the major skin barrier. It is of importance to know the SC structure and properties on the molecular level for studying drug delivery through the SC. In this respect, an important subject is the structure of the SC lipid matrix. The major component of the SC matrix is ceramide molecules [1]. Phospholipids are major component of plasma membranes. Ceramides are normally minor components of cell membranes. Recently, ceramides have been recognized as a “second messenger” in cellular signaling cascades for the induction of apoptosis, growth, differentiation, and cell senescence. These funding have led to the resurrection of interest in the physical properties and dynamic lateral microheterogeneity of mixed phospholipid/ceramide systems [2].

Experiment

In present report, the structure of mixed dipalmitoylphosphatidylcholine (DPPC) /ceramide 6 unilamellar and multilamellar vesicles was studied by SANS at 20, 32 and 60^{o}C.

Ceramide molecules are non soluble lipids in water. In our experiment, the DPPC bilayer was used as matrix for the solubilization of the ceramide molecules. Mixtures of DPPC/ceramide 6 with molar ceramide fractions X_{Cer6}=0, 0.13, 0.24, 0.32 were prepared by thin layer method and hydrated in D_2O. Unilamellar vesicles were prepared via extrusion through pores with diameter 500Å. Two types of DPPC were used. Fully protonated DPPC and deuterated (DPPC-d75). Deuterated DPPC has 75 deuterons and 5 protons.

Figure 1 demonstrates the SANS spectra recorded at T=20^{o}C and 60^{o}C for DPPC/ceramide 6 and DPPC-d75/ceramide 6 unilamellar vesicles. Table 1 presents the dependence of thickness parameter on the ceramide concentration for T=20^{o}C, 32^{o}C, and 60^{o}C. The membrane thickness increases linearly on increasing of X_{Cer6} for T=20^{o}C and 32^{o}C. At T=60^{o}C membrane thickness has permanent value.

Achievements and Main Results

Fractal analyses of SANS curves with deuterated DPPC shows that at 60^{o}C the membrane scattering is near to the scattering from ideally mixed lamellar system ($V \sim d \cdot R^2$) with decreased contrast [3]. Scattering at 20^{o}C poses properties of mass fractal ($V \sim L^{2.4}$). The membrane at 20^{o}C is not homogeneous and consists of domains with different content of DPPC. The origin of membrane heterogeneity is a difference in the hydrocarbon chain length of used lipids (DPPC has 16 carbons and ceramide 6 has 24 carbons). The lateral structure of membrane changes to homogeneous at 60^{o}C after chain melting.

The deuterated samples at different temperatures have the same contrast as seen from the Intensities at small value of Q. Non deuterated mixtures demonstrate pronounced difference in the contrast due to increase DPPC hydration at 60°C. This finding can be explained by permanent hydration of ceramide 6 polar head group at 20°C and 60°C.

The scattering on multilamellar vesicles from pure DPPC has diffraction peak at $q=2\pi/d$, where d is repeat membrane distance. The diffraction peak amplitude decreases under increase of ceramide concentration. The scattering from extruded unilamellar and nonextruded multilamellar vesicles are near the same at $X_{Cer6}=0.32$. This experimental fact demonstrates the decrease of membrane interaction under ceramide 6 influence.

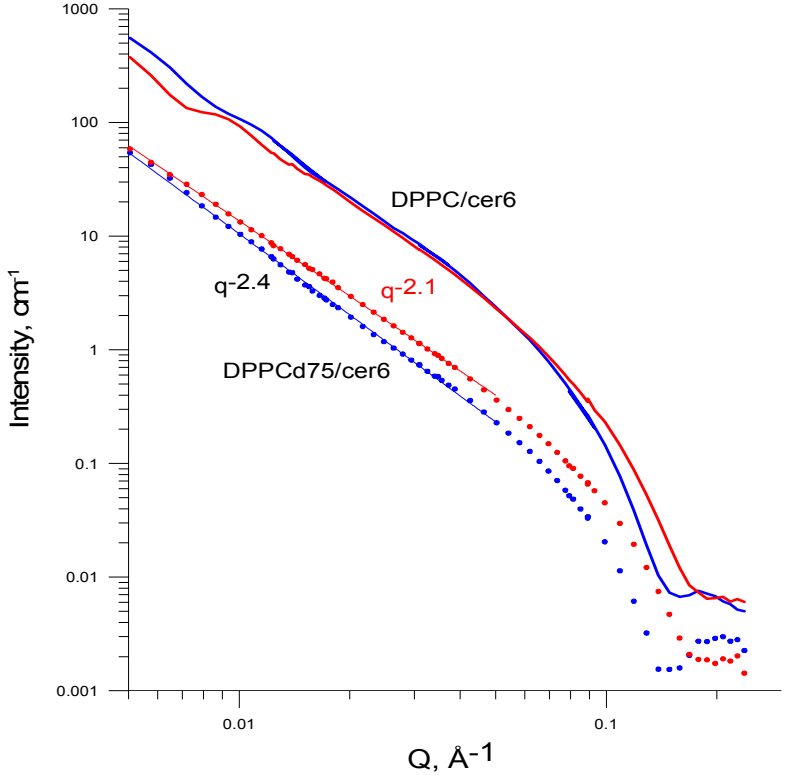


Figure 1: Coherent macroscopic cross section (Intensity) of vesicular populations recorded at T=20°C (blue curves) and T=60°C (red curves) for DPPC/ceramide 6 (solid line) and DPPC-d75/ceramide 6 (points) for $X_{Cer6}=0.32$.

Table 1: Dependence of membrane thickness parameter on the ceramide 6 concentration and temperature.

X_{Cer6}	T=20°C	T=32°C	T=60°C
0	43.9±0.4Å	43.9±0.4Å	39.8±0.4Å
0.13	44.5±0.5Å	45.3±0.5Å	Not measured
0.24	47.2±0.5Å	47.1±0.5Å	40.2±0.4Å
0.32	48.3±0.5Å	48.2±0.5Å	40.6±0.4Å

References:

[1] Neubert, R., Wohlrab, W., Marsch, W. Dermatopharmazie. Wiss. Verl.–Ges, Stuttgard, **2001**

[2] J.M. Holopainen, H.L. Brockman, R. E. Brown, P.K.J. Kinnunen. Interfacial interactions of ceramide with dimyristoylphosphatidylcholine: Impact of the N-Acyl Chain. *Biophys. J.,* **2001**, 80, 765-775.

[3] P.W. Schmidt. Use of scattering to determine the fractal dimension. Ed. D. Avnir. The Fractal approach to Heterogeneous Chemistry. John Wiley&Sons Ltd. **1989**.

GKSS FORSCHUNGSZENTRUM in der HELMHOLTZ-GEMEINSCHAFT	**EXPERIMENTAL REPORT**	**GeNF SANS-1**

Influence of Cholesterol on the Structure of SC Model Lipid Membrane Studied via Small Angle Neutron Scattering

Principal Proposer:	**Jaromila Zbytovská** [1]
Co-Proposers:	[1] Institute for Pharmaceutical Technology and Biopharmacy, Martin-Luther-University Halle-Wittenberg, W.-Langenbeck-Str. 4, D-06099, Halle/Saale, Germany
Experimental Team:	**V. Haramus[2], R. Neubert[1], S. Wartewig[1] and M.A. Kiselev[1,3]**
	[2] GKSS
	[3] Frank Laboratory of Neutron Physics, JINR, Dubna, Russia
User Group Leader:	**R. Neubert[1]**
Date(s) of Experiment:	September 2004

Objectives

Stratum corneum (SC), the outermost layer of the mammalian skin, represents a major limitation for the transdermal drug delivery. This unique membrane bases on lipid lamellae arranged in the intercellular spaces of SC. Unlike most biological membranes, which are composed of phospoholipids, the main components of SC lipid lamellae are ceramides (type 1-9), cholesterol, cholesterol sulphate and free fatty acids [1].

The aim of the present study was to investigate the membrane structure of a four-component SC model lipid membrane and to study an influence of cholesterol and cholesterol sulphate on the membrane.

Experiment

A basic SC lipid model sample consists of 55% ceramide 6 (α-hydroxy-N-stearoylphytosphingosine, Cer6), 25% cholesterol, 15% palmitic acid, and 5% cholesterol sulfate. Concentration of cholesterol or cholesterol sulfate has been varied in such way that the ratio between other components remained the same as in the basic sample. Unilamellar vesicles (ULVs) with a lipid concentration 1% w/w in Tris buffer in D_2O (pH=9) have been created from the systems. The measurements were carried out on the SANS1 spectrometer at 32°C, at the wavelength of 8.1Å.

The scattering curves obtained from the measurements are shown in fig. 1a. According to the model of separated form factors [2], a minimum (q_{dmin}) in these curves is observable. This minimum is proportional to the membrane thickness (d). The d-value can be calculated as:

$$d=2\pi/q_{dmin}$$

The membrane thickness of the measured samples obtained from the q_{dmin} values is summarized in table 1.

In contrary to scattering curves from phospholipid ULVs, a minimum relative to the vesicle radius (q_{Rmin}) is not perceptible in the curves of SC lipid vesicles. This indicates a higher polydispersity of the SC lipid ULV population in comparison to phospholipids.

The Kratky-Porod analysis has been used to evaluate the scattering curves [3]. The membrane thickness was estimated from the absolute value of the slope of Kratky-Porod plot (fig. 1b), so called gyration radius (R_g) as:

$$d_g^2=12R_g^2$$

The values of d_g of studied samples are presented in table 1.

Achievements and Main Results

The evaluation of the membrane thickness according to both methods provides similar results. The d-value of the basic sample with 25% cholesterol is 35.3Å. A decrease in the cholesterol concentration in the membrane evokes a distinct increase in the membrane thickness. This can be connected with the fact that cholesterol molecules are smaller than the long chain molecules of the other membrane components. Interestingly, though cholesterol sulphate has a similar molecule size to cholesterol, the increasing cholesterol sulphate concentration does not decrease the membrane thickness. This can be caused by the increasing hydration of the membrane via cholesterol suphate or perhaps by different location of the cholesterol sulphate molecules in the membrane (supposed they are closer to the external side of the membrane than the cholesterol ones).

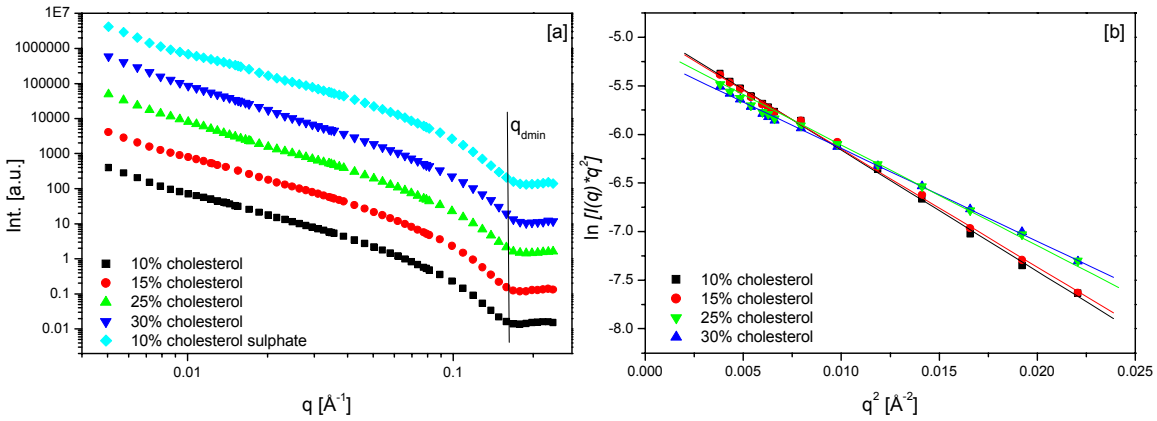


Figure 1: [a] The scattering curves from ULVs of the model SC lipid system with variation of cholesterol or cholesterol sulphate. The line shows the q_{dmin} area in the curves. [b] Kratky-Porod plots of the curves. The slope of this plot is proportional to the membrane thickness.

Table 1: Membrane thickness obtained from the q_{dmin} method and from the Kratky-Porod analysis.

Sample	**d (q_{dmin}) [Å]**	**d_g (K-P analysis) [Å]**
10% cholesterol	36.9	38.7
15% cholesterol	36.4	38.2
25% cholesterol	**35.3**	**35.3**
30% cholesterol	34.6	33.9
10% cholesterol sulfate	35.3	36.1

References:
[1] P. W. Wertz, B. van den Bergh, *Chem. Phys. Lipids*, **1998**, 91, 85-96.
[2] M. A. Kiselev, P. Lesieur, A. M. Kisselev, D. Lombardo, V. L. Aksenov, *Appl. Phys.*, **2002**, A 74, S1654-S1656.
[3] P. Balgavý, M. Dubníčková, N. Kučerka, M. A. Kiselev, S. P. Yaradaikin, D. Uhríková, *Biochim. Biophys. Acta*, **2001**, 1512, 40-52.

GKSS FORSCHUNGSZENTRUM in der HELMHOLTZ-GEMEINSCHAFT	**EXPERIMENTAL REPORT**	**GeNF SANS-1**

"Hydrophobic" effect of ethyl branching on the micellar structure of a long chain neoglycolipid

Proposer:	**Götz Milkereit,** [1] Inst. of Organic Chemistry, University of Hamburg, Hamburg
Co-Proposers:	**Volkmar Vill**[1]
Experimental Team:	**Vasyl Haramus**[2]**,** [2]GKSS
User Group Leader:	**Volkmar Vill**[1]
Date(s) of Experiment:	September 2004

Objectives

The main problem on investigation of the lyotropic properties of long chain n-alkyl glycosides and neoglycolipids with disaccharide headgroups is the high Krafft-eutectic temperature T_K [1], that makes the investigation of the lyotropic phases difficult [2,3]. The use of unsaturated or highly branched alkyl chains circumvented this problem, and became a standard procedure in liquid crystalline chemistry (see for example [4] and references cited herein). We synthesized a new neoglycolipid based on a secondary amino alcohol, that enables an easy structure variation (Fig. 1). The micellar structure in dilute solution was investigated and compared with similar maltosides (tetradecyl and stearyl).

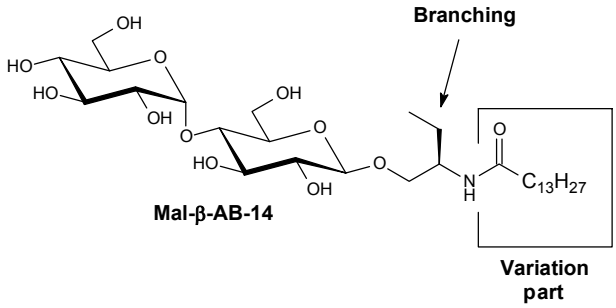


Figure 1: *Molecular structures of the new lipid* ***Mal-AB-14*** *(showing the main features that are different compared to normal alkyl glycosides).*

Experiment

Three different concentrations of **Mal-AB-14** in water were measured ($1x10^{-4}$, $5x10^{-4}$ and $1x10^{-3}$ g/mL, at 25 °C). For comparison solutions of stearyl maltoside (**Mal-βC18**) were prepared. The scattering curves of **Mal-AB-βC14** and **Mal-βC18** are typical for rod-like aggregates (Figure 2), i.e., at an intermediate q range the dependence of the differential cross section of neutron scattering is connected with $d\Sigma(q)/d\Omega \sim q^{-1}$ which reflects the scattering of the cross section of rod-like aggregates. In general the higher scattering of solutions of **Mal-AB-βC14** is connected with the formation of larger rod-like aggregates (micelles) compared to **Mal-βC18**.

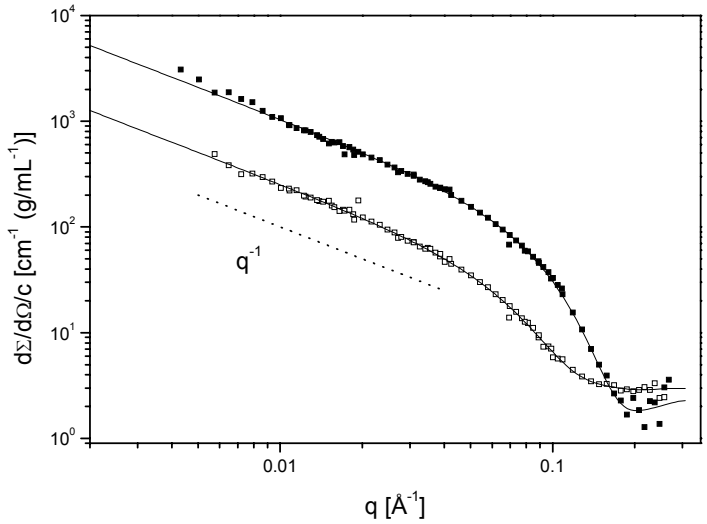


Figure 2: *Scattering data for **Mal-AB-14** at 25 °C (filled squares; c = 5x10^{-4} g/mL) and **Mal-β-C18** at 50 °C (empty squares; 4.3x10^{-4} g/mL) together with the model fits (solid lines). The dashed line shows the dependence $d\Sigma(q)/d\Omega \sim q^{-1}$.*

Achievements and Main Results

Micelles formed by **Mal-AB-14** are nearly two times larger than that formed by **Mal-βC18** and around six times larger than that formed by **Mal-βC14**. These differences cannot be explained by different experimental conditions. To our knowledge, the main effect arise from the fact that the amidic function builds up strong hydrogen bonding networks in the pure state and in solution [5, 6] that normally leads to the formation of rigid structures. The ethyl branching on the other hand disturbs the packing of molecules, leading to liquid crystalline phase behaviour already at ambient temperatures, or in this case to a better dissolving at ambient temperature compared to **Mal-βC18**. These two effects seem to be in equilibrium for **Mal-AB-14**, which leads to the formation of longer aggregates than formed by the alkyl glycosides of similar length. Another interesting observation is the fact, that the spacer despite the polar amido group does not increase the polarity. Otherwise an increase of the polarity would result in the formation of shorter micelles than observed for **Mal-βC14**. For **Mal-βC18** the minor axis values point on an extended conformation of the alkyl chains, also for **Mal-AB-14** the minor axis values are of similar size, suggesting an extended conformation of the alkyl chains too. It can be concluded that the molecules in **Mal-AB-14** micelles are more closely packed as in micelles formed by **Mal-βC18**. This can be possible due to an attractive interaction between the amidic groups, and / or a higher of hydration of the **Mal-βC18** carbohydrate headgroup.

Table 1: *Micellar form and parameter of micellar structure of the investigated compounds and literature data for comparison*

	T [°C]	c [g/mL]	Length [Å]	R_{CS} [Å]	a-axis [Å]	b-axis [Å]	axis ratio (ε)	M_L [g/cm]
Mal-β-AB-14	25	$5x10^{-4}$	1200 ± 200	22± 1	17	26	1.5	$1.69x10^{-13}$
Mal-β-C14[a]	25	$1x10^{-3}$	200	20± 1				
Mal-β-C18	50	$4.3x10^{-4}$	700 ± 100	27 ± 1	19	33	1.7	$3.48x10^{-14}$

[a] Data taken from Ref. [3]

References

[1] Laughlin, R.G., *The aqueous phase behaviour of surfactants*, Academic Press, London, **1994**.
[2] Hato, M., Minamikawa, H., *Langmuir*, 12, **1996**, 1658-1665.
[3] v. Minden, H.M., Brandenburg, K., Seydel, U., Koch, M.H.J., Garamus, V.M., Willumeit, R., Vill, V., *Chem. Phys. Lipids*, 106, **2000**, 157-179.
[4] Hato, M., *Curr. Opin. Coll. Interf. Sci.*, 6, **2001**, 268-276.
[5] Mitsutoshi, M., Vill, V., Shimizu, T., *J. Am. Chem. Soc.*, 122, **2000**, 12327-12333.
[6] Milkereit, G., Garamus, V.M., Veermans, K., Willumeit, R., Vill, V., *Chem. Phys. Lipids*, 131, **2004**, 51-61.

GKSS FORSCHUNGSZENTRUM in der HELMHOLTZ-GEMEINSCHAFT	**EXPERIMENTAL REPORT**	**GeNF SANS-1**

Segregated domains of fluorocarbon and hydrocarbon surfactants in vesicles revealed by SANS

Proposer: **Co-Proposers:**	**Tsuyoshi Asakawa**[1], Division of Material Sciences, Graduate School of Natural Science & Technology, Kanazawa University, Kanazawa 920-1192, Japan
Experimental Team:	**Vasyl Haramus,** GKSS
User Group Leader:	**Tsuyoshi Asakawa**[1]
Date(s) of Experiment:	24 September – 10 October 2004

Objectives

Mixtures of fluorocarbon and hydrocarbon surfactants show unusual characteristics of micellisation in aqueous solutions. Segregation within two types of micelles could occur owing to the variation of mutual solubility along with the micelle growth. It is hard to appreciate this behaviour due to experimental difficulties. The distribution of surfactants can be investigated by the contrast matching with SANS measurements. By varying the H_2O/D_2O ratio of the solvent, the contrast of either the hydrocarbon or fluorocarbon surfactant can be matched. The segregation within these micelles can be analyzed by SANS study.

Experiment

2-Hydroxy-1,1,2,3,3-pentahydroperfluoroundecyldiethylammonium chloride (IC11) in aqueous solutions self-assemble into vesicles with the addition of NaCl. Mixtures of hexadecyltrimethylammonium chloride (CTAC) and IC11 showed the presence of two types of micelles by pyrene fluorescence quenching method. With the addition of salts, the transition from coexistence of two types of micelles into mixed micelles could occur owing to the variation of mutual solubility along with the micelle growth. One type of mixed micelles with segregated domains of fluorocarbon and hydrocarbon surfactants within the micelles has been discussed. Experimental data to verify the feasibility of this hypothesis required for the demixing model.

SANS experiments were performed at the SANS1 instrument at the GKSS Research Centre, Geesthacht , Germany, as previously described.[1] The ranges of scattering vectors q were from 0.005 to 0.25 $Å^{-1}$.The SANS experiments were performed for different concentrations of IC11 in D_2O at 25□. The curves of SANS intensity versus q show the maxima at intermediate q values from 10mM to 100mM concentrations of surfactant. That means the strong interaction between charged micelles. The dependence of maximum on surfactant concentration reflects the mean distance between micelles, variation of size and shape. The data showed the change in the micelle structure from spherical one to some rod and/or disk-like micelles. The micellar growth of IC11 was perceived by the increase in surfactant concentration as well as the addition of salts.[2] In Fig. 1 the variation of SANS data with concentration of IC11 is shown. Data will be analyzed by model fitting of interactive charge spherical and vesicle aggregates.

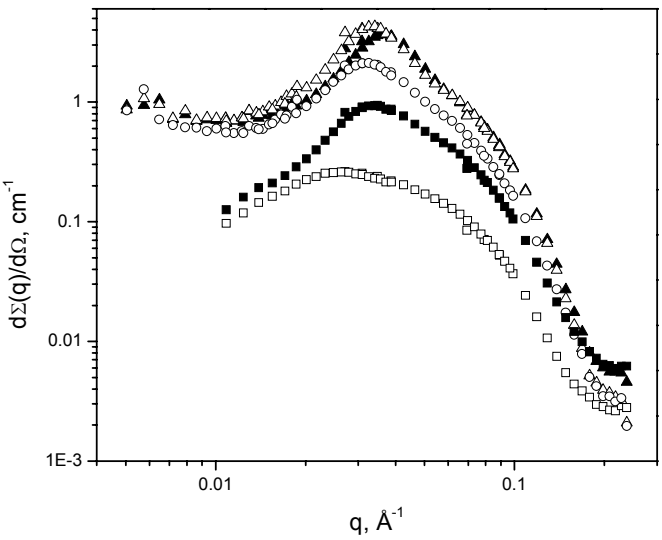


Figure 1. SANS data of IC11 in D_2O (IC11 concentration: empty squares 10 mM, filled squares 25 mM, empty circles – 50 mM, empty triangles – 75 mM, filled triangles – 100 mM).

Achievements and Main Results

The aggregation behaviour of fluorosurfactants in D_2O was studied by SANS experiments. We also studied the critical micelle concentration of IC11 by fluorescence quenching method using a halide sensitive probe. The degree of micellar counterion dissociation for IC11in D_2O gave lower than that in H_2O. The stronger hydrogen bonding in D_2O enhanced the micelle growth along with the counterion binding. The SANS data also suggest the larger aggregates of fluorosurfactants in D_2O.

References

1. Kadi M., Hansson P., Almgren M. Bergstrom M., Garamus M. V., *Langmuir* **2004,** *20,* 3933-3939.

2. Wang K., Karlsson G., Almgren M., Asakawa T., *J. Phys. Chem. B,* **1999** *103*, 9237-9246.

GKSS FORSCHUNGSZENTRUM in der HELMHOLTZ-GEMEINSCHAFT	**EXPERIMENTAL REPORT**	**GeNF SANS-1**

Determination of particle size in several micellar solutions dependent on antioxidants added

Proposer:	**Anja Heins,** [1] Department of Food Technology, CAU Kiel
Co-Proposers:	**Heiko Stöckmann**[1]
Experimental Team:	**Vasyl Haramus**[2], [2]GKSS
User Group Leader:	**Karin Schwarz**[1]

Date(s) of Experiment:	25.10.-9.11. 2004

Objectives

In dispersed systems, antioxidant activity is dependent on various factors related to the heterogeneous environment, and particularly influenced both by the molecular structure of the antioxidant and by the matrix constituents of the emulsion, e.g. emulsifiers[1]. The loss of effect is the result of interactions between antioxidants and emulsifiers at the interface [2]. To characterise these interactions various ^{1}H NMR-techniques [3-5] and ESR-measurements[6,7] have been carried out and consequently the different properties of emulsifiers could be correlated with the solubilization behaviour for antioxidants. It is of particular interest to ascertain whether the antioxidants are incorporated into the interior of the micelle or whether they are loosely associated with the exterior.

Experiment

The use of SANS was chosen to investigate the alteration of growth and shape of micelles with addition of small phenolic compounds with antioxidative properties. The surfactants were chosen due to their different charged and non-charged interfaces, like SDS with an anionic interface, CTAB with a cationic one and Brij 58 forming a non-ionic one. If the alteration of micelles could particularly be shown for CTAB micelles, our previous suggestion that CTAB shows different solubilization behaviour (incorporation) on antioxidants as non-ionic and anionic emulsifier (association with the exterior) could be supported. From this point it could be concluded, that differences in the activity of antioxidants with different emulsifiers occurs due to their different location of solubilization. It would be of interest as well, whether the increasing viscosity of CTAB solutions with different concentrations of added antioxidants is depending on swelling micelles[8], a chain of micelles[3] or building cylindrical micelles[9].

To investigate the growth and shape of the different micelles in the presence of antioxidants, different concentrations (0.1%, 0.2% and 0.3%) of propyl gallate were added to 1% CTAB. 1% SDS and 1% Brij 58 solution (0.2 sodium acetic buffer in D_2O). The scattering measurements were carried out on SANS-1 and the results were plotted by the scattering vector q (= $4\pi\sin(\theta/2)/\lambda$) against its intensity I(q) (Fig. 1, a-c). By fitting these scattering curves by IFT model for spherical micelles (Rg and I(0)) and by Debye-function for rod-like micelles (Rg and S(0)), radius of the spherical micelles as well as radius of cross-section and length of rodlike micelles could be calculated.

Achievements and Main Results

With SANS data it could be demonstrated that the surfactants lead to different solubilization behaviour of the propyl gallate. While propyl gallate did not impact the growth and shape of

Brij micelles, it had an increasing effect on micellar growth of CTAB micelles and a decreasing effect of SDS micelles. The Brij micelles kept spherical shape from a radius of 30.9 ± 0.31Å. SDS micelles had a spherical shape of 16.1 ± 0.1Å in absence of antioxidants but it decreased to 15.0 ± 0.1Å in presence of different propyl gallate concentrations.

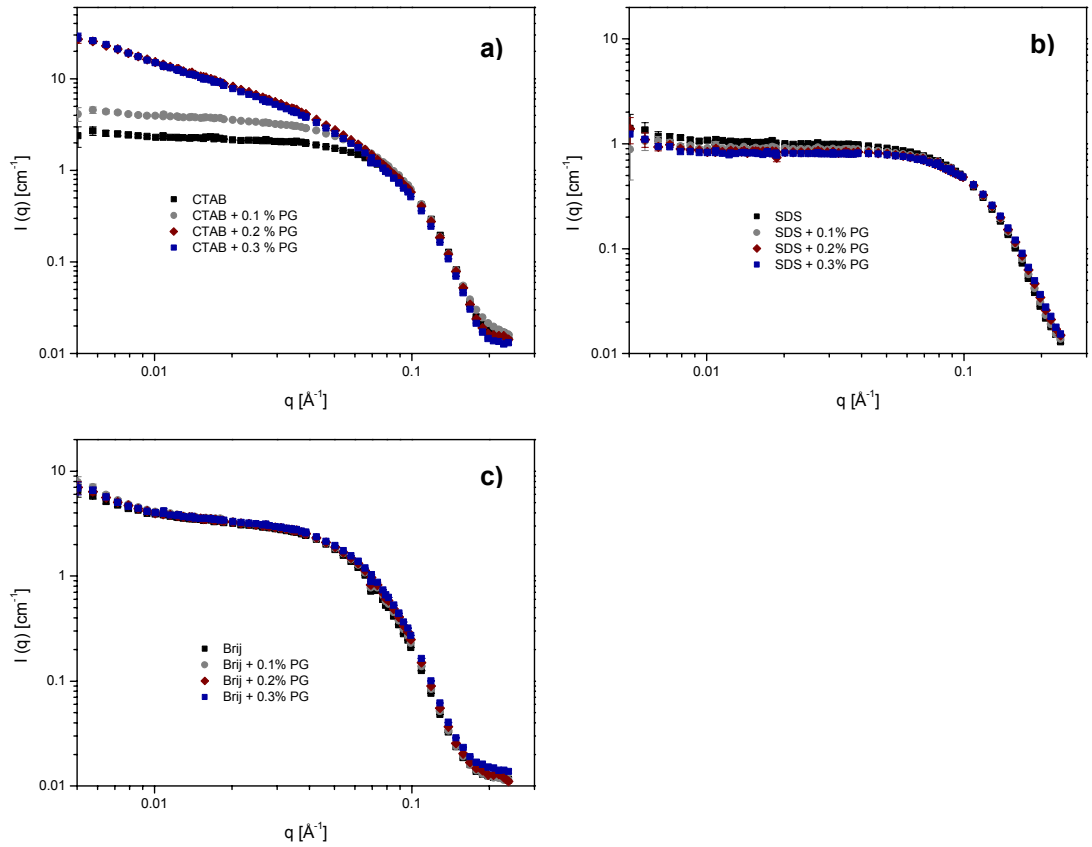


Figure 1: Scattering curves of different micelles in absence and presence of different concentrations of propyl gallate 1% CTAB (a), 1% SDS (b) and 1% Brij 58 (c).

However, CTAB micelle shape were altered from spherical (CTAB: 20.5 ± 0.1Å and CTAB + 0.1% PG: 23.8 ± 0.1Å) to rodlike micelles (0.2% PG: l = 609 Å r_{cs} = 21.6 Å and 0.3% PG: l = 713.4 Å, r_{cs} = 22.1 Å) with a one dimensional growing on increasing antioxidants concentration.

These results are in good accordance with the NMR data and demonstrated very well that antioxidants are incorporated in CTAB micelles, while they must be only loosely associated with the exterior of SDS and Brij micelles. From the obtained data it could be deduced that the activity of antioxidants is particularly affected by their location of solubilization that is dependent on nature of emulsifiers.

References

[1] *Stöckmann, H. & Schwarz, K.* (1999). Langmuir, 15, 6142-6149
[2] *Stöckmann, H.; Schwarz, K. und Huynh-Ba, T.* (2000) JAOCS, 77 (5):535-542
[3] *Rao, U.R.K., Manohar, C., Valaulikar, B.S. & Iyer, R.M.* (1987). Journal of Physical Chemistry, 91, 3286-3291.
[4] *Vermathen, M., Stiles, P., Bachofer, S.J. & Simonis, U.* (2002). Langmuir, 18, 1030-1042
[5] *Kreke, P.J., Magid, L.J. & Gee, J.C.* (1996). Langmuir, 12, 699-705.
[6] *McPhail, D.B., Hartley, R.C., Gardner, P.T. & Duthie, G.G.* (2003). J. Agri. Food Chem., 51, 1684-1690
[7] *Liu, Z.-L., Han, Z.-X., Chen, P. & Liu, Y.-C.* (1990). Chem. Phys. Lipids, 56, 73-80
[8] *Penfold, J., Tucker, I., Stables, E. & Thomas, R.K.* (2004). Langmuir (in press)
[9] *Goyal, P.S. & Aswal, V.K.* (2001). Current Science, 80, 972-979.

GKSS FORSCHUNGSZENTRUM in der HELMHOLTZ-GEMEINSCHAFT	**EXPERIMENTAL REPORT**	**GeNF SANS-1**

Investigations on Structure Changes and Length Scales in Copolymer/SDS mixtures

Proposer:	**Edda Kettler**[1], [1]Institut for Physical Chemistry, University of Aachen, Aachen, Germany
Co-Proposers:	**Walter Richtering**[1]
Experimental Team:	**Vasyl Haramus**[2], [2]GKSS
User Group Leader:	**Walter Richtering**[1]

Date(s) of Experiment:	15.–19. 11. 2004

Objectives

Measurements at SANS-1 on samples of methacrylic acid / ethyl acrylate copolymer with 150 ppm crosslinker and protonated as well as deuterated SDS shall help to evaluate how the two relaxation times seen in rheological flow curves (picture 1) correspond to structure changes in the copolymer or to interaction changes between copolymer and surfactant (SDS). To study structure and scattering contributions of the copolymer in these mixtures a little closer we measure a concentration line of copolymer (range 0.15 – 1.0 wt%) with 150 ppm crosslinker in basic D_2O without surfactant.

Experiment

- The Copolymer was obtained from Ciba Specialty Chemicals, Switzerland. Heavy water (99.96 %) was obtained from Merck, Germany. The anionic surfactant $C_{12}H_{25}SO_4Na$ (SDS) as well as NaOH for adjusting pH of all samples were obtained from Sigma, Germany. Deuterated SDS was obtained from Medical Isotopes Inc. Canada. Samples were prepared by mixing 0.6 wt% Copolymer with 0.27 mM protonated or deuterated SDS which is well above the cmc of SDS ($8.3 \cdot 10^{-3}$ mM) in heavy water and adjusting pH by adding NaOH in D_2O. The concentration line was prepared by adding 0.15, 0.30, 0.60 and 1.0 wt% Copolymer to heavy water and adjusting pH by adding NaOH. All samples were transparent and stable during the experiments.
- Three samples of 0.6 wt% methacrylic acid / ethyl acrylate copolymer with 150 ppm crosslinker content, pH 10 in D_2O (one sample contains 0.277 mmol (0.80 wt%) SDS and the third sample 0.277 mmol (0.87 wt%) deuterated SDS) showed by contrast variations between polymer and h-/d-SDS interactions and characteristic length scales between polymer and surfactant. A scattering peak with its maximum in the q-regime of 4-5 $Å^{-1}$ is related to the size of free SDS-micelles formed in the sample with h-SDS (Figure 1).
  The peak disappeares when deuterated SDS is used and only a small scattering contribution from the copolymer is seen.
- To elucidate the behaviour of copolymer in our mixtures we studied a concentration line of four samples of methacrylic acid / ethyl acrylate copolymer with 150 ppm crosslinker content in basic D_2O (polymer concentration 0.15, 0.30, 0.60 and 1.0 wt%). The scattering pattern is clearly changing with increasing polymer concentration. In the sample with the smallest copolymer content we can see a clear peak in a q-regime of 0.01 – 0.02 $Å^{-1}$ which belongs to the size of the polymer coil. This peak disappears by increasing the polymer content up to 1.0 wt%. The changes in scattering pattern may be due to a mixture of particles of different sizes and the growing of smaller particles.

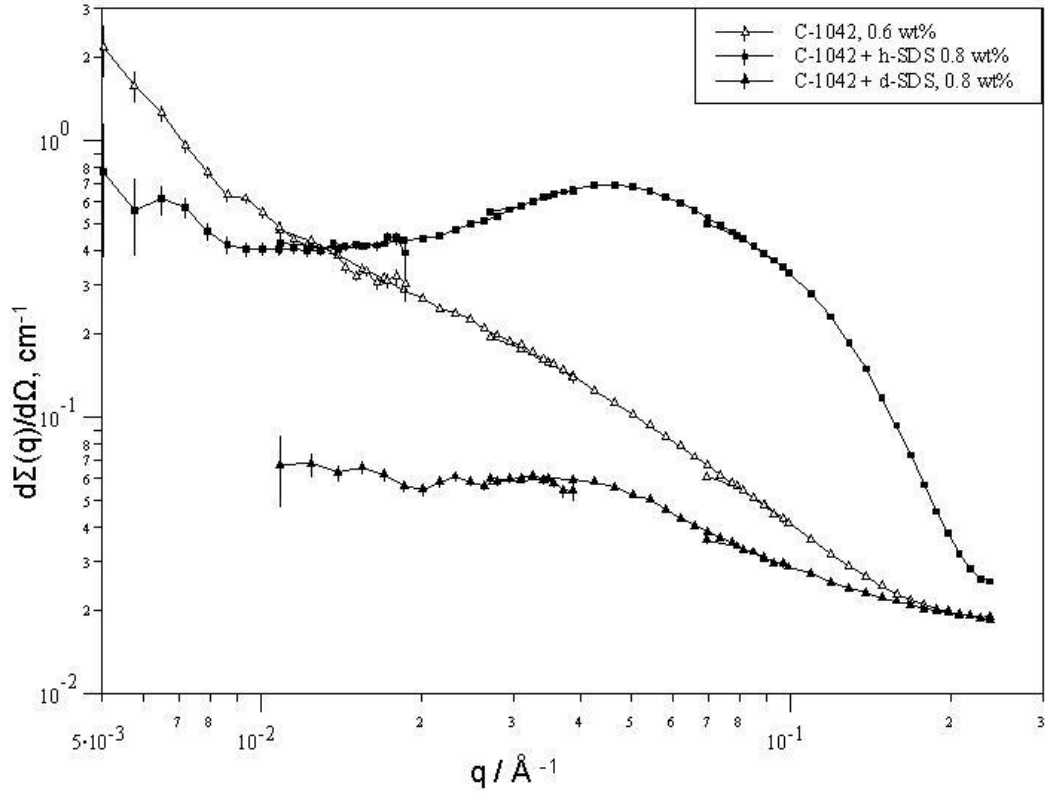


Figure 1. SANS data collected for polymer in heavy water, polymer/h-SDS and polymer/d-SDS in heavy water.

Achievements and Main Results

The first part of the experiment reveals scattering contributions of polymer and surfactant in a mixture of 0.6 wt% copolymer and 0.28 mM h-SDS. The clear peak seen in picture one is due to formation of h-SDS micelles in the mixture as we are well above the cmc of SDS. Only by using d-SDS we can clearly see the small scattering contribution of the copolymer in the mixture.

The results of the concentration line which was measured to clarify the behaviour of the copolymer are more complicated to interpret. We can see a scattering peak in the q-regime of 0.01 – 0.02 $Å^{-1}$ which belongs to the size of the polymer coils in dilute solution. But this peak disappears with increasing the copolymer concentration and at 0.6 wt% copolymer we got a steady decrease in scattering intensity with increasing q. Further increase of copolymer concentration up to 1 wt% leads to a plateau in scattering intensity in the q-regime of 0.02-0.04 $Å^{-1}$ followed by a steady decrease again.

GKSS FORSCHUNGSZENTRUM in der HELMHOLTZ-GEMEINSCHAFT	EXPERIMENTAL REPORT	GeNF SANS-2
Small-angle scattering instrument SANS-2		

Short Instrument Description:

Small angle neutron scattering using cold non-polarised/polarised neutrons is a powerful tool for investigating the structure of matter in the range between 1 and 100 nm. It is a non destructive method for a wide range of application in:

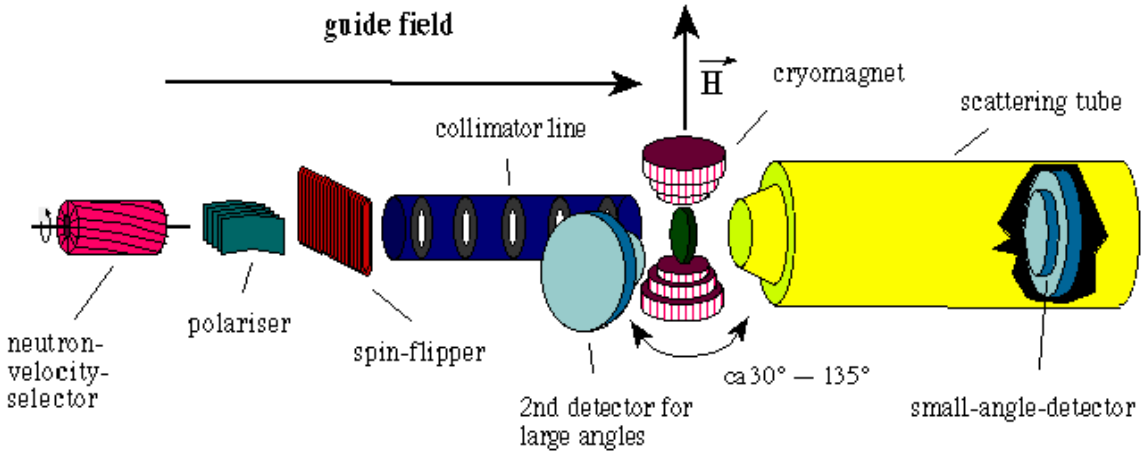
- Metal physics (precipitates, clusters, interfaces, grain boundaries,...)
- Materials science (defects, porosity,....)
- Nanocrystalline materials (grain size, magnetic structures,...)
- Polymers and polymer systems (blends, mixtures, structure and morphology,...)
- Biology (viruses, proteins,...)
- Complex liquids (microemulsions, colloids, liquid crystals,...)

Local Contact:

Helmut Eckerlebe
Phone/Fax : +49 (0)4152 87 – 1202 / +49 (0)4152 87 – 1338
e-mail: helmut.eckerlebe@gkss.de

Dr. P. Klaus Pranzas
Phone/Fax : +49 (0)4152 87 – 1326 / +49 (0)4152 87 – 1338
e-mail: pranzas@gkss.de

Schematic View of SANS-2:



Instrument Details:

Beamline:	beamline 8 - cold neutron guide NG-2, radius of curvature R = 900 m, cross section 3 x 4 cm^2
Monochromator:	helical slot velocity selector (Dornier)
Wavelength range at sample position:	0.3 to 2.0 nm
Wavelength resolution:	$\Delta\lambda/\lambda$ = 0.1 (2 additional velocity selectors with $\Delta\lambda/\lambda$ = 0.05 and 0.2 available)
Length of collimation:	max. 16 m (2 m elements)
Flux at sample position:	$\Phi_{max} = 2 \cdot 10^7$ cm^{-2} s^{-1} (1 m collimation, λ = 0.5 nm)
Range of momentum transfer:	$0.01 \leq q \leq 3$ nm^{-1} (small-angle scattering) $q \leq 25$ nm^{-1} (wide-angle scattering with 2. detector)
Distance sample to detector:	1.0 m ≤ d ≤ 22 m optional 2. detector for wide angles: d = 1 m
Detector: active area: resolution: background:	2-dim position-sensitive ^{3}He-counter 50 x 50 cm^2 0.25 x 0.25 cm^2 < 0.5 cps
Supplementary equipment:	- several electro-magnets up to 2.0 T (horizontal and vertical fields) - superconducting magnet up to 5.0 T - cryostats (8- 300 K) - furnace (-30 °C to +400 °C, atmospheric condition, inert gas and vacuum) - linear translation, rotary, tilting and lift tables (freely programmable sample position) - “HOLONS”: holographic combined with SANS setup (see table A)
Special features:	- Sample environment space is variable from a few mm up to 2500 mm - User-friendly software for data reduction and evaluation running on PC (SANDRA a. o.)

GKSS FORSCHUNGSZENTRUM in der HELMHOLTZ-GEMEINSCHAFT	EXPERIMENTAL REPORT	GeNF SANS-2 / DCD

Characterisation of the Effect of Space Debris Impact on Polymer Foils by SANS and USANS

Proposer:	**Eitan Grossman[1], Ronen Verker[1,2],** [1]Soreq NRC, Space Environment Division
Co-Proposers:	**Noam Eliaz[2],** [2]Tel Aviv University, Dept. Solid Mechanics, Materials and Systems
	Andreas Schreyer[3], P. Klaus Pranzas[3], [3]GKSS
Experimental Team:	**Eitan Grossman[1], Ronen Verker[1,2], P. Klaus Pranzas[3], Gerhard Kozik[3]**
User Group Leader:	**Eitan Grossman[1]**
Date(s) of Experiment:	April - May 2004

Objectives

In low-Earth orbit (LEO) Atomic Oxygen (AO), UV radiation and space debris particles are damaging polymer surfaces of spacecrafts. Hypervelocity space debris impacts can lead to degradation of satellite performance and, in extreme cases, might cause a total loss of a spacecraft. In this work the effect of simulated hypervelocity debris impact at extreme temperatures on Kapton, Teflon and other polymeric foils is studied [1, 2]. Conventional characterisation techniques such as light microscopy, SEM, XRD and tensile testing were applied. Additional small and ultra-small angle neutron scattering (SANS/USANS) are used to characterise the resulting damage structures like holes or cracks with sizes between 1 nm and several μm.

Experiment

For the simulation of hypervelocity debris with dimensions ranging from 10 to 100's μm and impact velocities of up to 3 km/s, the Laser-Driven Flyer (LDF) method was used to accelerate aluminium flyers to impact velocities as high as 2.9 km/s against polymer films. Resulting damage structures in Kapton, Teflon and inorganic/organic hybrid polymer foils with thicknesses of 50 and 125 μm, caused by impacts of different energies at room temperature and at -75°C, are characterised using small and ultra-small angle neutron scattering (SANS/USANS).

At the SANS instrument SANS-2 neutrons with wavelengths of 0.58 and 1.16 nm (resolution $\Delta\lambda/\lambda = 0.1$) and distances between sample and detector of 1, 3, 9 and 21 m were used to cover the range of scattering vector q from 0.01 to 2.4 nm^{-1}. More than 20 Kapton, Teflon and inorganic/organic hybrid polymer samples were measured at the impact area surrounding the penetrating hole using an aperture in front of the sample with a diameter of 4 mm.

USANS measurements were carried out at the double-crystal diffractometer DCD with a wavelength of 0.44 nm resulting in an accessible range of scattering vector q from 10^{-5} to 10^{-2} nm^{-1}. With this technique particle sizes up to 24 μm are detectable. The investigations were performed with about 15 chosen samples to get information about larger structures with sizes up to the μm-range.

Achievements and Main Results

In figure 1 the combined DCD and SANS curves of three Kapton foils each with a thickness of 125 μm after impact of high-velocity debris with different energies at room temperature or at -75°C are exemplary shown.

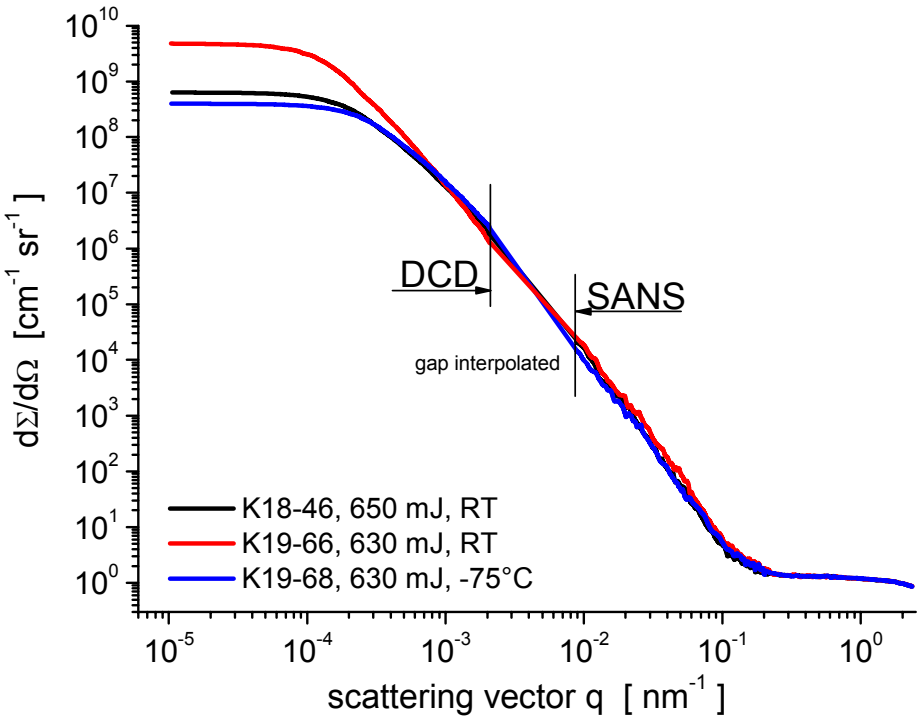


Figure 1: DCD and SANS scattering patterns of 3 125 μm-thick Kapton foils after impact of high-velocity debris with different energies at room temperature or -75°C.

The scattering curves are almost identical in the SANS region, whereas in the low q-range of DCD distinct differences are visible. This indicates that structural differences in these samples can be found only in the μm-range. Equal scattering curves were obtained for the Teflon and hybrid polymer samples.

In addition to the neutron scattering experiments, advanced X-ray scattering techniques in HASYLAB, Hamburg, were carried out. Synchrotron radiation-based X-ray absorption micro computerized tomography (μ-CT) as well as small and ultra-small angle X-ray scattering (SAXS/USAXS) were used to obtain complementary results [3]. Neutron and X-ray scattering curves will be compared. In a first evaluation a rod-like model system was found to be best fitted to the scattering curves. The rod-like structures with cross-sections up to 800 nm can be interpreted as the fiber-like structures which were found by Environmental Scanning Electron Microscopy (ESEM) in the ductile fracture region around the central penetration hole of the impacted area. The combined results of the applied methods will help in determining phase transformations, introduction of pores or microcracks into the polymer, following the exposure of the material to space-simulating environment.

Acknowlegdement

This research project has been supported by the European Commission under the 6th Framework Programme through the Key Action: Strengthening the European Research Area, Research Infrastructures. Contract n°: RII3-CT-2003-505925'

References

[1] E. Grossman and I. Gouzman, Space environmental effects on polymers, Nuclear Instruments and Methods B 208, 48-57 (2003)

[2] E. Grossman, I. Gouzman, G. Lempert, Y. Noter and Y. Lifshitz, Assessment of atomic oxygen flux in LEO ground simulation facilities, J. of Spacecraft and Rockets 41(3), 356-359 (2004)

[3] R. Verker, N. Eliaz, I. Gouzman, S. Eliezer, M. Fraenkel, S. Maman, F. Beckmann, K. Pranzas, and E. Grossman, The efect of simulated hypervelocity space debris on polymers, Acta. Mat. 52, 5539-5549 (2004)

GKSS FORSCHUNGSZENTRUM in der HELMHOLTZ-GEMEINSCHAFT	EXPERIMENTAL REPORT	GeNF SANS-2 / PNR

2D-multi-wire neutron detector for REFSANS at FRM-II: Performance of the final detector and its prototype

Principal Proposer:	**R. Kampmann[1,2], M. Marmotti[2], M. Haese-Seiller[1], V. Kudryashov[1,3]** [1] GKSS Forschungszentrum, Institut für Werkstoffforschung, D-21502 Geesthacht, [2] DENEX GmbH, Moldenweg 9a, D-21339 Lüneburg, Germany [3] Petersburg Nuclear Physics Institute, Gatchina, 188350, Russian Federation
Experimental Team:	**R. Kampmann, M. Haese-Seiller, V. Kudryashov**
Date:	2004

Abstract

A two-dimensional position-sensitive multi-wire gaseous detector with a large sensitive area of 500 × 500 mm^2 and high spatial resolution has been developed for the reflectometer REFSANS at FRM-II [1, 2]. The improvement in performance of the detector in comparison with its prototype [3] is outlined in this report.

Design and requirements on the detector

The REFSANS detector is a ^{3}He and CF_4 filled multi-wire proportional counter (MWPC) with delay line read-out, its design is based on that of detectors with smaller active areas developed previously at GKSS [4, 5]. REFSANS needs a detector which meets requirements both of reflectometers and SANS instruments [1]:

1.	Sensitive area:	$500 \times 500\,\mathrm{mm}^2$;
2.	Spatial resolution:	$\approx 2\,\mathrm{mm} \times 3\,\mathrm{mm}$;
3.	Wavelength range:	$0.3\,\mathrm{nm} < \lambda < 3\,\mathrm{nm}$;
4.	Read-out:	fast, ToF-application;
5.	Background:	very low;
6.	γ-sensitivity ε_γ:	extremely low ($\varepsilon_\gamma \ll 10^{-6}$).

Tab. 1: Specifications of the REFSANS detector

All electrodes are made of tungsten wires with a pitch of 2 mm. Drift electrodes limit the detection volume which has a depth of 3 cm to achieve a high detection probability *p* at rather low ^{3}He partial pressure. The anode is located in the centre of the detection volume. Its distance to the pick-up electrodes is only 5 mm to achieve high capabilities for both good position resolution and high local count rates.

Performance of the detector and its prototype

The prototype REFSANS detector was manufactured and characterised with neutrons in 2003 [3]. It was filled with only 0.8 bar ^{3}He and 1 bar CF_4 and is used in the SANS-2 at the GKSS Research Centre. The final REFSANS detector (Fig. 1) differs from the prototype in

- higher partial gas pressures of 1.25 bar ^{3}He and 1.5 bar CF_4,
- a thinner Al-window with a thickness of 15 mm (prototype: 20 mm), and
- an improved drift electrode affixed directly to the entrance window to avoid any dead volume behind the window whereas the prototype detector has a 2 mm thick dead volume.

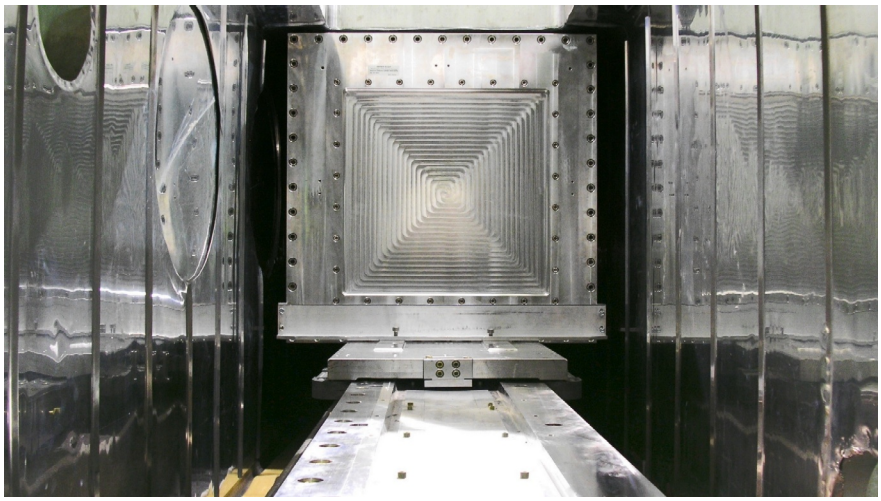


Figure 1: REFSANS detector mounted on the 12 m long translation table in the scattering tube.

The detection probability of the detectors was measured with a well collimated neutron beam at SANS-2 and PNR at GKSS in comparison with an almost black ^{3}He counter tube. Due to the improved design the final detector surpasses its prototype especially in the detection probability of neutrons. The quantum efficiency of the final detector (and its prototype) has a maximum of ~ 80% (and 60%) for λ ~0.9 nm and exceeds ~ 60% (and 35%) over the broad wavelength range from 0.3 nm to 3 nm (Fig. 2). In both cases, the measured efficiency is close to the calculated ideal one accounting for the absorption in the detection volume as well as the losses in the detector window and the dead volume [3, 6].

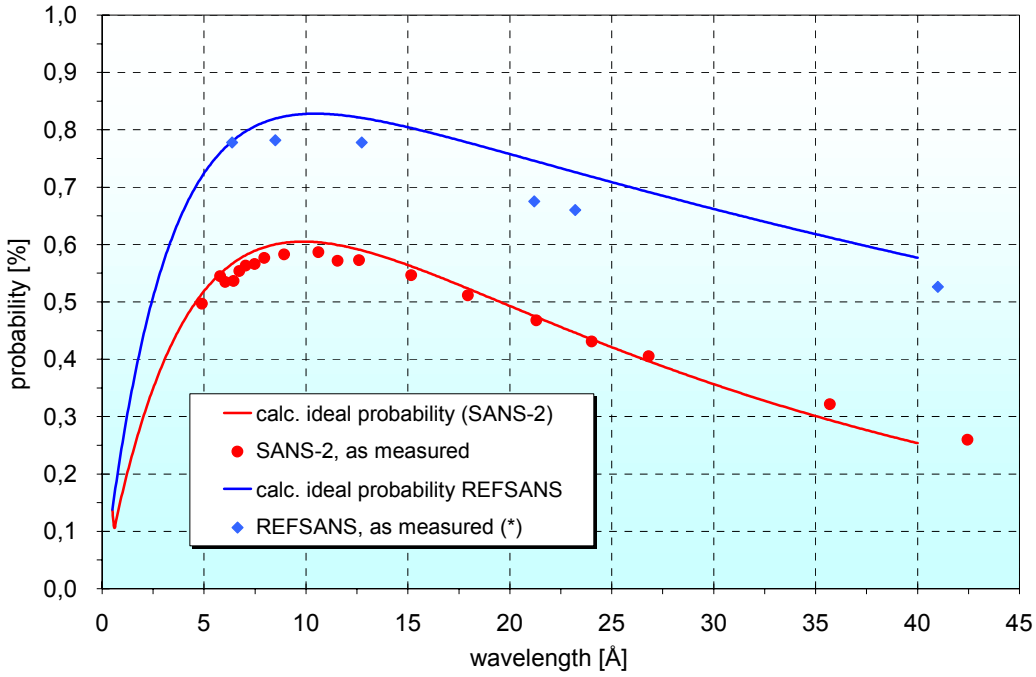


Figure 2: Neutron detection probability of the REFSANS detector and its prototype (SANS-2).

The γ-efficiency was measured without changing the setting of the analogue electronics as used for measuring the efficiency of the detectors. Radioactive sources were positioned at short distance ($\approx$ 10 cm) in front of the detector. Extremely low γ-sensitivities of $\varepsilon_\gamma < 10^{-8}$ and $\varepsilon_\gamma < 10^{-6}$ were measured for the case of the prototype and the final detector [3, 6].

Due to its higher CF_4-partial pressure the final detector surpasses the prototype in spatial resolution which is higher in the direction parallel (Δz) than perpendicular (Δy) to the anode wires. Values of $\Delta z \approx 2$ mm (3.1 mm) and $\Delta y \approx 3$ mm (4.1 mm) were derived from measurements with well collimated neutron beams for the final detector and the prototype [3, 6].

Summary

In accordance with its improved design and higher partial pressures of ^3He and CF_4 the final REFSANS detector surpasses its prototype in quantum efficiency and spatial resolution. The prototype has successfully been operated in SANS-2 at GKSS for almost 2 years and the final detector has been integrated in REFSANS at FRM-II. The REFSANS detector has been licensed by GKSS to DENEX.

Acknowledgements

The support of H. Eckerlebe, U. Tietze, M. Pauls and K. P. Pranzas during tests of the detectors at SANS-2 and PNR / GKSS is gratefully acknowledged. The development of REFSANS has been supported by the German Federal Ministry of Education, Research and Technology (BMBF) under contracts 03-KA5FRM-1 and 03-KAE8X-3.

Bibliography

[1] Kampmann, R., Haese-Seiller, M., Marmotti, M., Burmester, J., Deriglazov, V., Syromiatnikov, V., Okorokov, A., Frisius, F., Tristl, M., Sackmann, E.: Applied Physics A, 74, (2002), 249-251.
[2] Kampmann, R., Haese-Seiller, M., Kudryashov, V., Daniel, C., Nickel, B., Rädler, J., Schreyer, A., Sackmann, E.: in this annual report.
[3] Kampmann, R., Marmotti, M., Haese-Seiller, M., Kudryashov, V.: Nuclear Instruments and Methods A 529, (2004), 342-347.
[4] Marmotti, M., Burmester, J., Haese-Seiller, M., Kampmann, R.: Nuclear Instruments and Methods A 477, (2002), 347-352.
[5] Marmotti, M., Haese-Seiller, M., Kampmann, R.: Applied Physics A, 74, (2002), 252-254.
[6] Kampmann, R., Marmotti, M., Haese-Seiller, M., Kudryashov, V.: to be published.

GKSS FORSCHUNGSZENTRUM in der HELMHOLTZ-GEMEINSCHAFT	EXPERIMENTAL REPORT	GeNF SANS-2

Precipitation kinetics of a tool steel containing carbides and intermetallic phases

Principal Proposer:	**M. Bischof[1]** [1]University of Leoben, Department of Physical Metallurgy and Materials Testing, Leoben, Austria
Experimental Team: User	**M. Bischof[1], H. Eckerlebe[2], G. Kozik[2], K. Pranzas[2], P. Staron[2],** [2]GKSS Research Center
Group Leader:	**M. Bischof[1]**
Date of Experiment:	April and August 2004

Introduction

Precipitates in the size range from nanometers to microns are affecting the mechanical and thermophysical properties of various materials, e.g. Ni-based superalloys, refractory metals, intermetallics and tool steels. The Department of Physical Metallurgy and Materials Testing at the University of Leoben, Austria, is presently developing a novel tool steel (product code: K011) which is age hardening not only due to the formation of fine secondary carbides during annealing at elevated temperatures (Figure 1), but also through the precipitation of fine intermetallic phases (Figure 2). The formation of both carbides and intermetallic phases causes an improved thermal stability compared to conventional tool steels which are age hardening through carbides solely.

However, the precipitation sequence of this steel is not fully understood and some phenomena occurring during annealing cannot be explained yet. For example, an annealing temperature of about 600°C causes significant embrittlement. It is assumed that precipitates, in particular their nucleation sites, have a great influence on this behaviour. Preliminary

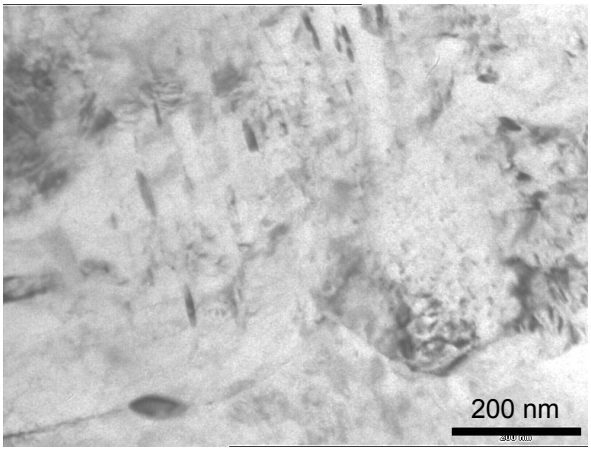


Figure 1: TEM image of small M_2C particles in K011, 610°C / 1000 min

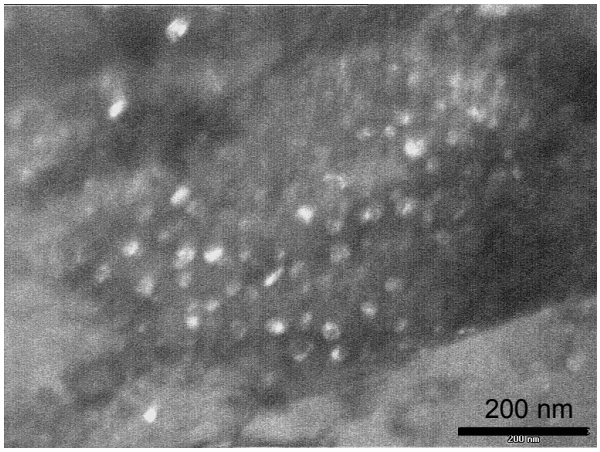


Figure 2: TEM dark field image of NiAl precipitates in K011, 610°C / 10000 min

investigations have been performed by atom probe field ion microscopy (APFIM) and transmission electron microscopy (TEM) to determine the chemical composition, the structure, and nucleation sites of the precipitates under varied annealing conditions.

Small-angle neutron scattering (SANS) was used for the study of changes of the particle size distribution as a function of the annealing condition. In succession, the experimentally obtained data are going to be compared with data derived from thermodynamic calculations. These calculations will be performed using a new thermodynamic model, capable of simulating precipitation sequences in multi-component, multi-phase and multi-particle systems. The comparison shall verify the correctness of this model as well as enable necessary adjustments.

Experiment

The nominal composition of the investigated material is as follows:

Table 1: Nominal composition of K011 (wt %)

C	Cr	Mo	Ni	V	Co	Al	Si	Mn	Fe
0.3	2.4	2.5	6.5	0.26	1.18	2.6	1.18	0.23	balance

The heat treatments of samples Q to 30 (see Table 2) have been performed on a quenching-dilatometer in order to get a good reproducibility of the temperature – time sequence. The quenching rate λ was chosen as high as 0.3 which is about the rate of quenching in oil. The samples were rod-shaped with a diameter of 4 mm and a length of about 10 mm in this case. For the SANS-measurements discs of 1mm were cut off these rods.

Samples Q2, 5k and 10k were heat treated in a standard furnace. The origin shape was a cuboid of about 2x4x4 cm³. The SANS-samples made of them were discs with a thickness of 1 mm and a diameter of 25 mm.

All samples have been solution annealed at 990°C for 30 minutes, quenched and, except for specimens Q and Q2, subsequently heat treated as listed in Table 2. An annealing time of 0 min thereby means that the sample was heated up until the target temperature was reached and cooled down immediately.

Table 2: Summary of measured samples

Sample	Heat Treatment
Q	990°C, 30 min, λ 0.3
0	990°C, 30 min, λ 0.3 / 610°C, 0 min, λ 0.3
0.5	990°C, 30 min, λ 0.3 / 610°C, 0.5 min, λ 0.3
1	990°C, 30 min, λ 0.3 / 610°C, 1 min, λ 0.3
30	990°C, 30 min, λ 0.3 / 610°C, 30 min, λ 0.3
Q2	990°C, 30 min, Oil
5k	990°C, 30 min, Oil / 610°C, 5000 min, Air
10k	990°C, 30 min, Oil / 610°C, 10000 min, Air

Measurements were carried out at the SANS-2 facility. Scattered neutrons were detected by a position-sensitive detector with a resolution of 256x256 pixels. Four detector distances (1 m, 3 m, 9 m and 21 m) were used with appropriate apertures and collimators to cover scattering vectors Q from 0.025 nm^{-1} to 2.5 nm^{-1}. The measurements were performed using neutrons at a wavelength of λ=0.58 nm and a wavelength spread of $\Delta\lambda/\lambda$=10%. The neutron beam impinging on the samples had a diameter of 4 mm. The samples were magnetized to saturation in a field of 2 T. Measured intensities were corrected for sample transmission, background and detector efficiency. The nuclear cross sections were measured at azimuthal

detector angels of α=0° and 180°, while the sum of nuclear and magnetic cross section was measured at angels of α=90° and 270°, where α is the angle between the scattering vector and the magnetization. The scattered intensity was averaged over sectors of 20° around the given mean angles. Absolute cross sections were calculated by comparison with the incoherent scattering of vanadium.

Results

Size distributions were determined from magnetic scattering curves by means of a fitting software called “SansFit” which is provided by GKSS. This software tool performs an indirect transformation as it was described by Glatter [1]. A calculated scattering curve is thereby fitted to the magnetic scattering curve by means of a least-square procedure. Up to 15 log-normal distributions were used to find the specific optimum for each curve between small error values and little fitting deviation. The magnetic scattering curves were calculated by subtracting nuclear scattering cross sections from the sum of magnetic and nuclear cross sections. Both curves can be measured directly as described above. Three exemplary sets of scattering curves are displayed in Figure 3.

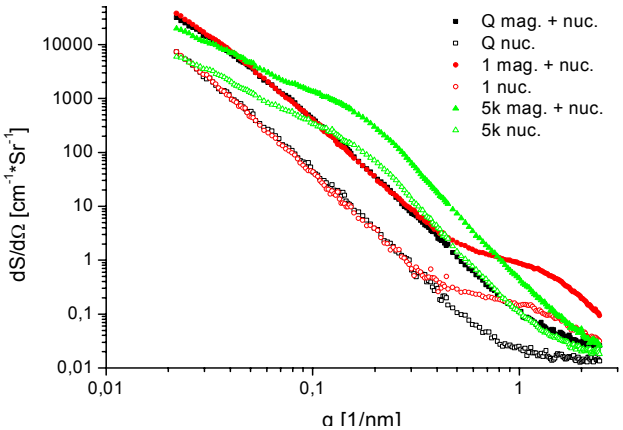


Figure 3: Scattering curves of samples Q, 1 and 5k. Open symbols: α=0°, full symbols: α=90° (see text).

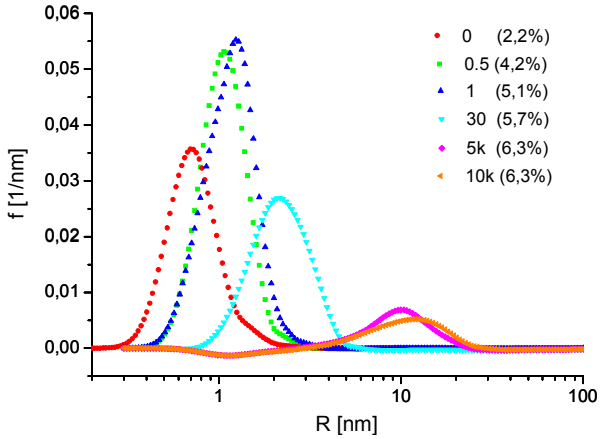


Figure 4: Particle size distributions of the annealed steel samples. Size distributions of as-quenched samples subtracted (see text).

The magnetic scattering length densities were calculated from matrix compositions as determined by atom-probe measurements. These calculated values were available for samples Q, 1, 30 and 10k, intermediate sample states were estimated by interpolation.

Figure 4 shows the particle size distributions of all samples expect Q and Q2. These samples were used as a reference state of the material and its particle size distribution was subtracted from the size distribution of the appropriate samples, namely Q from 0, 0.5, 1 and 30 and Q2 from 5k and 10k. This was necessary as the obtained data is going to be compared with simulated data. Since the simulation of the precipitation kinetics starts just after quenching, particles which were already present in the specimens prior to annealing should be filtered out. This approach will deliver accurate results only for very short annealing times as particles which were present in the “as quenched” sample will change their morphology during heat treatment. However, good agreement between simulation results and SANS data could so far only by achieved by subtracting the corresponding as-quenched particle size distribution from all heat treated samples.

As it can be seen in Figure 4, a significant volume fraction of extremely small particles or clusters is present even after a heat treatment without any holding time at target temperature (sample 0). The total volume fraction of particles grows rapidly and reaches 5.1 vol% after a

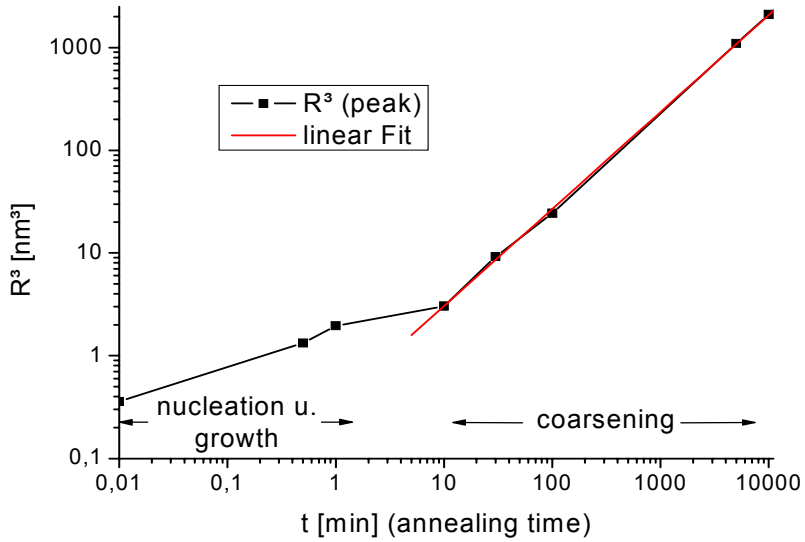


Figure 5: Growth kinetics of precipitates in steel K011 as determined by SANS.

holding time of only 1 min. At longer annealing times, only minor changes occur to the total volume fraction of particles, but as it can be seen from the shifting peaks of the size distributions, the particles are growing constantly. After 10000 min a peak value of about 15 nm is reached, which agrees well with the size of NiAl particles which was determined using TEM (Figure 2). It is known from thermodynamic calculations as well as from APFIM and TEM results that NiAl is the prevailing particle class in this steel and therefore the particle size distribution as determined by SANS has its main focus on NiAl.
Having a closer look on the growth kinetics of the precipitates (Figure 5) it is evident that diffusion controlled coarsening, which is determined by a linear volume growth of the particles, starts very early and is predominant at longer annealing times. The mean particle volume at a given time was calculated from the peak values of the particle size distribution, giving again a very strong emphasis on NiAl.

Conclusions

Particle size distributions of variably heat treated steel samples, which are age hardening through the formation of fine NiAl precipitates as well as through secondary hardening carbides, were determined using SANS. First comparisons with results derived from novel software currently being developed, capable of simulating the precipitation kinetics in multiphase systems, were very promising. However, as the volume fractions of carbides are small compared to NiAl, the SANS results are very focussed on the kinetics of NiAl since no separable carbide peaks could be identified in the calculated particle size distributions.

The particle growth kinetic in this steel is very fast, leading to a high particle volume fraction even after an annealing time of 1 min, while coarsening of NiAl particles is rather slow, leading to mean particle diameters of only 30 nm after an annealing time of 10000 min.

Acknowlegdement

This research project has been supported by the European Commission under the 6th Framework Programme through the Key Action: Strengthening the European Research Area, Research Infrastructures. Contract n°: RII3-CT-2003-505925'

References

[1] O. Glatter, J. Appl. Cryst. 13 (1980) 7-11

GKSS FORSCHUNGSZENTRUM in der HELMHOLTZ-GEMEINSCHAFT	**EXPERIMENTAL REPORT**	**GeNF SANS-2**

Dipole-field controlled spin disorder in a nanocomposite ferromagnet

Proposer:	**Andreas Michels,** [1] Paul Scherrer Institute, Villigen PSI, Switzerland
Co-Proposers:	**Oscar Moze,** [2] INFM – S[3], Dipartimento di Fisica, Università degli Studi di Modena e Reggio Emilia, Modena, Italy
	Kiyonori Suzuki, [3] School of Physics and Materials Engineering, Monash University, Melbourne, Australia
Experimental Team:	**Andreas Michels[1] ,Oscar Moze[2], Carlo Vecchini[2]**
	P. Klaus Pranzas[4], Gerhard Kozik[4], [4]GKSS Forschungszentrum
User Group Leader:	**Andreas Michels**[1]
Date(s) of Experiment:	24–28 May 2004

Objectives

Our objective is to study the magnetic microstructure, i.e., the variation of the magnetization vector as a function of position and applied magnetic field in nanocrystalline two-phase ferromagnets by means of field dependent small-angle neutron scattering.

Experiment

We report results of SANS experiments on a nanocomposite material of the Nanoperm ($Fe_{89}Zr_7B_3Cu_1$) type. The magnetic field dependent SANS data from this material are in most aspects closely compatible with what was found in a previous study of Vitroperm [1]. Both materials are nanocomposite materials of similar structure: ferromagnetic nanocrystals of Fe (Nanoperm) or FeSi (Vitroperm) embedded in a ferromagnetic amorphous matrix. However, for the Nanoperm samples we find an unusual field dependence in the magnetic scattering at high fields. The spin-misalignment scattering in the approach-to-saturation range exhibits pronounced lobes of high intensity at azimuth angles θ around ± 30–40° relative to the magnetic field axis. We suggest that this is the signature of local spin misalignment which decorates the dipole stray fields due to the mismatch of the saturation magnetization values between the bcc Fe particles and the amorphous magnetic matrix. This is contrary to what has been observed in similar studies of single-phase nanocrystalline magnets [3-5], where the various magnetic anisotropy energy terms control the spin disorder.

Achievements and Main Results

Figure 1 shows color-coded plots of $d\Sigma/d\Omega$ in the plane of the two-dimensional detector at different applied magnetic fields **H**. Superimposed are polar plots of $d\Sigma/d\Omega$ versus the angle θ included between **H** and the scattering vector **q**, at an arbitrary magnitude of **q**, q = 0.17 nm^{-1}. The plots emphasize the angular anisotropy of the scattering. The graph at the highest applied field (Fig. 1d) exhibits the well-known $\sin^2\theta$ scattering law of uniformly magnetized particles. The large aspect ratio indicates that the magnetic scattering is much stronger than the isotropic nuclear scattering. At $\mu_0 H$ = 21 mT (Fig. 1b), just above the onset of domain formation [2], the pattern agrees qualitatively with the $(1 + \cos^2\theta)$-dependence which is expected for spin-misalignment scattering in the single-domain state [3]. The scattering in the remanent state (Fig. 1a) is nearly isotropic. This is compatible with randomly oriented domains, and it indicates the absence of significant induced uniaxial anisotropy, in agreement with the processing conditions. Contrary to the good agreement with previous SANS results for nanocrystalline ferromagnets is the finding that the scattering data at intermediate fields, such as Fig. 1c at $\mu_0 H$ = 85 mT, exhibit lobes of maximum $d\Sigma/d\Omega$ roughly at angles of about 30–40° to the magnetic field axis. Since this feature develops as the magnetic field is varied, and since the graphs at the lowest and highest fields give no

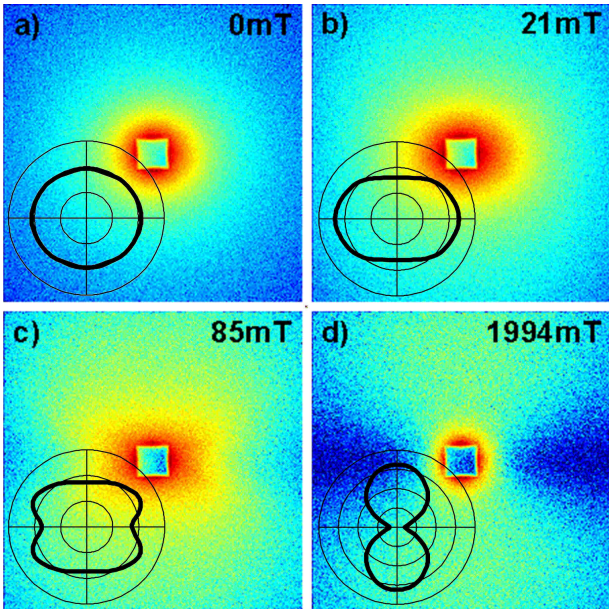


Figure 1: Color-coded graphs of dΣ/dΩ in the plane of the 2D-detector at different applied magnetic fields as indicated in the figure. Field direction is horizontal. Pixels in the corners have momentum transfer q = 0.54 nm^{-1}. Insets: polar plots of intensity at q = 0.17 nm^{-1}. Circular grid lines are spaced 0.5 times radial average intensity.

evidence of this type of symmetry, it is concluded that the scattering cannot arise from an anisotropy in the nuclear microstructure. Instead, the unusual angular dependence indicates a structure in the spin system which exhibits the strongest Fourier coefficients at angles of roughly 40° to the magnetic field axis. Nanoperm is a two-phase system (mean particle size: 12 nm), and an important feature, compared to homogeneous, single-phase nano-crystalline ferromagnets, is that the jump in the saturation magnetization M_S at the internal interface between the crystallites (larger M_S) and the matrix (smaller M_S) gives rise to a dipole field with a magnitude proportional to the difference ΔM_S in the saturation magnetizations of the two phases. Assuming $\mu_0 M_S$ = 2.2 T for the crystallites of bcc Fe and a volume fraction x_C = 0.4 [2], the experimental value $\mu_0 M_S$ = 1.3 T for the composite obtained from a magnetization isotherm implies $\mu_0 M_S$ = 0.7 T for the amorphous matrix, and hence $\mu_0 \Delta M_S$ = 1.5 T. Results of Mössbauer spectroscopy data are in agreement with this estimate, which indicates a quite appreciable jump in M_S at the particle-matrix interface, and correspondingly large dipole fields. The normal component of that dipole field acts as a torque which deflects the magnetization locally from the aligned state. Thus, an important consequence of the two-phase nature of Nanoperm is the existence of an extra perturbing term, which is simply the contribution of the normal component of the net dipole field from all particles. The angular symmetry of the perpendicular component of the dipole field outside of a uniformly magnetized spherical crystallite is described by a term proportional to $\sin^2\varphi \cos^2\varphi$, where φ denotes the angle between the magnetization and the position vector [2]. This last expression has maxima at φ = ± 45°, which compares favorably with the experimental observation in Fig. 1c [2]. Our findings suggest that, in the approach to saturation, the most significant contribution to the perturbing field which leads to spin misalignment in our sample is the dipole stray field originating from crystallites of bcc Fe with a large saturation magnetization M_S embedded in an amorphous matrix of significantly lesser M_S. This is expected to be a general situation in soft magnetic nanocomposites where the two phases have an appreciable difference in M_S.

References

[1] A. Michels, R. N. Viswanath, J. Weissmüller, Europhys. Lett. **64**, 43 (2003).
[2] A. Michels, C. Vecchini, O. Moze, K. Suzuki, J. M. Cadogan, P. K. Pranzas and J. Weissmüller, submitted (2004).
[3] J. Weissmüller, A. Michels, J. G. Barker, A. Wiedenmann, U. Erb, R. D. Shull, Phys. Rev. B **63**, 214414 (2001).
[3] J. Weissmüller, A. Michels, D. Michels, A. Wiedenmann, C. E. Krill III, H. M. Sauer, R. Birringer, Phys. Rev. B **69**, 054402 (2004).
[5] A. Michels, J. Weissmüller and R. Birringer, Eur. Phys. J. B **29**, 533 (2002).

GKSS FORSCHUNGSZENTRUM in der HELMHOLTZ-GEMEINSCHAFT	EXPERIMENTAL REPORT	GeNF SANS-2

The study of new magnetic nanocomposites based on mesoporous silica with embedded Fe-particles by SAPNS: technology

Principal Proposer: S.V. Grigoriev, A.I. Okorokov, N. Grigorieva
Petersburg Nuclear Physics Institute

Experimental Team: A.I. Okorokov, S.V. Grigoriev, Yu.O. Chetverikov, PNPI;
H. Eckerlebe, K. Pranzas, GKSS

Date(s) of Experiment: 5 / 2004

Scientific Objective. At least 10 years more the main branch of industry of the information carriers will rely upon magnetic information storage with high density of the recording. The further improvement of the density requires the development of principally new magnetic materials and storage techniques to solve the problem, which appear with decreasing the magnetic bit size to the atomic scale. From a technological point of view, the special role in creation of the components for magnetic information storage belongs to high-quality nanostructures and nanocomposites. The aim of the proposal was to investigate magnetic and structural features of a new class of nanocomposites based on silica matrix (MCM-41) with embedded iron particles. n-Alkyltrimethylammonium bromides of different alkyl chain lengths C12, C16 and C18 were used as a template for syntheses of the three types of the silica matrices with the different structural parameter of pores a_0 and their diameter. The a_0 value and pore diameter becomes larger with increasing the carbon chain length of the alkyl group in the template. Thus the pore size and the regularity of the matrix can be controlled by varying the template parameters. A hydrophobic metal complex $Fe(CO)_5$ was introduced into the hydrophobic part of the as-prepared meso-SiO2/surfactant composite. Decomposition of $Fe(CO)_5$ was carried out by UV-irradiation in vacuum for 10 hours. To provide better crystallinity of iron nanowires we performed additional annealing in hydrogen flow at temperatures of 260, 300, 350, 375 and 400°C for 3 hours. The samples obtained were denoted as msN, msN-260, msN-300, msN-350, msN-375 and msN-400, where N=12,16 and 18.

Experimental Technique. The SAPNS experiments were carried out at the SANS-2 scattering facility of FRG-1 research reactor in Geesthacht (Germany). A polarized beam of neutrons with an initial polarization of P_0=0.94, the neutron wavelength λ=5.8 Å ($\Delta\lambda/\lambda$=0.1) and a divergence of 1.5 mrad was used. The scattered neutrons were detected by a position sensitive detector with 128x128 pixels.

Results. A typical 3-dimensional picture of the neutron scattering for mesoporous silica samples is presented in Fig.1. The ring of scattering intensity corresponds to the scattering on the regular two-dimensional structure of nanotubes in the randomly oriented single particles. The period of the structure d is readily obtained from the Bragg law $\lambda = 2d\sin(\theta/2)$, or, $d = 2\pi/q_c \cong 3.4$nm, 4.1nm, 4.8nm for ms12, ms16 and ms 18, respectively (Fig.2).

Fig.1

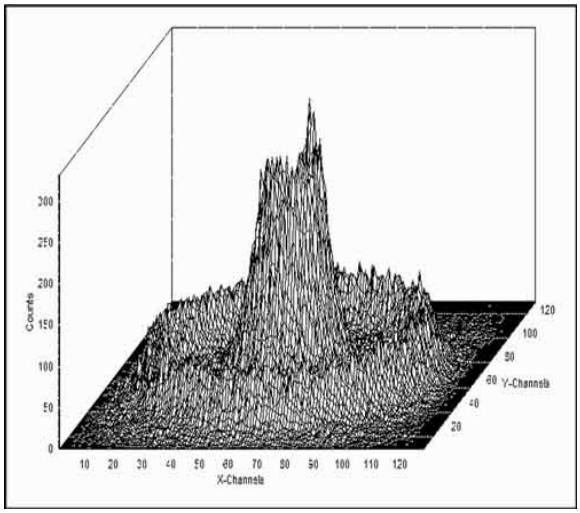
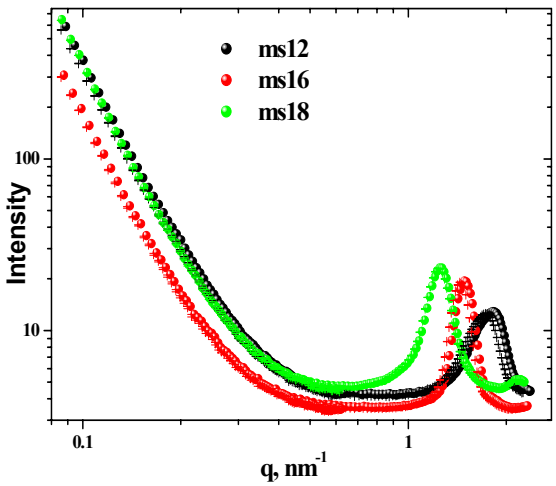


Fig.2



$$I(q) = A_1 \frac{1}{q^4} + A_2 \exp\left(-\frac{(q-q_c)^2}{2\omega^2}\right) + A_3 \int \left[\frac{2J[1,(qR)]}{(qR)}\right]^2 \exp\left(-\frac{(R-R_c)^2}{2\Delta R^2}\right) dR + I_{bg}(q)$$

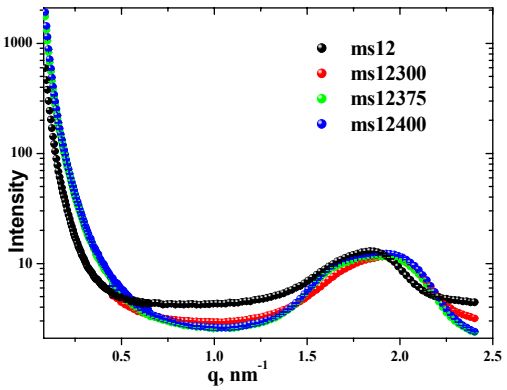


Fig.3

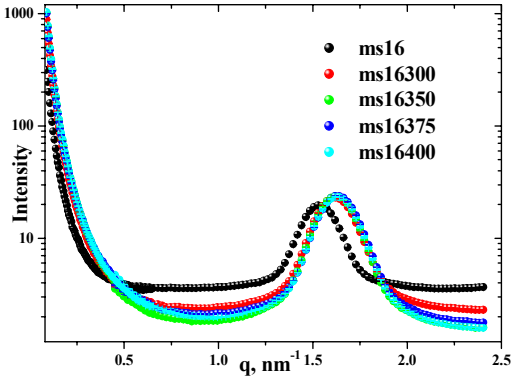


Fig.4

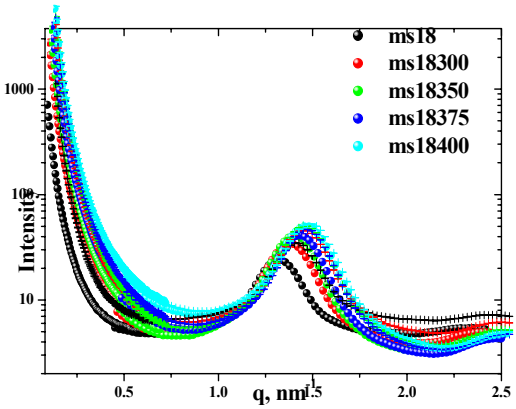


Fig.5

The q-dependence of the neutron intensity I(q) were fitted with the expression above. The first term describes scattering on a powder consisting of large particles (its Porod approximation). The second term describes the diffraction peak centered at q_c with a width of ω (the scattering on the regular structure of pores / nanowires). The third term represents an additional scattering, if any, on an individual nanowire, or on a nanotube, or on a bunch of them. This scattering appears from the samples with iron particles inside the pores. The term I_{bg} is to describe the background scattering, which were the same for the all samples. The intercalation of iron into the matrix leads to a shift of q_c toward larger q (Fig.3 – 5). It is related with the decomposition and evaporation of the template's atoms during UV irradiation and annealing. The period of the annealed systems with the iron are (d = 3.3nm, 3.8nm, 4.6nm) for ms12, ms16 and ms18 matrices, respectively. It is well seen in Fig.3-5 that the scattering intensity increases both at small q ($0.2nm^{-1}<q<1nm^{-1}$) and at the diffraction peak for the samples with iron. These contributions to the scattering are related to an increase of crystallinity of the wires (temperature of the annealing) and are maximal for the samples msN-375 and msN-400 for all matrices.

Conclusion. The intercalation the iron into the matrix SiO_2 and annealing at different temperatures does not destroy the matrix but forms the system of nanowires of iron. The data demonstrate the coexistence of the long-range iron structure related to increase of the diffraction peak and the short-range ordering connected to the scattering at small q. From the analysis of the scattering at small q follows that a compact bunches of R_c = 5 nm with the small spread of 1 nm are formed in all samples with iron. It is obviously in this case that a bunch consists of six cylindrical pores with the needles of crystallized iron inside formed by the shape and size of the primitive hexagonal structure. As to the long-range structure, we suppose that the iron nanowires in the whole particle consist of the partially crystalline and partially amorphous pieces, which are randomly distributed along the SiO_2-tubes.

In short, the system of the iron nanowires is fabricated on the basis of the MCM41 matrix. The iron is partially crystallized in the matrix and partially amorphous. The crystallized part of the iron is ferromagnetic while the amorphous part is paramagnetic. Further investigations are demanding in order to transform all nanowires into the crystallized and therefore into ferromagnetic state.

GKSS FORSCHUNGSZENTRUM in der HELMHOLTZ-GEMEINSCHAFT	**EXPERIMENTAL REPORT**	**GeNF SANS-2**

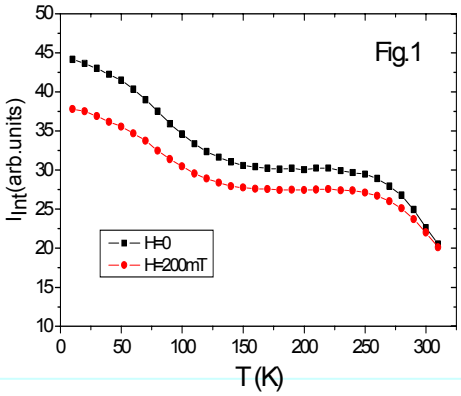
The study of the static and dynamic spin chirality in the reentrant spin-glass system $Fe_{40}Ni_{40}Mn_{20}$ by means of small angle scattering of polarized neutrons

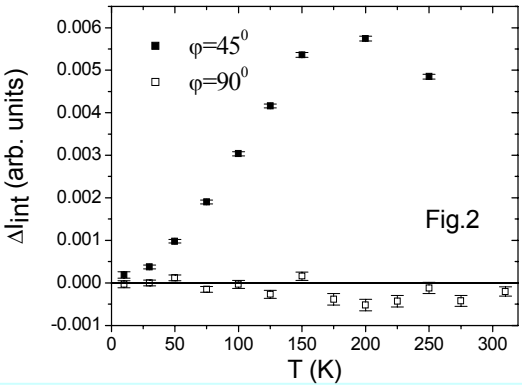
Principal Proposer: A.I. Okorokov, S.V. Grigoriev
Petersburg Nuclear Physics Institute
Experimental Team: H. Eckerlebe, Yu.O. Chetverikov, S.V.Metelev
GKSS, PNPI

Date(s) of Experiment: 06 / 2004

Scientific Objective. Static and dynamic spin chirality in the single crystal $Fe_{40}Ni_{40}Mn_{20}$ has been investigated. Due to competition of exchange spin interactions this system has a nontrivial magnetic mesostructure with the ferromagnetic transition at T_C = 280 K and the reentrant spin-glass transition at T_{SG} = 80 K. Recently, Kawamura proposed the chiral mechanism for explanation of the spin-glass phase transition [1]. He suggested that not pair correlation of the Ising's spins, but the chiral three-spin fluctuation is the key object of such a transition. The first goal of this experiment was to observe such a static chiral objects in the spin-glass state. On the other hand one could not easily predict what will happens with spin-waves below and above T_{SG} point. So, the second goal was to investigate the spin-waves behaviour.

Experimental Techniques. The SAPNS experiments were carried out at the SANS-2 scattering facility of FRG-1 research reactor in Geesthacht (Germany). A polarized beam of neutrons with an initial polarization of P_0=0.9, the neutron wavelength λ=5.8 Å ($\Delta\lambda/\lambda$=0.1) and a divergence of 1.0 mrad was used. The scattered neutrons were detected by a 256x256 position sensitive detector within an angular range of ± 80 mrad. Sample has a tablet shape of 8 mm in diameter and 1 mm of thickness. Inclined and perpendicular geometries were used, allowing one extract from the data dynamical and static chiral objects scattering correspondingly [2,3]. The sample was magnetized by an electromagnet. Both static and dynamic chiral objects were studied in the magnetic field of 0.2 T, applied along the diameter of tablet. Scattering from static chiral objects has been studied in the perpendicular geometry in temperature range 10 – 310 K. The external magnetic field in this case was applied at an angle of $\varphi=90^o$ with respect to the incident beam. Spin wave dynamics has been studied in the inclined geometry, in the temperature range 10 – 250 K. The external magnetic field was applied at an angle of $\varphi=45^o$ with respect to the incident beam. The presence of chirality in the magnetic system leads to the observation of the left-right asymmetry in SAPNS pattern [2-5]. The magnetic cross section has the form $\sigma(q, \omega) = \sigma_0(q,\omega) + (\mathbf{q}, \mathbf{P_0})(\mathbf{q}, \mathbf{m})\sigma_{ch}(q,\omega)/q^2$, where the second term is determined by chiral dynamical or static spin fluctuations and $\mathbf{P_0}$ and $\mathbf{m}$ are neutron polarization and direction of the sample magnetization or spiral direction, respectively. Following [4-5] we investigate experimentally the quantity $\Delta I_a(\theta)$ and $I(\theta)$, where $I(\theta) = [I_+(\theta)+I_+(-\theta)+I_-(\theta)+I_-(-\theta)]$ and $\Delta I(\theta) = [I_+(\theta)+I_-(-\theta)-I_+(-\theta)-I_-(\theta)]$ and $I_+(\theta)$ and $I_-(\theta)$ are the intensities with the polarization directed along and opposite to the field.





Results. The temperature dependence of the integrated intensity $I_{int} = \int_0^{max} d\theta \cdot I(\theta)$ for the applied magnetic field H = 200 mT and for H = 0 is shown in Fig.1. The intensity increases with decrease of the temperature near T_C~ 280 K and then at T_{SG} ~ 80 K. The increase of the scattering intensity near T_C is related with the enhancement of the dynamical critical spin fluctuations, while its increase at T_{SG} is attributed to the degeneration of the spin state and therefore to the static (frozen) spin fluctuations. The temperature dependence of the integrated intensity of the asymmetric left and right scattering for the perpendicular and inclined geometry is shown in Fig.2. There was no polarization-dependent asymmetry found in case of perpendicular geometry. Therefore, one may conclude that the static spin fluctuations have a collinear but not a chiral nature in this substance. In the case of inclined geometry such an asymmetry was observed through the whole temperature range, showing the presence of the dynamical chirality, for instace, spin waves and excitations. Fig.3 shows the anti-symmetrical part of scattering in the **k-H** plane ΔI_A as a function of the scattering angle θ for temperatures of T=30 K and 200 K at H=200 mT. The solid line represents the theoretical model [4] calculated with the SW parameters of the fit. From the point of view of this model, damping is very big and does not allow one to precisely determine other parameters. The fit procedure is unstable and very sensitive to the choice of the initial conditions. The only certain conclusions one can made is that SW stiffness D in ferromagnetic region is almost constant and is approximately equal to 40 A^2 meV. The spin wave damping decreases with temperature. Thus, determination of the spin wave behaviour in this substance requires further modeling and data analysis.

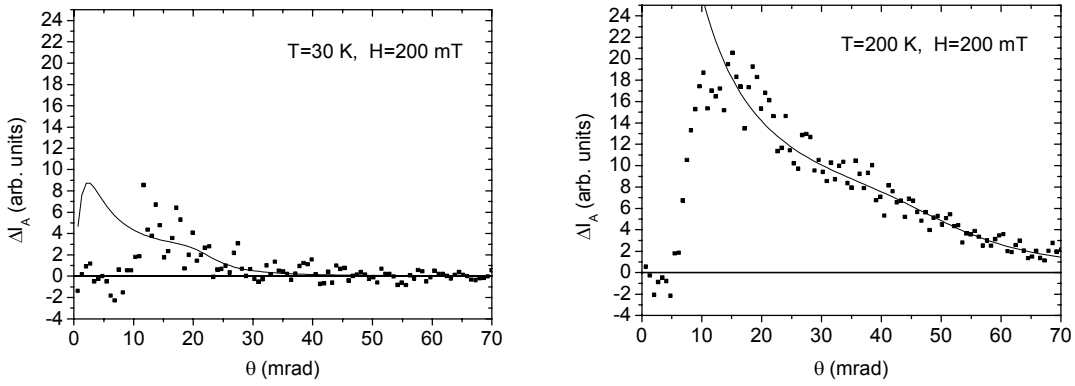


Fig.3

References:
1. H. Kawamura, M. Suan Li, Phys. Rev. Lett. **87** (2001) 187204 (1-4).
2. S.V. Maleyev, Phys.Rev.Lett., **75** (1995) 4682;
3. D.N. Aristov, S.V. Maleyev, Phys.Rev.B, **62** (2000) R751
4. V. Deriglazov, A. Okorokov, V. Runov, B. Toperverg, R.Kampmann, H. Eckerlebe, W. Schmidt, W. Lobner, Physica B **181-182** (1992) 262
5. B.P.Toperverg, V.V.Deriglazov, V.E.Mikhailova, Physica B **183** (1993) 326

GKSS FORSCHUNGSZENTRUM in der HELMHOLTZ-GEMEINSCHAFT	EXPERIMENTAL REPORT	GeNF SANS-2

Study of the mosaic of the spin spiral structure of MnSi

Principal Proposer: A.I. Okorokov, S.V. Grigoriev, P.Böni, R.Georgii
Petersburg Nuclear Physics Institute, TU-München

Experimental Team: H. Eckerlebe, K. Pranzas, A.I. Okorokov, S.V. Grigoriev, Yu.O.Chetverikov, D. Lamago, GKSS, PNPI, TU-München

Date(s) of Experiment: 06 / 2004

Scientific Objective. The proposal was aimed to study a **mosaic** of the spin spiral structure in a single crystal MnSi below T_C by means of small angle diffraction of polarized neutrons. The magnetic structure of MnSi is a helical spin density wave below 29 K with a propagation vector $(2\pi/a)(\zeta,\zeta,\zeta)$ with $\zeta = 0.017$ and $a = 0.4558$ nm [1,2]. The helicity is realized by an antisymmetric Dzyaloshinski-Moriya (DM) exchange interaction caused by the lack of a center of symmetry in Mn atomic arrangement [3-5]. This DM interaction itself is isotropic but yet another weak exchange interaction, connected to anisotropy of the crystal, fixes the direction of the magnetic spirals $\mathbf{m} = [\mathbf{S}_1 x \mathbf{S}_2]/S^2$ along the axes [111]. When an external magnetic field **H** is applied, the direction of the magnetic spiral **m** follows that of the magnetic field. The period does not depend on the direction of **m**. Nevertheless, the effect of the magnetic field on the spiral structure in MnSi was never understood. Therefore a detailed both experimental and theoretical study is very desired.

Experimental Technique. The small angle neutron diffraction experiments were carried out at the SANS-2 scattering facility of FRG-1 research reactor in Geesthacht (Germany). A polarized beam of neutrons with an initial polarization of $P_0=0.94$, the neutron wavelength $\lambda=5.8$ Å ($\Delta\lambda/\lambda=0.1$) and a divergence of 2.5 mrad was used. The scattered neutrons were detected by a position sensitive detector with (256x256) pixels. The scattering intensity was measured in the temperature range from T = 10 K to T_C = 28.7 K. The external magnetic field **H** from 1 to 400 mT was applied perpendicularly to the incident beam and the polarization followed the direction of the magnetic field. The sample used was a disk with diameter of 20 mm and the thickness of 2 mm cut from the single crystal of MnSi. Its structural mosaic of 0.22^o was determined with the neutron spectrometer "Reflex" at FZ Julich. The single crystal was oriented in such a way that two axes [111] were set in a plane perpendicular to the incident beam.

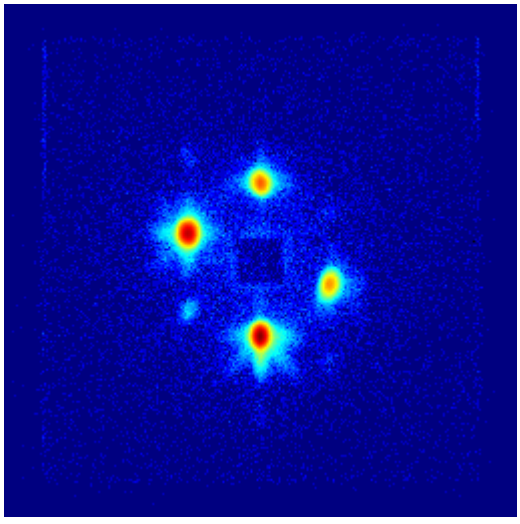


Fig. 1a

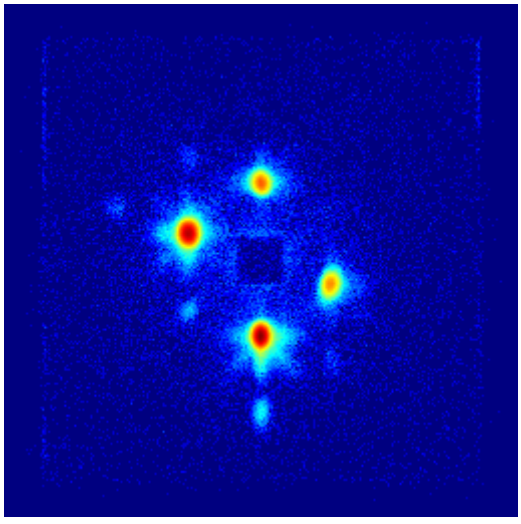
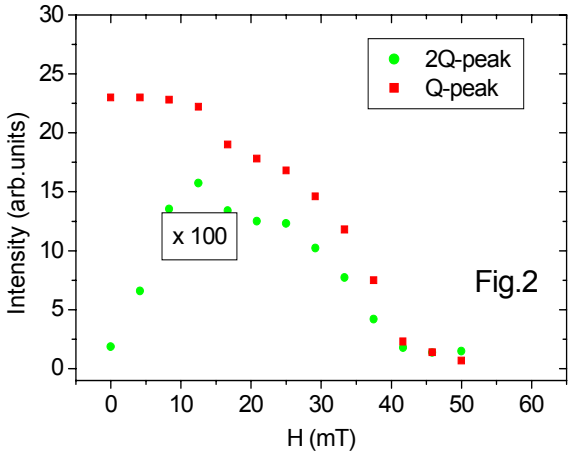
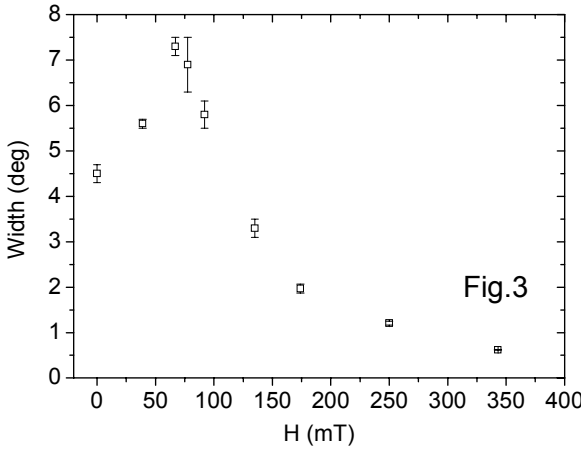
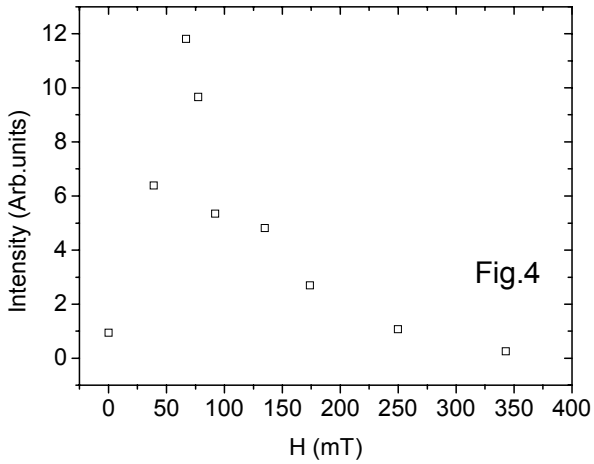


Fig. 1b







Results: Fig.1 gives the two maps of the diffraction peaks in a logarithmic scale at two different values of the magnetic field H = 0, 20 mT and at T = 10 K. The contour map at H = 0 shows the four major peaks (Fig.1 a), which are reflections for four scattering vectors collinear to the axes [111] and [11-1] and visible in this geometry of the experiment. When a relatively small magnetic field is applied (H < 150 mT), new small peaks at **q** = 2**Q** arise (Fig.1 b). The magnetic field dependence of the intensity for the large peak at **q** = **Q** and for the small peak at **q** = 2**Q** is given in Fig.2. It was found that these small Bragg peaks arise when the field has a component perpendicular to the helix scattering vector $\mathbf{Q}_{1,2}$. This demonstrates the deformation of the spiral structure within the plane of the spins. The circular rotation of the spin arrow is replaced now by the ellipsoidal rotation. This ellipse has an elongated axis along the applied field and reduced axis perpendicular to it. The quantitative description will be given soon.

The coexistence of two peaks both at **q** = ± **Q** may be explained by the mosaic of the *magnetic* rather than the crystallographic structure of MnSi. The mosaicity of the magnetic structure was determined by measuring the rocking curve of two magnetic reflections at **q** = $\mathbf{Q}_{1,2}$ of the same magnetic spiral along the axis (111) (Fig.3). The FWHM of the curves exceeds the value of 4^o at H = 0 what is much bigger than that of the crystallographic structure (0.2^o). The measured value of the masaic of the magnetic structure is bigger than that of the Bragg angle $\theta_B \approx \lambda/d \approx 1.85^o$. Thus we conclude that the mosaicity of the magnetic structure provides the possibility to observe many Bragg peaks simultaneously. The magnetic field dependence of the width of the magnetic Bragg peak and its intensity is shown in Fig.3 and Fig.3. It is well seen that the masaic has its maximum at H = 70 - 80 mT. The whole range of the large masaic spreads from H = 0 to H = 150 mT and then it decreases to the cristallographic value with further increase of the field. The intensity of the peak shows a very similar behaviour as the width of th epeak does. Both these facts show that the magnetic structure of the MnSi is strongly unstable in the range of small fields at H < 150 mT. The theoretical description of this phenomenon is in the progress.

References

1. Y. Ishikawa, K. Tajima, D. Bloch, M. Roth, Solid State Commun. **19** (1976) 525.
2. Y. Ishikawa, G. Shirane, J.A. Tarvin, M. Kohgi, Phys.Rev.B **16** (1977) 4956.
3. I.E.Dzyaloshinskii, Zh.Eksp.Teor.Fiz. **46** (1964)1420
4. P. Bak, M.H. Jensen, J.Phys.C **13** (1980) L881.
5. D. Nakamishi, A. Janase, A. Hasejawa, M. Kitaoka, Solid State Commun. **35** (1980) 995.

GKSS FORSCHUNGSZENTRUM in der HELMHOLTZ-GEMEINSCHAFT	EXPERIMENTAL REPORT	GeNF SANS-2 / DCD

Investigation of structural changes of nanocrystalline Mg/MgH_2 during absorption and desorption of hydrogen

Proposer:	**Thomas Klassen,** GKSS Forschungszentrum
Co-Proposers:	**M. Dornheim, A. Schreyer, P. K. Pranzas,** GKSS Forschungszentrum
Experimental Team:	**D. Bellmann, P. K. Pranzas,** GKSS Forschungszentrum
User Group Leader:	**P. K. Pranzas**
Date(s) of Experiment:	June – December 2004

Objectives

Before hydrogen can be widely used as an alternative fuel, efficient and safe ways of storage have to be developed. Magnesium hydride is considered to be one of the most interesting alternatives for the reversible storage of hydrogen, especially for mobile applications, because it is abundant, inexpensive, harmless to the environment, and because of its high hydrogen storage capacity of 7.6 wt.%. Nanocrystalline magnesium hydride offers a safe alternative to the storage of hydrogen in compressed or liquid form. Absorption and desorption kinetics of hydrogen on MgH_2 are well known [1-3]. The sorption properties are distinctly enhanced by the addition of metal-oxide catalysts. However, structural changes during absorption and desorption of hydrogen as well as the mechanisms of the catalytic reactions have hardly been investigated up to now. In this project structural changes of nanostructured MgH_2 during these processes will be characterised using small and ultra-small-angle neutron scattering (SANS/USANS).

Experiment

Nanocrystalline powder Mg/MgH_2 samples with different hydrogen contents were measured at the instruments SANS-2 and DCD at room temperature in quartz cuvettes with a thickness of 1 mm.

At SANS-2 distances between sample and detector of 1, 3, 9 m (λ = 0.58 nm) and 21 m (λ = 0.58 nm and 1.16 nm, $\Delta\lambda/\lambda$ = 0.1) were used to cover the range of scattering vector q from 0.009 nm^{-1} to 2.4 nm^{-1}. Scattering data were normalized by monitor counts and corrected for sample transmission and detector response. The differential scattering cross section was obtained by calibration with a Vanadium reference sample with a thickness of 1.28 mm.

Ultra small-angle neutron scattering (USANS) measurements were carried out at the double-crystal diffractometer DCD with a wavelength of 0.443 nm resulting in an accessible range of scattering vector q from 10^{-5} to 10^{-2} nm^{-1}. With this technique particle sizes up to 24 µm are detectable.

The schematic flow chart showing the preparation of the measured Mg/MgH_2 samples after 20 h high-energy ball milling and after several hydrogen desorption and absorption cycles is demonstrated in figure 1. The hydrogen/magnesium ratio is used for the sample names, the hydrogen contents in weight percent are mentioned below.

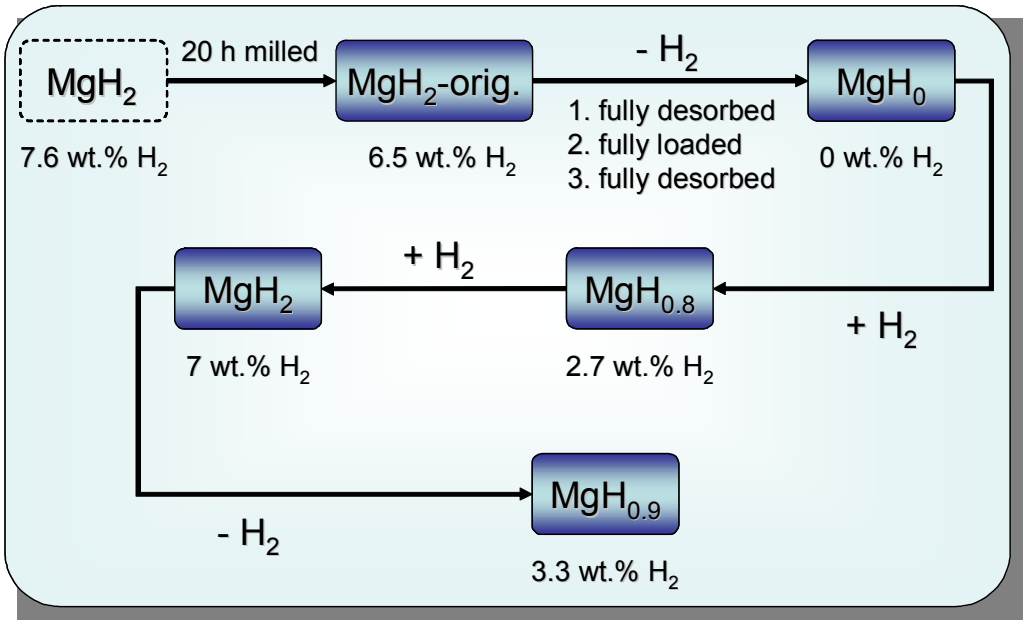


Figure 1: Schematic flow chart of the preparation of the measured MgH_x samples after 20 h high-energy ball milling and after several hydrogen desorption and absorption cycles.

Achievements and Main Results

Figure 2 shows the combined SANS-DCD scattering curves for the samples illustrated in figure 1.

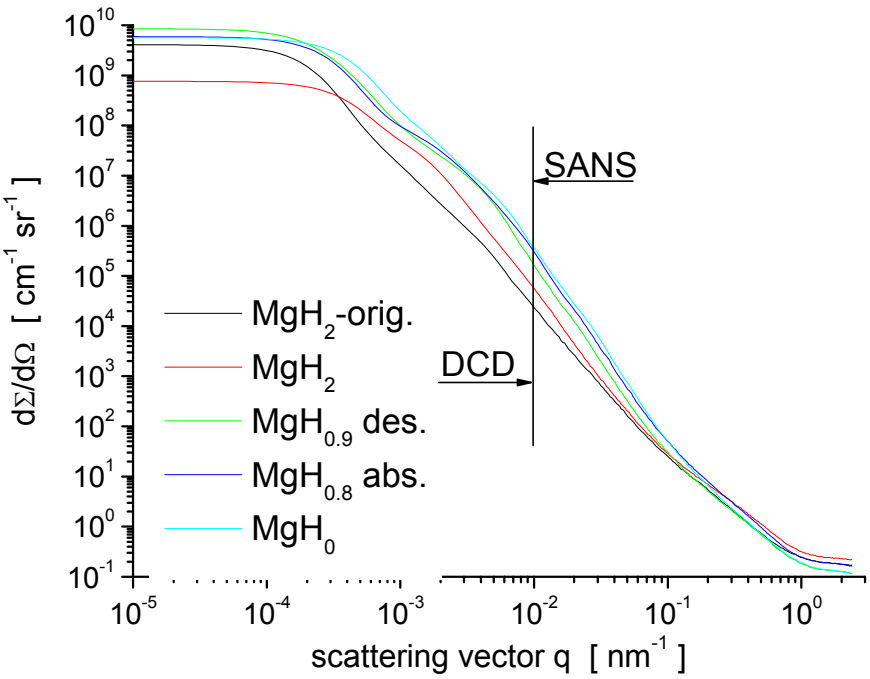


Figure 2: Combined DCD-SANS curves for high-energy ball milled MgH_x samples after absorption or desorption of hydrogen.

The differences in the curves exhibit structural changes in nanocrystalline Mg/MgH_2 during different stages of the hydrogen absorption and desorption cycling process. The formation of a shoulder at approximately 0.002 nm^{-1} with decreasing hydrogen content indicates the development of large structures with sizes up to several µm. At large values of the scattering vector q the varying incoherent scattering background due to the different hydrogen content is visible.

To get a rough estimate of the structural changes in the Mg/MgH_2 system, the size distributions shown in figure 3 were calculated using as first approximation a 2-phase hard spheres model and the scattering length densities differences Δη between MgH_x and air.

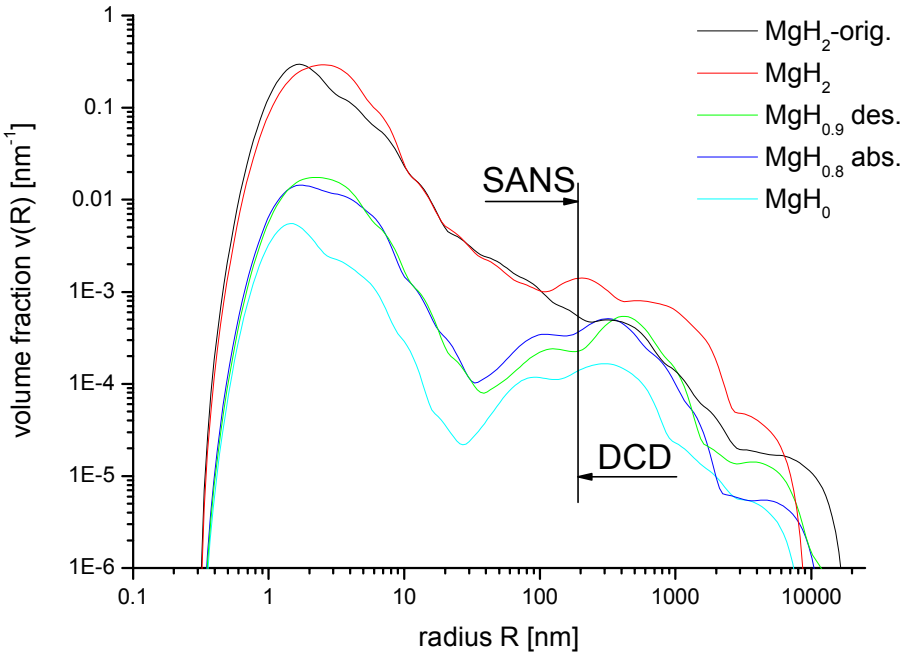


Figure 3: Size distributions calculated from the data shown in figure 2 using as first approximation a 2-phase hard spheres model and the scattering length densities differences Δη between MgH_x and air.

Structural changes are visible in the range of a few nm as well as in the µm-range. Due to the different signs of the scattering lengths of H and Mg ($b_{c,H}$= -0.374E-12, $b_{c,Mg}$= +0.537E-12 cm), the scattering length density of $MgH_{1.5}$ is about zero and therefore small deviations of the hydrogen content in this range have a large effect on the volume fraction. To eliminate these uncertainties it is planned to use deuterium ($b_{c,D}$= +0.667E-12 cm) instead of hydrogen in the preparation of the magnesium hydride samples. Together with additionally performed SAXS/USAXS measurements at HASYLAB, Hamburg the results obtained in these experiments will provide information about the growth and the formation of the α-MgH_2 phase during the absorption and the β-Mg phase during desorption respectively.

References

[1] G. Barkhordarian, T. Klassen, R. Bormann, J. Alloys Comp. 364, 242 (2004)
[2] G. Barkhordarian, T. Klassen, R. Bormann, Scripta Mater. 49, 213 (2003)
[3] W. Oelerich, T. Klassen, R. Bormann, J. Alloys Comp. 315, 237 (2001)

GKSS FORSCHUNGSZENTRUM in der HELMHOLTZ-GEMEINSCHAFT	EXPERIMENTAL REPORT	GeNF SANS-2, DCD

Characterisation of particles in dispersoide strengthened tantalum

Principal Proposer:	**M. Bischof[1]** [1]University of Leoben, Department of Physical Metallurgy and Materials Testing, Leoben, Austria
Experimental Team:	**M. Bischof[1], H. Eckerlebe[2], G. Kozik[2], K. Pranzas[2], P. Staron[2], D. Bellmann[2],** [2]GKSS Research Centre
Group Leader:	**M. Bischof[1]**

Date of Experiment:	August 2004

Introduction

Technically pure tantalum shows a number of unique properties such as a high melting temperature (2998 °C), high corrosion resistance, and good workability. Therefore, it is widely used as a preferred material in chemical industry, as furnace equipment, and in electronic components. But its limited strength at high temperatures prevents it from usage in some technically interesting applications. Small particles (precipitates or dispersoides) should prevent the Ta-grains from growing and thereby ensure both a sufficient high-temperature strength and ductility. For this, the particles have to be thermodynamically stable and sufficiently small.

One set of doped Ta-specimen had previously been investigated using SANS [1]. The particle size distribution was found to depend strongly on the foregoing thermal and mechanical treatment of the material. Moreover, large particles being out of the detectable size range of SANS were expected to be present. Therefore, a new series of specimen doped with Si, Y or both Si and Y was prepared to recover the dependence of particle size distributions on varying annealing conditions as well as on different kinds and amounts of doping elements. Complementary DCD-measurements were performed with selected specimens in addition to SANS to cover a larger size range of detectable particles.

Experiment

The new set of samples comprised four different materials, which were produced powder metallurgically and formed by several cold rolling and intermediate annealing steps until a final cross section of 6 mm x 6 mm was reached. The intermediate annealing was performed at 1350 °C for 2 h in a vacuum furnace in order to achieve a recrystallised microstructure. The forming conditions were identical for all tested samples. After the final forming step some specimens were left in a cold worked condition while others were annealed at different temperatures. Table 1 gives a detailed overview over all samples and the corresponding annealing conditions. The thickness of all samples was about 2 mm. All samples in Table 1 were analysed by SANS, but DCD was only performed on specimens marked by (*).

The SANS-experiments were carried out at the SANS-2 small-angle scattering facility. Scattered neutrons were detected by a position-sensitive detector with a resolution of 256x256 pixels. The range of the scattering vector q (0.025 nm^{-1} - 2.5 nm^{-1}) was covered using 4 different distances between detector and sample (1 m, 3 m, 9 m and 21 m). Appropriate apertures and collimators were used. The measurements were performed using neutrons at a wavelength of λ = 0.58 nm. The measured intensity was corrected for sample transmission, background and detector efficiency. The scattering data were averaged over

Table 1: Overview over all investigated Ta-samples. Samples marked with (*) were also analysed by DCD.

sample	nominal composition	working condition
1 c (*)	Ta + 400ppm Si + 100ppm YN	cold rolled
1 a12 (*)	Ta + 400ppm Si + 100ppm YN	annealed (1250°C/2h)
1 a13 (*)	Ta + 400ppm Si + 100ppm YN	annealed (1350°C/2h)
1 a14 (*)	Ta + 400ppm Si + 100ppm YN	annealed (1450°C/2h)
2 c	Ta + 400ppm Si	cold rolled
2 a13	Ta + 400ppm Si	annealed (1350°C/2h)
3 c	Ta + 800ppm Si	cold rolled
3 a13	Ta + 800ppm Si	annealed (1350°C/2h)
4 c	Ta + 100ppm YN	cold rolled
4 a14	Ta + 100ppm YN	annealed (1350°C/2h)

azimuthal scattering angle and absolute cross sections were calculated by comparison with the incoherent scattering of vanadium.

The double crystal diffractometer (DCD), working at a wavelength of 0.44 nm, was used to extend the *q*-range for two orders of magnitude to observe scattering from larger particles [2]. The DCD works with a slit collimation and the corresponding smearing has to be taken into account in the data analysis [3]. The scattering cross section of the Ta samples was rather small and multiple scattering did not play a significant role.

Results

The size distributions in Figure 1 and 2 were determined from the scattering curves by means of the fitting software “SansFit” which is provided by GKSS and performs an indirect transformation as it was described by Glatter [4]. A calculated scattering curve is thereby fitted to a measured scattering curve by means of a least-square procedure. Between 8 and 10 log-normal distributions were used to find the specific optimum for each curve between small error values and little fitting deviation. In the case of DCD only one log-normal distribution was used as the use of more distributions could have led to an over-interpretation of the scattering curve causing large errors in the size distribution. A scattering length density difference (s.l.d.d.) of 5.44×10^{9} cm^{-2} was used for all samples. This is the value for Ta_2Si in a pure Ta matrix, which was used because in Si-containing materials larger Ta_2Si particles (~100 nm in diameter) were detected by means of electron diffraction. Small particles were also found in the transmission electron microscope (Figure 3); however, their chemical composition is unknown and it should be noted that other particles than Ta_2Si (e.g. oxides) present in all materials will have other s.l.d.d.’s and that the chosen value must definitely be wrong for materials containing no Si. The presented particle volume fractions should thereby not be understood as absolute values but only as a preliminary discussion basis.

Figure 1 shows the evolution of the particle size distribution of the material containing both Si and Y with increasing annealing temperatures. It is obvious that a large portion of small particles dissolves after annealing at 1250 °C for 2 h. The volume fraction in the size interval between 2 and 20 nm decreases from 1.6% to 0.09%. However, the volume fraction of larger particles in the size range 50 - 200 nm remains almost constant (~1.8%). After annealing at 1350 °C the volume fraction of small particles is similarly small, but in contrast to annealing at 1250 °C also larger particles disappear. The volume fraction in the range between 50 and 200 nm is only 0.7% in this case. After annealing at 1450 °C the size distribution is similar to

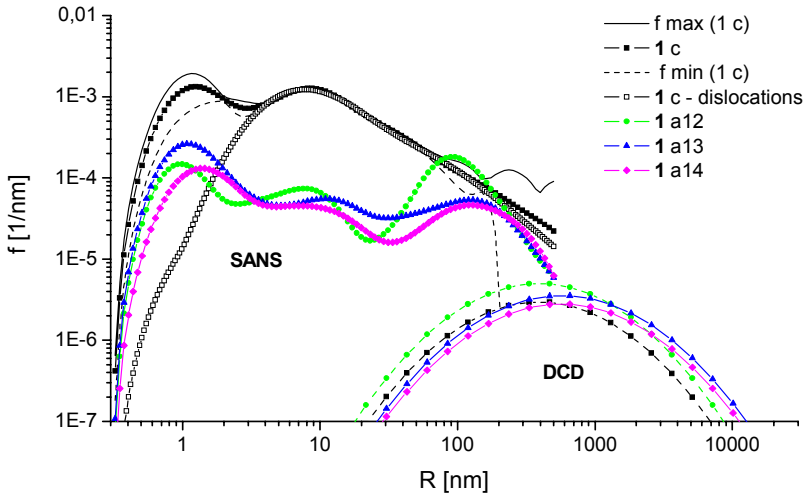


Figure 1: Evolution of the volume fraction of particles in material 1

the one obtained after annealing at 1350 °C. Having a look at the size range covered by DCD it is apparent that only little changes occur during annealing. The fraction of large particles in the interval 200 nm to 10 µm is 0.6% in the cold worked sample becomes slightly larger during annealing. It reaches a maximum at 1% after annealing at 1350 °C and decreases to 0.8% after annealing at 1450 °C. The peak of the DCD-based distribution shifts from 300 nm to about 600 nm indicating that the dissolution of small particles is accompanied by a coarsening of large particles. At 1450 °C even the largest particles start to dissolve.

For the cold worked sample a second size distribution is displayed (symbol □). This takes into account the influence of dislocations on the scattering curves at large scattering vectors. Neutron scattering from dislocation cores as well as from the surrounding strain fields at a dislocation density of $3 \cdot 10^{11}$ cm^{-1} was included into our consideration, following [5]. As the estimated dislocation density is a reasonable value for cold worked Ta it seems obvious that a significant contribution to scattering at large scattering vectors comes from these dislocations. Existing peaks in the particle size distributions at very small sizes (~1 nm) apparently are caused by dislocations. For the sake of a better readability of the graphs this effect is only displayed for one sample.

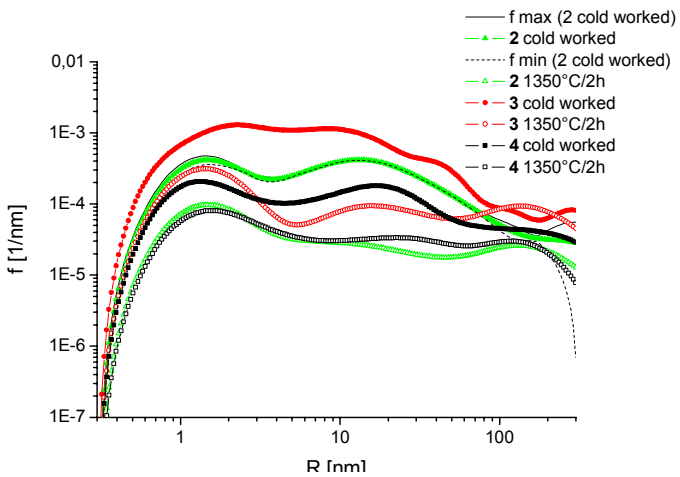


Figure 2: Particle size distributions for materials 2-4

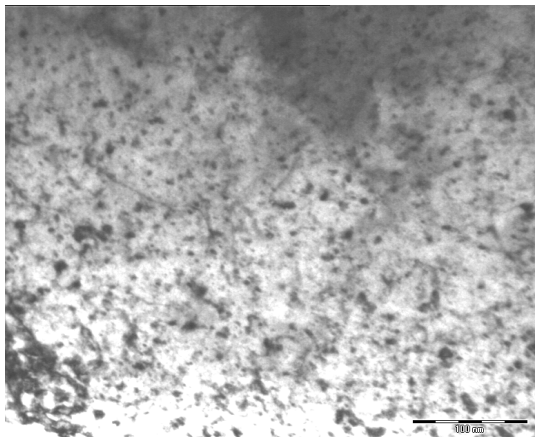


Figure 3: TEM bright field image of material 1, annealed at 830 °C for 30min.

Figure 2 shows the particle size distributions of the differently doped materials 2-4 in the as-worked condition as well as after annealing at 1350 °C. Material 3, which is doped with a nominal amount of 800 ppm Si has the largest particle fraction under both conditions. Material 2, doped with 400 ppm Si, comes next, followed by material 4 which is doped with 100 ppm YN solely. The large difference between cold rolled and annealed samples is similar to the difference previously discussed for material 1.

The calculated volume fractions cannot be explained by the presence of doping elements alone; therefore, chemical analyses were performed to determine the actual chemical composition of the samples. These analyses revealed a significant deviation of the actual dopant contents from their nominal composition as well as large and varying contents of O. For example, it seems apparent that the large difference in the volume fraction of small particles between material 1 and material 2 is not the result of a Y-content of only 20 ppm in material 1 but rather a result of a relatively high O-content of 125 ppm in material 1, compared to 50 ppm in material 2. The average s.l.d.d. of all prevailing particles seems to be larger than the above given value we used so far for the calculation, leading to more realistic volume fractions.

Conclusions

A combination of SANS and DCD was used to determine the dependence of particle size distributions from varying annealing conditions as well as from different kinds and amounts of doping elements in Ta. A large dependence from annealing temperatures could clearly be proved for a material containing small amounts of Si and Y. At 1250 °C primary small particles dissolve while larger ones tend to coarsen. At temperatures as high as 1450 °C larger particles dissolve, too. Therefore, it is apparent that at high temperatures only elements in solid solution seem to be responsible for a limited grain growth and sufficient strength. Doping with Si has a great influence on the volume fraction of small particles. The higher the Si content is, the higher the volume fraction gets. While this effect could clearly be proven, the effect caused by Y was superposed by “unintentional dopants” like O. The influence of the impurity content, namely primarily the content of O, has a great influence on the particle fraction and should be considered separately.

Acknowlegdement

This research project has been supported by the European Commission under the 6th Framework Programme through the Key Action: Strengthening the European Research Area, Research Infrastructures. Contract n°: RII3-CT-2003-505925'

References

[1] M. Bischof et al., Z. Metallkunde 95 (2004), 573-578
[2] D. Bellmann, P. Staron, P. Becker, Physica B 276-278 (2000) 124-125
[3] P. Staron, D. Bellmann, J. Appl. Cryst. 35 (2002) 75-81
[4] O. Glatter, J. Appl. Cryst. 13 (1980) 7-11
[5] M. Maxelon et al., Acta mater. 49 (2001), 2625-2634

GKSS FORSCHUNGSZENTRUM in der HELMHOLTZ-GEMEINSCHAFT	**EXPERIMENTAL REPORT**	**GeNF SANS-2**

Aggregation behavior of poly(2-oxazoline)-based A-B-C triblock copolymers in aqueous solution

Proposer:	**Dr. Ruzha Ivanova[1],** [1]Physik Department E13, TU-München
Co-Proposers:	**Prof. Dr. Christine M. Papadakis[1], Tune Bonné[1],**
Experimental Team:	**Prof. Dr. Christine M. Papadakis[1], Tune Bonné[1],** **Helmut Eckerlebe[2],** [2] GKSS Research Centre
User Group Leader:	**Prof. Dr. Christine M. Papadakis[1]**
Date(s) of Experiment:	20–26 September 2004

Objectives

The present study is focused on the aggregation behavior and the micellar network formation in aqueous solutions of novel poly(2-oxazoline)-based triblock copolymers and polymer surfactants containing lipophilic, hydrophilic and fluorophilic moieties. Two representatives of poly[(2-*n*-nonyl-2-oxazoline)$_n$-*b*-(2-methyl-2-oxazoline)$_m$-*b*-(2-perfluorobutyl-2-oxazoline)$_k$] triblock copolymers (PNOx$_n$-PMOx$_m$-PFOx$_k$) and C_8F_{17}-poly(2-methyl-2-oxazoline)$_m$-C_nH_{2n+1} polymer surfactants (F_8-PMOx$_m$-L$_n$) are selected. The central question is the micellar network structure, i.e. whether the network consists of separate micelles with lipophilic and fluorophilic cores linked by the hydrophilic blocks or of mixed lipophilic/fluorophilic micelles. Other questions are the micellar size and shape, the effect of the polymer concentration, the hydrophilic block length and the side-chains on the network structure.

Experiment

Small angle neutron scattering (SANS) was chosen as main experimental method in this study. SANS has the advantage to allow matching the contrast of the copolymer blocks by variation of the solvent scattering length density using mixtures of D_2O and H_2O. This technique is effective in microstructure determination of novel and complex systems and especially helpful in the present case to determine the structure of the micellar network, i. e. the formation of separate or mixed micelles.

Two triblock copolymers, PNOx$_7$-PMOx$_{38}$-PFOx$_7$ and PNOx$_{12}$-PMOx$_{64}$-PFOx$_9$, were chosen in order to study the effect of the hydrophilic block length. Two polymer surfactants with the same hydrophilic middle block PMOx but linear end-groups, F_8-PMOx$_{25}$-L$_{18}$ and F_8-PMOx$_{70}$-L$_{16}$, were also studied. In both cases the polymers were selected so to have comparable main chain length of the fluorophilic and the lipophilic moieties and significantly different degree of polymerization of the hydrophilic blocks. The comparison of the polymer surfactants to the ABC triblock copolymers reveals the role of the side-chains in end blocks and shows their influence on the micelle formation and microstructure.

Aqueous samples of the triblock copolymers and the polymer surfactants with various polymer concentrations in 12/88 wt% D_2O/H_2O mixture matching the scattering length density

of the hydrophilic block (PMOx, δ = 1.17×10^{10} cm^{-2}) were prepared. The scattering patterns were recorded at 25 °C at four different sample-to-detector distances (1 m to 21 m) in order to cover the entire *q*-range of interest 0.016 nm^{-1} to 2.6 nm^{-1} at λ = 0.57 nm. Measurements of the background scattering by the D_2O/H_2O mixture and the empty sample holder were also performed. In order to transform the scattering patterns on an absolute scale, the scattering of a vanadium single crystal and the sample transmissions were measured. For calibration of the detector response, the scattering pattern of polyethylene was recorded. The isotropic 2D scattering patterns were azimuthally averaged.

The triblock copolymers spontaneously aggregate into micelles at concentrations higher than the critical micelle concentration. At even higher concentrations, the solutions transform into gels. The scattering profiles of the solutions show one characteristic peak related to the correlations between the micelles (Fig. 1, left). The profiles of the gels show more than one peak, i. e. higher correlation between the micelles and/or highly ordered structure as illustrated in Fig. 1, left. With increasing the polymer concentration even further, the correlation peaks become more intense and pronounced but remain at the same *q*-position that indicates an increase of the order in the microstructure without change of the correlation length (Fig. 1, right).

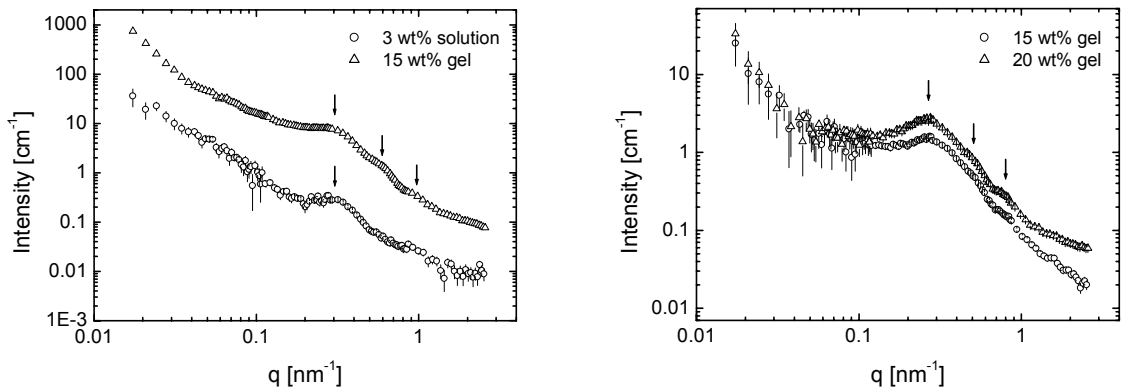


Figure 1. SANS scattering profiles: (left) $PNOx_7$-$PMOx_{38}$-$PFOx_7$ and (right) $PNOx_{12}$-$PMOx_{64}$-$PFOx_9$. The arrows mark the characteristic peaks.

The microstructure of the gels is expected to be that of a micellar network consisting of separate lipophilic or fluorophilic micelles [1]. This assumption is supported by our previous SANS experiments showing that the corresponding diblock copolymers do not form mixed lipophilic/fluorophilic micelles. In the case of $PNOx_{12}$-$PMOx_{64}$-$PFOx_9$ the gel formation starts at about 6 wt% (5.6 mmol/l), while in the case of $PNOx_7$-$PMOx_{38}$-$PFOx_7$ at about 12 wt% (17.6 mmol/l). Or in other words, the shorter the hydrophilic block (acting as a spacer separating the lipophilic and the fluorophilic micelles) the higher molecular concentration is needed in order to bridge the two types of micelles and form a gel.

The behavior of the polymer surfactants in aqueous solutions is quite similar. At concentrations higher than 20 wt%, they also form gels. Again more than one characteristic peaks are registered in the scattering patterns indicating the presence of order in the microstructure (Fig. 2). The peak positions for both polymers are shifted to higher *q*-values in comparison to the triblock copolymers reflecting smaller characteristic length-scales.

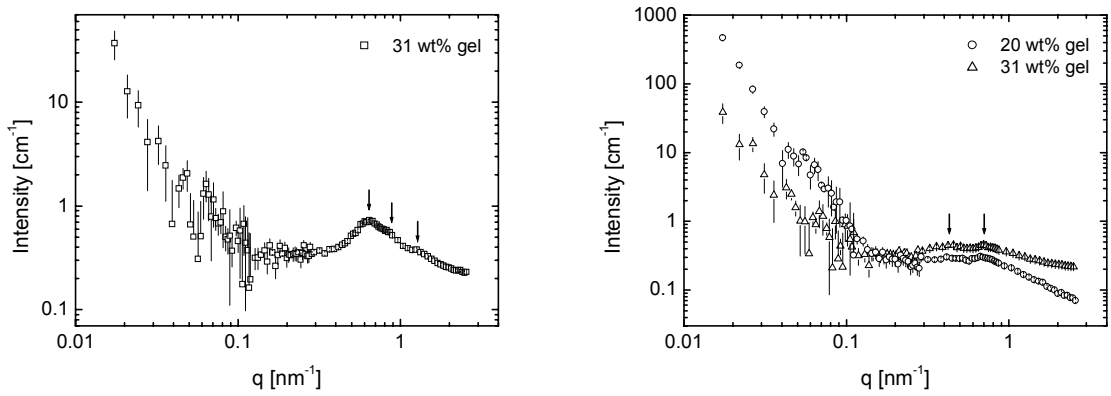


Figure 2. SANS scattering profiles: (left) F_8-$PMOx_{25}$-L_{18} and (right) F_8-$PMOx_{70}$-L_{16}. The arrows mark the characteristic peaks.

In order to determine the gel microstructure and prove the formation of a micellar network consisting of separate lipophilic and fluorophilic micelles, further data evaluation such as construction of the most suitable model and fits are ongoing. The obtained measurements on an absolute scale are essential in order to create the best model of the scattering curves.

Achievements and Main Results

The aggregation of novel poly(2-oxazoline)-based ABC triblock copolymers and polymer surfactants containing lipophilic, hydrophilic and fluorophilic moieties in aqueous solutions was studied. The formation of micellar solutions at low and of gels at high concentrations was shown. The size and the shape of the micelles as well as the effect of the copolymer concentration, the hydrophilic block length and the side-chains on the microstructure were studied. The ongoing quantitative data evaluation will allow to determine the gel microstructure and the type of the micellar network.

The studied novel poly(2-oxazoline)-based polymers represent a versatile system with readily adjustable molecular architecture, hydrophilic-lipophilic balance and degree of block segregation [1-3]. The aggregation behavior of block copolymers containing fluorophilic moieties (which increase strongly the degree of block segregation) is currently a topic of large interest and a variety of chemical compositions and architectures are investigated, e.g. [1,4]. The polymers studied here offer the possibility to design aqueous multi-compartment systems where two kinds of solvates can be dissolved, which have large practical potential, for example in the pharmaceutical industry as selective vehicles for drug delivery.

References

[1] R. Weberskirch, J. Preuschen, H. W. Spiess, and O. Nuyken *Macromol. Chem. Phys.* **2000**, *201*, 995-1007.
[2] R. Jordan, K. Martin, H. J. Raedler, K. K. Unger *Macromolecules* **2001**, *38*, 8858.T.
[3] T. Komenda, PhD thesis, TU München, 2004.
[4] Zh. Li, E. Kesselman, Y. Talmon, M. A. Hillmyer, and T. P. Lodge *Science* **2004**, *306*, 98-101.

GKSS FORSCHUNGSZENTRUM in der HELMHOLTZ-GEMEINSCHAFT	**EXPERIMENTAL REPORT**	**GeNF SANS-2**

Spin structure probed by SANS in $Bi_{0.125}Ca_{0.875}MnO_3$

Proposer:	**Trevor A. Tyson**[1], [1]New Jersey Institute of Technology, Department of Physics, New Jersey, USA
Co-Proposers:	**Yuhai Qin**[1],
Experimental Team:	**Yuhai Qin**[1], **P. Klaus Pranzas**[2], [2]GKSS
User Group Leader:	**Trevor A. Tyson**[1]

Date(s) of Experiment:	8. – 19. October 2004

Objectives

The CMR (Colossal Magnetoresistance) effect in proveskite manganite, $A_{1-x}B_xMnO_3$, has gained intensive studies in recent years. A complete understanding of CMR lies in the knowledge of competing/cooperating magnetic, structural and charge interactions in these compounds. $Bi_{1-x}Ca_xMnO_3$ constitutes a very interesting but less-studied system, which is ideal for understanding those correlations. In the high calcium doping region ($0.6<x<1$), a ferromagnetic (FM) moment of ~1.2 Bohr magnetons per Mn site is found for x~0.875. The magnetic moment per Mn site maintains a value ~1/3 the theoretical limit even in fields a high as 60 T. The physical origin of this high moment region is not well understood. Various models including canted ferromagnetism and ferromagnetic clusters hosted by an antiferromagnetic background have been proposed. Jirak et al. interpreted in terms of the heterogeneous coexistence of two phases (pure FM and AF phases), while Yoshizawa et al. suggest homogeneous CAF ordering. The homogeneous CAF model is crucial for the interpretation of some extremely large CMR effect, because the electron-phonon and/or electron-magnon coupling play a central role in this model. On the other hand, a heterogeneous model gives somewhat different interpretation of CMR effect. That is, CMR effect is interpreted to be caused by the growth of a FM-phase region, at an expense of a AF-phase region. Under this condition, our aim is to SANS to unveil the presence of mesoscopic FM clusters in the AF background matrix and give the size variation of them when temperature and external magnetic field changed. So we can test the "phase-coexistence" picture and have a better understanding to the CMR effect.

Experimental Techniques

Polycrystalline Bi0.125Ca0.875MnO3 sample was synthesized by standard ceramic technique and then small-angle neutron scattering (SANS) was conducted at the SANS-2 facility of GKSS research centre. Neutrons with a mean wavelength of λ=0.58nm (for detector distance of d=0.98m, 2.98m, 8.98m and 21.7m) andλ=1.16nm(for detector distance of d=21.7m) were selected by a rotating monochromator. Four different detector distances at d=0.98m, 2.98m, 8.98m and 21.7m were used in order to cover the full q spectrum ($0.01nm^{-1}$ ~ $2.5nm^{-1}$). The powder sample was centred in the sample chamber and then both temperature (T=20K, 100K, 108K, 120K, 200K) and magnetic field dependent (T=0T, 0.1T, 1T and 1.75T) measurements for the differential scattering cross section ($d\Sigma/d\Omega$) were performed. The data acquisition times were 30 to 60 min per measurement depending on the used distance. Scattered neutrons were recorded with an area detector of 256*256 pixels.

The measured data were calibrated by the incoherent scattering of vanadium and corrected for the sample transmission, background scattering (from the sample holder) and detector response. The resulted data were processed by the software of SANDRA and SANSMAN.

Achievements and Main Results

In order to remove the non-magnetic background scattering, correction was made by subtracting the intensity of 200K from those of 20K, 100K, 108K, 120K and 150K. In this case, intensity of scattering at 200K is considered purely from a non-magnetic background as is based on the macroscopic magnetization measurements (no macroscopic magnetic effect is observed at T=200K).

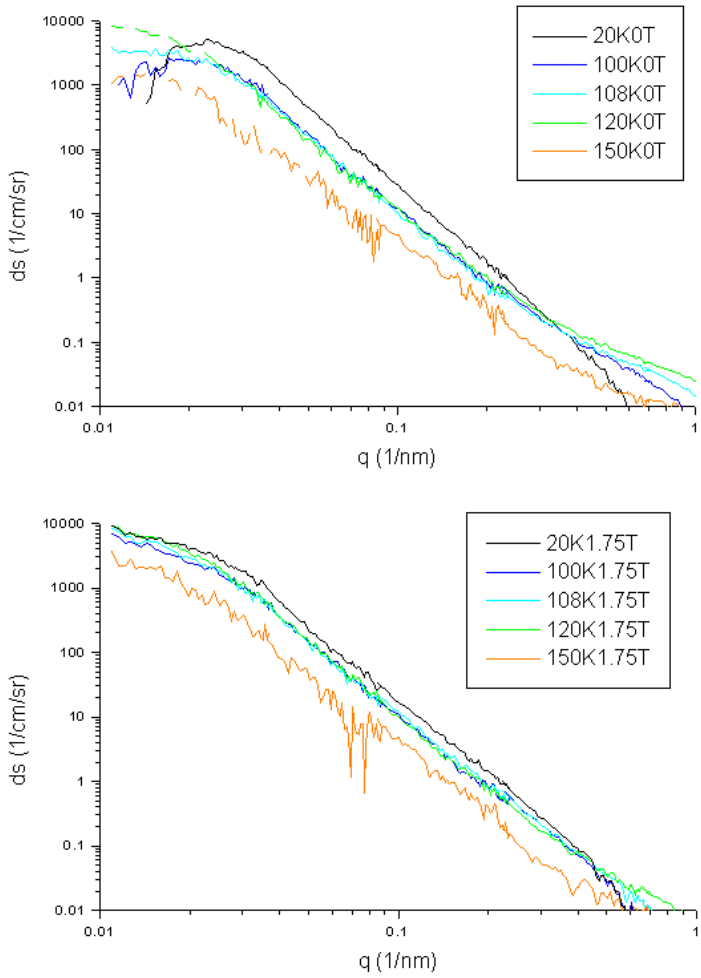


Fig.1. Magnetic differential cross section of Bi0.125Ca0.875MnO3 in the low q range.

Cluster-like spin structure was observed in the data of Fig.1. At both zero external field and 1.75Tesla, the intensity curves between q=0.04~0.2nm^{-1} follow Porod's q^{-4} law very well below Tc=108K, as indicates presence of round-shape spin clusters. When temperature was increased above Tc, the scattering intensity curves began to deviate from Porod's law but still maintain a power law (Aq^{-4}) which simply implies the collapse of spin clusters during this process. We can also find the magnetic component occurs above Tc, even at T=150K.

Below q~0.03nm^{-1}, the scattering curves began to deviate from Porod's law. The beginning of deviation point q_0 roughly gives the average radius of the spin clusters with $R_0 \sim 1/q_0$ = 33nm.

With an external field, 1.75Tesla for instance, the clusters begin to be correlated and grow in size. As can be found by comparing the upper and lower parts of Fig.1, because at T<Tc the "crossover" from q^{-4} was drastically lowered when the external field was applied.

Conclusion

These initial results clearly demonstrate that with increasing of external field, the clusters grow and the correlation is enhanced. The high moment suggests, that the spins inside the clusters are gradually aligned at temperature is reduced or a magnetic filed is applied. More detailed modelling is being conducted to extract the cluster distribution functions.

References

[1] H. Chiba, et al., Solid State Commun. 99, 499 (1996)
[2] Z. Jirak, et.al., J. Magn. Mater. 15-18, 519 (1980)
[3] H. Yoshizawa, et.al., Phys. Rev. B 52, 13145 (1998)
[4] T. Kasuya, A. Yanase, Rev. Mod. Phys. 40, 684 (1968)
[5] S. Zhang, J. Appl. Phys. 79, 4542 (1996)
[6] J. W. Lynn, et.al., Phys. Rev. Lett. 77, 4046 (1996)
[7] M. Uehara, et.al., Nature 399, 560 (1999)
[8] S. Mori, et.al. Phys. Rev. B 59, 13573 (1999)
[9] N. Fukumoto, et.al., Phys. Rev. B 60, 12963 (1999)
[10] H. Woo, T. A. Tyson, et.al., Phys. Rev. B 63, 13412 (2001)

GKSS FORSCHUNGSZENTRUM in der HELMHOLTZ-GEMEINSCHAFT	EXPERIMENTAL REPORT	GeNF SANS-2

Reinvestigation of magnetic critical phenomena in MnSi

Proposer:	**D. Lamago[1],** [1]Technische Universität München
Co-Proposers:	**R. Georgii[1], P. Böni[1],**
Experimental Team:	**D. Lamago[1], H. Eckerlebe[2], P. K. Pranzas[2],** [2]GKSS, **A.I. Okorokov[3], Yu.O.Chetverikov[3],** , [3]Petersburg Nuclear Physics Institute
User Group Leader:	**D. Lamago[1]**
Date(s) of Experiment:	11 / 2004

Objectives

The predictions of Kawamura [1] on the existence of new universality classes for magnetic systems with chiral symmetry motivated several theoretical and experimental investigations of critical phenomena in helical magnets. In spite of some experimental validation of the hypothesis of new chiral universality classes, the Kawamuras predictions are still subject of controversy. Azaria et al. [2] suggest that the lack of universality of experimental results on Ho, Dy and Tb can be understood as the consequence of a tricritical mean-field behavior for the Heisenberg-like spin-order. Experimental and theoretical investigations of the magnetic critical behavior in the intermetallic compound MnSi could help to explain the phase transitions in helimagnets since MnSi is known as a typical chiral magnet and exhibits a complex magnetic transition at 29 K. Due to the lack of inversion symmetry of the tetrahedral $P2_13$ structure, the Dzyaloshinskii-Moriya interaction leads to a helical modulation of the ordered magnetic moments with a period of about 180 Å. The Q-Vector of the helix lies along [111], though a small external magnetic field will orient Q in any direction [3,4].
Here we report critical on small angle polarized neutron scattering measurements of a single crystal of MnSi. A precise alignment of the single crystal allows to study the critical behavior of each magnetic satellite separately and thus to evaluate with high accuracy the critical exponents of the phase transition.

Experiment

The measurements were done using the (FRG-1) SANS-2 instrument of the GKSS research center in Geesthacht (Germany). The incident neutrons with a wavelength λ=5.8 Å have an initial polarization P_0=0.95.The scattered neutrons were detected by a position sensitive detector with (128x128) pixels. The scattering intensity was measured in the magnetic field range from H = 0 to H = 600 mT applied perpendicularly to the incident beam and the polarization followed the direction of the magnetic field. The high quality single crystal was oriented in such a way that two axes [111] were set in a plane perpendicular to the incident beam. The possibility to rotate the sample was given by a low temperature piezo-rotator [5]. The sample could be rotated only around the vertical axis, it was not possible to tilt the sample. This set-up allowed us to select a magnetic satellite of interest and then to perform a field and/or a temperature scan. In our previous experiment it was quite difficult to satisfactorily align the crystal since there was no goniometer available.

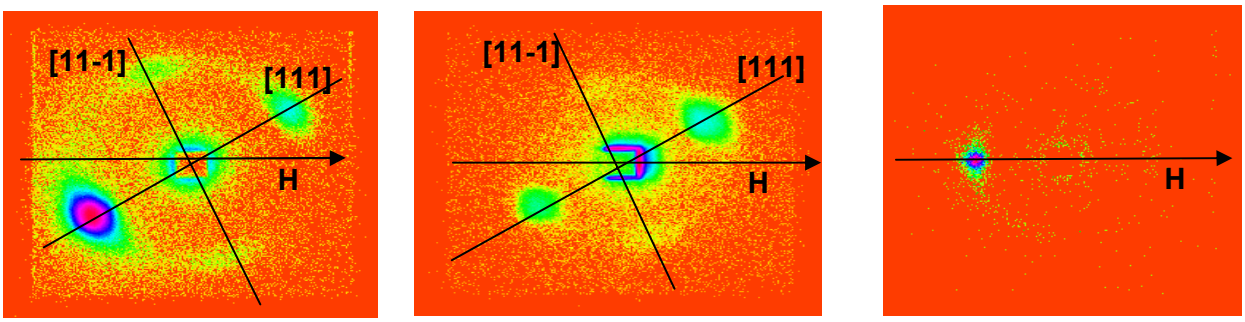
Achievements and Main Results

Fig 1a displays a typical diffraction pattern of a helical magnet at zero field for T = 17K. We denote the appearance of four magnetic peaks due to the reflection of the chiral vectors collinear to the two [111] axes. There are no additional peaks as in our previous measurements, which indicates a better crystal orientation. The sample was then rotated in

such a way that only the magnetic satellites along one of the [111] direction were visible as shown in Fig.1b. It should be noticed that the other peaks were not dissolved completely since it was not possible to tilt the sample. In this geometry we changed the magnetic field from H =0 to 600 mT.

In order to prove the wave-vector reorientation [3,4] taking place as the magnitude of the magnetic field is changed we show in Fig.2a the dependence of the scattering intensity with the applied magnetic field. Fig.2b displays the polarization of the selected peak. As soon as a magnetic field is applied, the selected satellites move towards the direction of the field so that at H_c=350 mT the peaks collapse to the direction of the magnetic field and only one satellite is visible (Fig 1c). The intensity of this peak begins to decrease with further increase of the magnetic field and finally vanished, i.e. no scattering is observed anymore. From the dependence of the scattering intensity with the reduced magnetic field $I \propto (H - H_C)^{\beta}$, we find the critical exponent $\beta = 0.23 \pm 0.013$ of the phase transition due to the wave-vector rotation towards the [111] direction.

Because of the difficulties encountered with the temperature control we were not able to performed further temperature scans. This should be achieved during the next experiments in order to estimate with this geometry the chiral critical exponents.



a H = 0, T = 17K **b** H = 0, T = 17K **c** H = 350mT, T= 17K

Figure 1:SANS scattering patterns observed in MnSi at T = 17K with magnetic fields applied perpendicularly to the two [111] directions.

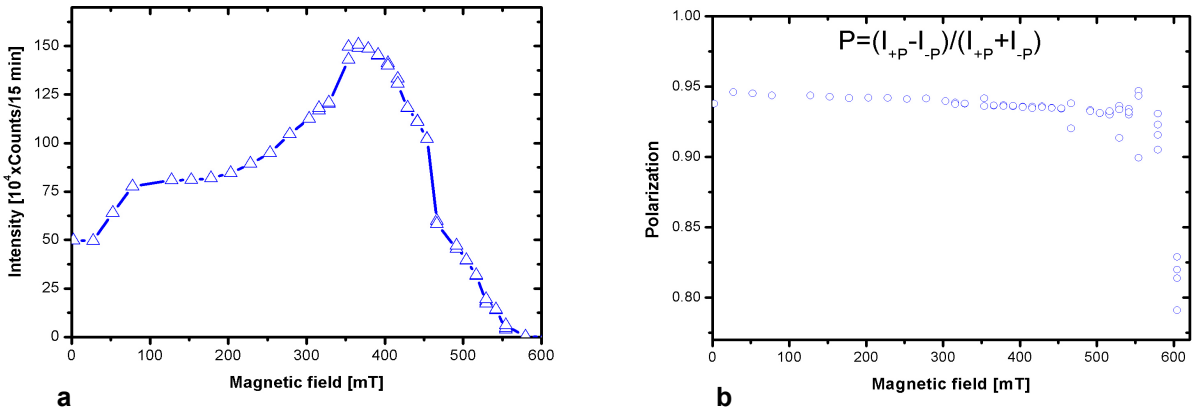


Figure 2: Intensity (a) and polarization (b) of the magnetic satellite as function of the magnetic field

References

1. H. Kawamura, J. Appl. Phys. **63,** 3086 (1988).
2. P. Azaria, B. Delamotte, T. Jolicoeur, J. Appl. Phys. **69**, 8 (1991).
3. M.L. Plumer, M.B. Walker, J.Phys. **C14** (1981) 4689.
4. M.B. Walker, Phys.Rev.B **40** (1989) 9315
5. Inertial Positioner ANR100, User manual Attocube systems, www.attocube.com

GKSS FORSCHUNGSZENTRUM in der HELMHOLTZ-GEMEINSCHAFT	**EXPERIMENTAL REPORT**	**GeNF SANS-2**

SANS study of the magnetic structure of YMn_6Sn_6 compound

Principal Proposer: S.V. Grigoriev, A.N.Pirogov, A.I. Okorokov
Petersburg Nuclear Physics Institute

Experimental Team: H. Eckerlebe, K. Pranzas, A.I. Okorokov, Yu.O.Chetverikov GKSS, PNPI

Date(s) of Experiment: 11 / 2004

Scientific Objective. The proposal was aimed to investigate the magnetic structure in the intermetallic compound YMn_6Sn_6 by means of small angle neutron scattering (SANS). In the intermetallic materials the competition between different exchange interactions results in a variety of the magnetic structures. The use of SANS allows one to observe the peaks originated from the scattering from the long periodical helical structure. The sample under study is a compound crystallized in $HfFe_6Ge_6$-type structure (space group *P6/mmm*) [1]. The rare earth R (non magnetic Y) and Mn atoms occupy three positions: 2e, 2d and 2c. The lattice has an intrinsically layered structure. The structure can be described as built of magnetic Mn (001) planes stacked along the c axis with R and Sn_3 atoms between Mn planes. There are two types of the interplane coupling interactions in YMn_6Sn_6: J'_1 through the Sn_3 plane, namely the "Mn-X-X-Mn" slab, and J'_2 through the R plane, namely the "Mn-R-Mn" slab. Moreover, it should be noted that the Mn-Mn interplane distance corresponding to J'_1 is slightly larger than that corresponding to J'_2. Below the Neel temperature T_N=333K the YMn_6Sn_6 compound is a helical antiferromagnet: the Mn atoms are arranged ferromagnetically within each layer, and the direction of magnetic moment rotates from one layer to another in a complex way [2]. Thus the direction of the magnetic spirals is along the c-axis [001].

Experimental Technique. The small angle neutron diffraction experiments were carried out at the SANS-2 scattering facility of FRG-1 research reactor in Geesthacht (Germany). A polarized beam of neutrons with an initial polarization of P_0=0.94, the neutron wavelength λ=5.7 Å ($\Delta\lambda/\lambda$=0.1) and a divergence of 2.5 mrad was used. The scattered neutrons were detected by a position sensitive detector with (256×256) pixels. The scattering intensity was measured in the temperature range from T = 10 to 320 K. The external magnetic field **H** from 1 to 500 mT was applied to the sample perpendicularly to the incident beam and the polarization followed the direction of the magnetic field. The sample was a powder compressed into a tablet. This geometry of the experiment allows one to observe many diffraction peaks in a range of small-angle scattering that originates from the particles accidentally oriented such that the Bragg condition is fulfilled: $2d \sin(\theta/2) = \lambda$, or $q = 2\pi/d$.

The samples. The sample was prepared by melting the high purity metals in an induction furnace in argon atmosphere following by the homogenization annealing in argon at 800 C for 48 hours.

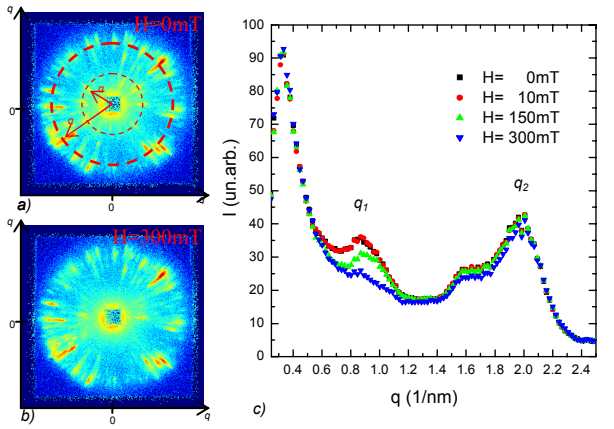


Figure 1. Magnetic field dependence of SANS intensity for T=293K. a), b)- detector maps for B= 0mT and B= 300mT, respectively. c) q-dependence of scattering intensity for different fields.

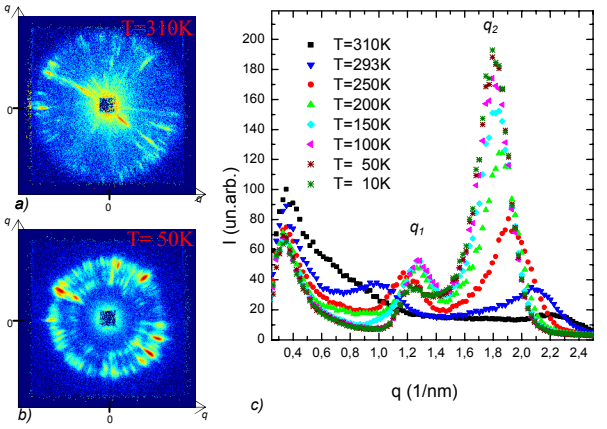


Figure 2. Temperature behavior of SANS intensity. a), b)- detector maps for T=310K and T=50K, respectively. c) q- dependence of scattering intensity for different temperatures.

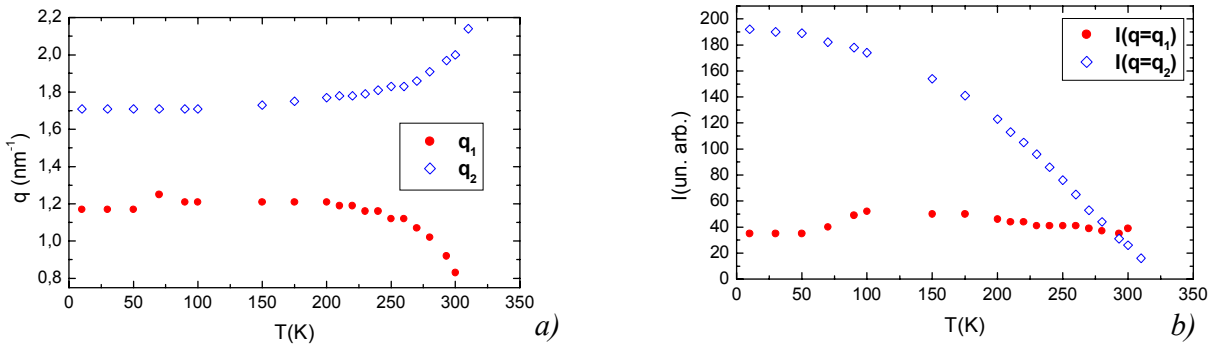


Figure 3. Temperature dependences of the peak's position *a)* and peak's intensities *b)*.

Results. Fig.1a and b give the maps of the SANS intensity in a logarithmic scale at H=0 and H = 300 mT, respectively, at T = 293 K. Due to random orientation of the crystallites in the sample many diffraction peaks, reflections from the magnetic periodical structure, are visible. These reflections are concentrated near two rings centered at q = 0 with the average radiuses q_1=0.9 nm-1 and q_2=2.0 nm^{-1}. The q-dependence of the neutron intensity averaged over the ring at constant |q| is presented in Fig.1c. The shape of the peak at q_2=2.0 nm^{-1} is asymmetric. This may imply a new peak aside the major one. The coexistence of several reflections at different values of |q| originates from complex magnetic structure. It is also seen from Fig.1c that the magnetic field tends to suppress the peak at small q (q_1=0.9 nm^{-1}), while this field does not change the neutron scattering at large q (q_2=2.0 nm^{-1}). The temperature behavior of this magnetic system is shown in Fig.2. The system changes dramatically close to the phase transition (T_N =333K). The neutron scattering intensities and the positions of the peaks as a function of the temperature are shown in Fig.3a and Fig.3b, respectively. It is interesting to note that the value of q_1 decreases down to zero as temperature approaches T_N, while the value of q_2 increases with an increase of the temperature. The intensity of the first peak has no significant change with the temperature, while the intensity of the second peak decreases dramatically as T approaches T_N. The observed structures at q_1 and q_2 demonstrate alternative types of the behavior with the temperature and magnetic field.

References

1. R.R. Olenich, L.G. Akselrud, Y.P. Yarmoliuk, Dopov. Akad. Nauk Ukr. RSR Ser. A (2) (1981) 84.

2 G. Venturini, D. Fruchart, B. Malaman, J. Alloys Comp. 236 (1996) 102

3. N.K. Zajkov, N.V. Mushnikov, E.G. Gerasimov, V.S. Gaviko, M.I. Bartashevich, T.Goto, V.I. Khrabrov, J. of Alloys and Compounds 363 (2004) 40–45

GKSS FORSCHUNGSZENTRUM in der HELMHOLTZ-GEMEINSCHAFT	**EXPERIMENTAL REPORT**	**GeNF SANS-2**

The study of magnetic nanocomposites based on porous glasses with embedded Fe_3O_4-particles by SAPNS

Principal Proposer: S.V. Grigoriev, I.V. Golosovsky, Petersburg Nuclear Physics Institute

Experimental Team: H. Eckerlebe, K. Pranzas, Yu.O. Chetverikov, A.I. Okorokov, GKSS, PNPI

Date(s) of Experiment: 11 / 2004

Scientific Objective.

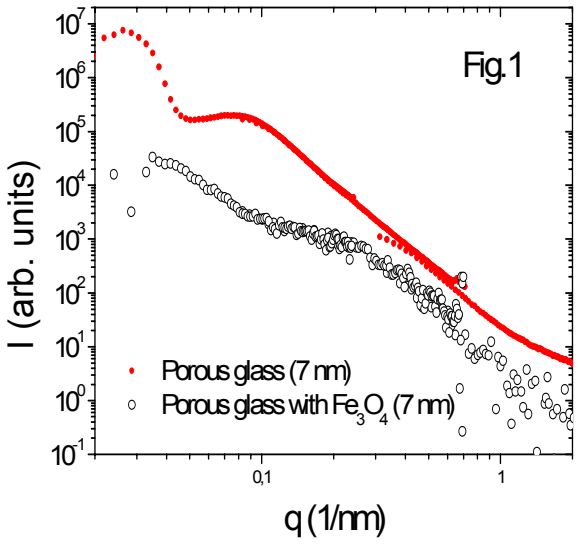
The proposal was aimed to study the topology and magnetic properties of the nanocomposites based on porous glasses SiO_2 with embedded magnetite particles. The large scale structure of the vycor glasses used to be considered as a randomly disordered porous medium. Nevertheless, the short range ordering on the large scale might take place in such a medium. This structure is not clarified yet. The magnetic structure of the sample should coincide with the structure of the pores. This also should be proven by the independent experimental methods.

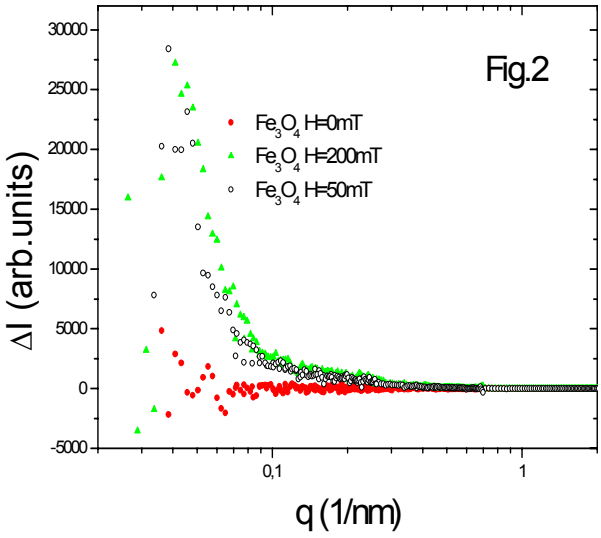
Samples.

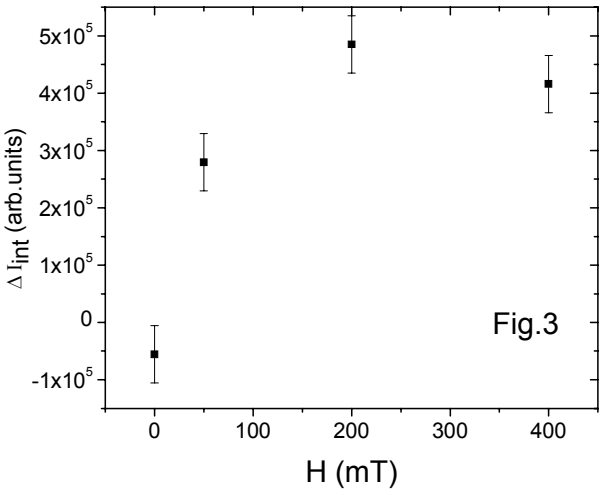
Different samples of the porous glass with a diameter of 2, 5, 7 nm were chosen for study of the structural features of the system. A magnetite had been embedded in a vycor porous glass with the mean diameter 7 nm by " bath deposition method". The synthesis of Fe_3O_4 within nanopores was done for the first time, nevertheless the neutron diffraction experiment and the profile analysis showed that impurities do not exceed some percents.

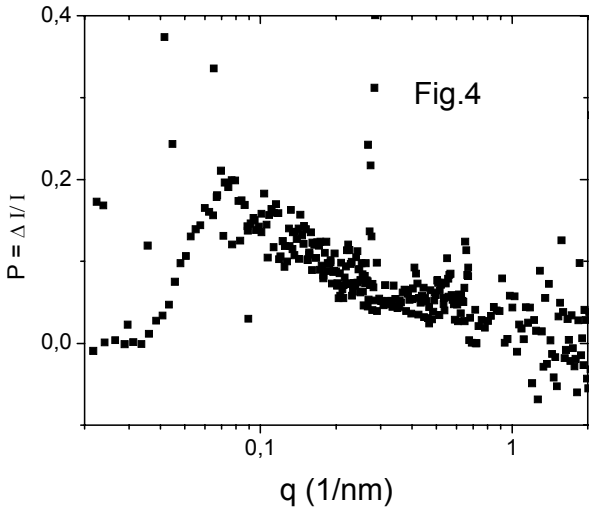
Experimental Technique.

The small angle neutron diffraction experiments were carried out at the SANS-2 scattering facility of FRG-1 research reactor in Geesthacht (Germany). A polarized beam of neutrons with an initial polarization of P_0=0.94, the neutron wavelength λ=5.8 Å ($\Delta\lambda/\lambda$=0.1) and a divergence of 2.5 mrad was used. The scattered neutrons were detected by a position sensitive detector with (256x256) pixels. The external magnetic field **H** from 1 to 400 mT was applied perpendicularly to the incident beam and the polarization followed the direction of the magnetic field. Theoretically, the small angle polarized neutron scattering consists of three contributions: nuclear scattering, magnetic scattering and the nuclear-magnetic interference contribution. The nuclear (magnetic) scattering cross-section may be given as: $\sigma_{n(m)}(\mathbf{q}) = |A_{n(m)}|^2 (\langle \mathbf{m}_\perp^2 \rangle) F_{n(m)}(\mathbf{q})$ and the interference term: $\sigma_{Int}(\mathbf{q},\mathbf{P}_0) = 2 \langle \mathbf{P_0}\, \mathbf{m}_\perp \rangle A_n A_m \mathrm{Re}(F_{nm}(\mathbf{q}))$, where A_n , A_m are the nuclear and magnetic contrasts, $\mathbf{m}_\perp = \mathbf{m} - (\mathbf{me})\mathbf{e}$, **m** is the magnetization and $\mathbf{e} = \mathbf{q}/q$. The pure nuclear or magnetic scattering is polarization-independent. Besides the magnetic scattering amplitude A_m is often smaller than nuclear one A_n, for which reason the magnetic scattering becomes statistically indistinguishable. In this case, the polarization dependent part, or interference term, may bring the information on the magnetic scattering, since it is linearly, but not quadratically, proportional to A_m. The interference term of the scattering is determined as the difference $\Delta I(q) = I^+(q) - I^-(q)$ of the intensities for neutrons polarized parallel (+) and anti-parallel (-) to the magnetic field.









Results.

The q-dependence of the neutron intensity I(q) for the pure matrix with the pore size of 7 nm and for the sample with embedded Fe_3O_4 is shown in Fig.1. It is seen that the scattering intensity for pure matrix has two maximums at q = 0.025 nm^{-1} and q = 0.09 nm^{-1}. The scattering intensity for the sample with Fe_3O_4 is, first, of one order less amplitude and, second, has two minima at the same q, where the were maximums for the pure matrix. This change in the neutron scattering spectra is attributed to the change of the scattering contrast due to iron oxide embedded to the pores of the matrix.

A nuclear scattering cross-section dominates at the magnetic one in this experiment so that the magnetic scattering is a few percents of the nuclear one only. Nevertheless, the nuclear-magnetic interference term exceeds 10-20 % of the total scattering. The q-dependence of the neutron intensity difference $\Delta I(q)$ at H = 0, 50, 200 mT K is shown in Fig.2 This kind of scattering implies the presence of the magnetic structures correlated with the nuclear one. The magnetic field dependence of the interference intensity ΔI_{int} integrated over all q is given in Fig.3. It is seen that the interference scattering is absent at H = 0, while it increases with the increase of the magnetic field and then is saturated at H > 100 mT. To see better the structural factor of the magnetic contribution, the interference scattering was normalized by the total (nuclear) scattering. The polarization $P = \Delta I(q)/I(q)$ for H = 200 mT is shown in Fig.4. It has a pronounced maximum at q_m = 0.07 nm^{-1}. The interference correlation length may be estimated as $R_{int} \sim 2\pi/q_m \approx 90$ nm. The interpretation of the presented data is in progress.

GKSS FORSCHUNGSZENTRUM in der HELMHOLTZ-GEMEINSCHAFT	**EXPERIMENTAL REPORT**	**GeNF SANS-2**

Crystallisation of polymer micelles at solid interfaces

Proposer:	**Max Wolff**[1], [1]Festkörperphysik, Ruhr-Universität Bochum
Co-Proposers:	**Hartmut Zabel**[1]
	Vincent Leiner[2], [2]GKSS
Experimental Team:	**Max Wolff**[1],
	Vincent Leiner[2], **P. Klaus Pranzas**[2]
User Group Leader:	**Max Wolff**[1]

Date(s) of Experiment:	6. – 20. December 2004

Objectives

Recently we have started grazing incident small angle neutron scattering (GISANS) studies of micelle polymer systems close to solid surfaces with different chemical termination [1]. For distinct interactions between the micelle corona and the interface we find different crystallographic structures [1, 2]. As an additional parameter we started to investigate the influence of shear on the near surface structure [3]. All our previous GISANS measurements were made on a reflectometer with a very precisely defined wave length ($\Delta\lambda < 1$ %) of the incoming neutron beam. Accordingly the Bragg reflections under investigation could not be fully excited and the intensity was rather low [1]. Therefore only few data points could be collected. To obtain information on the depth dependence of the structures and their formation we need to measure at different temperatures and incident beam angles. The aim of the present experiment was to use the relaxed wave length resolution of a SANS instrument to speed up data collection. In particular GISANS measurements should provide information on the reorientation process of different domains and an evaluation of the intensity distribution for changing incident beam angles should reveal the depth dependence of the structures.

Experiment

As samples we have investigated different solutions of the three-block copolymers, called Pluronics, solved in deuterated water. Pluronics consist of a centre block of polypropylene oxide terminated by two sequences of polyethylene oxide. The polypropylene oxide has a hydrophobic character and accordingly, for higher concentrations and temperatures, the molecules tend to agglomerate when they are solved in water. For the present experiment we were working in the micelle (agglomerations of 50-100 molecules) phase. As with increasing temperature more and more molecules agglomerate at a certain point the critical micelle concentration for crystallization is reached and the micelles form a well defined structure. All samples were prepared to get the critical micelle concentration at a temperature of about 305 K. As it is supposed that the interaction between the single chain and an interface is depended on the length of the different parts we prepared four samples (F127 ($PEO_{99}PPO_{67}$ PEO_{99}), F68 ($PEO_{78}PPO_{30}PEO_{78}$), F88 ($PEO_{103}PPO_{39}PEO_{103}$), P85 ($PEO_{26}PPO_{40}PEO_{26}$)). The F127 was dissolved in deuterated water by 20 % (in weight), the F68 by 37 %, the F88 by 35 % and the P85 by 40 %. All samples were prepared and filled into the sample cell at low temperatures to prevent shear alignment of the crystalline phase before starting the measurement.

For all measurements we used two pinholes with a diameter of 20 mm at the position KB1 and KB5 meaning a divergence of roughly 0.14°. The weave length was 5.7 Å and all the collimators were in the beam. To cut down the beam size in front of the sample an additional pinhole of 3 mm diameter was used as sample diaphragm.

Figure 1 (left panel) shows the GISANS geometry. Neutrons from the source enter a silicon block at the smaller side, get scattered at the solid-liquid interface and are then registered at the PSD. The panel on the right side shows a typical diffraction pattern. The Bragg-reflections visible can be indexed by a cubic close packing close to the interface with a lattice constant of about 29 nm for the FCC unit cell and rotational freedom around the normal of the interface. The indices and dashed indices mark the point where the Debye-Scherrer ring and the Ewald sphere intersect. The R marks the position of the reflected beam and BS that of the direct beam blocked by the beam stop.

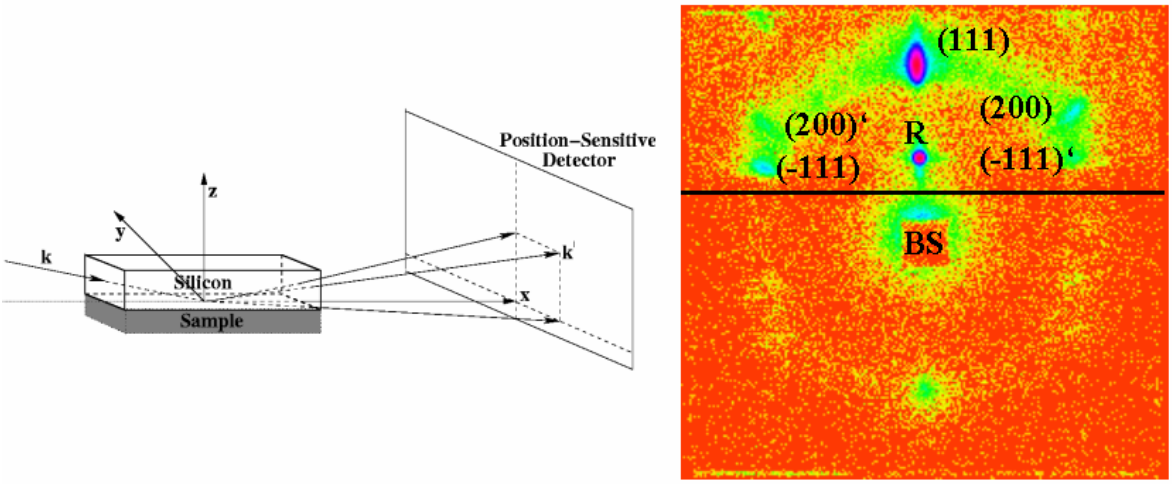


Figure 1 : Scattering geometry for a SANS experiment in grazing incident geometry (left panel). The right panel depicts a typical scattering pattern as obtained for the Pluronic samples in the cubic phase. Exemplary a horizontal scattering geometry is shown. However, the present experiment was performed in a vertical geometry.

Achievements and Main Results

Four different samples were measured in contact with an attractive interface for different temperatures. For F127 we additionally varied the incident beam angle to get a depth sensitivity. To get an impression of the large variety of the possible crystallisation scenarios we have chosen in Figure 2 one example PSD image for every sample, taken at a temperature of 318 K. All data were taken under the same incident angle but with different distances between sample and detector. The main subject of the experiment was to study the crystallisation process for different temperatures. As the beam intensity was found lower than expected we decided to skip the repulsive interface as in this case the crystallisation is mostly suppressed.

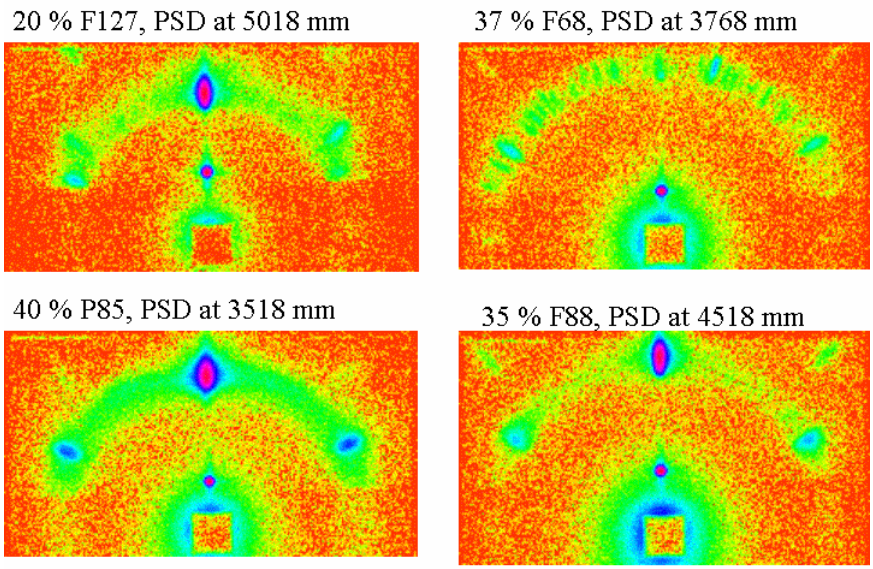


Figure 2 : Exemplary scattering patterns for the four samples at an attractive interface in the cubic phase at a temperature of 318 K.

Figure 3 shows as an example a temperature loop measured for the F127 sample. The panel on the left and right side depict the intensity of the (111) reflection and the difference between the corresponding reflection and dashed reflection. For low temperatures the sample is in the liquid micelle phase and the intensity at the position of the (111) reflection is low, related to the liquid structure factor of the micelles. For higher temperatures the intensity increases which can be explained by the formation of a cubic structure. Above 320 K the intensity decreases again as the crystal starts to melt. The surprising feature is that the crystallisation is not reversible for decreasing temperatures. Nevertheless, after cooling down into the liquid phase and measuring a second loop, the same intensities are obtained. Qualitatively the intensity difference found in the right panel shows the same progression as the intensity of the (111) reflection. This means that not only more lattice planes contribute to the (111) reflection for 318 K but also a texture is formed with respect to the rotational freedom around the surface normal.

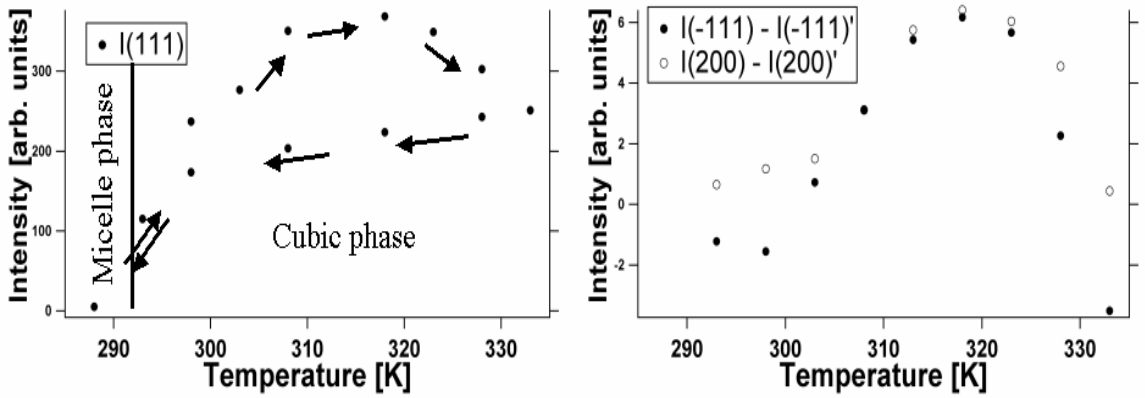


Figure 3 : In the left panel the intensity of the (111) Bragg reflection is shown for different temperatures. The differences in the intensities of the corresponding reflections due to the texture formation that develop in the cubic phase are shown in the right panel.

The detailed data evaluation is currently under process. The main focus will be drawn on analysing the intensity distribution of the different Bragg reflections and on the Debye-Scherrer rings to learn how the texture is formed for the different samples. In addition we hope that the data taken for F127 at different temperatures and incident angles will bring us in a position to make conclusions about the dependence between texture and the distance of the solid interface.

References:

1. Wolff, M. Scholz, U., Hock, R. Magerl, A. and Zabel, H., *Crystallisation of micelles at chemically terminated surfaces*, Phys. Rev. Lett., **92**, 255501 (2004).
2. Wolff, M., A. Magerl and H. Zabel, *Structure of polymer micelles close to the solid interface*, Euro. Phys. J. E, **16**(2), (2005, in press).
3. Wolff, M., Magerl, A and Zabel, H., *Structure of polymer micelles at the solid interface*, Physica B, doi:10.1016/j.physb.2004.11.027 (2005, in press).

GKSS FORSCHUNGSZENTRUM in der HELMHOLTZ-GEMEINSCHAFT	**EXPERIMENTAL REPORT**	**GeNF SANS-2**

The search of the static spin chirality in the spin-glass like system $(Pd_{0.984}Fe_{0.016})_{0.95}Mn_{0.05}$ by small angle scattering of polarised neutrons

Principal Proposer:	**G.P.Gordeev[1], L.A.Axelrod[1], S.V.Grigoriev[1], I,M. Lasebnik[1], V.N.Zabenkin[1]** [1]Petersburg Nuclear Physics Institute (PNPI), Russia
Experimental Team:	**L.A.Axelrod[1], V.N.Zabenkin[1], H.Eckerlebe[2],** [1]Petersburg Nuclear Physics Institute (PNPI), Russia [2]GKSS Research Centre
Date(s) of Experiment:	December 2004

Scientific Objective.

The experiment is aimed to search the static spin chirality in the dilute alloy $(Pd_{0.984}Fe_{0.016})_{0.95}Mn_{0.05}$ in a wide temperature range below T_C by means of small angle polarised neutron scattering (SAPNS). Due to competition of exchange spin interactions this system has a nontrivial magnetic mesostructure with the ferromagnetic transition at $T_C = 41$ K and the spin-glass like state at the temperature below 30 K. Recently, Kawamura proposed the chiral mechanism for explanation of the spin-glass phase transition [1]. He suggested that not pair correlation of the Ising's spins, but the chiral three-spin fluctuation is the key object of such a transition. Kawamura supposed that experimentally observed effects at such transitions in Heisenberg magnetics should be referred to a chiral rather than an ordinary spin glass. This approach requires reconsideration of the spin glass transition both from theoretical and experimental point of view. In this connection it is interesting to perform a thorough study of the polarised neutron scattering in the spin (chiral) glass systems in an external magnetic field. The use of Polarised Neutrons allows one, first, to separate chiral contribution in the scattering from that of the ordinary pair spin correlation extracting the asymmetrical part of SAPNS. Second, the inclined and/or perpendicular experimental geometry of the magnetic field [2] makes it possible to separate the dynamic and static contributions in the chiral scattering in the spin glass system.

We had studied in detail the asymmetrical scattering of SAPNS intensity in the inclined geometry was studied in detail in the spin glass like system $(Pd_{0.984}Fe_{0.016})_{0.95}Mn_{0.05}$ on SANS2 [3]. However, the static contribution to the asymmetric (chiral) scattering had not been found out at that time.

Experimental Techniques.

We had measured momentum transfer dependences of SANPS intensity in the wide range of q, provided that the sample is magnetized in the direction being perpendicular to the neutron velocity ($\varphi=90^0$). This geometry results in suppression of the dynamic contribution in chiral scattering. In this case the information about the static chirality might be obtained by evaluation of the difference in scattering in two experiments with incident polarization of the opposite signs.

The measurements were carried out at temperature both below and above $T_C = 41$ K. Before measurements the sample was cooled in the magnetic field starting $T = 60$ K. The wavelength of neutrons was 0.57 nm. The "sample-detector" distance was about 1 m. The measurements were carried out in magnetic field interval 1-100 mT.

Results.

The dependences of unpolarised neutron scattering $J = I(P) + I(-P)$ versus temperature for

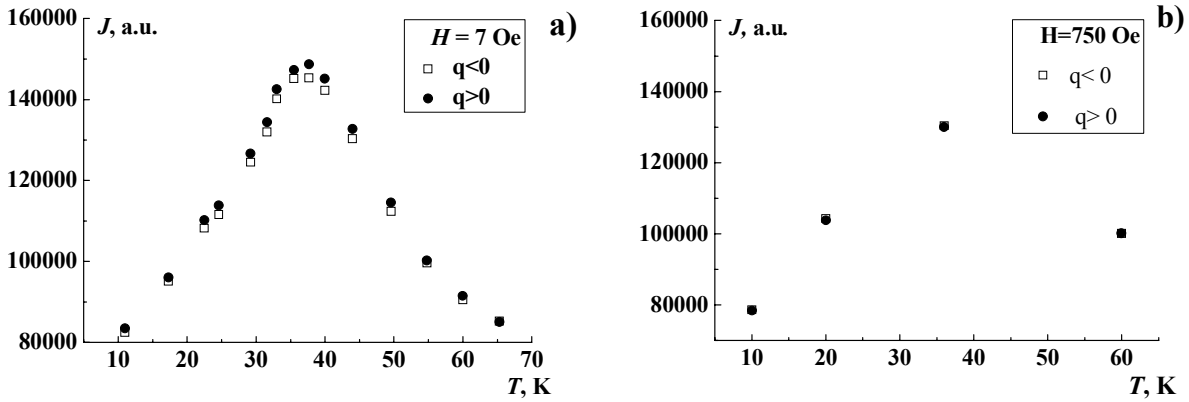


Figure 1.

a both small and large magnetic field are presented in Fig.1(a,b). Maximum of the scattering is observed at $T = 36$ K which is lower that the ferromagnetic transition temperature $T_c = 41$ K for a given alloy. The state of the sample below $T = 36$ K is defined firstly by magnetization decreasing with conservation of its collinear component and secondly by nonmonotonous behaviour of neutron depolarization when magnetic field is changing [4]. This state referred to as a spin-glass like state is a subject of our interest.

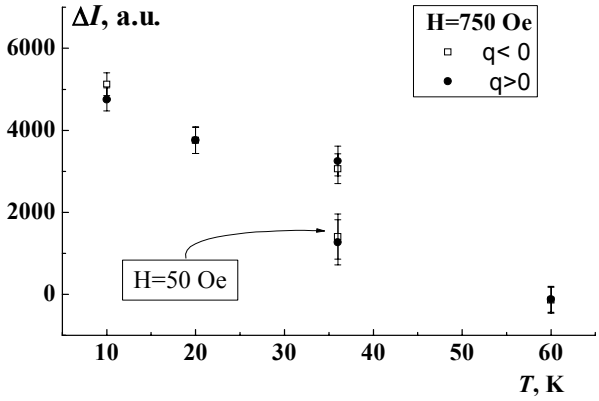


Figure 2.

As to a spin dependent scattering of polarized neutrons, it is observed at larger fields (Fig.2) and only at the case of $\mathbf{q} \perp \mathbf{H}$ (Fig.3) but it is q-symmetric. In the case of $\mathbf{q} \parallel \mathbf{H}$ a spin dependent scattering is absent. This means that the static spiral fluctuations of magnetic moments are absent. In the

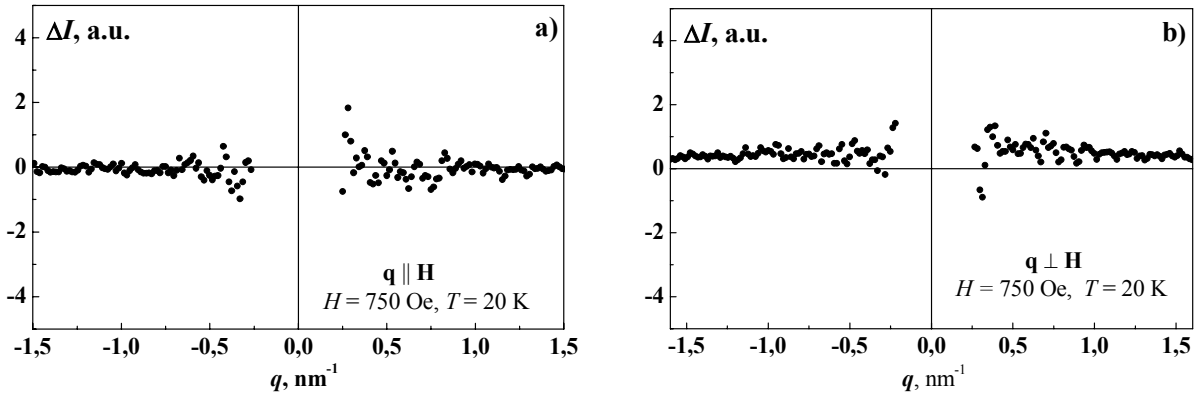


Figure 3.

large field the system is defined by the interference of magnetic and nuclear scattering. This interference scattering increases when temperature is decreasing because the magnetic induction rises into inhomogeneities. There is a remarkable fact that this scattering appeares only at the field more than 30 mT. At least it is right at $T = 36$ K (Fig.2). Now it is not clear whether this original threshold remains at lower temperature. In small fields no spin dependent scattering $\Delta I = I(P) - I(-P)$ is probably observed (Fig.4). Insufficient statistics (Fig.5) does not permit to make any undoubted remark

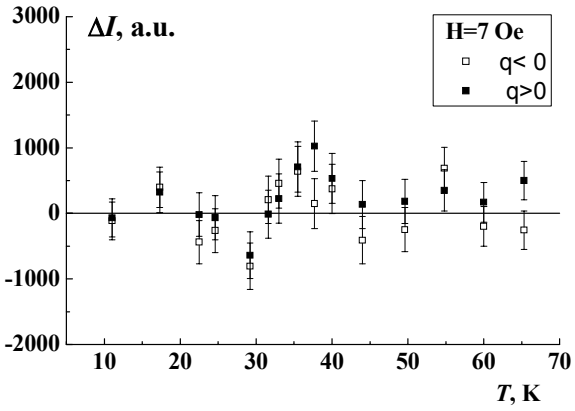


Figure 4.

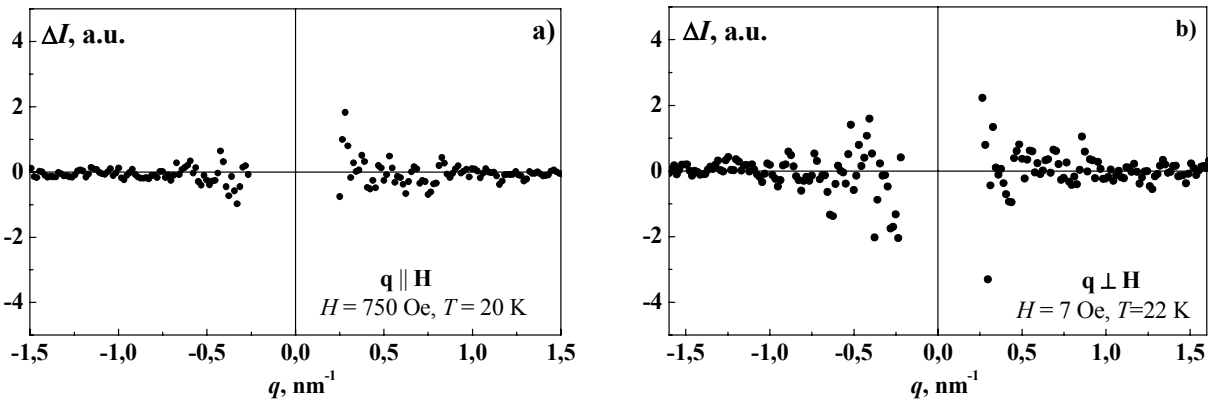


Figure 5.

Conclusion.

Magnetic state of at $T < 36$ K is alike one that does not result to the asymmetric spin dependent scattering of polarised neutrons in perpendicular geometry ($\varphi = 90^{o}$) of magnetic field neither at large nor small values of its. Evidently, in this state static spiral fluctuations (static chirality) do not exit or they are insignificant extremely.

Acknowledgement.

The authors are indebted to G.Kozik for technical assistance and FRG-1 reactor staff for the possibility to carry out the experiment.

References.

1. H. Kawamura, M. Suan Li, Phys. Rev. Lett. **87** (2001) 187204 (1-4).
2. Deriglazov, A. Okorokov, V. Runov, B. Toperverg, R.Kampmann, H. Eckerlebe, W.Schmidt, W. Lobner, Physica B 181-182 (1992) 262
3. G.P.Gordeev, L.A.Axelrod, S.V.Grigoriev, I.M.Lazebnik, V.N.Zabenkin, V.Wagner, H.Eckerlebe, G.Kozik, GeNF-Experimental Report 2003.
4. G.Gordeev, L.Axelrod, S.Grigoriev, V.Zabenkin, V.Wagner, H.Eckerlebe, Physica B 350 S1 (2004) E95-E98.

GKSS FORSCHUNGSZENTRUM in der HELMHOLTZ-GEMEINSCHAFT	EXPERIMENTAL REPORT	GeNF DCD
Double crystal diffractometer DCD		

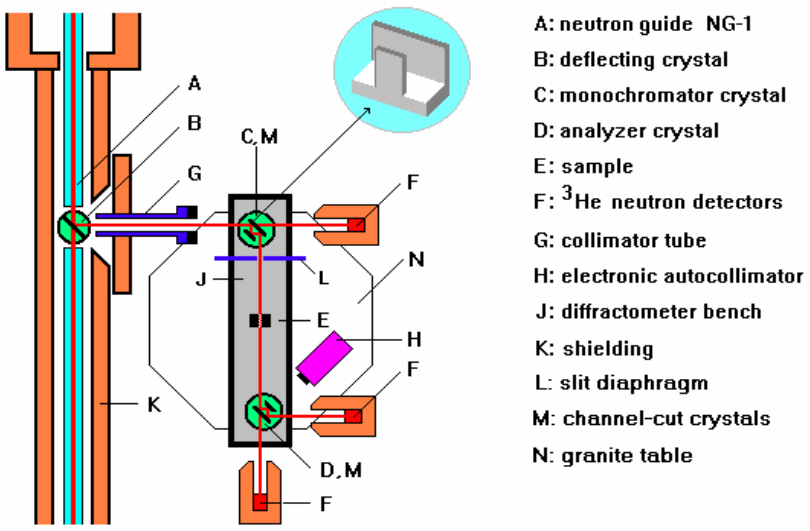
Short Instrument Description:

The double crystal diffractometer for ultra small angle neutron scattering (USANS) uses non-polarised cold neutrons to characterise in materials large creep pores, fatigue and sintering cavities, precipitates, voids, bubbles, etc. with particle sizes in the range with about 100 nm to 40 μm in diameter.

Local Contact:

Dr. P. Klaus Pranzas
Phone/Fax : +49 (0)4152 87 – 1326 / +49 (0)4152 87 – 1338
e-mail: pranzas@gkss.de

Schematic View of DCD:



Instrument Details:

Beamline:	beamline 8 - cold neutron guide NG-1, max. beam cross section 30 x 40 mm^2
Deflecting crystal:	Si(111), Si(311), mosaic spread 0.1 mrad
Monochromator / analyser:	channel-cut perfect Si crystals
Wavelength resolution	$\Delta\lambda/\lambda = 1 \cdot 10^{-5}$ (λ = 0.443 nm)
Max. flux at deflecting crystal	$\Phi = 2.3 \times 10^8$ cm^{-2} s^{-1}
Flux at sample position:	$\Phi \approx 500$ cm^{-2} s^{-1} (Si(111), λ = 0.443 nm) $\Phi \approx 180$ cm^{-2} s^{-1} (Si(311), λ = 0.232 nm)
Range of momentum transfer:	$1 \cdot 10^{-5}$ $nm^{-1} \leq Q \leq 5 \cdot 10^{-2}$ nm^{-1}
Detectors:	three ^{3}He-detectors
Control of crystal alignment:	electronic autocollimator, angular resolution < 0.05 μrad

GKSS FORSCHUNGSZENTRUM in der HELMHOLTZ-GEMEINSCHAFT	EXPERIMENTAL REPORT	GeNF SANS-2 / DCD

Investigation of structural changes of nanocrystalline Mg/MgH_2 during absorption and desorption of hydrogen

Proposer:	**Thomas Klassen,** GKSS Forschungszentrum
Co-Proposers:	**M. Dornheim, A. Schreyer, P. K. Pranzas,** GKSS Forschungszentrum
Experimental Team:	**D. Bellmann, P. K. Pranzas,** GKSS Forschungszentrum
User Group Leader:	**P. K. Pranzas**
Date(s) of Experiment:	June – December 2004

Objectives

Before hydrogen can be widely used as an alternative fuel, efficient and safe ways of storage have to be developed. Magnesium hydride is considered to be one of the most interesting alternatives for the reversible storage of hydrogen, especially for mobile applications, because it is abundant, inexpensive, harmless to the environment, and because of its high hydrogen storage capacity of 7.6 wt.%. Nanocrystalline magnesium hydride offers a safe alternative to the storage of hydrogen in compressed or liquid form. Absorption and desorption kinetics of hydrogen on MgH_2 are well known [1-3]. The sorption properties are distinctly enhanced by the addition of metal-oxide catalysts. However, structural changes during absorption and desorption of hydrogen as well as the mechanisms of the catalytic reactions have hardly been investigated up to now. In this project structural changes of nanostructured MgH_2 during these processes will be characterised using small and ultra-small-angle neutron scattering (SANS/USANS).

Experiment

Nanocrystalline powder Mg/MgH_2 samples with different hydrogen contents were measured at the instruments SANS-2 and DCD at room temperature in quartz cuvettes with a thickness of 1 mm.

At SANS-2 distances between sample and detector of 1, 3, 9 m (λ = 0.58 nm) and 21 m (λ = 0.58 nm and 1.16 nm, $\Delta\lambda/\lambda$ = 0.1) were used to cover the range of scattering vector q from 0.009 nm^{-1} to 2.4 nm^{-1}. Scattering data were normalized by monitor counts and corrected for sample transmission and detector response. The differential scattering cross section was obtained by calibration with a Vanadium reference sample with a thickness of 1.28 mm.

Ultra small-angle neutron scattering (USANS) measurements were carried out at the double-crystal diffractometer DCD with a wavelength of 0.443 nm resulting in an accessible range of scattering vector q from 10^{-5} to 10^{-2} nm^{-1}. With this technique particle sizes up to 24 µm are detectable.

The schematic flow chart showing the preparation of the measured Mg/MgH_2 samples after 20 h high-energy ball milling and after several hydrogen desorption and absorption cycles is demonstrated in figure 1. The hydrogen/magnesium ratio is used for the sample names, the hydrogen contents in weight percent are mentioned below.

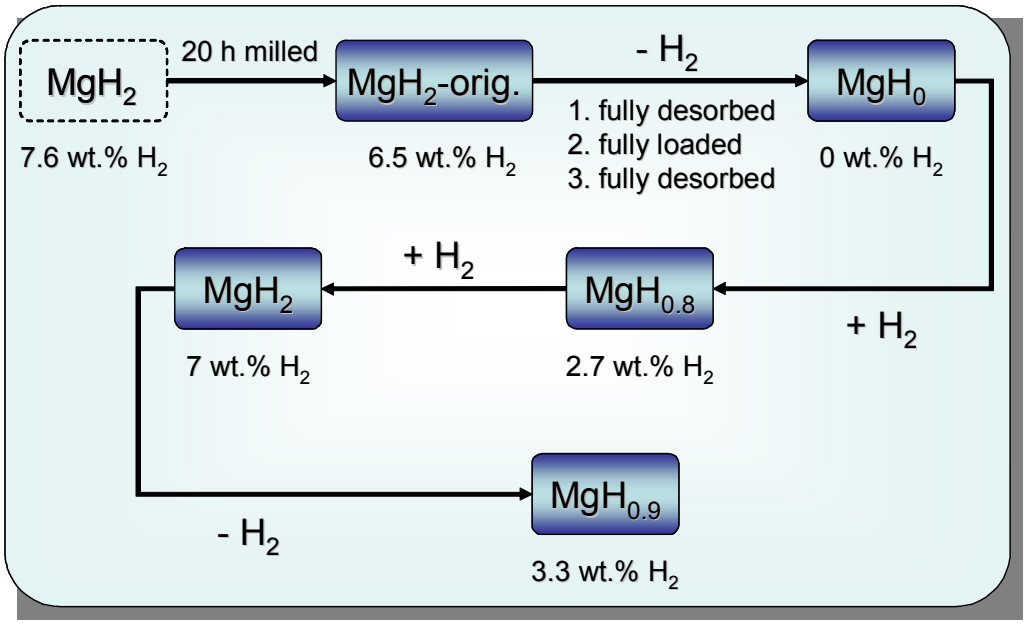


Figure 1: Schematic flow chart of the preparation of the measured MgH_x samples after 20 h high-energy ball milling and after several hydrogen desorption and absorption cycles.

Achievements and Main Results

Figure 2 shows the combined SANS-DCD scattering curves for the samples illustrated in figure 1.

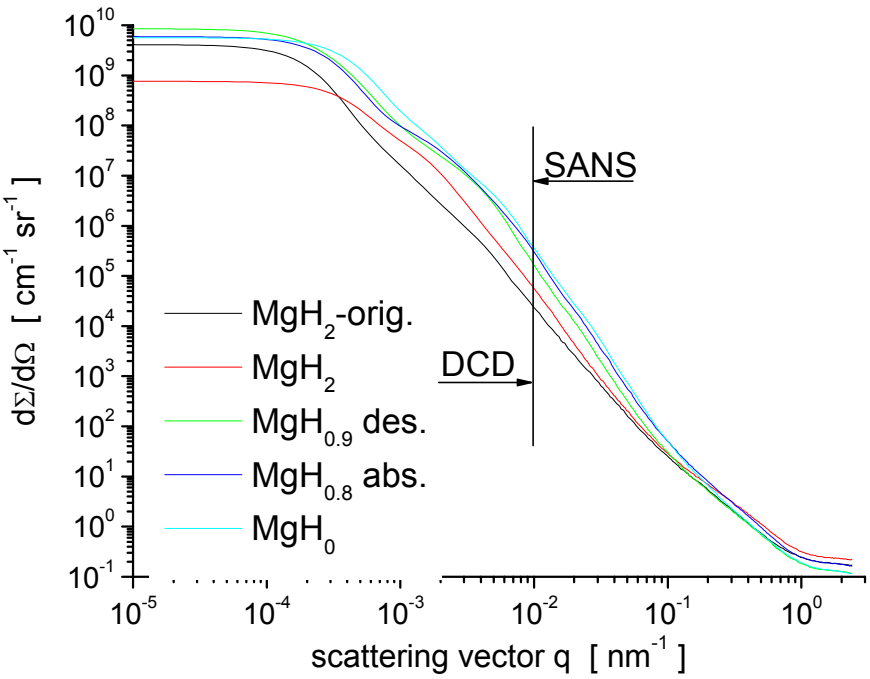


Figure 2: Combined DCD-SANS curves for high-energy ball milled MgH_x samples after absorption or desorption of hydrogen.

The differences in the curves exhibit structural changes in nanocrystalline Mg/MgH_2 during different stages of the hydrogen absorption and desorption cycling process. The formation of a shoulder at approximately 0.002 nm^{-1} with decreasing hydrogen content indicates the development of large structures with sizes up to several µm. At large values of the scattering vector q the varying incoherent scattering background due to the different hydrogen content is visible.

To get a rough estimate of the structural changes in the Mg/MgH_2 system, the size distributions shown in figure 3 were calculated using as first approximation a 2-phase hard spheres model and the scattering length densities differences Δη between MgH_x and air.

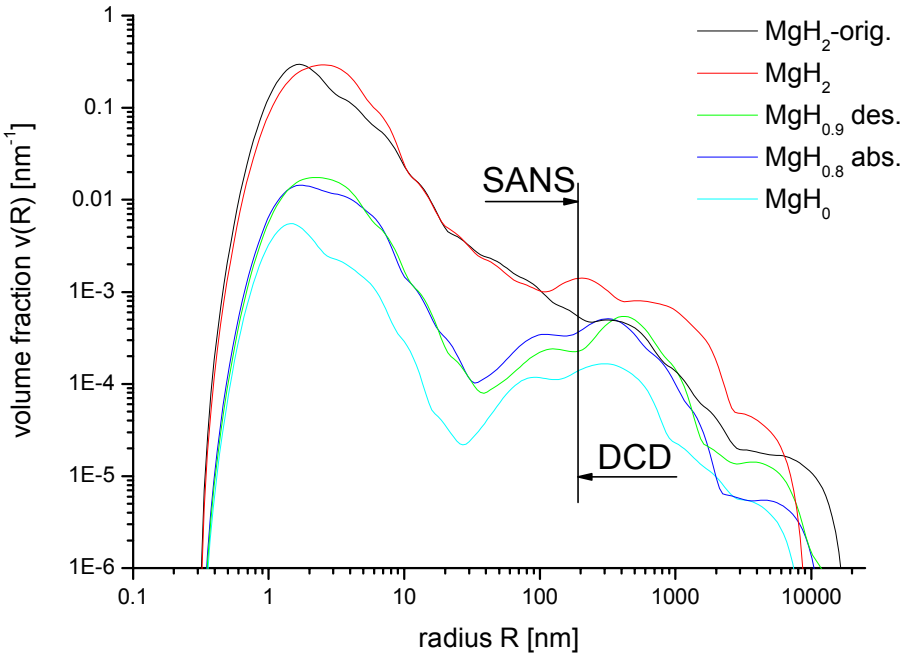


Figure 3: Size distributions calculated from the data shown in figure 2 using as first approximation a 2-phase hard spheres model and the scattering length densities differences Δη between MgH_x and air.

Structural changes are visible in the range of a few nm as well as in the µm-range. Due to the different signs of the scattering lengths of H and Mg ($b_{c,H}$= -0.374E-12, $b_{c,Mg}$= +0.537E-12 cm), the scattering length density of $MgH_{1.5}$ is about zero and therefore small deviations of the hydrogen content in this range have a large effect on the volume fraction. To eliminate these uncertainties it is planned to use deuterium ($b_{c,D}$= +0.667E-12 cm) instead of hydrogen in the preparation of the magnesium hydride samples. Together with additionally performed SAXS/USAXS measurements at HASYLAB, Hamburg the results obtained in these experiments will provide information about the growth and the formation of the α-MgH_2 phase during the absorption and the β-Mg phase during desorption respectively.

References

[1] G. Barkhordarian, T. Klassen, R. Bormann, J. Alloys Comp. 364, 242 (2004)
[2] G. Barkhordarian, T. Klassen, R. Bormann, Scripta Mater. 49, 213 (2003)
[3] W. Oelerich, T. Klassen, R. Bormann, J. Alloys Comp. 315, 237 (2001)

GKSS FORSCHUNGSZENTRUM in der HELMHOLTZ-GEMEINSCHAFT	**EXPERIMENTAL REPORT**	**GeNF DCD**

USANS investigations of organized nanostructures of diblock copolymers in immiscible solvents

Proposer:	**Ryukhtin, Vasyl**[1], [1] Nuclear Physics Institute, Academy of Sciences of the Czech Republic, 25068 Řež near Prague, Czech Republic
Co-Proposers:	**Stepanek, Petr**[2], [2] Institute of Macromolecular Chemistry, Heyrovský Sq. 2, 16206 Prague 6, Czech Republic
Experimental Team:	**Pranzas, P. Klaus**[3], **Bellmann, Dieter**[3], [3] GKSS Forschungszentrum
User Group Leader:	**Pranzas, P. Klaus**[3]
Date(s) of Experiment:	30.November–6.December 2004

Objectives

When a diblock copolymer A-B is dissolved in a partially miscible mixture of solvents a and b, where a is a solvent selective for block A and b is a solvent selective for block B (and a precipitant for the block A), periodic multilayered anisotropic nanostructures can be expected, formed by periodically arranged layers of the solvents a and b, stabilized by the block copolymer forming a double brush on the a/b interface. The studied system is formed of diblock copolymers in which one block is polystyrene (PS) and the second is either poly (ethylene propylene) (PEP) or polyisoprene (PI) or polybutadiene (PB), in mixtures of dimethylformamide (DMF) (a selectively good solvent for polystyrene) and cyclohexane (CX) (a selectively good solvent for the other block). The coexistence curve of the solvent mixture has an upper critical temperature (48.2 ^{o}C at 39 vol.% DMF).

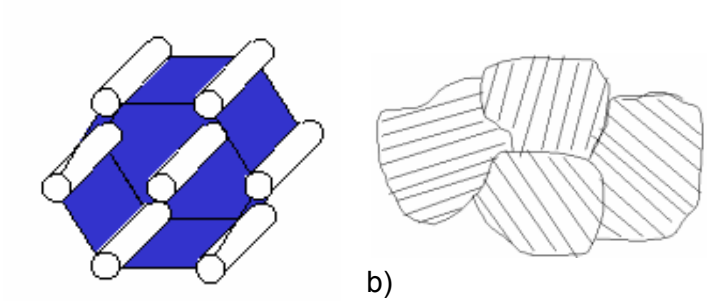


Fig. 1. Hexagonal cylinders (a) forming the grains (b) of the material.

Our previous experiments with conventional SANS have shown that the ordered structure has either a hexagonal (see Fig. 1a) or cubic symmetry. The long range periodic structure is limited in extend, typically it consists of grains (see Fig. 1b) that have an expected size of about several μm, as was estimated by birefringence measurements on similar systems [1]. DC-SANS technique has been used for characterization of the grains in such materials.

Table 1. Concentrations of CX and DFM.

Samples	d-CX, %	DFM, %
CP1	2.00	12.0
CP4	1.99	24.1
CP6	4.02	18.0
CP7	2.94	18.6
CP8	1.48	18.2

Experiment

The set of immiscible solvents diblock copolymers in CX and DMF (see Table 1) has been measured at DC-SANS setup (DCD, GKSS) with neutron wavelength of 4.43 Å. The samples were contained in 1 mm thick quartz cuvettes and have been measured at room

temperature and some of them at higher temperatures of 43 ^{0}C, 52 ^{0}C, 56 ^{0}C and 60 ^{0}C. Obtained USANS results measured at room temperature with fitted curves are shown in Fig. 2. Fitting procedure was carried out by means of Profit 5.0 program [2] based on iFT method [3]. A model of incoherent spherical particles with log-normal size distribution has been chosen for the data fitting.

Table 2. Mean radii and volume fractions of the grains.

Samples	<R>, μm	φ, %
CP1	3.08±0.07	24.9±0.6
CP4	1.01±0.01	52.4±0.6
CP6	1.19±0.01	53.8±0.9
CP7	1.22±0.01	44.4±0.7
CP8	1.70±0.02	34.3±0.5

Mean radii and volume fractions values obtained by fitting are shown in Table 2. The volume fraction values are relative because exact value of scattering contrast, Δρ, is unknown. The scattering lengths density difference between grains and surrounded media, Δρ, was used equals to $0.6 \cdot 10^{10}$ cm^{-2} for the data interpretation. However, this uncertainty has no influence on absolute values of mean sizes of grains.

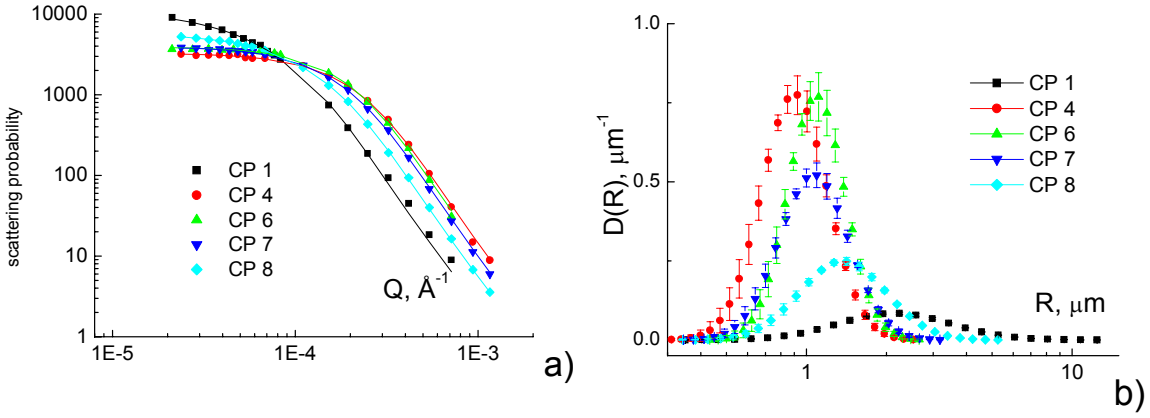


Fig. 2. USANS scattering data with fitted lines (a) and size distributions of grains obtained (b).

Achievements and Main Results

USANS technique was applied successfully for characterization of the grains of copolymers in mixtures of cyclohexane (CX) and dimethylformamide (DMF). Biggest grains were detected in sample with minimum concentration of DFM (CP1, 12.0 %, see Table 1). However, the size distribution for this sample (see Fig. 2 b) is very broad in comparison with others. The size of grains increases with decreasing of CX concentration for the mixtures with constant concentration of DMF (CP6, CP7 and CP8). The volume fraction values were estimated qualitatively only, since the exact scattering contrast is unknown. Nevertheless, the volume fraction has tendency to decrease with increasing mean size of grains. Scattering intensities decrease at higher temperatures for most of the samples. Scattering curves in the region of ultra small Q have a different behaviour and significantly lower intensities at higher temperatures. This demonstrates that grains dissolve gradually with increasing temperature.

References

1. N.P. Balsara, B.A. Garetz, H.J. Dai, Macromolecules 25, 6072 (1992).
2. J. Šaroun, "SASProFit - program for USANS data evaluation", IConUSAS conference, Oak Ridge, 9-10 July 2003, http://omega.ujf.cas.cz/~saroun/SAS/.
3. O. Glatter, 1977, Acta Phys. Austr. 47, 83-102.

GKSS FORSCHUNGSZENTRUM in der HELMHOLTZ-GEMEINSCHAFT	EXPERIMENTAL REPORT	GeNF PNR
Reflectometer for polarised neutrons PNR		

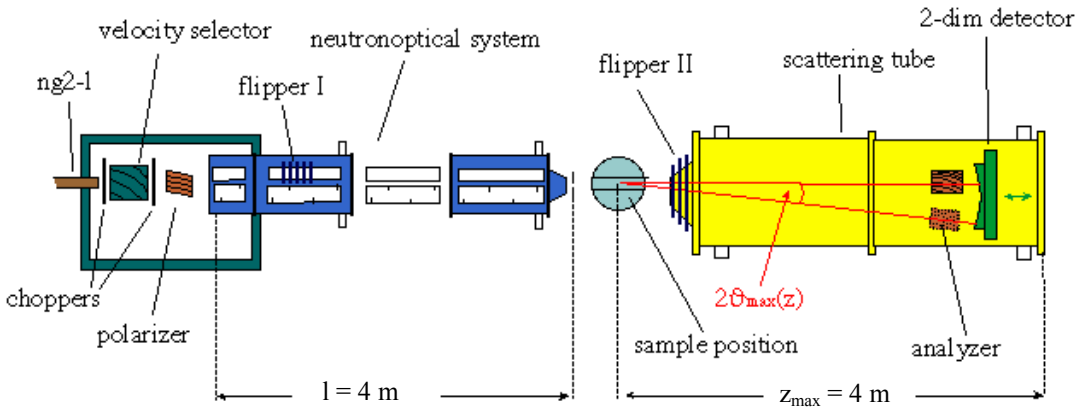
Short Instrument Description

The polarised neutron reflectometer is used to study magnetic and other surfaces, layers, thin films and membranes applying cold non-polarised/polarised neutrons at high fluxes.

Local Contact:

Dr. Danica Solina
Phone/Fax : +49 (0)4152 87 – 1373 / +49 (0)4152 87 – 1338
e-mail: danica.solina@gkss.de

Schematic View of PNR:



Instrument Details:

Beamline:	beamline 8 (NG-2l), cross section 30 x 40 mm^2
Monochromator:	helical slot selector
Wavelength:	$\lambda \geq 0.635$ nm
Wavelength resolution:	$\Delta\lambda/\lambda = 0.05$
TOF equipment:	2 choppers, to be used if a resolution better than 0.05 is required
Polariser and analyser:	set of bent supermirrors
Spin flipper:	hf-flipper or Mezei-coil-flipper
Collimation lengths:	4 m
Flux at sample position: (beamsize: 0.5 x 40 mm^2)	$\Phi_{nonpol} = 1 \cdot 10^5$ cm^{-2} s^{-1}(unpolarised) $\Phi_{pol} = 3 \cdot 10^4$ cm^{-2} s^{-1} (polarised neutrons)
distance sample-detector:	3 m to 4 m
angular range:	0° ≤ □ ≤ 4°
Detector:	2-dim position-sensitive ^{3}He-counter
Ancillary equipment:	- refrigerator cryostat – temp.-range: 12 – 475 K - electro magnet up to 0.9 T - superconducting magnet up to 5 T

GKSS FORSCHUNGSZENTRUM in der HELMHOLTZ-GEMEINSCHAFT	**EXPERIMENTAL REPORT**	**GeNF PNR**

Feasibility study - Complementarity of neutron reflection and PALS for soft matter interface investigations

Proposer:	**Dirk W. Schubert,** [1] Freudenberg Forschungsdienste KG, Weinheim
Co-Proposers:	**Franz Faupel,** [2]Technische Fakultät der Universität Kiel
	Jörn Kranzow[2], Jan Kruse[2]
Experimental Team:	**Danica Solina**, [3] GKSS Forschungszentrum, Geesthacht
	Ursula Tietze[3]
User Group Leader:	**Dirk W. Schubert[1]**

Date(s) of Experiment:	23.Feb. – 1. Mar 2004

Objectives

The goal of this work is to evaluate the complementary application of neutron reflectometry (NR) and PALS (positron annihilation lifetime spectroscopy) [1-3] techniques for interface investigation. Within the reported NR experiment a PS(D) – PEMA – bilayer is used as model system for the evaluation of novel techniques to reveal interfacial profiles.

Experiment

In continuation of previous experiments at PNR [1] a bilayer sample consisting of weak incompatible polymers, deuterated polystyrene (PS(D)) and non-deuterated polyethylmethacrylate (PEMA) is choosen as a large interface modell system after annealing at 140°C [4]. The initial state with a sharp polymer / polymer interface before annealing is characterized using the neutron reflectometer PNR [1].

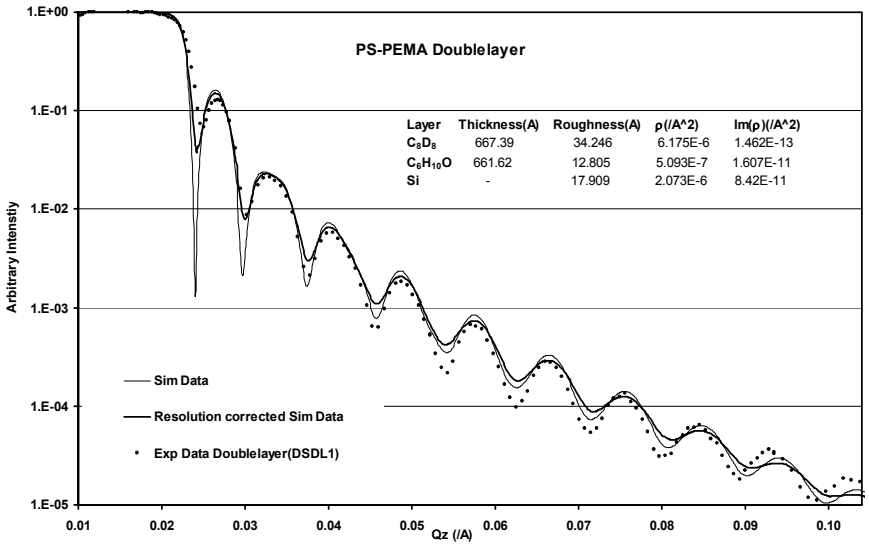


Fig. 1: Neutron reflection curve of PS(D)-PEMA bilayer before annealing.

The large interface profile after annealing is however close to resolution limit of NR experiments and gives at least a chance to estimate the interface width.

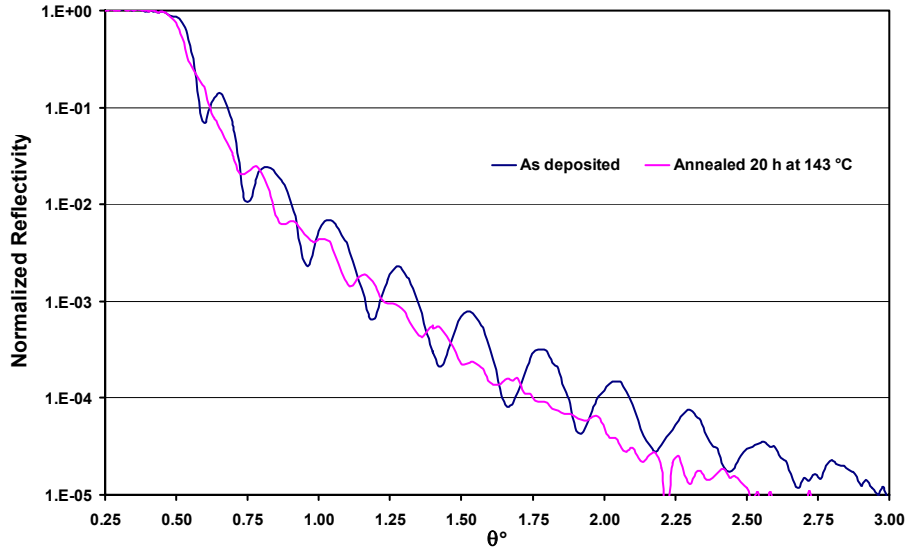


Fig. 2: Neutron reflection curve of PS(D)-PEMA bilayer after annealing.

The as deposited sample has a well defined interference pattern. The appearance of another (faster) oscillation in the neutron reflectivity data of the annealed sample indicates the inter-diffusion between the PS (D) layer and PEMA layer. The small reduction in the overall critical angle of the annealed sample also demonstrates that the initial deuterated PS(D) contains a significant fraction of PEMA.

One can also estimate from figure 2 that the interface width is larger than 20 nm. A comparative TOF-SIMS study yields a rather complicated profile which is consistent to the NR result.

Achievements and Main Results

Results from non destructive NR yield a good starting point for further investigations. As a next step PALS results can be analyzed for interface characterization which can enable a novel complementary technique for large softmatter interfaces.

References:

1. D.W. Schubert, F. Faupel, J. Kanzow: Initial interface formation of polystyrene /polyethylmethacrylate bilayers, GeNF-Experimental Report 2003, GKSS 2004/1, (2004)
2. K. Günther-Schade, D.W. Schubert, F. Faupel: Determination of the binodal and spinodal phase separation temperatures in the blend system P a $MS_{0.5}$-co-$AN_{0.5}$(Luran)/$PMMA_{0.95}MA_{0.05}$(Lucryl) with positron annihilation lifetime spectroscopy. **,** Macromolecules, 35, 9074 (2002)
3. F. Faupel, J. Kanzow, K. Günther-Schade, C. Nagel, P. Sperr, G. Kögel: Positron annihilation spectroscopy in polymers, Plenary talk at the Int. Conf. Positron Annihilation (ICPA-13), Kyoto, September 7-13, 2003, *Mat. Sci. Forum* Vol. 445-446, p. 219-223 (2004).
4. D.W. Schubert, M. Pannek, A. H. E. Müller, Compatibility of a statistical copolymer P(EMA-co-MMA) with PS and PMMA, Macromol. Symp. 149, 47, (1999)

GKSS FORSCHUNGSZENTRUM in der HELMHOLTZ-GEMEINSCHAFT	**EXPERIMENTAL REPORT**	**GeNF PNR**

High resolution 2D-multi-wire neutron detector for MIRA at FRM-II

Proposer:	**Robert Georgii,** [1]Technische Universität München, ZWE FRM-II
Co-Proposer:	**Reinhard Kampmann,** [2]GKSS Forschungszentrum Geesthacht
Experimental Team:	**Robert Georgii [1],** **Reinhard Kampmann [2],** **Martin Haese-Seiller[2]**
User Group Leader:	**Reinhard Kampmann [2]**
Date(s) of Experiment:	August 2004

Objectives

A high-resolution two-dimensional position-sensitive multi-wire gaseous detector with a sensitive area of 200 × 200 mm2 and high spatial resolution of ~ 1 × 2 mm2 has been developed for the reflectometer MIRA at FRM-II. The performance of the detector has been tested at PNR/GKSS.

Experiment

The 2D-MIRA detector is a ^{3}He and CF_4 filled multi-wire proportional counter (MWPC) with delay line read-out produced by DENEX GmbH. Main requirements on the detector are shown in Tab. 1.

i)	Sensitive area:	$200 \times 200\,\mathrm{mm}^2$;
ii)	Spatial resolution:	$\approx 1\,\mathrm{mm} \times 2\,\mathrm{mm}$;
iii)	Wavelength range:	$0.5\,\mathrm{nm} < \lambda < 3\,\mathrm{nm}$;
v)	Background:	very low;
vi)	γ-sensitivity ε_γ:	low ($\varepsilon_\gamma \ll 10^{-4}$).

Tab. 1: Specifications of the MIRA detector

The anode has wire pitch of 2mm and is located in the centre of the detection volume. The pick-up electrodes have a wire pitch of only 1mm and are located at a distance of 5 mm from the anode to achieve high capabilities for both good position resolution and high local count rates. Drift electrodes limit the detection volume which has a depth of 3 cm to achieve a high detection probability *p* at rather low ^{3}He partial pressure. One of the drift electrodes is made of a metal sheet fixed to the entrance window to avoid any dead volume between the window and the electrode. The detector was filled with 1.8 bar ^{3}He and 3.0 bar CF_4. The design of the detector is similar to that of the much larger REFSANS detector which was put into operation recently [1].

Achievements and Main Results

The detector was characterised with neutrons at the reflectometer PNR at FRG-1 / Geesthacht. A well collimated neutron beam (width: 0.5mm; height: 40mm) was used for determining the detection probability as the ration of the count rate obtained with the MIRA detector and that of an almost black ^{3}He counter tube (Ø: 25mm; active height: 100mm; ^{3}He-pressure: 10 bar). Both detectors were moved alternately into the beam. An excellent quantum efficiency of the MIRA detector of more than 80% was found which is in good agreement with the expected one (Fig. 1).

For testing the spatial resolution as well as the linearity the MIRA detector was moved on a linear table and spectra were measured after shifts of 10 mm or 20 mm perpendicular to the beam. The superposition of horizontal cuts of the spectra is shown in Fig. 2 which demonstrates the excellent separation of peaks even if their distance is only 10 mm.

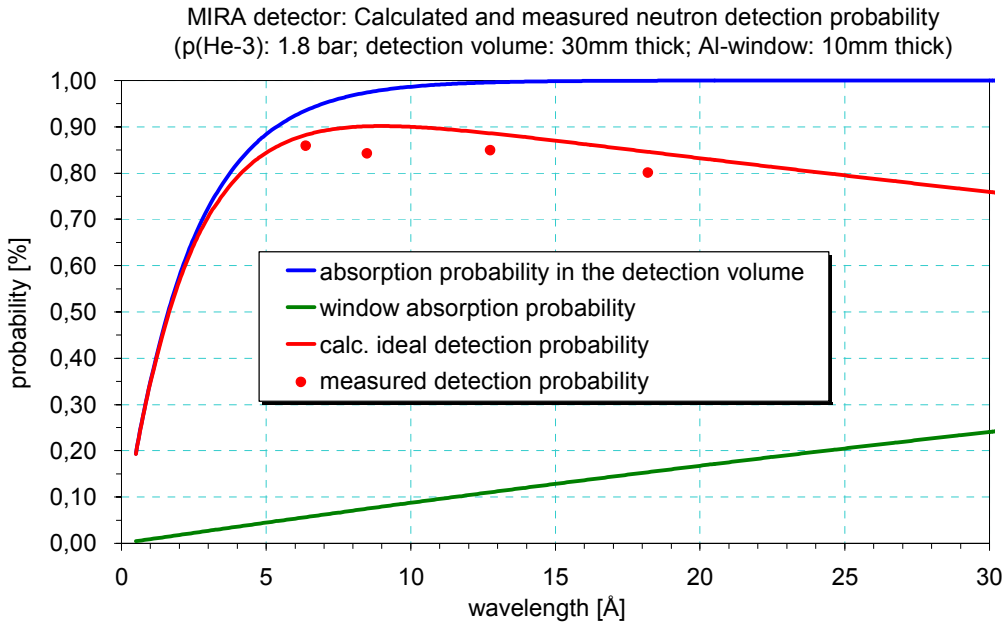


Fig. 1: Quantum efficiency of the MIRA detector
(anode and drift voltages: +4.7 kV and -3.0 kV).

The profile of one cut in high resolution shows a FWHM of only 5 channels corresponding to 1.4 mm (Fig. 3). Accounting for the beam width of 0.5 mm a spatial resolution ~ 1mm parallel to the anode wires is achieved. This high resolution reflects the stopping power of the detection gas containing 3 bar CF_4 and meets a main requirement on the MIRA detector.

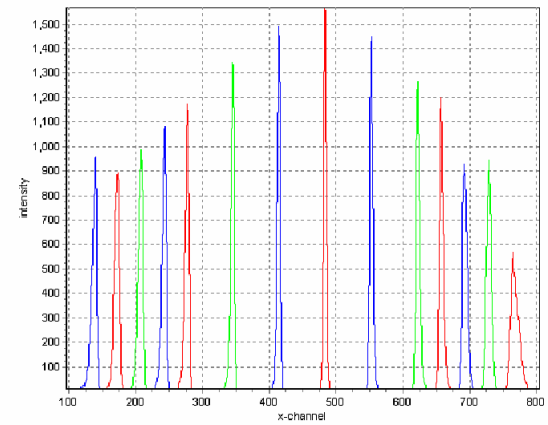


Fig. 2: Superposition of horizontal cuts of spectra measured with the MIRA detector after horizontal shifts of 10 mm (outer regions) and 20 mm (inner regions).

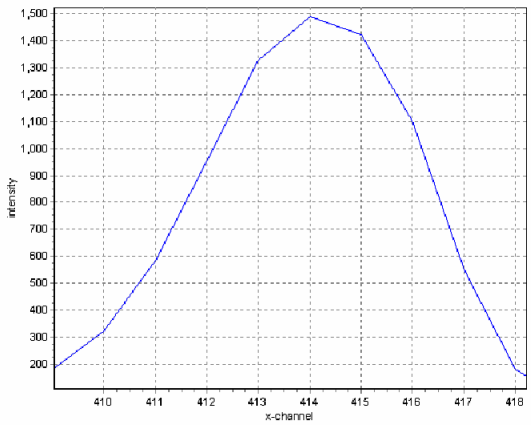


Fig. 3: Horizontal cut of one spectrum measured with the MIRA detector at PNR (horizontal beam width: 0.5 mm; anode wires: horizontally oriented; calibration: 0.287 mm per channel).

Acknowledgements

The support of U. Tietze and M. Pauls during tests of the detector at PNR / GKSS is gratefully acknowledged.

Reference

[1] Kampmann, R., Marmotti, M., Haese-Seiller, M., Kudryashov, V.: Nuclear Instruments and Methods A 529, (2004), 342-347.

GKSS FORSCHUNGSZENTRUM in der HELMHOLTZ-GEMEINSCHAFT	EXPERIMENTAL REPORT	GeNF NeRo
Neutron reflectometer NeRo		

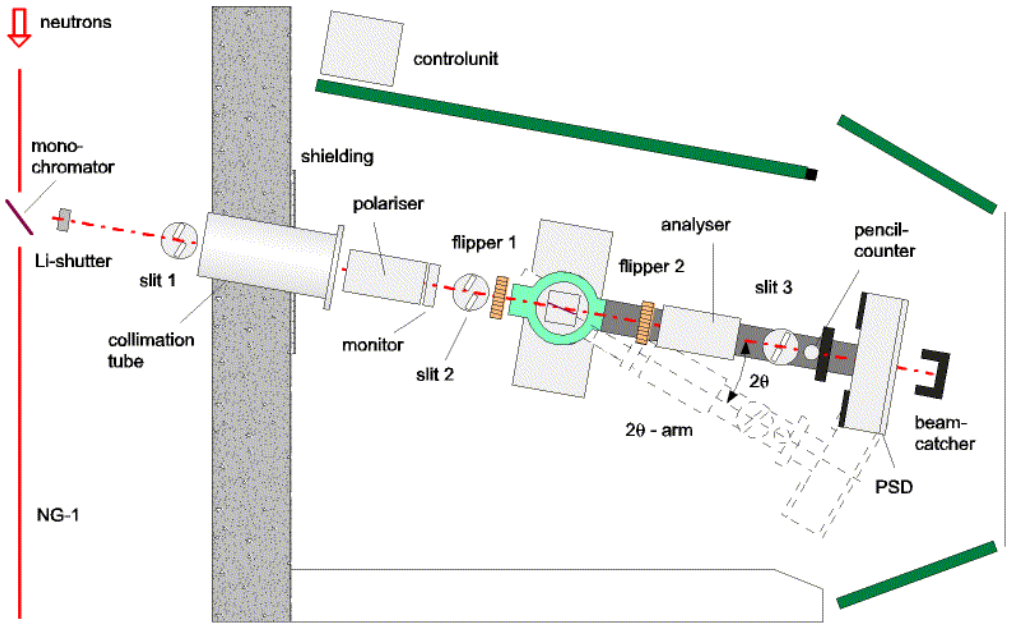
Short Instrument Description

The new Neutron Reflectometer NeRo has been built at the former location of TOREMA 2. The instrument is designed for measurements of thin film systems including polymer and magnetic systems using cold non-polarised/polarised neutrons with high resolution.

Local Contact:

Dr. Dieter Lott
Phone/Fax : +49 (0)4152 87 – 1372 / +49 (0)4152 87 – 1338
e-mail: dieter.lott@gkss.de

Schematic View of NeRo:



Instrument Details:

Beamline:	beamline 8 (NG-1)
Wavelength:	λ = 0.435 nm;
Wavelength resolution	$\Delta\lambda/\lambda$ = 0.02
Angular range	$0 \leq \theta \leq 10°$
Flux at sample position:	$\Phi = 5 \cdot 10^4$ cm^{-2} s^{-1} (unpolarised, standard collimation)
Detectors:	2-dim position-sensitive ^{3}He-counter ^{3}He pencil counter
Ancillary equipment:	refrigerator cryostat - temp.-range: 12 - 475 K electro magnet with field up to 0.9 T

GKSS FORSCHUNGSZENTRUM in der HELMHOLTZ-GEMEINSCHAFT	EXPERIMENTAL REPORT	GeNF ARES
Diffractometer for the analysis of residual stresses ARES		

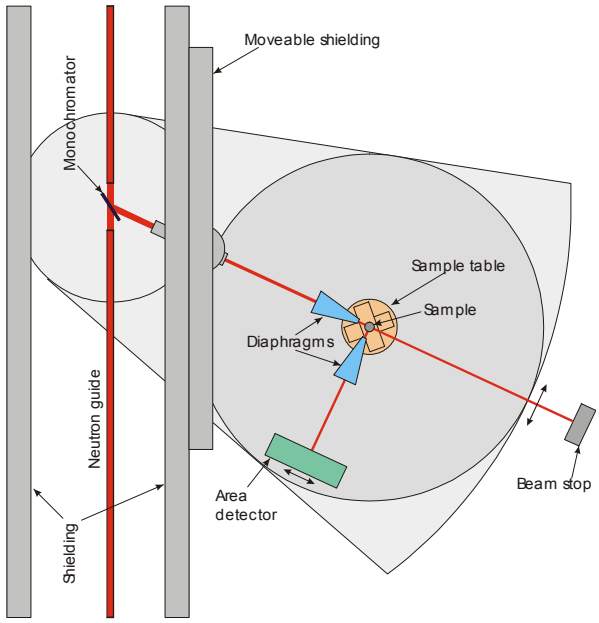
Short Instrument Description:

The diffractometer ARES is designed for the analysis of residual stresses ('strain scanner') in specimens with technical sizes (up to approx.100 kg) using thermal neutrons.

Local Contact:

Dr. Peter Staron
Phone/Fax : +49 (0)4152 87 – 1208 / +49 (0)4152 87 – 1356
e-mail: peter.staron@gkss.de

Schematic View of ARES:



Instrument Details:

Location at FRG-1:	beamline 7; thermal neutron guide, cross section 42 × 90 mm^2, (supermirrors on top and bottom wall)
Monochromator:	**elastically bent perfect Si monochromator,** **Si (311), Si (220), double focussing**
Take-off angle:	57° to 120°, continuously selectable
Wavelength:	λ = 0.16 - 0.23 nm (with Si 311)
Flux at sample position:	$\Phi \approx 5 \cdot 10^5$ cm^{-2} s^{-1}
Sample displacements:	x, y (range 200 mm), z (range 150 mm), □
Detector:	2-dim. position-sensitive ^{3}He-counter
Distance sample-detector:	100 - 150 cm
Sample environment:	load frame for in-situ tests planned

GKSS FORSCHUNGSZENTRUM in der HELMHOLTZ-GEMEINSCHAFT	**EXPERIMENTAL REPORT**	**GeNF ARES**
Residual Stress in IN718 Turbine Discs		
Proposer:	**U. Cihak,** [1]Mining University Leoben, Leoben, Austria	
Co-Proposers:	**W.Marketz,** [2]Böhler Schmiedetechnik, Kapfenberg, Austria	
Experimental Team:	**U. Cihak,** [1]	
	P. Staron, [3]GKSS Research Centre	
User Group Leader:	**P. Staron**[3]	
Date(s) of Experiment:	29.3.–30.4.2004, 2. 8.–31.8.2004, 6.9.–10.9.2004, 16.11.–30.11.2004	

Objectives

During the production of forged components like turbine discs, which are machined to the final form after forging, remaining residual stresses are responsible for distortions during the machining process. Finite Element Simulations (FEM) have been performed to determine these stresses as a function of processing parameters. In order to verify these simulation results whole turbine discs pre-forms have been examined by neutron diffraction. These investigations have been continued with model plates with a simpler geometry of the same material to clarify the influence of micro-stresses and refine the agreement between measurement and FEM results.

Experiment

According to the studied processing route the examined discs made of the alloy IN718 are quenched in water after forging, leading to high residual stresses. The reference value of the unstressed lattice parameter d_0 has been determined by measuring small cubic samples (4x4.1x4.2 mm^3) cut out of the disc at the locations of the strain measurement by spark erosion. According to literature [1] this procedure relieves macro-stresses and the obtained d-value can be taken as virtually free of macro-stress.

Major focus has been set on the reproducibility of the strain measurements. E.g., to exclude systematic errors, the disc and its reference samples have been measured without changing the slits (Fig. 1). Additionally, the reference samples have been studied in more detail. An examination of 21 cubes in 3 directions revealed no significant variations along the radius or the thickness of the disc, indicating that the discs are chemically homogeneous (Fig.2). Using different slit sizes for the determination of the reference value did not lead to different strain results either.

In order to check the common recommendation [2] of using the (311) peak for the macro-stress evaluation in our IN718 material, other reflections were examined as well (Fig. 3). These measurements have been performed on thinner model plates to cut down the required beam time. Plates have been machined out of the pre-material and the forged disc material and exposed to the same thermal treatment.

Another plate has been examined as well in the aged condition, containing high amounts of γ" precipitates. The peak shape, although being different from the as-quenched condition, did not indicate a double peak, and a contribution of γ" precipitates could, however, not be separated. The stress states derived from the (311), (220), (200), and (111) reflection in the aged condition were different to the ones in the as-quenched condition shown in Fig. 3.

Achievements and Main Results

Detailed studies on turbine discs and model plates in the as-quenched and aged condition as well as on corresponding stress-free reference samples have led to the following conclusions:

- The results of the strain measurements are reproducible.
- The investigated material is chemically very homogeneous so that only one reference sample should generally be needed for the whole specimen.

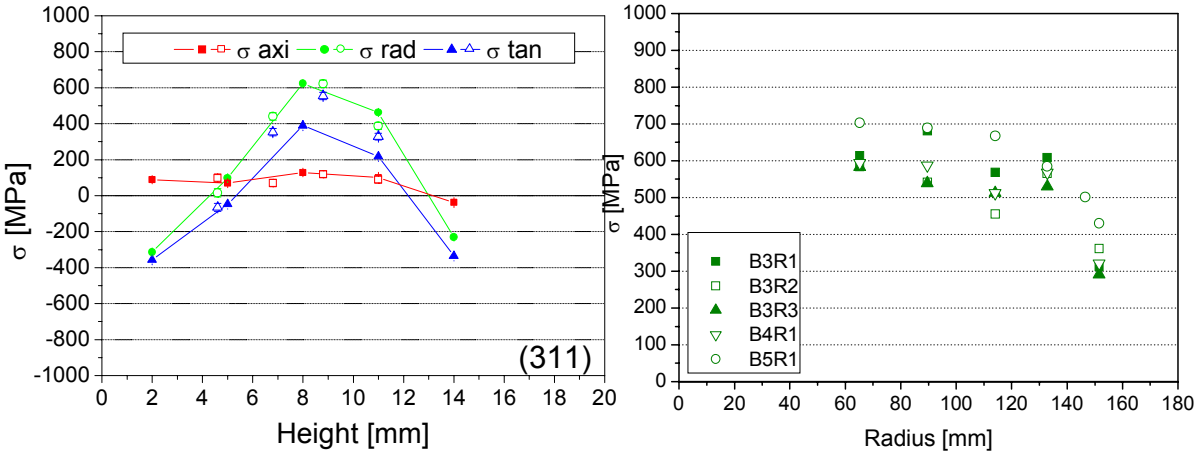


Figure 1: a) Residual Stresses along a through thickness scan of the water-quenched turbine disc. The open symbols indicate the results obtained from the measurement with different slits, the closed symbols stand for the measurement with one slit for all measurement points including the reference samples. b) Residual Stresses along the radius of the turbine disc. The symbols indicate scans in different discs.

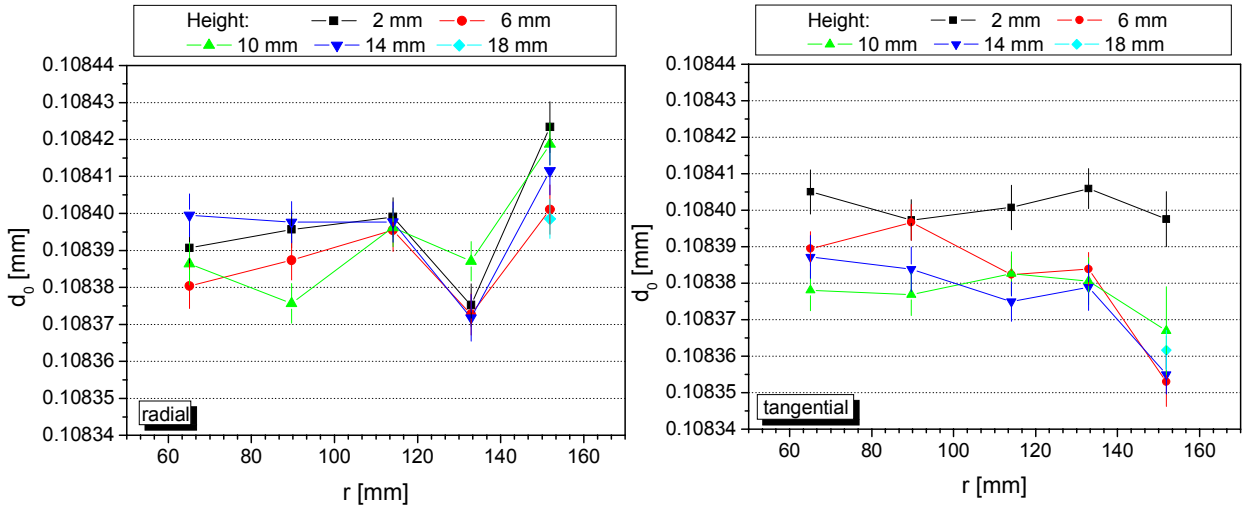


Figure 2: Lattice parameter of the 21 reference cubes in the radial and tangential direction. The impact of these variations on the stress level is equivalent to the measurement error.

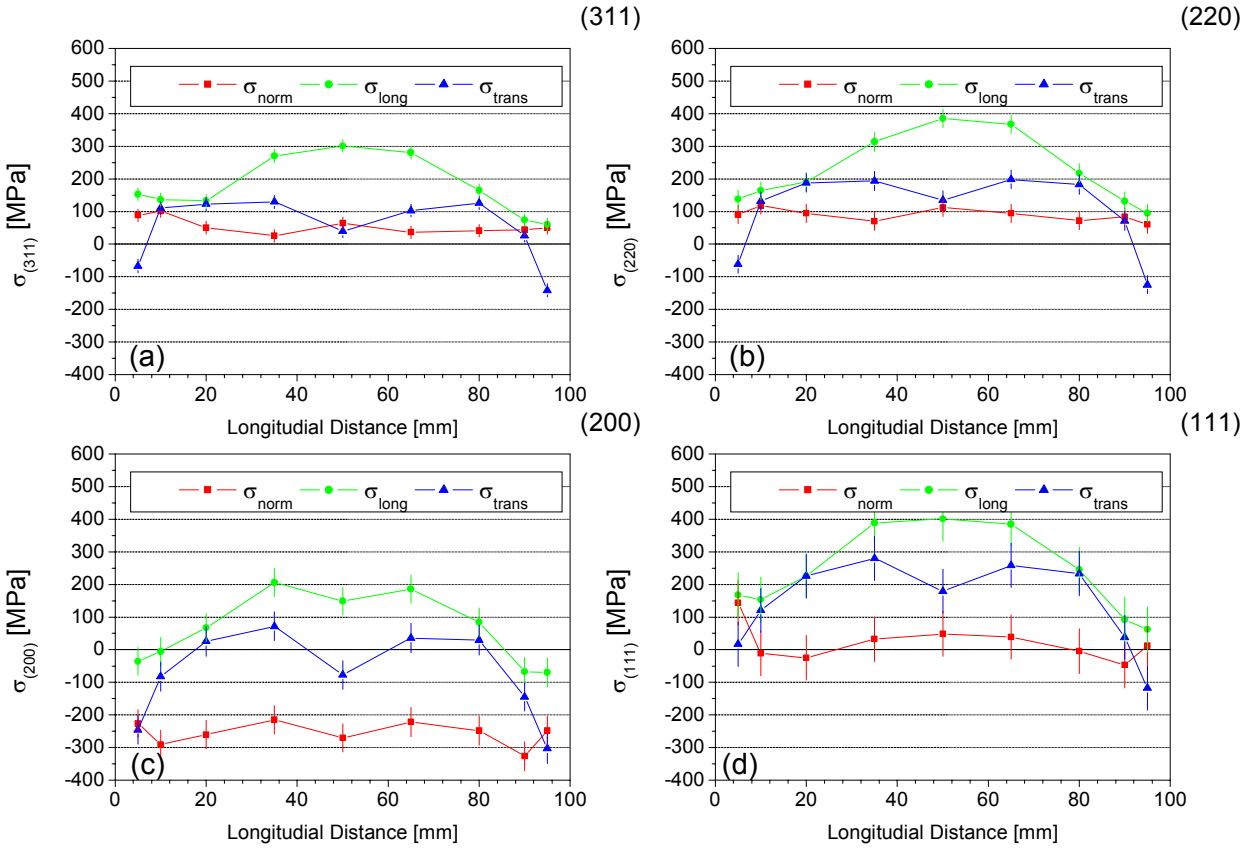


Figure 3: Residual Stress Results of the water-quenched model plate for four lattice planes: a) (311), b) (220), c) (200), d) (111).

- The calculated residual stresses depend on the reflection used for the corresponding strain measurement. Even with the (311) reflection, which is generally recommended for this purpose, micro-stresses seem to play a non-negligible role, e.g. leading to non-zero axial stresses for a thin plate. As nickel has an anisotropic deformation behaviour, significant micro-stresses develop during the cooling process and influence the result of diffraction strain measurements.

Therefore, in-situ tensile test are planned to quantify the contribution of micro-stresses for the IN718 alloy and to develop a correction, if possible.

Acknowlegdement

This research project has been supported by the European Commission under the 6th Framework Programme through the Key Action: Strengthening the European Research Area, Research Infrastructures. Contract n°: RII3-CT-2003-505925'

References

[1] Dye D., Roberts S. M., Withers P. J., Reed R. C.; J. Strain Analysis; 35; (4); 2000; 247-259.

[2] ISO Technology Trends Assessment (TTA) 3:2001 "*Polycrystalline materials – Determination of residual stresses by neutron diffraction*".

[3] Cihak U., Staron P., Marketz W., Leitner H., Tockner J., Clemens H.; Z. Metallkd., 95, (7), 2004, 663-667.

GKSS FORSCHUNGSZENTRUM in der HELMHOLTZ-GEMEINSCHAFT	EXPERIMENTAL REPORT	GeNF ARES

Residual stresses in laser beam welded Al sheets

Principal Proposer:	**W.V. Vaidya, M. Kocak** GKSS
Experimental Team:	**P. Staron** GKSS
Date of Experiment:	07.10.-26.10.04; 05.11.-15.11.04

1 Introduction

Aluminium alloys are potential materials for light-weight structures in transportation industry. Laser beam welding (LBW) is a joining technique that is well suited especially for Al alloys because of the low localised heat input leading to low distortion [1]. In addition, high strength joints can be produced with high processing speeds.

However, significant levels of residual stress can be present in the weld zone that can in general depend on the alloy composition and temper, and the welding parameters. In addition to the heating cycle other influences like e.g. sheet thickness or a rigid clamping arrangement for fixing of the workpiece during welding can also influence the residual stress state after welding. Residual stresses can have an influence on the service performance of the welded material with respect to fatigue and corrosion properties. Therefore, a careful evaluation of the residual stress state after laser beam welding is important. In this investigation, the transverse stress distribution should be measured for materials that have undergone different heat treatments.

2 Experimental

The investigated specimens were five aluminium sheets (AA6056) with a size of 300 mm × 200 mm that have been joined using LBW. The thicknesses and treatments of the five sheets are given in Table 1. Internal strains were measured at 19 points along a 100 mm long scan line in the middle of a sheet using neutron diffraction.

Neutrons of 0.1637 nm wavelength from an elastically bent perfect Silicon (311) monochromator were used. Strain measurements in three perpendicular directions are required to determine the stresses in these directions. The three directions are chosen as the principal sample axes *x* (longitudinal), *y* (transverse), and *z* (through thickness). The gauge volumes in which the strains are measured are defined by Cd diaphragms. For all sheets a matchstick-like gauge volume of nominal size 2×2×30 mm^3 was used for measurements of transverse (*y*) and normal (*z*) strains for improving the intensity [2]. A cubic gauge volume of approximate size 2×2×2 mm^3 was used for measurements of longitudinal strains, because large stress gradients are expected in the transverse direction [2]. In order to increase the number of diffracting grains for the small gauge volume, the gauge volume was shifted by 20 mm in longitudinal

Table 1: Samples.

Sample name	Thickness [mm]	Description
IA16A	3.2	T4 material, welded
IA13B	3.2	T4 material, welded, T6 heat treated
IA14C	3.2	T4 material, welded, T78 heat treated
LAD83A	3.2	T6 material, welded
LED122A	6	T6 material, welded

(x) direction during the measurement. Thus, approximately the same volume as in the two other directions is analysed. Finally, the grain size of the material proved to be small enough to ensure a good grain statistics even with the small gauge volume of approx. 8 mm^3. The Al (311) diffraction peak was recorded with an area detector at an angle of about 84° [3]. This peak is recommended because the influence of micro-stresses on the stress results should be small, i.e. the (311) peak gives a good measure for the macro-stresses [4]. In general, diffractometric elastic constants have to be used here for E and ν, which depend on the hkl of the reflection that is used for the strain measurement [6]. However, the elastic anisotropy of Al is small and the macroscopic values $E = 70$ GPa and $\nu = 0.33$ were used for the Al(311) reflection [6].

For the determination of a triaxial stress state, the knowledge of the unstrained lattice parameter d_0 (or the peak position θ_0) at each measured point inside the sample is required (cf. equation 1). As the lattice parameter can change e.g. with the solute content (Vegard's law, [7]), or, more generally, with the chemical composition of the material, d_0 can depend on the heat input the material has experienced during welding. Therefore, proper reference material is required for the determination of the stress-free lattice parameter d_0. For this purpose a reference sample could be cut out of a sheet, in which macroscopic stresses can relax. Here, this problem was overcome by assuming a plane stress state in the material [5]. From the condition $\sigma_z = 0$, d_0 can be calculated for each point.

3 Results

Fig. 1 shows that variations of d_0 occur in the weld and heat affected zone (HAZ) of one sheet. The variations are relatively small and more or less oscillating. Differences between different sheets can be due to slight differences in the chemical composition of the parent material.

The stress distributions in the three sheets IA16A, IA13B, IA14C (3.2 mm thick) are very similar:

- tensile longitudinal stresses in the HAZ are up to 100 MPa with a double-peak distribution and a minimum of 40 MPa in the weld centre;
- slightly compressive stresses (20-40 MPa) beyond the HAZ;
- the tensile zone has a width of approximately 15 mm;
- transverse stresses are close to zero, slightly tensile.

The stress distribution in the sheet LAD83A (3.2 mm thick) shows higher stresses and a narrower tensile zone:

- tensile longitudinal stresses in the HAZ up to 180 MPa with a double-peak distribution and a minimum of 90 MPa in the weld centre;
- the tensile zone has a width of approximately 10 mm.

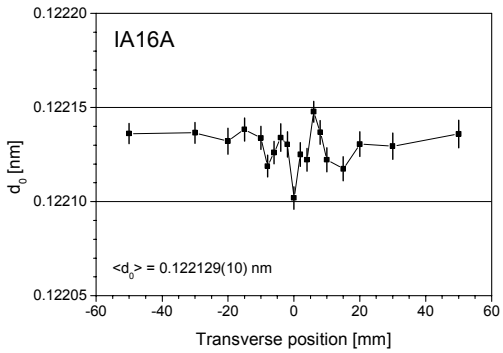


Fig. 1: Unstrained lattice parameters for sheet IA16A as calculated from the plane stress assumption.

The stresses in the sheet LED122A (6 mm thick) are larger than the stresses in the 3.2 mm thick sheets:

- tensile longitudinal stresses in the HAZ up to 200 MPa with a double-peak distribution and a minimum of 70 MPa in the weld centre;
- slightly compressive stresses (40 MPa) beyond the HAZ;
- the tensile zone has a width of approximately 15 mm;
- transverse stresses are close to zero, slightly tensile.

References

[1] E. Schubert, M. Klassen, I. Zerner, C. Walz, G. Sepold, J. Mater. Processing Technol. 115 (2001) 2-8.

[2] L. Pintschovius, V. Jung, E. Macherauch, O. Vöhringer, Mat. Sci. Eng. **61** (1983) 43-50.

[3] B. Clausen, T. Lorentzen, T. Leffers, Acta Mater. **46** (1998) 3087-3098.

[4] ISO Technology Trends Assessment (TTA) 3:2001 "*Polycrystalline materials – Determination of residual stresses by neutron diffraction*".

[5] A.J. Allen, M.T. Hutchings, C.G. Windsor, C. Andreani, Advances in Physics **34** (1985) 445-473.

[6] V. Hauk, "*Structural and Residual Stress Analysis by Nondestructive Methods*", Amsterdam, Elsevier (1997).

[7] H.G. PRIESMEYER, in "*Measurement of residual and applied stress using neutron diffraction*", (eds. M.T.Hutchings and A.D. Krawitz), NATO ASI series E **216** (1992) 277-284.

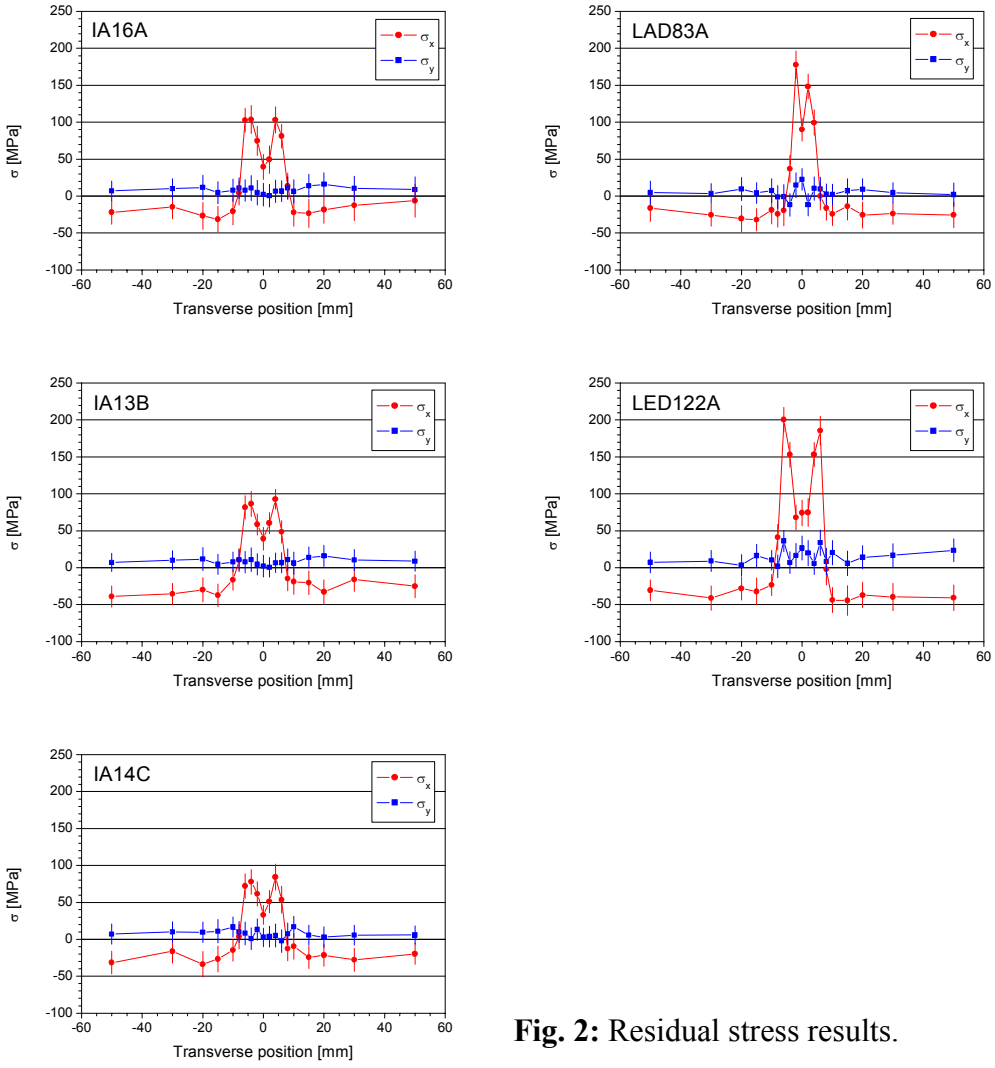


Fig. 2: Residual stress results.

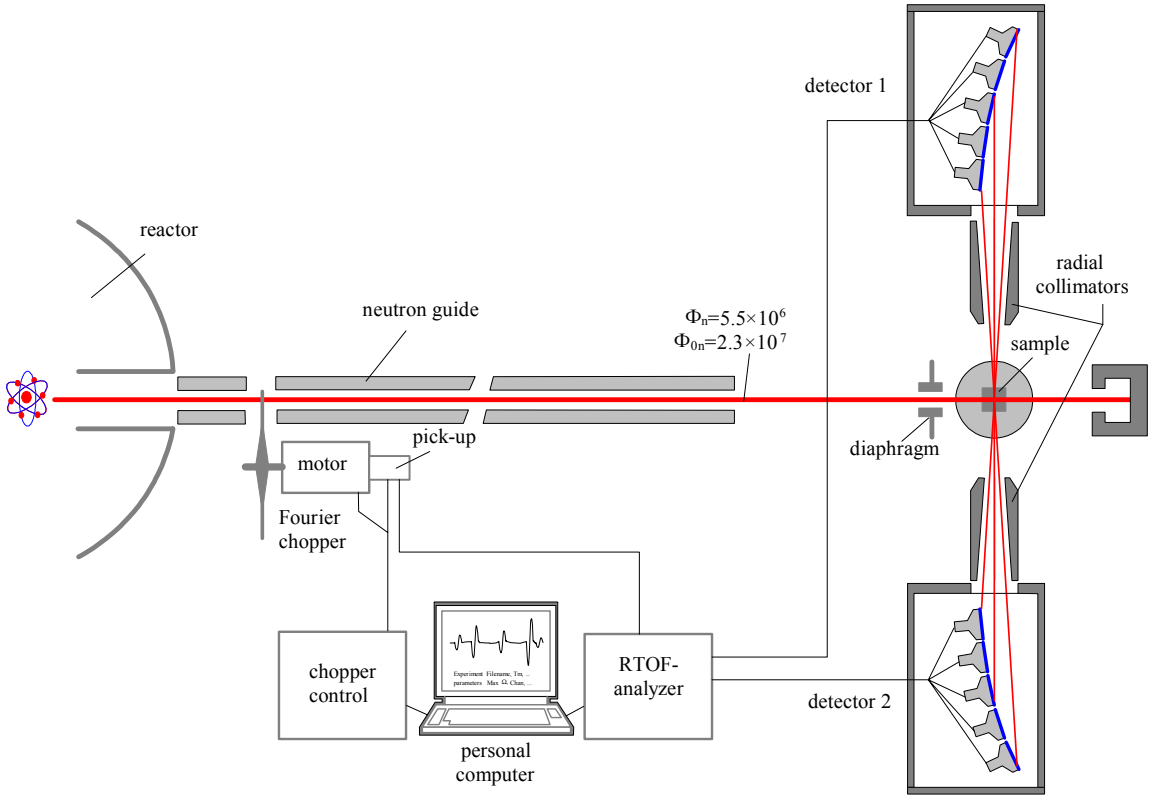
GKSS FORSCHUNGSZENTRUM in der HELMHOLTZ-GEMEINSCHAFT	EXPERIMENTAL REPORT	GeNF FSS
Neutron time-of-flight spectrometer FSS		

Short Instrument Description:
The spectrometer FSS is a Fourier reverse time-of-flight spectrometer (system Hiismäki) to investigate residual stresses in polycrystalline material specimens with technical sizes using thermal neutrons. Details can be found in P.Hiismäki, Modulation Spectrometry of Neutrons with Diffraction Applications, World Scientific, 1997.

Local Contact:

Prof. Dr. Hans-Georg Priesmeyer
Phone/Fax : +49 (0)4152 87 – 1315 / +49 (0)4152 87 – 1338
e-mail: priesmeyer@gkss.de

Schematic View of FSS:



Instrument Details:

Location at FRG-1:	beam line 9, thermal neutrons
Flight path:	21.15 m Ni-coated curved neutron guide, radius of curvature: 3000 m characteristic wavelength: λ_{char} = 0.183 nm beam size: 2 x 20 mm^{-2} to 15 x 108 mm^{-2}
Fourier chopper:	1024 slits, 1760 rpm max. operating speed
Flux at sample position:	$\Phi = 5.5\cdot10^6$ cm^{-2} s^{-1}
Wavelength range:	λ = 0. 1 nm to 0.4 nm

GKSS FORSCHUNGSZENTRUM in der HELMHOLTZ-GEMEINSCHAFT	EXPERIMENTAL REPORT	GeNF FSS

Application of Rietveld profile refinement at FSS	
Principal Proposer:	**Gizo Bokuchava**[1] [1]Institut für Experimentelle und Angewandte Physik, Universität Kiel
Experimental Team:	**Hans G.Priesmeyer**[1]**, Gizo Bokuchava**[1] [1]Institut für Experimentelle und Angewandte Physik, Universität Kiel
Date(s) of Experiment:	January 2004

Application of Rietveld profile refinement at FSS

The Rietveld method introduces the parametric description of the intensity of the measured diffraction spectrum which allows the least square method and any other technique for functional minimisation to be employed to determine crystal characteristics of interest.
From a proposed crystal structure, a theoretical diffraction profile is predicted. The variation of intensity with time of flight (or angle) is dependent on a large number of parameters, including multiplicity and structure factors, peak shape parameters, and lattice parameters. By using a set of these as fitting parameters, the predicted profile is fitted to the experimental profile by least squares minimisation. The algorithm may also be used for accurate lattice parameter determination, when the crystal structure is already known. It is in this manner that Rietveld refinement is used to measure elastic strain averaged on all available reflection (hkl). Since the entire profile is fitted, the positions of all diffraction peaks are taken into account. This greatly improves the counting statistics relative to a single peak fit, leading to more precise strain determination using a shorter count time.

Rietveld (1967, 1969) proposed to fit parameters of a model function describing the whole measured pattern depending on crystallographic parameters of the sample, parameters describing the used instrument plus some numerical parameters against the measured data. With this approach, also the overlapping peaks contribute their information about the structure to the refinement. From some ’appropriate’ starting values the fit minimizes the difference between a calculated curve and the measured data by adjusting the values of scaling factors, lattice parameters, atomic positions, atomic displacement factors etc.

In recent years, the determination of texture and strain became possible with the Rietveld method. Supported by publications like Rietveld refinement guidelines like the ’Rietveld book’ (Young, 1993), the application of the Rietveld method has become common practice in many fields dealing with crystal structure determination.

As explained above, strain varies between grain families, due to single crystal anisotropy. Therefore, if peak positions are determined by varying only lattice parameters, the predicted profile cannot perfectly match the experimental profile of a strained polycrystal, if there is significant single crystal anisotropy.
Nevertheless, since some peak positions are overestimated while others are underestimated, it has been shown that the refinement gives a good estimate of the average elastic phase strain. This offers a considerable advantage over conventional residual stress measurements made at steady state neutron sources, which usually rely on the collection of a single diffraction peak. Commonly in such experiments, the chosen reaction is a `good actor' in that

it is known to exhibit a stress - elastic strain response which is close to that of the bulk material, and remains nearly linear even in the plastic regime. Nevertheless, a single reaction is inevitably affected by intergranular stress, and taking many reactions into account undoubtedly improves the reliability of the measurement.
By providing a measure of elastic phase strain, Rietveld refinement is very useful for the determination of interphase strain in a multiphase material. The lattice parameters of each phase are determined independently, since different peaks within a profile correspond to different phases.
Rietveld refinement can also be used to determine the preferred orientation of grains, called texture. Texture causes the relative intensities of diffraction peaks to differ from those expected by scattering from a randomly oriented polycrystal. By incorporating a parameterised description of the orientation distribution function (ODF) into the Rietveld refinement, the parameters may be found by fitting the observed intensities, thereby estimating the ODF. For a full texture determination using this method, spectra must be collected with the sample positioned in many different orientations relative to the incident beam and detectors. However, fewer spectra are required if the texture is assumed to have a particular symmetry. Even if texture is not of primary interest, it is still necessary to include texture parameters in the Rietveld refinement of a sample which exhibits preferred orientation, in order to obtain a good fit between the predicted and experimental profiles.
To the author's knowledge, there has been no work to demonstrate that the strain determined by Rietveld refinement remains a good estimate of the average elastic phase strain in the case of a strongly textured material. Therefore, caution should be applied when analysing the diffraction spectra of such a material in terms of bulk elastic strains.
One of the original motivations for the introduction of Rietveld analysis was to be able to extract information from overlapping diffraction peaks. This is indeed a great advantage of the method, but it should be noted that if there are few diffraction peaks and these are overlapping, there may be a systematic error in the refined lattice parameter. This is particularly likely in a strongly textured, multiphase material.
Rietveld refinement was used to determine volume-averaged elastic phase strains. However, it was found that the volume-averaged elastic phase strain of cementite could be reliably determined, since Rietveld refinement takes into account all reactions and therefore benfits from improved counting statistics.

References

1. Rietveld H.M., *Line Profiles of Neutron Powder-diffraction Peaks for Structure Refinement*, Acta Crystallogr., 22 (1967) 151-2.
2. Rietveld H.M., *A Profile Refinement Method for Nuclear and Magnetic Structures*. J. Appl. Crystallogr., 2 (1969) 65-71.
3. Young R.A., *The Rietveld Method*, Oxford University Press (1993).

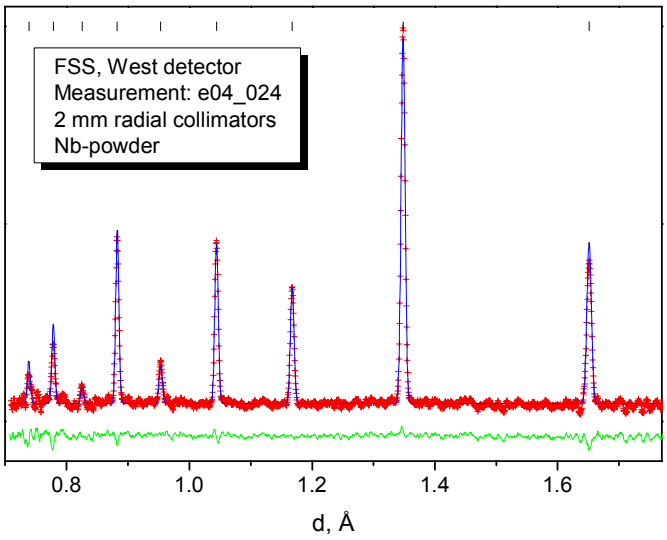


Fig. 2: Fourier neutron time-of-flight spectrum from Nb powder. Experimental points, profile calculated by the Rietveld method and residuals curve are shown.

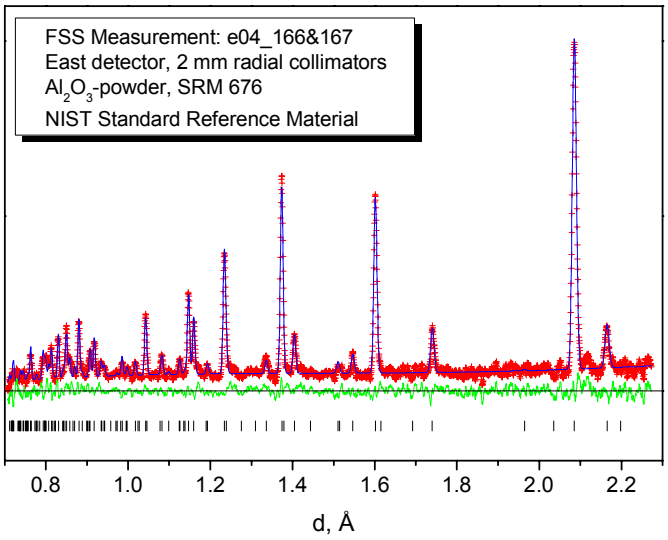


Fig. 1. Part of the neutron diffraction pattern from Al_2O_3 powder (SRM 676 NIST Standard Reference Material) measured on FSS by East detector. Experimental points, profile calculated by the Rietveld method and residuals curve are shown.

GKSS FORSCHUNGSZENTRUM in der HELMHOLTZ-GEMEINSCHAFT	EXPERIMENTAL REPORT	GeNF FSS

Software development and experimental test of the Neutron Activation Calculator (NAC)	
Principal Proposer:	**Hans G.Priesmeyer**[1] [1]Institut für Experimentelle und Angewandte Physik, Universität Kiel
Experimental Team:	**Hans G.Priesmeyer**[1]**, Anne Drews**[2] [1]Institut für Experimentelle und Angewandte Physik, Universität Kiel [2]Fachhochschule Lübeck
Date(s) of Experiment:	April 2004

Software development and experimental test of the Neutron Activation Calculator (NAC)

According to the effective health physics regulatory requirements in Germany calculations must now be made in addition to measurements to estimate the amount and type of activation products, whenever a specimen had been investigated in a neutron beam. Since such calculations are advisable before an experiment, a software program was needed that would be both reliable and easy to handle. On the basis of are freeware program called Neutron Activation Calculator a specially designed version was written and tested. The most recent data files of neutron capture data were implemented (Evaluated Nuclear Data Library ENDF – B) and compositional data of most common materials of technological interest were included. Specimens of steel, copper, nickel, brass and aluminium were then irradiated in the well – defined neutron flux at the neutron radiography laboratory GENRA at FRG-I, so that calculations could be checked by actual measurements.



Fig. 1: Test specimens to check activation calculations

In some cases differences have been found which could be explained by material composions differing from the specifications.

GKSS FORSCHUNGSZENTRUM in der HELMHOLTZ-GEMEINSCHAFT	**EXPERIMENTAL REPORT**	**GeNF FSS**

The diffraction-thermal expansion constants (CTE) of copper

Principal Proposer:	**Hans G.Priesmeyer**[1] [1]Institut für Experimentelle und Angewandte Physik, Universität Kiel
Experimental Team:	**Hans G.Priesmeyer**[1]**, Gizo Bokuchava**[1] [1]Institut für Experimentelle und Angewandte Physik, Universität Kiel
Date(s) of Experiment:	May 2004

The diffraction-thermal expansion constants (CTE) of copper

The elastic constants c_{ij} can be calculated from

$$c_{ij} = \frac{\partial^2 E(x_1, ..., x_6)}{\partial x_i \cdot \partial x_j}$$

if the deformation energy is known. This energy has a strong repulsive part in the near atom region which continues on to an attractive part, which levels off with distance. This asymmetric shape of the potential helps to understand the thermal expansion of a crystalline solid. The mean location of oscillating atoms is shifted further away with increasing temperature. For isotropic cubic crystals thermal expansion can also be expected to be independent of the crystal orientation. But copper for instance is elastically rather anisotropic, which means that the shapes of the potential gradient change with crystal orientation

It was therefore considered to be justified to search for an influence of the crystal orientation on the thermal expansion coefficient.

Figure 1 shows a typical T neutron time-of-flight spectrum measured at FSS

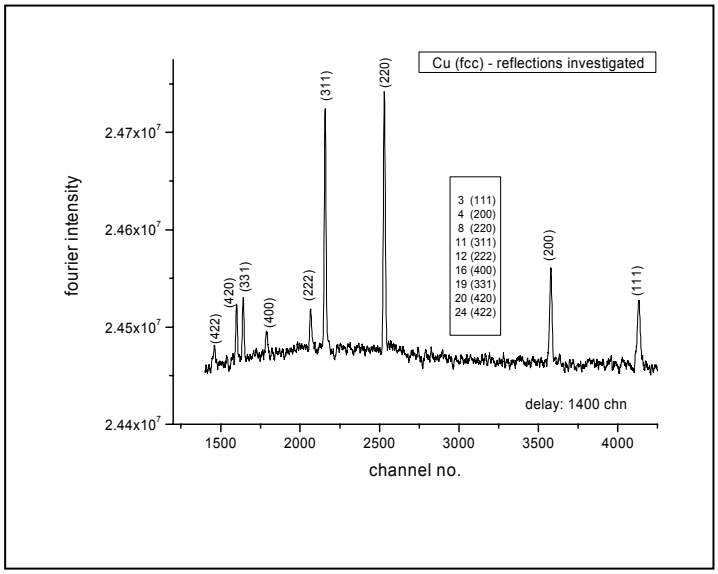


Fig.1: Copper TOF spectrum

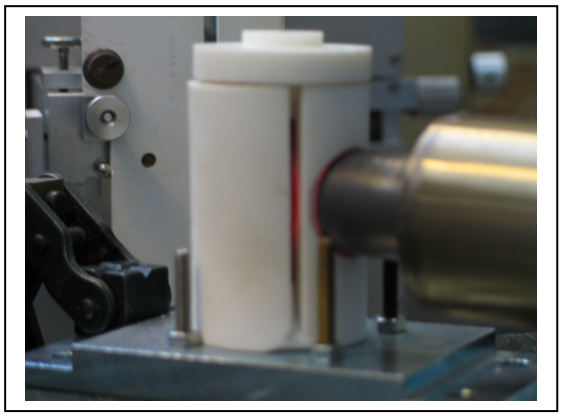


Fig. 2: Sample in MACOR insulating containment with
hot air blower at 600 °C

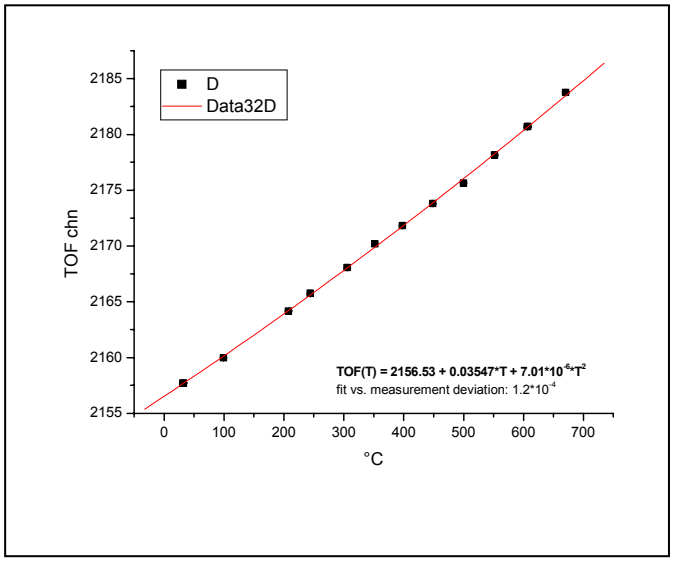


Fig. 3: Centre of gravity of
Cu (220) – peak as a function
of temperature

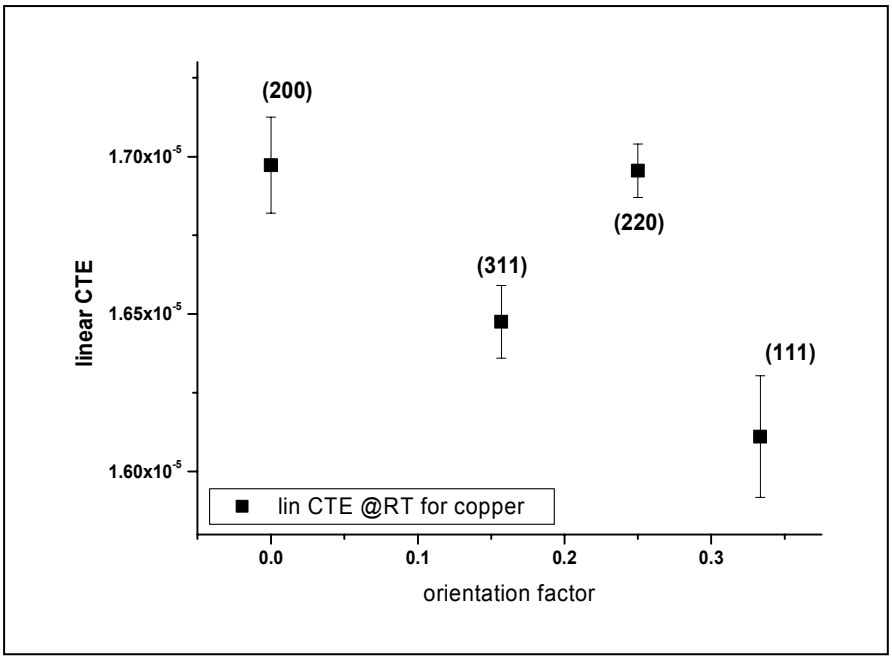


Fig. 4: Linear coefficient of thermal expansion for four copper reflections

GKSS FORSCHUNGSZENTRUM in der HELMHOLTZ-GEMEINSCHAFT	EXPERIMENTAL REPORT	GeNF FSS

Investigation of Residual Stresses in Cast AZ 91	
Principal Proposer:	**Norbert Hort** GKSS, Abt. WZT
Experimental Team:	**Hans G.Priesmeyer[1], Gizo Bokuchava[1]** [1]Institut für Experimentelle und Angewandte Physik, Universität Kiel
Date(s) of Experiment:	2004

Investigation of Residual Stresses in Cast AZ 91

Cast rings and cylinders of the alloy AZ 91 with differing compositions have been investigated neutron – diffractometrically, in order to minimize the residual stresses after cooling to room temperature.

The following figures show the types of specimen used.

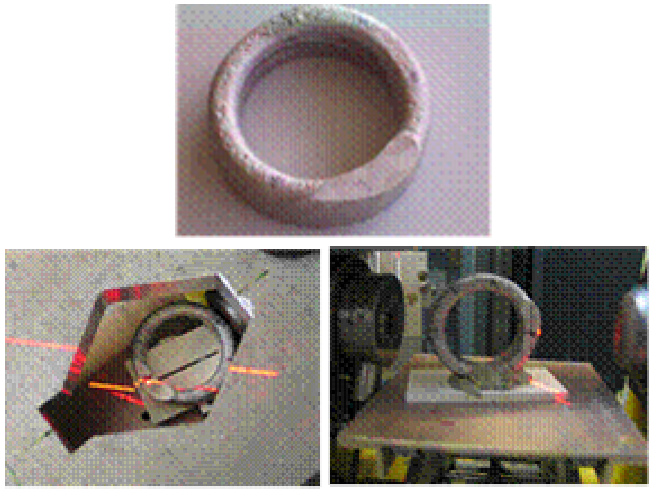


Fig. 1 : Cast Ring of AZ 91 (∅ = 65 mm),
in horizontal and vertical position at FSS

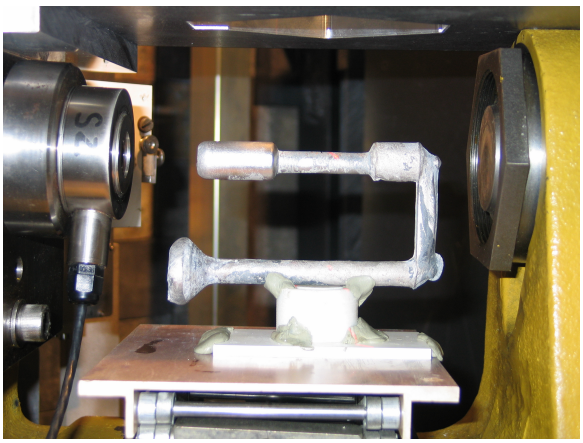


Fig. 2: Cast Cylinder in measuring position at FSS

All measurements had to be performed twice: first in the as received state and then again after thermal treatment.

Fig. 3 shows a typical result for the stress relief achieved by the thermal treatment.

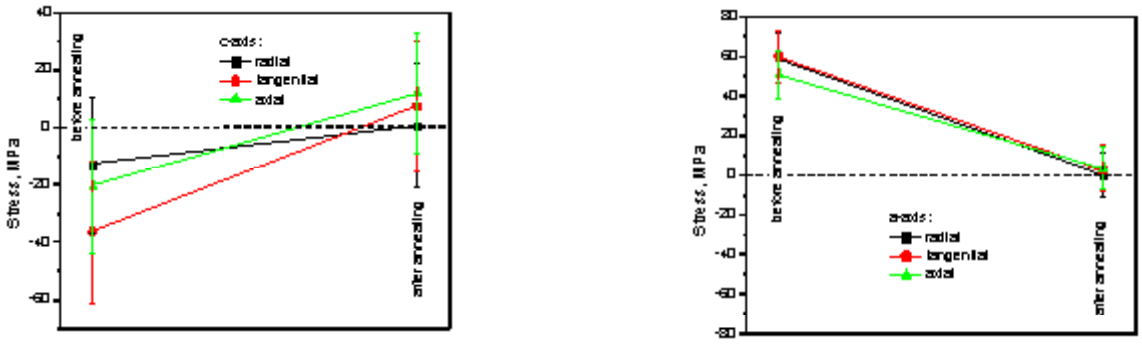


Fig 3: Typical relief of residual stress in AZ 91

The results are analysed within the GKSS advanced engineering materials research program for automotive lightweight constructions.

GKSS FORSCHUNGSZENTRUM in der HELMHOLTZ-GEMEINSCHAFT	EXPERIMENTAL REPORT	GeNF FSS

Investigation the Elastic Constants of AZ 31	
Principal Proposer:	**Jürgen Göken** GKSS Abt WZC
Experimental Team:	**Hans G.Priesmeyer[1], Gizo Bokuchava[1]** [1]Institut für Experimentelle und Angewandte Physik, Universität Kiel
Date(s) of Experiment:	2004

Investigation the Elastic Constants of AZ 31

In order to be able to calculate stresses from strains, measured in a diffraction experiment, the diffraction elastic constants must be known. The differ in principle from the macroscopic elastic constants because of the anisotropy of the material and should be determined empirically. Such measurements were made using the stress rig at FSS:

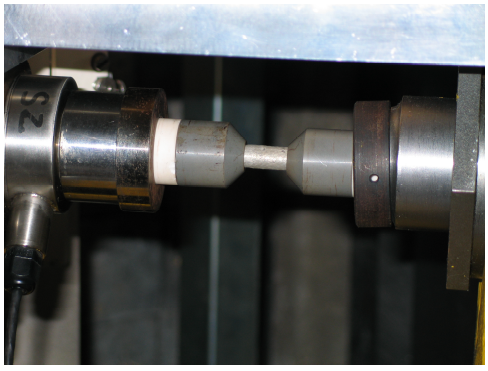


Fig. 1: AZ 31 Cylinder (30mm x 10 mm Ø) in FSS stress rig(RT Experiment)

Compressive force has been applied, resulting on a strong change of the material texture and effects which can be understood as twin formation, starting at about 80 MPa:

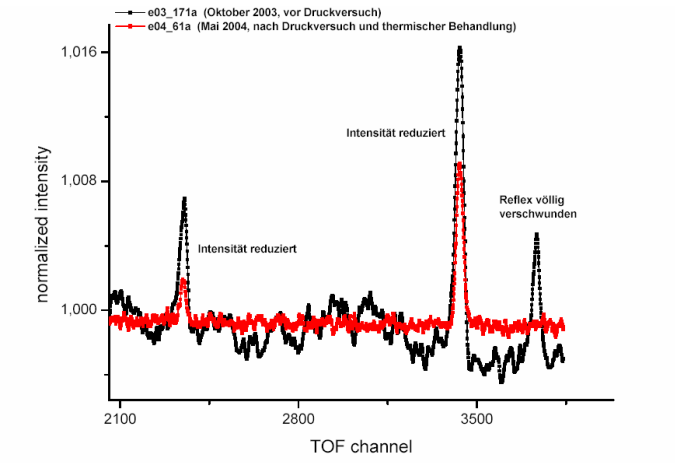


Fig. 2: Clear texture change under compressive force in AZ31

GKSS FORSCHUNGSZENTRUM in der HELMHOLTZ-GEMEINSCHAFT	**EXPERIMENTAL REPORT**	**GeNF FSS**

Positron annihilation experiments

Principal Proposer:	**Hans G.Priesmeyer**[1] [1]Institut für Experimentelle und Angewandte Physik, Universität Kiel
Experimental Team:	**Hans G.Priesmeyer**[1]**, Gizo Bokuchava**[1] [1]Institut für Experimentelle und Angewandte Physik, Universität Kiel
Date(s) of Experiment:	November / December 2004

Positron Annihilation as an additional Source of Information about Plastic Deformation in Structural Materials.

Neutron absorption is always a competing process to neutron scattering. Therefore during strain measurements by neutron diffraction additional information is available through simultaneous gamma-ray spectroscopy. Neutron capture leads to the emission of isotope – specific high-energy prompt gamma radiation, which in turn produces positrons within the bulk of the specimen. The subsequent decay of these so called antiparticles and the resulting annihilation radiation are influenced by material properties like crystalline defects, such as dislocations created by plastic deformation. Experimentally, this leads to an increase in the mosaic spread of the Bragg reflections for elastically scattered neutrons as well as changes of the shape of the 511 keV line of the positron annihilation radiation. Suitable collimation can assure that the information from both neutron diffraction and positron annihilation comes from the same gauge region. Correlation between the width of the Bragg reflections and the S-parameter (describing the shape of the annihilation line) as a function of the degree of plastic deformation has been established. Experimental work of simultaneous on-line investigation of the plastic deformation behaviour of copper and steel as model substances is performed at the FRG-I research reactor at GKSS and will be reviewed. This work was funded by DFG Pr 267/13-1 and GKSS Research Centre Geesthacht GmbH.
The analysis of the annihilation line shape is done by calculating and comparing the shape parameters S (centre) and W (wing), defined in the following figure:

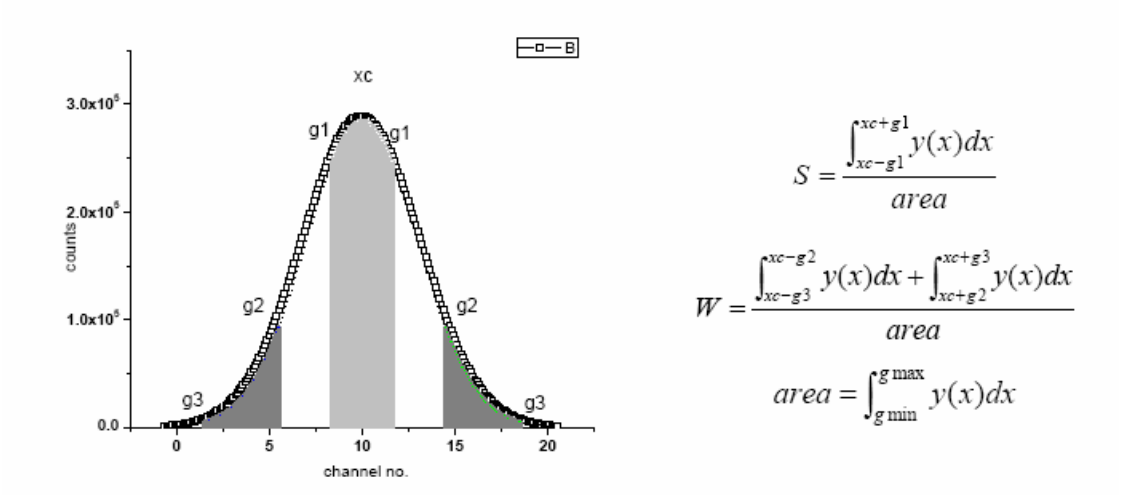


Fig. 1: Definition of the shape parameters S and W

The cross section for pair production in a material depends on its atomic number and the energy of the incident gamma ray according to the relation

$$\sigma_{e+} \approx Z^2 \cdot \ln E_\gamma$$

Materials with low atomic number like Aluminium or Magnesium are therefore less utilizable than Iron, Nickel or Copper. A figure-of-merit (FoM) , which gives an estimate for positron production resp. the measuring time needed to arrive at good statistical accuracy, is given by the product of the capture gamma yield Yγ and the square of the atomic number 2 *Z* . Specimens of steel, Titanium-Aluminide (TiAl), Aluminium and the Magnesium alloy AZ31 have been investigated. The number of time – coincident annihilation events is plotted in Fig.2 as a function of the FoM, and shows the expected linear relationship.

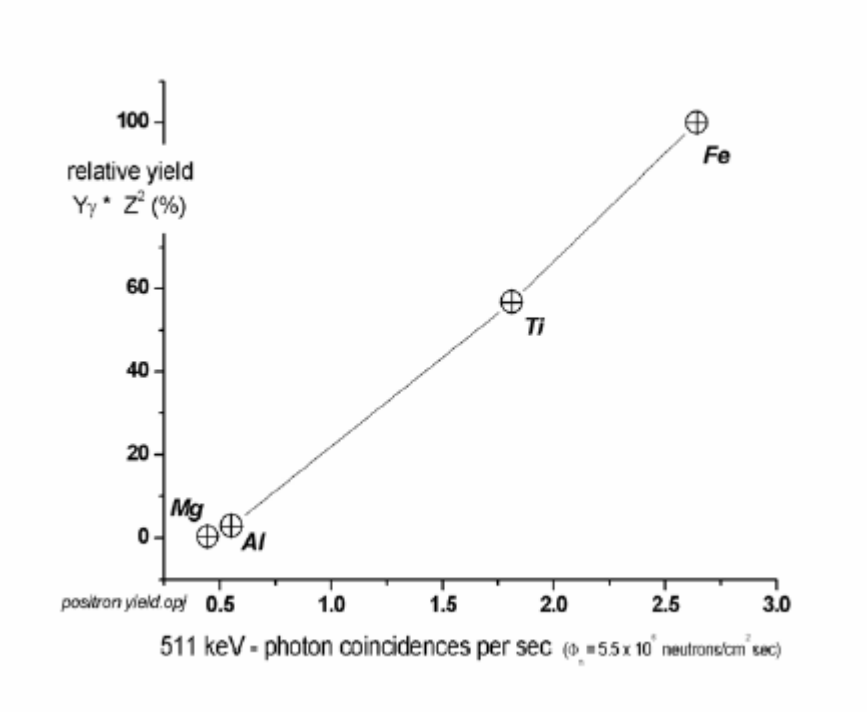


Fig.3: Positron Yield at FSS

The accuracy with which the shape parameters can be determined requires a certain number counts per peak. The following formula describes the uncertainty of the *S* - parameter:

$$\delta S = \sqrt{S \cdot (1-S)/N}$$

where *N* is the total number of counts per peak.

This relation has been checked experimentally:

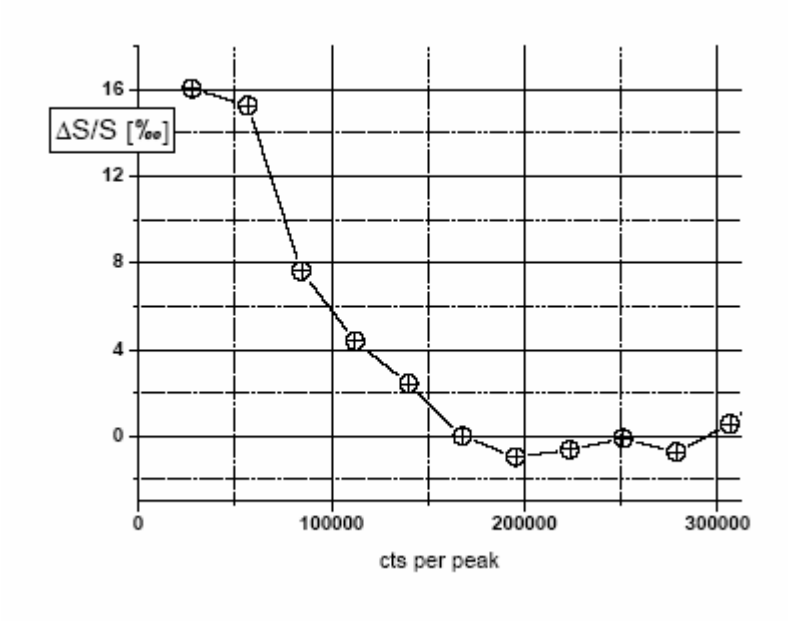


Fig. 4 : Sufficient stability of the shape parameter S is reached after 150000 cts per peak

Plastic deformation and the resulting increase of the dislocation density have a measurable influence both on the mosaic width of the Bragg reflections and the shape of the e+ - annihilation peak. This behaviour has been tested using plastically deformed copper samples. Copper is a good candidate for positron investigations, since neutron capture produces the isotope ^{64}Cu, which is itself a positron emitter. Good correlation is received between the S – parameter and thr width of the diffraction peaks (Fig. 5)

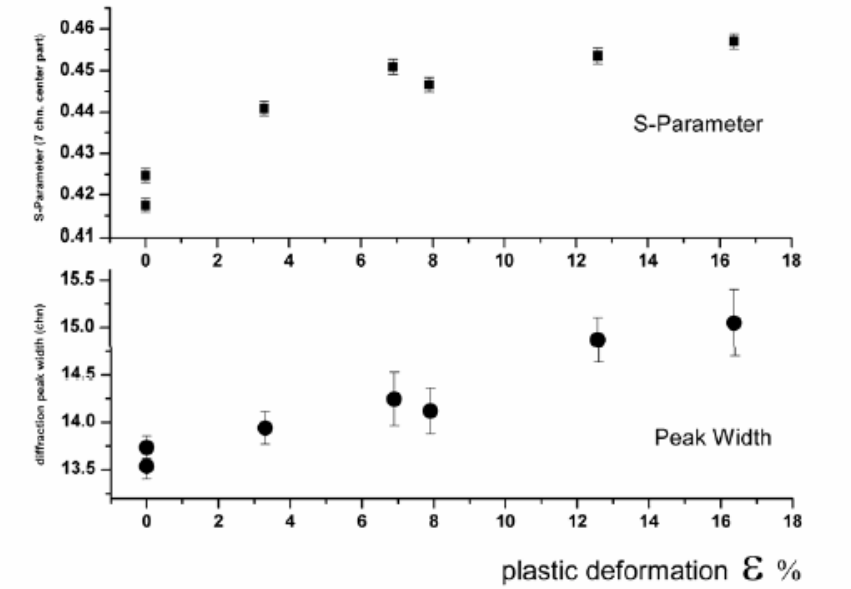


Fig. 5: Correlation between annihilation line shape variation and width of diffraction peak copper (220)

The measurements have been extended to a friction stir welded Al2024 sample, an aluminium alloy with a copper content of ~ 3.5 %, which finds its application in aerospace industry. The following figure shows how the S-parameter correlates with the independently measured Vickers hardness gradient near the welding seam.

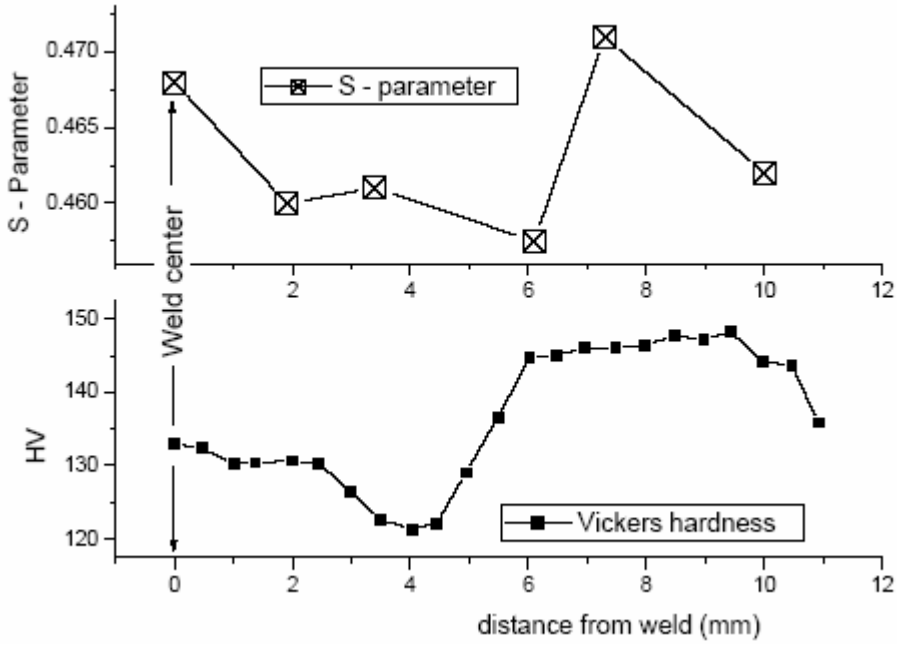


Fig. 6: Correlation between S – parameter and Vickers hardness near friction stir weld

It is the aim of this project to determine the degree and the significance of the correlation between the width of the Bragg reflections, determined by high-resolution neutron diffraction and the shape parameter S of the positron annihilation radiation, determined by highresolution gamma spectroscopy, in order to extract more information about both the elastic and plastic status in a gauge volume within the bulk of a material. The experimental investigations performed so far suggest the possibility to measure shift and width of the diffraction peaks and the gamma line shape parameter S simultaneously. For materials with low atomic number like Al and Mg , it will be necessary to optimise the collimation and coincidence geometry and to try to increase their positron output by virtue of additional efficient, gamma - emitting neutron absorbers.
A first experiment performed at the FSS diffractometer at GKSS has not yet provided full evidence because of minute stability problems and will be repeated with an improved electronic system. Certain positron emitting isotopes like 22 Na simultaneously emit a gamma ray. This associated electromagnetic radiation is then used to trigger a lifetime measurement in the 10^{-12} sec time range. A systematic search for associated gammas in neutron-activated isotopes may reveal such possibilities also for isotopes contained in the bulk of the material, like ^{64}Cu in aluminium alloys. While it could be shown for a time-of-flight system that at least in steel and Titanium positrons generated in a two – stage process by neutrons have intensities sufficiently high to arrive at satisfactory statistical accuracy during the measuring time of a diffraction experiment, it must also be mentioned that bremsstrahlung with energy above the threshold energy of 1.02 MeV has already been used to produce positrons within the bulk of material for solid state investigations [1]. Very high energy synchrotron radiation will allow access to this field of research.

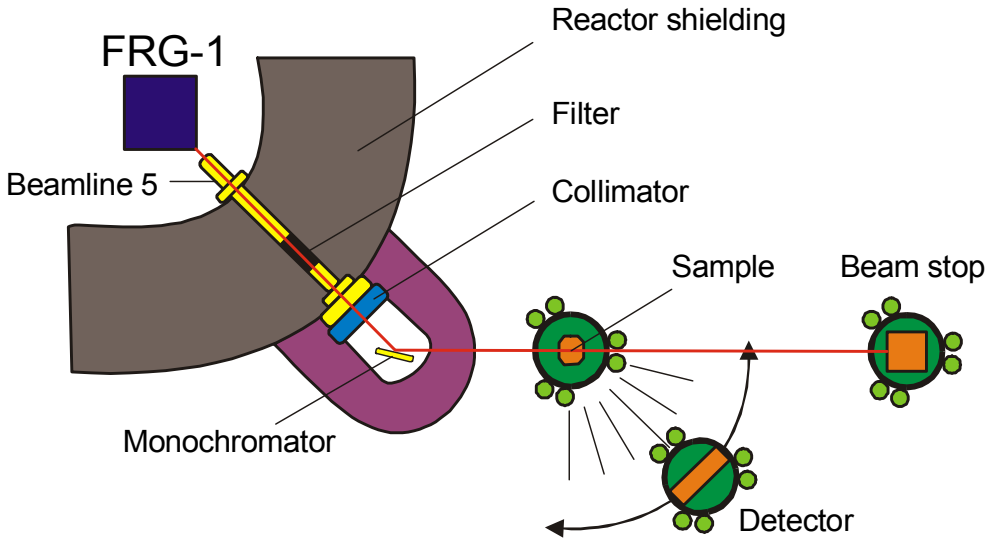
[1] F.A. Selim, D.P. Wells, J.F. Harmon, W. Scates, J. Kwofie, R. Spaulding, S.P. Duttagupta, J.L. Jones, T. White, T. Roney, Nucl.Instr.Meth. in Physics Research B182 (2002) 197 – 201

GKSS FORSCHUNGSZENTRUM in der HELMHOLTZ-GEMEINSCHAFT	EXPERIMENTAL REPORT	GeNF TEX-2
Neutron texture diffractometer TEX-2		

Short Instrument Description
The four circle neutron texture diffractometer is used to characterise textures in metallic, ceramic and geologic materials applying thermal, non-polarised neutrons.

Local Contact:
Prof. Dr. Heinz-Günter Brokmeier
Phone/Fax:+49 (0)4152 87 – 1207+49 (0)4152 87 – 1338
e-mail: brokmeier@gkss.de

Schematic View of TEX-2:



Instrument Details:

Location at FRG-1:	beamline 5, thermal neutrons maximum beam cross section: 45 x 45 mm^2
Primary collimation:	30', 42', 51'
Monochromator:	Cu (111), Cu (200), PG (002), Ge (311)
Take-off angle:	17.2°, 27.2°, 37.2°, 47.2°, 57.2°
Wavelength range:	λ = 0.08 – 0.27 nm (in steps)
Flux at sample position:	$\Phi = 0.3 - 2 \cdot 10^6$ cm^{-2} s^{-1}
Angular range	Φ: -360° to +360° X: -360° to +360° Ω: -46° to + 46° 2Φ: -75° to +120°
Detector:	^{3}He- single detector 38° JULIOS-PSD 2-D-pos. sensitive detector (active area 30 x 30 cm^2)

Instrument Details (continued)**:**

Sample geometries (standard): (various):	cube 10 mm edge, sphere 15-20 mm ∅ cylinder 10-15 mm ∅, 10-15 mm high e.g. wires, tubes, tensile samples
Distances: sample-^{3}He detector sample –JULIOS	40 - 200 cm 70 - 100 cm
Sample environment:	mirror furnace up to 2000 K loading device: tension up to 15 kN, compression up to 20 kN sophisticated set of sample holders

GKSS FORSCHUNGSZENTRUM in der HELMHOLTZ-GEMEINSCHAFT	**EXPERIMENTAL REPORT**	**GeNF TEX-2**

Global textures of ECAP deformed Al alloy 5109

Proposer:	**Werner Skrotzki** Institute of Structural Physics, Division of Metal Physics, Dresden University of Technology, D-01062 Dresden
Co-Proposer:	**Nils Scheerbaum** Institute of Structural Physics, Division of Metal Physics, Dresden University of Technology, D-01062 Dresden
Experimental Team:	**Heinz-Günter Brokmeier** Institut für Werkstoffkunde und Werkstofftechnik, TU Clausthal
User Group Leader:	**Heinz-Günter Brokmeier**

Date(s) of Experiment:	1.4. – 6.4.04; 9.7. – 14.7.04; 21.9. – 25.9.04

Objetives

ECAP is at present one of the most promising techniques to produce bulk nanostructured or ultrafine-grained materials (grain size in the range of 100-1000nm) for structural applications. The process has received considerable attention in the last few years due to the advent of nano-technology, and it continues to receive attention of the scientific community due to its future industrial potential [1, 2]. In ECAP a billet is deformed in a narrow deformation zone at the plane of intersection of two die channels of equal area cross-section and the strain mode approximates closely to simple shear (Fig. 1). As the overall billet geometry remains nearly constant during ECAP, multiple passes through the die are possible without any reduction in cross-sectional area. This allows materials to be deformed to very high plastic strains that cannot be readily obtained in more conventional processes, such as rolling. Large plastic deformation results in the development of texture, which will be demonstrated here for Al-Mg alloy AA 5109. Special attention is focussed on the effect of initial texture.

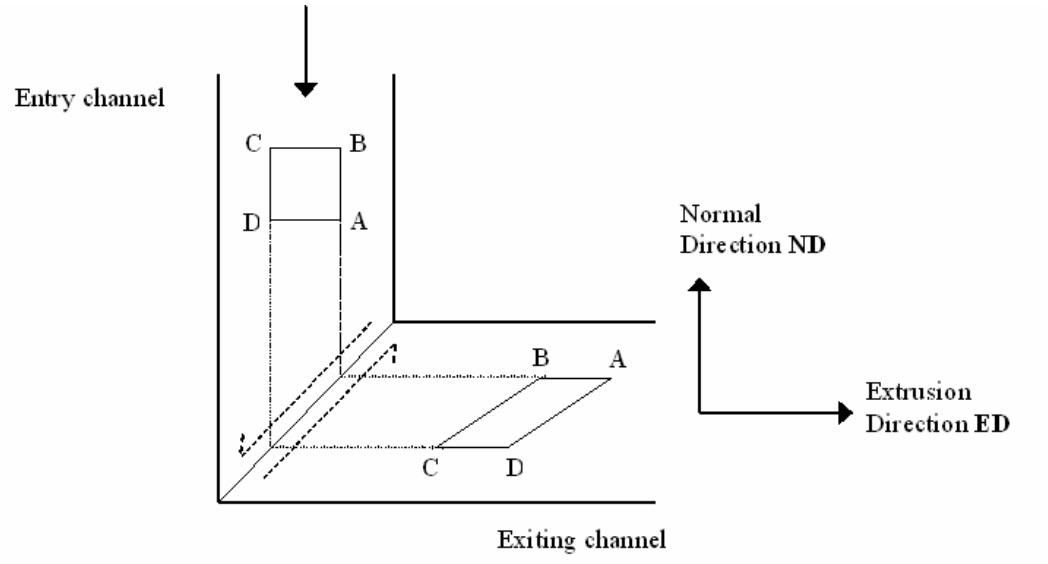


Fig. 1: Simple shear model of ECAP testing.

Experiment

The material used was rolled Al-Mg alloy AA 5109 with a strong cube texture and a grain size of the order of 60μm. Specimens with 10mm x 10mm square cross section and 100mm length were machined from the rolled plate parallel (0°) and at 45° to the rolling direction. ECAP was carried out at a crosshead speed of 1 mms^{-1} at room temperature using a Zwick 200kN screw driven machine and a die set with rectangular intersection of the extrusion channels without any rounding of the corner region. The specimens were extruded in series, as they left the die they showed more and more sheared shape, as if they were sheared on the ND plane in the direction of ED. The number of ECAP passes was limited to 3. Between individual passes the specimen was introduced in the same sense (route A, that is no rotation around the specimen longitudinal axis between intermediate passes).

Achievements and Main Results

Neutron texture measurements were done on a cube of 10mm x 10mm x 10mm taken from the middle part of the extruded bar. The results are presented in Fig. 2 in the form of (111) pole figures. It is obvious that the shear process during ECAP produces a characteristic type of texture depending on the initial texture of the material. A detailed analysis of the texture components with respect to intensity and deviation from ideal simple shear positions is in progress.

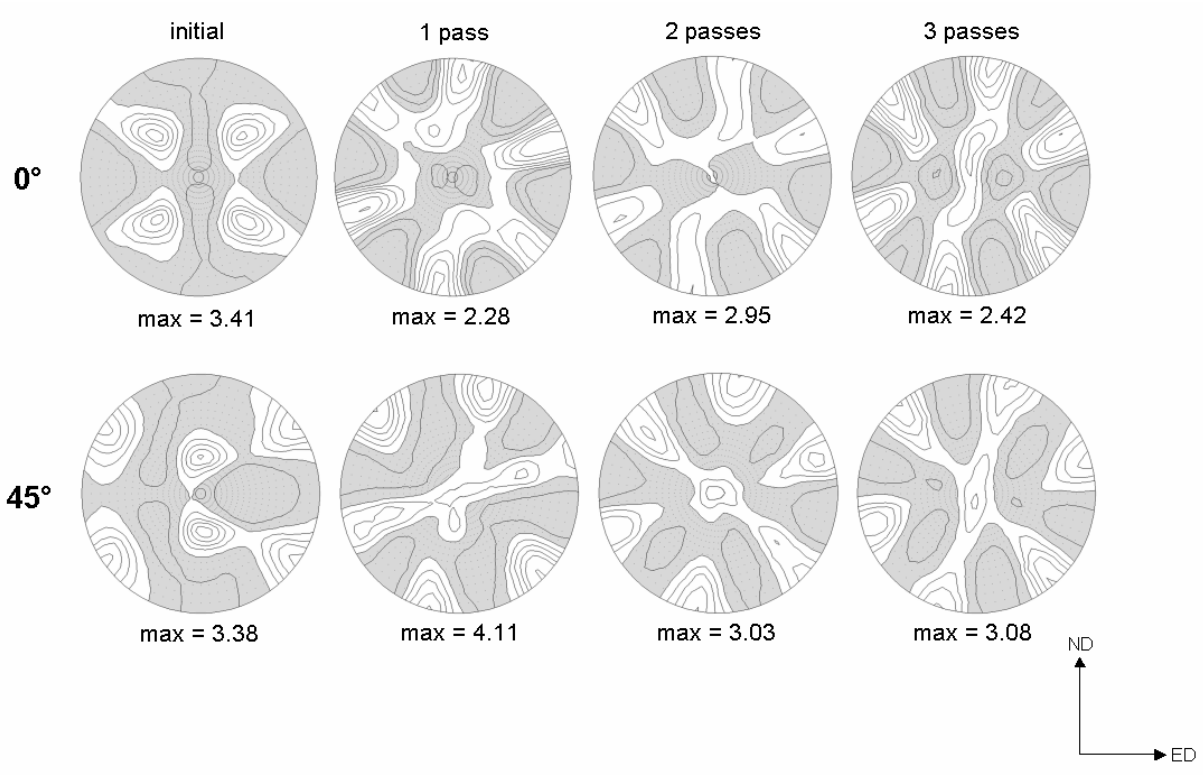


Fig. 2: (111) pole figures of Al alloy AA 5109 with two initial textures deformed by ECAP.

References

[1] V.M. Segal, Mater. Sci. Eng. A 97 (1995), 157.
[2] R.Z. Valiev, Mater. Sci. Eng. A 234 (1997), 59.

GKSS FORSCHUNGSZENTRUM in der HELMHOLTZ-GEMEINSCHAFT	**EXPERIMENTAL REPORT**	**GeNF TEX-2**

Texture Measurements of ECAE Processed Mg-Zn-Y-Zr Alloy and Hot Compressed SiCw/AZ91 Composite

Proposer:	**M. Y. Zheng[1], W. M. Gan [1], S. W. Xu[1], K. Wu[1]** [1] School of Materials Science and Engineering, Harbin Institute of Technology, Harbin 150001, China
Co-Proposer:	**H.-G. Brokmeier[2]** [2]Institut für Werkstoffkunde und Werkstofftechnik, TU Clausthal
Experimental Team:	**W. H. Ye[2], S. B. Yi[2], H.-G. Brokmeier[2]** [2] Institut für Werkstoffkunde und Werkstofftechnik, TU Clausthal,
User Group Leader:	**H.-G. Brokmeier[2]**
Date(s) of Experiment:	29.5. – 4.6.2004

Objectives

High performance magnesium alloys and magnesium matrix composites have great potential in aerospace and other high technological applications. In order to improve their properties, these magnesium matrix materials are usually subjected to thermal deformation processes. As a result, high intensity of texture is attained in the materials. Therefore, it is crucial to understand the correlation between deformation mechanisms, texture and properties in the deformed magnesium matrix materials [1]. In this research, textures in normal-extruded and ECAE(equal channel angular extrusion) processed Mg-Zn-Y-Zr alloy [2] were measured. In addition, textures in hot compressed SiCw/AZ91 composite [3] were also measured.

Experiment

The Mg- 5.00Zn- 0.92Y- 0.16Zr (ASTM designation: ZWK510) containing quasicrystal phase was initially hot extruded at 350 ^{o}C at a rate of 0.2m/min to give rectangular bars with 15mm in thickness and 15mm in width corresponding to a reduction ratio of 9:1. The extrusion rods were cut into 10×10×60 mm^3 rectangular billets for ECAE. The ECAE processing was conducted on the billets by the die with a channel angle of 90^{o} and a curvature angle of 37° through the die using processing route B_C. The specimen was ECAE processed at 250 ^{o}C for the first pass, 200 ^{o}C for the second to the eighth pass at a pressing speed of 40 mm/min.

Hot extrusion experiment of the squeeze-cast SiCw/AZ91 composite was carried out at temperature of 350 ^{o}C with extrusion ratio of 10. Specimen with 8 mm in diameter and 12mm in length machine from the extruded SiCw/AZ91 composite were compressed at 470 ^{o}C to the strain of 45% using Gleeble-1500 thermal simulator.

Texture measurements were carried out using neutron diffractometer TEX-2. Four completed pole figures, i.e. (0002), (10-10), (11-20), (10-11), were measured for the as-extruded and as-ECAEed alloy. As for SiCw/AZ91 composite before and after compression test, two completed poles of the matrix alloy, (10-10) and (10-12), were measured.

Results

The pole figures of the as-extruded and as-ECAEed ZWK510 alloy are shown in Figure 1. As shown in Figure 1 (a) and (b), the as-extruded ZWK510 alloy exhibits an ED // $<1010>$ fiber

texture. ECAE can modify the texture in the magnesium alloy. After 8-pass ECAE processing, as can be seen from Figure 1 (c) and (d), basal planes are inclined about 45^{o} to the extrusion direction, which can result in high schmid factor, leading to lower yield strength in the ECAEed alloy. The tensile stress-strain curves of the alloy are shown in Fig. 2. After 8-pass ECAE, the alloy exhibits lower yield strength and higher elongation compared with the as-extruded alloy, although the grain is significantly refined after ECAE. Further effort will be focused on the texture evolution and modeling during different ECAE processes.

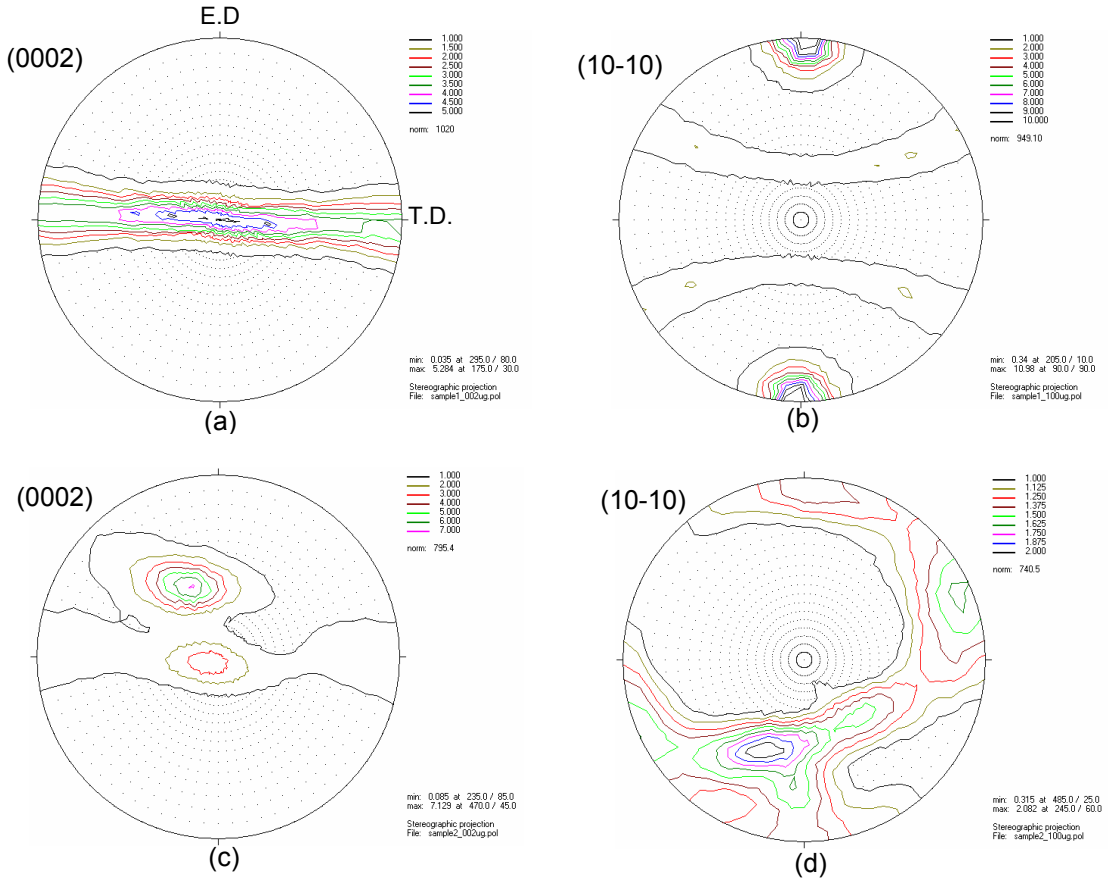


Figure 1: Pole figures of the (a), (b) as-extruded and (c), (d) as-ECAEed ZWK510 alloy.

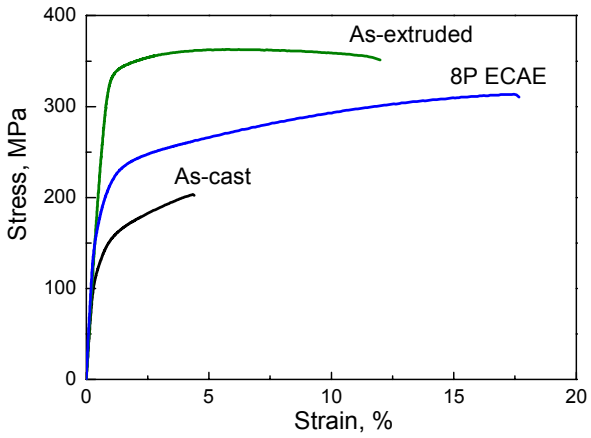


Figure 2: Tensile stress-strain curves of ZWK510 magnesium alloy.

The pole figures of the as-extruded and as-compressed SiCw/AZ91 composite are shown in Figure 3. As shown in Figure 3(a) and (b), certain preferred orientation is formed in the as-extruded SiCw/AZ91 composite. After hot compressed to strain of 45%, the texture is

modified, as shown in Figure 3(c) and (d). Further work will be focused on the texture evolution of the composite during different extrusion and hot compression conditions, and the effect of ceramic reinforcement on the texture evolution of the matrix.

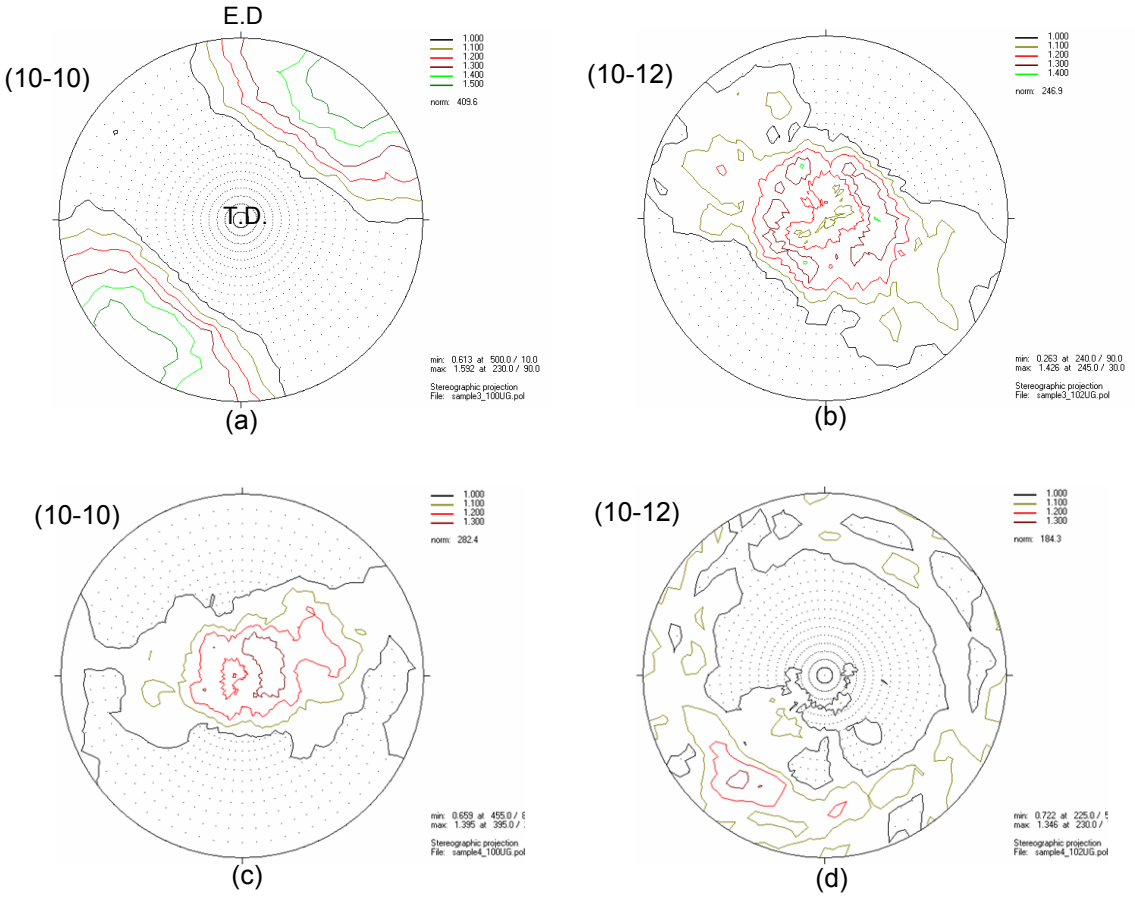


Figure 3: Pole figures of the (a), (b) as-extruded and (c), (d) as-compressed SiCw/AZ91 magnesium matrix composite.

References

[1] S. R. Agnew, M. H. Yoo, C. N. Tomé. Acta mater. 2001, 49(20): 4277-4289
[2] M. Y. Zheng, X. G. Qiao, S. W. Xu, K. Wu, S. Kamado, Y. Kojima. Mater. Sci. Forum. 2004, 475-479: 469-472
[3] M. Y. Zheng, K. Wu, C. K. Yao, Mater. Sci. Eng. A, 2001, A318: 50-56.

GKSS FORSCHUNGSZENTRUM in der HELMHOLTZ-GEMEINSCHAFT	**EXPERIMENTAL REPORT**	**GeNF TEX-2**

Bone fossilization and Sauropod Texture

Proposer:	**Anke Pyzalla[1],** [1]Institute for Material Science and Technology, TU Wien, Austria
Co-Proposers:	**Magdalena Stempniewicz[1],**
Experimental Team:	**Rayen Ferreyro[1],** Institute for Material Science and Technology, TU Wien,
	S.-Y. Li[2], H.-G. Brokmeier[2,3], [2]GKSS, [3]TU Clausthal
User Group Leader:	**Anke Pyzalla[1]**

Date(s) of Experiment:	14.6. – 8.7.2004

Objetives

Sauropod dinosaurs were the largest and heaviest animals that ever walked on Earth. Their weight is estimated to have reached as much as 100t. The implications of the large size and weight on sauropod biology and physiology are the subject of a researcher group we co-operate with (spokesman: Doz. Dr. Martin Sander, University of Bonn).

In the framework of this research group we aim at determining the influence of sauropod body size on their bone structure. The bone structure of sauropods, however, has been altered during the nearly 150 million years of the bone's burial due to taphonomic and diagenetic processes.

Experiment

We looked at long bones (tibia and femora) originating from the large dinosaur excavation in Tendaguru, Tanzania and from the National Dinosaur Monument, Utah, USA. In particular we chose the species Braiosaurus brancai, Barosaurus africanus and Apatosaurus. The relatively large number of bones of different individuals of the same species found in Tendaguru due to including samples from animals that died at various stages of their ontogeny enables studies of growth and remodeling processes within their long bones.

The dinosaur bones were first characterised regarding their histology using optical, scanning and transmission electron microscopy. The local distribution of chemical elements within the dinosaur bones was determined using proton induced X-ray emission analysis (PIXE) at the Hahn-Meitner-Institute, Berlin, Germany /1/ and X-ray fluorescence spectroscopy at the Atominstitut, Vienna, Austria.

At GKSS we aimed at determining the texture of sauropod bones originating from different species and in different excavation places. We also studied texture in sauropods that died at different ontogenetical ages.

The experiments were performed as pole figure measurements. We took one complete pole figure and due to the long times needed for the measurement and the clear fibre texture of the specimen then decided to determine only the 0002 pole figure in longitudinal direction of the specimens. Even these need measurement times of at least some hours. These large data acquisition times are due to the fact that the hydroxyapatite (or fluorapatite) is nanocrystalline and the textures are not very sharp.

Achievements and Main Results

The texture measurements and their evaluation are still in progress. So far the results of the experiments revealed that all samples contain fibre textures of the hydroxyapatite. The calcite, which now due to the diagenesis and the interdiffusion processes with the environment occupies most of the cavities in the bones has a random texture. The pole figures obtained so far indicate that there may be differences in the texture of ontogenetically young and old dinosaurs. We further noticed different textures in ontogenetically young sauropods which were of similar size. This may be a clue to different growth processes depending e.g. on nutrition or gender, however we need more measurements to verify of falsify this. Texture measurements at different positions across the long bone cross-sections revealed that bone texture is different in the endosteal and periosteal region of the sauropod bones.

In future we also aim at comparing the texture in dinosaur bones to textures in bones of modern mammals.

Publications are in preparation.

References

/1/ M. Stempniewicz, P. Hinkel, S. Weiss, A. Denker, M. Sander, A. Pyzalla, Anwendung präparativer Methoden aus der Werkstoffkunde zur Untersuchung von Sauropodenknochen, Praktische Metallographie, Sonderband 36 (2004) 217 - 221

GKSS FORSCHUNGSZENTRUM in der HELMHOLTZ-GEMEINSCHAFT	**EXPERIMENTAL REPORT**	**GeNF TEX-2**

Texture analysis of cast stripped Mg-AZ31

Proposer:	**Lutz Wondraczek,** IMET – TU Claustahl
Co-Proposers:	**Heinz Palkowski**, IMET- TU Clausthal
	Heinz-Günter Brokmeier, IWW – TU Clausthal / GKSS - WFN
Experimental Team:	**Sang Bong Yi,** IWW – TU Clausthal / GKSS - WFN
	Bend Schwebke, IWW – TU Clausthal / GKSS - WFN
User Group Leader:	**Heinz-Günter Brokmeier,** IWW – TU Clausthal / GKSS - WFN
Date(s) of Experiment:	20.8. – 23.8.2004

Objectives

The development of new casting technologies like thin slab casting or strip casting with an in-line rolling process is expected to result in a shorter processing time featuring a high potential of saving energy, time and cost. Particular attention is paid to the casting process parameters such as casting speed and solidification speed. In dependence of solidification parameters and geometry of the strip, a typical microstructure development occurs. For characterising the microstructure of cast strip, grain size, grain size distribution and texture development of cast strip was under examination. The microstructure of rolled cast material was examined too.

Experiment and Results

The laboratory single belt caster allows production of cast magnesium strips with a width of about 160 mm and a thickness of 10 to 15 mm. The length of the cast strip lies between 5 and 7 m (according to the amount of molten metal) [1]. Experiments were done with AZ31.

Al	Zn	Mn	Si	Fe	Cu	Ni	Mg
2,92	1,1	0,15	0,02	0,002	0,002	<0,001	Balance

Within the experiments, a model for the calculation of temperature spread in the cast strip was developed. This model is able to describe the temperature profile in strip height and length in dependence of the temperature of the liquid ($T_{gieß}$), the casting speed, the strip thickness and the heat transfer parameters [1,2]. Different calculations were done to determine maximum casting speed. The calculations showed that a typical temperature profile in strip thickness occurs. The temperature profile is effected by the heat transfer parameters at the top and the bottom side of the strip, the casting temperature, the cooling strategy and the casting speed. The use of different protective cover gases within the solidification area effects the heat transfer parameters at the top side of the strip and therefore the solidification of the strip. By casting with optimised casting parameters such as casting temperature and casting speed a cast strip with a thickness of 10 mm and a length of more than 5 m could cast. The surface quality is quite good so that no machining is necessary before rolling.

For characterising microstructure development of cast strip and of rolled cast material, grain size, grain size distribution, segregations, porosity and texture were examined. Grain size of cast strip was between 80 and 140 µm, following the temperature spread during solidification. Porosity was between 4 and 12 %, depending on used covering gas and casting temperature, Porosity at top side of the cast strip was higher than on bottom side [1, 2]. The texture of the cast strip as well as for different rolling (40% and 67% rolling parallel,

70% cross rolling and 68 % was examined by neutron diffraction. By neutron diffraction one loses the surface information such as shearing but gets a quite good average over the whole cross section and is of course independent on grain size variations. The basal pole figures in Fig. 1 show on hand a nearly random average texture of block cast material, strip cased material develops a slight texture that is caused by solidification gradient and the casting direction. On the other hand rolling yields to an increase of the orientation density which depends on the degree of rolling (40% versus 68%). Moreover the texture symmetry influences by rolling mode (cross rolling or transverse rolling) leads to a symmetric texture.

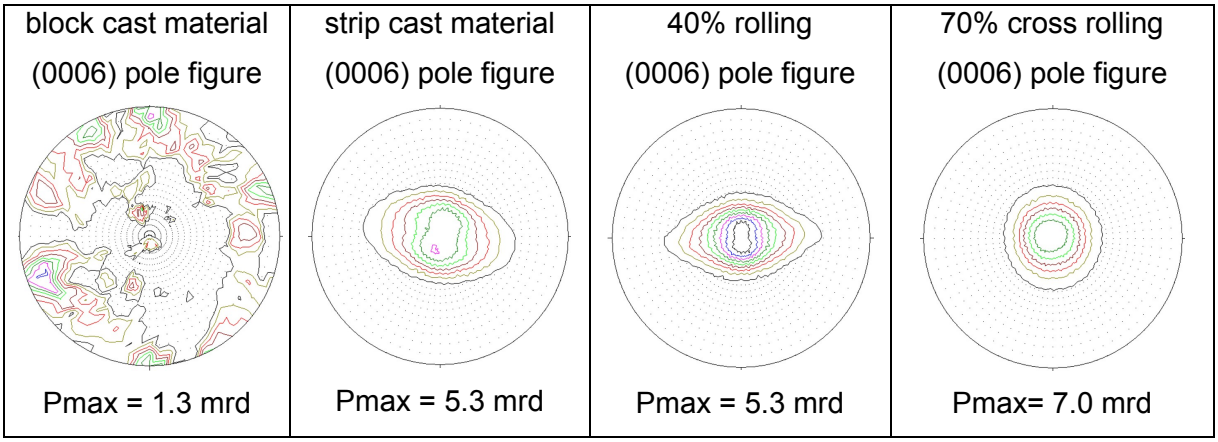


Fig. 1: Basal plane raw data pole figures of AZ31 at different states

Because of the finer microstructure an adapted rolling strategy for rolling of the strip cast AZ31 material was developed (Fig. 2). It could be shown, that minimal grain size is about 10 µm after a 60 % of total deformation. Porosity is totally closed after first rolling pass without any occurrence of cracks.

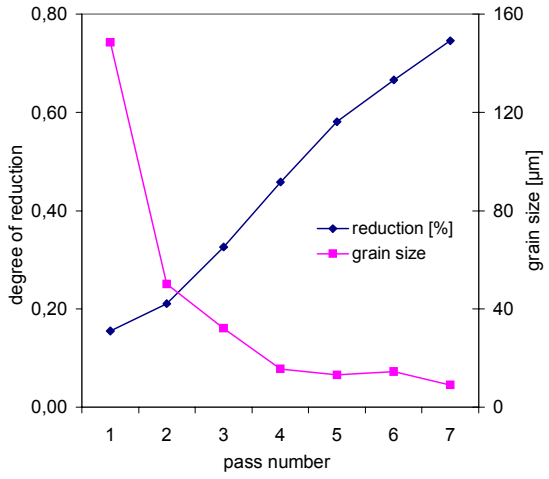


Fig. 2: Rolling strategy and grain size development

A strip casting process for casting of AZ31 magnesium strip could be developed. Strip thickness is between 8 and 12 mm, strip width is 160 mm. The microstructure development is effected by casting parameters and follows a typical temperature spread. Texture development also follows the temperature spread during solidification. Compared to conventional cast material, homogeneous microstructure with a finer grain size and finer segregations allows a adapted rolling strategy with a higher degree of deformation for every single rolling pass.

References

1 L. Wondraczek
Untersuchungen zur Herstellung von Magnesiumbändern mit dem DSC-Verfahren
Promotionsschrift Technische Universität Clausthal

2 H. Palkowski, L. Wondraczek
Direct Strip Casting of Magnesium
Zeitschrift für Metallkunde 95 (2004), 1080-1086.

GKSS FORSCHUNGSZENTRUM in der HELMHOLTZ-GEMEINSCHAFT	**EXPERIMENTAL REPORT**	**GeNF TEX-2**

Title Equal Channel Angular Pressing of Mg and Mg Alloys

Proposer:	**Prof. Y. Estrin**[1], [1]IWW, TU Clausthal
Co-Proposers:	**Prof. H.S. Kim**[2], [2]Chungnam National University, Korea
Experimental Team:	**S.B. Yi**[1,3], **B. Schwebke**[1,3], [3]GKSS
User Group Leader:	**Prof. H.-G. Brokmeier**[1,3]
Date(s) of Experiment:	31.8. – 5.9.2004

Objectives

The present study was part of a larger program of employing equal channel angular pressing (ECAP) as a processing method of severe plastic deformation for grain refinement [1-5] and investigating the microstructural features and the mechanical properties of the ECAP-processed Mg and Mg alloys. The main target of this study was an investigation of the deformation texture development with the number of ECAP passes. This was done using the neutron diffraction facilities at GKSS.

Experiment

ECAP was carried out on Mg and an AZ31 Mg alloy (10x10x65 mm^3) using a preheated (200° C) SKD 61 die with channel angle of 90°, corner angle of 20°, and ram speed of 2 mm/s (Fig. 1). A MoS_2 lubricant was used. Repetitive pressing was performed up to 1, 2, 4 and 8 passes, equivalent to a strain of about 1, 2, 4 and 8, by rotating each sample about the longitudinal axis by 90° in the same direction between consecutive passes (route B_C). Texture analysis was used as a means of relating the role of microstructure and texture evolution in the variation of the mechanical properties. Deformation texture was measured using neutron diffraction (TEX-2) for (10.0), (00.2), (10.1) and (11.0) pole figures.

Microstructures analysis was done using standard light and electron microscopy techniques. The mechanical properties were determined using Vickers hardness measurements as well as compressive and tensile testing.



Fig. 1 ECAP die. Left: the actual experimental rig used; right: schematics of the process.

HCP metals such as Mg and Ti are known to develop a simple $\langle 10\bar{1}0 \rangle$ fiber texture that is parallel to axial direction after axisymmetric deformation, such as wire drawing or extrusion at low temperature. In Mg, the basal plane rotates until it contains the wire axis, which tends to coincide with the $\langle 10\bar{1}0 \rangle$ direction in the basal plane. Rolling tends to rotate the slip plane of HCP metals into the plane of the rolled sheet and the predominant textures are {0001} $\langle 11\bar{2}0 \rangle$ or {0001} $\langle 10\bar{1}0 \rangle$ Therefore, for the rolled and extruded materials slip on the basal

plane is inhibited. Strength is known to increase for HCP metals with limited non-basal slip activity. In the case of FCC or BCC metals, pole figures are symmetric with respect to the middle point, while for HCP metals, asymmetric pole figures are observed, owing to the limited number of active slip or twinning systems [5]. Interestingly, as seen in Fig. 2, asymmetric (twisted) deformed geometry of the specimens was observed as a result of ECAP deformation of AZ31, and this phenomenon – not observed for FCC or BCC materials - is believed to be associated with anisotropy in mechanical properties resulting from texture. It was found that the sample reached final state (saturated) texture, (100)//shear direction, after just two ECAP passes. Consequently, AZ31 sample showed anisotropic deformation flow during subsequent ECAP processing. The fact that asymmetry of the specimen cross-section continued to accumulate beyond the second ECAP pass, when texture had saturated, suggests that some further factors may be responsible for this behaviour.

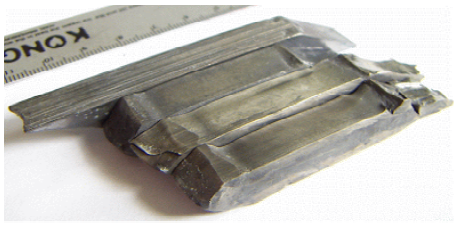


Fig. 2 Deformed AZ31 samples after ECAP (from upper left: 1, 2, 4 and 8 passes).

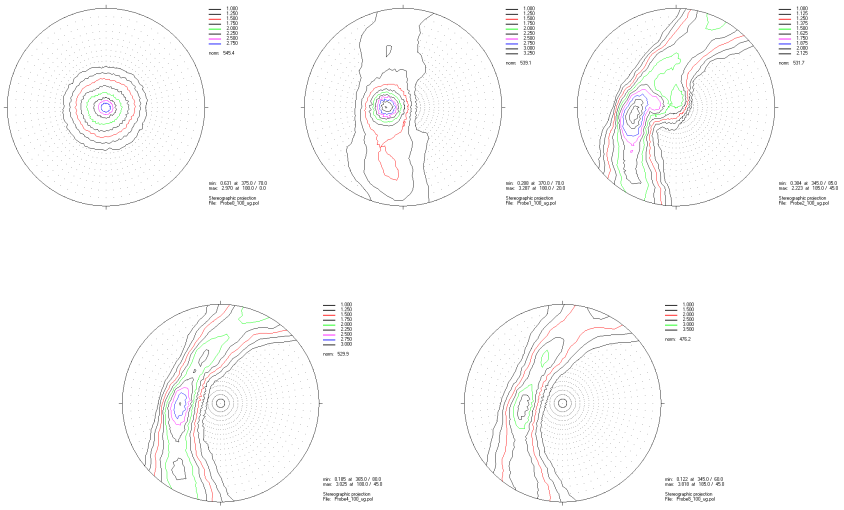


Fig . 3. Texture of AZ31 Mg alloy for different numbers of ECAP passes as seen in (10.0) pole figures. The initial figure refers to the number of passes, *viz.* 1, 2, 4, 8.

Achievements and Main Results

In this experiment, technical purity Mg and a Mg alloy were processed by 1-8 ECAP passes (Route B_c) and characterized with respect to specimen geometry, microstructure, mechanical properties and texture, the focus being on texture measurements by neutron diffraction. A particularly striking result is a twisted shape of the ECAP workpieces, which was found to be associated with anisotropy introduced by texture development.

References

[1] R.Z. Valiev, R.K. Islamgaliev and I.V. Alexandrov: Prog. Mater. Sci. 45 (2000) 103.
[2] H.S. Kim, S.I. Hong and M.H. Seo: J. Mater. Res. 16 (2001) 856.
[3] T. Mukai, M. Yamanoi, H. Watanabe and K. Higashi: Scripta Mater.45 (2001) 89.
[4] A. Yamashita, Z. Horita, T.G. Langdon: Mater. Sci. Eng. 300A (2001) 142.
[5] S.R. Agnew, J.Z. Horton, T.M. Lillo and D.W. Brown: Scripta Mater. 50 (2004) 377.

GKSS FORSCHUNGSZENTRUM in der HELMHOLTZ-GEMEINSCHAFT	**EXPERIMENTAL REPORT**	**GeNF TEX-2**

Tectonic fabric in "undeformed" clays: comparison between AMS and neutron diffractometry data

Proposer:	**Massimo Mattei**[1], [1] Università Roma TRE, Dipart. di Scienze Geologiche
Co-Proposers:	**Francesca Cifelli**[1], [1] Università Roma TRE, Dipart. di Scienze Geologiche
Experimental Team:	**S.B. Yi**[2,3], **B. Schwebke**[2,3], [2]IWW, TU Clausthal, [3]GKSS
User Group Leader:	**H.-G. Brokmeier**[2,3]
Date(s) of Experiment:	8.9. – 20. 9.2004

Objetives

The purpose of this research is to try an integrated approach of magnetic and mineral fabric investigations in order to detect grain scale and regional deformation pattern in weakly deformed extensional basins, where macroscopic evidence of deformation is often not visible.

Neutron diffraction analysis, using TEX-2, was employed in order to determine the crystallographic preferred orientation of clays forming minerals causing the magnetic fabric. In fact, neutron texture analysis represents a unique tool for mineral fabric investigation in clays. The high penetration of neutron beam makes this method particularly suitable in detecting the mineral fabric in such sediments whose original mineral texture may be easily modified by specimen cutting and polishing.

Experiment

Due to the large availability of different-shaped specimens holders of the TEX-2, measurements can be done on the standard paleomagnetic cylinder. As a consequence, specimen preparation is not necessary, avoiding possible artifact texture arising from cutting and polishing. Moreover, the texture can be compared directly to the AMS (anisotropy of magnetic susceptibility) fabric.

Previous X-ray diffraction scans identified chlorite as the principal iron-bearing mineral in studied sediments. The density distributions of the chlorite c-axes (perpendicular to basal plane) obtained by TEX-2 measurements are presented as contoured plots.

Achievements and Main Results

The orientation distributions of the poles to the chlorite basal planes were evaluated by the means of the multiples of random distribution (m.r.d.) values (Fig. 11). The observed phyllosilicate fabric is well defined in most of the specimens. The basal planes of chlorite (orthogonal to the c-axis) describe a well-defined mineralogical foliation, sub-parallel to the bedding plane. In some cases, the c-axes of the phyllosilicate grains tend to show a girdle distribution around the bedding plane sometimes with several maxima implying kinking of the phyllosilicate basal planes. This spatial configuration imaged by AMS and neutron pole figure measurements, reflects basin scale deformation processes. The integrated approach of magnetic and mineral fabric investigations may therefore represent a valid tool to study strain mechanism on the grain scale and regional deformation pattern in weakly deformed extensional basins, even if macroscopic evidence is not visible in field observations.

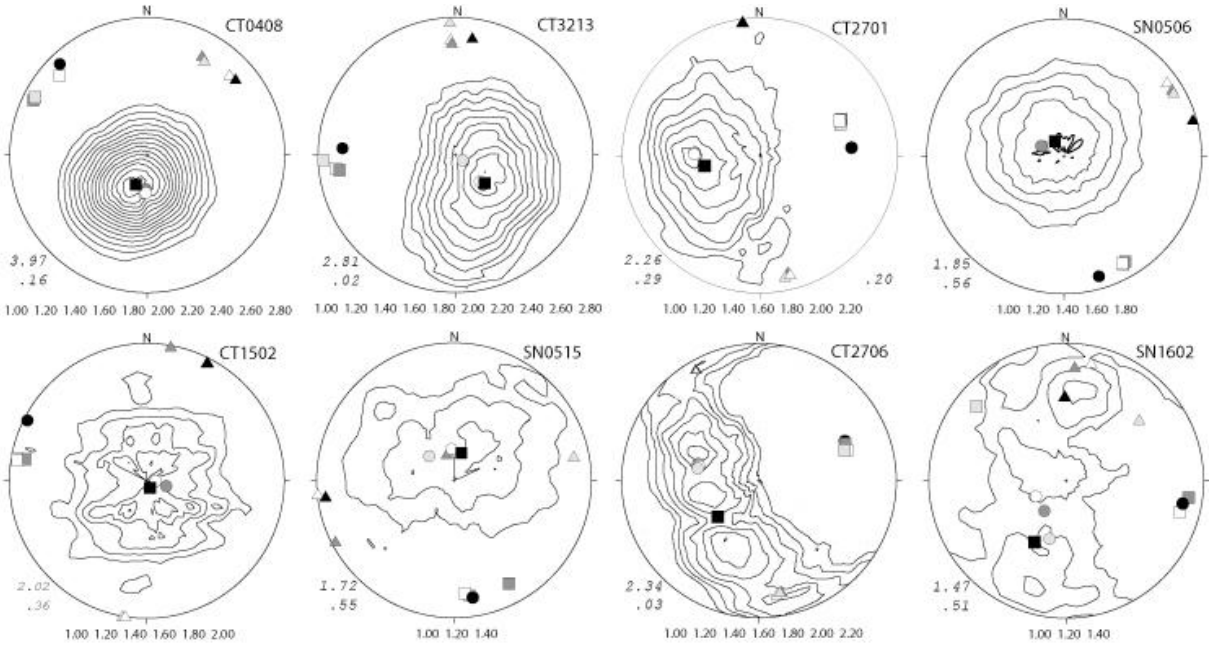


Fig. 1. Pole figures of chlorite basal planes of some representative samples measured by Tex-2. Plots are contoured in multiples of random distribution (m.r.d.) with contour interval of 0.2 m.r.d., above 1 m.r.d. Maximum and minimum m.r.d. values are expressed in the lower left of each plot. The principal directions of the orientation tensor, HFP (high-field paramagnetic), AMS at low temperature and AMS at room temperature tensors are represented with black, dark gray, light gray, and white symbols, respectively. Squares, triangles, and circles represent the maximum, intermediate and minimum directions, respectively. Data are shown on equal-area, lower hemisphere projections plotted in geographical coordinate system.

GKSS FORSCHUNGSZENTRUM in der HELMHOLTZ-GEMEINSCHAFT	**EXPERIMENTAL REPORT**	**GeNF TEX-2**

FATIGUE PERFORMANCE OF METASTABLE BETA TITANIUM ALLOYS: EFFECTS OF MICROSTRUCTURE AND SURFACE FINISH

Proposer:	**Lothar Wagner**, Institute of Materials Science and Engineering, Clausthal University of Technology, Germany
Co-Proposers:	**Marcin Kocan,** Institute of Materials Science and Engineering, Clausthal University of Technology, Germany
	Henry Rack, School of Materials Science and Engineering, Clemson University, USA
Experimental Team:	**Heinz-Günter Brokmeier, Sangbong Yi,** Institute of Materials Science and Engineering, Clausthal University of Technology, Germany
User Group Leader:	**H.-G. Brokmeier**
Date(s) of Experiment:	16. – 22. November 2004

Objetives

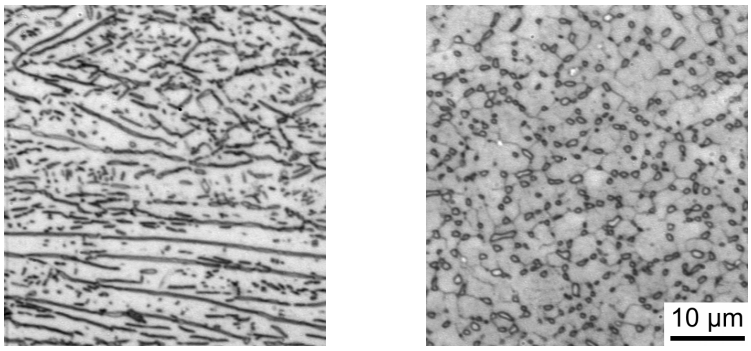
Metastable beta-titanium alloys because of their high specific strengths, low elastic moduli and high corrosion resistance are presently being considered as candidates for suspension spring materials. This investigation is aimed at optimizing the microstructure of TIMETAL LCB (Ti-6.8Mo-4.5Fe-1.5Al), one of prime candidates for suspension spring application.

Experiment

Metastable beta-titanium alloys because of their high specific strengths, low elastic moduli and high corrosion resistance are presently being considered as candidates for suspension spring materials. Indeed, it has been proposed that substitution of these alloys for conventional steel springs will result in a weight reduction of approximately 40%. Furthermore, this substitution will eliminate the need to include a corrosion resistant coating as presently required for steel springs. This investigation is aimed at optimizing the microstructure of TIMETAL LCB (Ti-6.8Mo-4.5Fe-1.5Al), one of prime candidates for suspension spring application. Various methods for altering the microstructure and mechanical behavior of this alloy have been explored.

The alloy examined in this investigation was received from TIMET, Henderson, NV (USA) as 14.3 mm diameter round rod. Its chemical composition as determined by TIMET was (wt.%): 4.5 Fe, 6.6 Mo, 1.5 Al, 0.142 O, balance Ti. Two processing procedures were examined. The first involved aging of the solution treated alloy for various times and temperatures between 450 and 650°C with and without prior tensile pre-straining. The second involved resolution heat-treatment and swaging at 760°C to a 50% reduction of cross-section followed by a recrystallization anneal at 760°C for 30 minutes. This recrystallized material was aged under conditions similar to that of the original solution-treated material, again with and without tensile pre-straining.

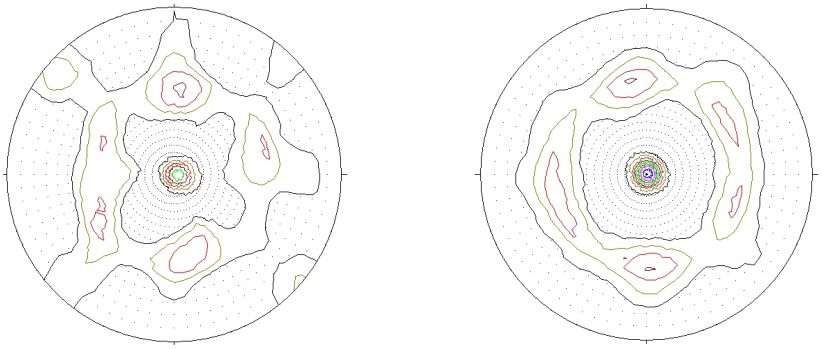
The microstructures of the original solution treated (AR) and recrystallized (RX) conditions are illustrated in Figure 1. Figure 1a shows that the primary alpha grains (dark) that surround the beta grains (light) were elongated in the longitudinal direction of the rods, this direction corresponding to the flow direction of the prior working. In contrast, swaging plus solution heat treatment (RX), Figure 1c, resulted in a fine equiaxed beta grain structure with almost complete spheroidization of the primary alpha phase.



a) AR (L →) b) RX (L →)

Figure 1: Microstructures of LCB material

To characterize crystallographic textures of examined conditions pole fiures were measured by means of neutron diffraction. (110)-pole figures are shown in Figure 2.



a) AR (L →) Pmax= 1.8 mrd b) RX (L →) Pmax = 2.8 mrd

Figure 2: (110)-pole figures of beta phase of LCB material

Two texture components can be seen in (110)-pole figures. Swaging followed by recrystallization treatment resulted in sharpness increase of the first texture-component (maximal intensity from 1.7mrd to 2.8 mrd). Second component seems to remain unchanged with maximal intensity of about 1.5 mrd.

Achievements and Main Results

Hot swaging followed by subtransus solution anneal resulted in a fine equiaxed beta and spheroidized primary alpha microstructure in LCB. Compared to the as-received microstructure consisting of elongated beta grains and a semi-continuous grain boundary alpha layer, this microstructure was superior with regard to yield stress, true fracture strain and HCF strength.

Only slight change of the crystallographic texture was noted. Influence of the crystallographic texture on the mechanical properties (esp. fatigue performance) of TIMETAL LCB will be studied in the future.

References

[1] M. Kocan, T. Ludian, M. Ishii, H. J. Rack, L. Wagner, “Optimization of Microstructure of TIMETAL LCB for Application as Suspension Springs”, Light Materials for Transportation Systems (W. E. Frazier, Y. D. Han, N. J. Kim and E. W. Lee, eds.) CAAM (2004) 417

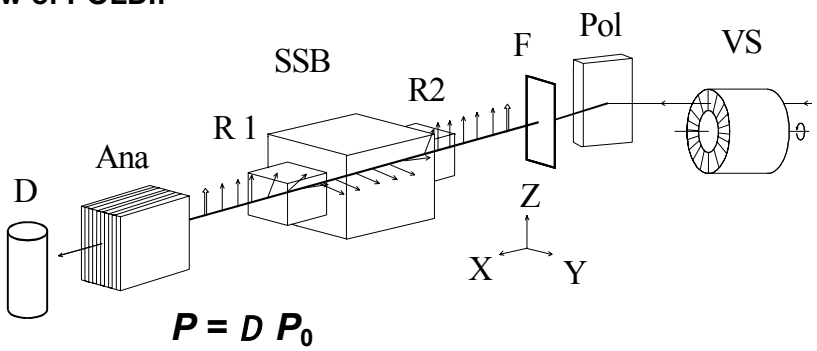
[2] M. Kocan, H.J. Rack, L. Wagner, “Fatigue performance of metastable beta titanium alloys: effects of microstructure and surface finish”, Beta Titanium Alloys of the 00's (R. R. Boyer, R. F. Denkenberger, J. Fanning and H. J. Rack, eds.) TMS (in press)

GKSS FORSCHUNGSZENTRUM in der HELMHOLTZ-GEMEINSCHAFT	EXPERIMENTAL REPORT	GeNF POLDI
Polarised diffractometer POLDI		

Short Instrument Description:
With the polarised diffractometer 3-D depolarisation analysis is used to investigate magnetic properties and correlations in magnetic materials. With minor modifications a time of flight option in non-polarised mode is additionally available for the purpose of dosemeter calibration.

Local Contact:
Dr. Dieter Lott
Phone/Fax : +49 (0)4152 87 – 1372 / +49 (0)4152 87 – 1338
e-mail: dieter.lott@gkss.de

Schematic View of POLDI:



Set-up for full 3-dimensional neutron depolarisation analysis in the transmitted beam

Instrument Details:

Location at FRG-1:	beamline 7, thermal neutrons cross section 10 x 4 cm^2,
Polariser / monochromator (Pol)	Cu_2MnA (111), PG(002), Si (311) doubly focussing; helical slot selector (VS)
Take-off-angle:	$10° < 2\,\Theta_M < 65°$
Wavelength:	λ = 0.1 to 0.36 nm, 2^{nd} order suppression by velocity selector (VS)
Flux at sample position:	$\Phi_{max} = 0.8 \cdot 10^5$ cm^{-2} s^{-1} (polarised)
Analyser (Ana):	Co/Ti-supermirror
Overall polarisation:	0.94
3D depolarisation analysis in transmitted beam:	accuracy < 1% for any component of ***D***
Sample environment fitting in the magnetically shielded sample box (SSB) for 3D depolarisation analysis:	- refrigerator T >12 K, - DC magnetic field < 160 A/cm - pulsed field < 8.0 kA/cm
Detector (D):	^{3}He-counter
Instrument control / data acquisition:	remote internet PC control IEEE bus, serial bus and special interfaces

GKSS FORSCHUNGSZENTRUM in der HELMHOLTZ-GEMEINSCHAFT	EXPERIMENTAL REPORT	GeNF Poldi

Thermal Neutron Imaging with ^{6}Li-foil converters coupled to Gas Electron Multipliers (GEMs)

Proposer:	**Volker Dangendorf,** [1] PTB Braunschweig
Co-Proposers:	**Hans Friedrich**[1]**,**
Experimental Team:	**Volker Dangendorf**[1]**, Hans Friedrich**[1]**,** **Frank Kaufmann**[1]**, Adalbert Reiske**[1]**,** **Kai Tittelmeier**[1]**,** **Jürgen Vollbrandt**, [2] GKSS-Forschungszentrum, Geesthacht
User Group Leader:	**Volker Dangendorf**
Date(s) of Experiment:	23.Feb. – 1. Mar 2004

In recent years we have investigated position sensitive detectors for thermal neutrons based on solid neutron converters and low-pressure gaseous amplification devices [1,2]. While earlier work was focussed on Gd-foil converters coated with CsI as an efficient secondary electron emitter, recent interest shifted to the development of durable metallic ^{6}Li neutron converters for gaseous imaging detectors.

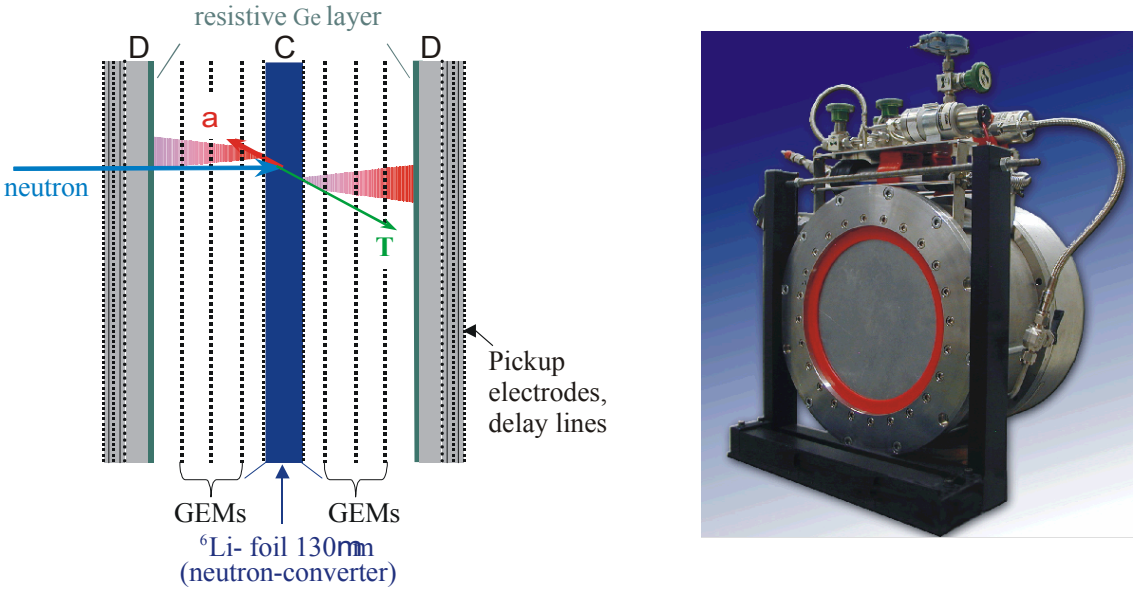


Fig.1: Schematic view and photo of the thermal neutron detector

In 2003 a new detector was developed, consisting of a ^{6}Li neutron converter foil and a triple GEM (Gas Electron Multiplier, [3]) readout device. Fig. 1 shows the principle of the detector. Charged particles from a neutron interaction in the converter foil can escape into the gas volume near the cathode of the first GEM. Ionisation electrons are effectively amplified by 3 cascaded GEMS and the final charge is collected on a resistive anode. The neutron is localised by a galvanic isolated electrode behind the anode using a delayline readout.

In comparison to the earlier low-pressure wire-chamber (MWPC) the present detector has the advantage of being of rugged design, the GEMs can be made with standard industrial methods and the detector is operated at atmospheric pressure with stationary gas filling. Operation of the detector is also much simpler because the first stage of the GEM detector is operated in ionisation chamber mode, while the previous MWPC based detectors were equipped with a preamplification stage for active collimation, which is delicate to operate. The expected disadvantage of the present detector is a somewhat inferior position resolution due to the geometrical spread of the ionisation electrons in the gas volume close to the neutron converter. The investigation of the position resolution was the goal of the experiment at Poldi in February 2004. The prototype detector investigated in this experiment consists of a single sided electron amplifier behind a ^{6}Li converter of 10 by 10 cm sensitive area.

Fig. 2. shows images of a 0,1 mm slit for several positions of the detector which was moved in 10 mm steps by a precision-controlled linear movement table. The projected width of a slit segment is shown in fig 3, from which the position resolution Δx was determined to be Δx_{fwhm}= 0,81 mm. As expected, this is inferior to the earlier values of 0,4 mm [1] obtained with Li converters and MWPC readouts, but it seems acceptable because of the advantages of the detector mentioned above.

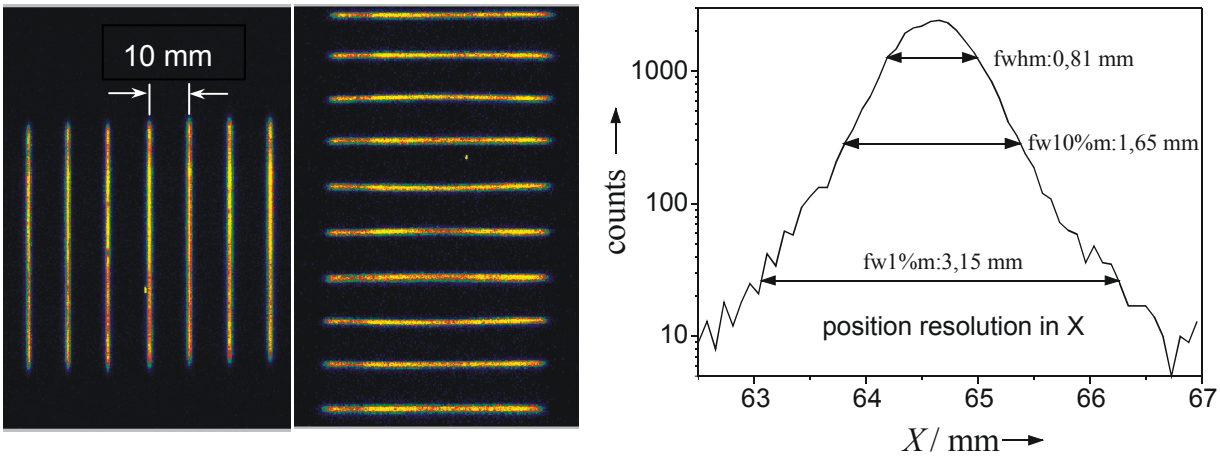


Fig. 2.: Image of 0,1 mm slits in 10 mm distance and projection of a slit segment to measure the position resolution of the detector.

References:

1. V. Dangendorf, A. Demian, H. Friedrich, V. Wagner, A. Breskin, R. Chechik, S. Gibrekhterman, A. Akkerman; *Thermal neutron imaging detectors combining novel composite foil convertors and gaseous electron multipliers* Nucl. Inst. Meth. A350 (1994) 503-510
2. A. Bäuning-Demian, H. Schmidt-Böcking, V. Dangendorf, H. Friedrich, A. Breskin, R. Chechik, A. Gibrekhterman; *Detection efficiency study of an imaging detector for low energy neutrons.* Proc. SPIE, Vol 2867 (1996) 562-565
3. F. Sauli, "*GEM: A New Concept for Electron Amplification in Gas Detectors*", Nucl. Instrum. Meth. A386 pp. 531, 1997

GKSS FORSCHUNGSZENTRUM in der HELMHOLTZ-GEMEINSCHAFT	**EXPERIMENTAL REPORT**	**GeNF POLDI**

Neutron imaging with a Micromegas detector

Proposer:	**Fabien Jeanneau**[1] [1]DRT/DeTeCS, CEA Saclay, Gif/Yvette, France
Experimental Team:	**V. Dangendorf**[2]**, H. Friedrich**[2]**, F. Jeanneau**[1]**, J. Pancin**[3]**, M. Voytchev**[1] [2]PTB, Braunschweig, Germany [3]DSM/DAPNIA, CEA Saclay, Gif/Yvette, France
Date(s) of Experiment:	February 2004

Objectives

Micromegas (MICRO-MEsh GAseous Structure) is a double-stage parallel-plate gaseous detector developed since 1996 at CEA Saclay and initially designed as a precision tracker for high-energy particle beams. Using a neutron converter (6Li, 6LiF and 10B) at its entrance, this device can operate as a thermal neutron detector applied for imaging purposes.

A tomography was carried out with a one-dimensional prototype, and it explains the needs for a good neutrons beam in terms of divergence. A two-dimensional neutron imaging study was also performed with a new 2D micro-pattern readout.

Detection principle

When charged particles travel through the gas, electrons are produced between the drift electrode and the micromesh by ionization process and drift towards the micromesh under the action of the electric field (~1 kV/cm) applied in the conversion gap (0.7 mm). After the micromesh, they are multiplied in the narrow amplification gap (50 or 100 µm) – see figure 1 – and the subsequent electron avalanche induces a current on the anode strips.

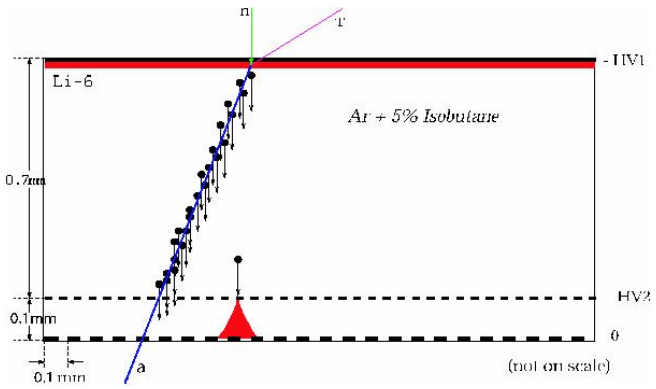


Fig. 1. Micromegas principle for neutron detection.

However, a neutron/charged particle converter is necessary to produce ionization. The conversion reactions used are neutron capture on ^{6}Li (or ^{6}LiF) and ^{10}B (respectively with cross section of 940 and 3840 barns), deposited on the drift electrode:

$$^{6}_{3}Li + n \rightarrow {}^{4}_{2}He(2.05MeV) + {}^{3}_{1}H(2.73MeV) \qquad Q = 4.78 \text{ MeV}$$

$$^{10}_{5}B + n \rightarrow ^{4}_{2}He(1.47MeV) + ^{7}_{3}Li(0.83MeV) \qquad Q = 2.7 \text{ MeV}$$

The 384 strips are readout by 4 GASSIPLEX electronics cards, each card multiplexing 96 channels . This electronics is controlled by a VME standard acquisition system and a pedestal subtraction is applied before storing the data, allowing a maximum acquisition rate about 2.4 kHz. After data analysis, the barycentre of each event is determined and after selections on different parameters (charge, cluster size, multiplicity, …), the spatial resolution – thus the reconstructed image – can be improved.

Results

A tomography section has been performed with a one-dimensional detector in a thermal neutron flux of 8.104 n.cm-2.s-1 at the POLDI facility. The setup is represented in figure 2 and the tomographic reconstruction is given in figure 3. Some details of the multi-wire cable are distinct but some defects are induced by the pillars which support the mesh.

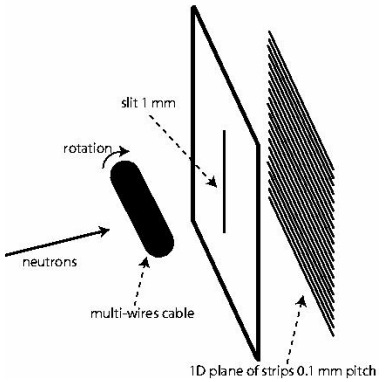


Fig. 2. Schematic view of the tomographic setup (not on scale)

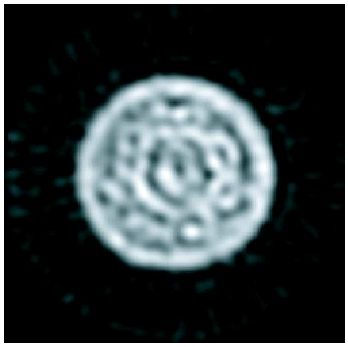


Fig. 3. Tomography of a multi-wire cable

A prototype built with the same detection principle but with a two-dimensional readout has been also tested by performing the image of holes in a Cd foil in order to determine the spatial resolution. Figure 4 represents a hole profile fitted by the convolution of a step function and a Gaussian distribution. The Gaussian standard deviation gives a spatial resolution of 166 µm. An image of letters etched in 100 µm thick Gd foil has also been carried out and is represented on figure 5.

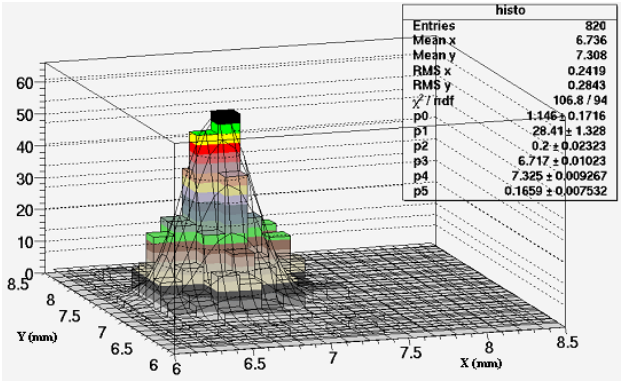


Fig. 4. Profile of a hole (2D spatial resolution σ=166 µm)

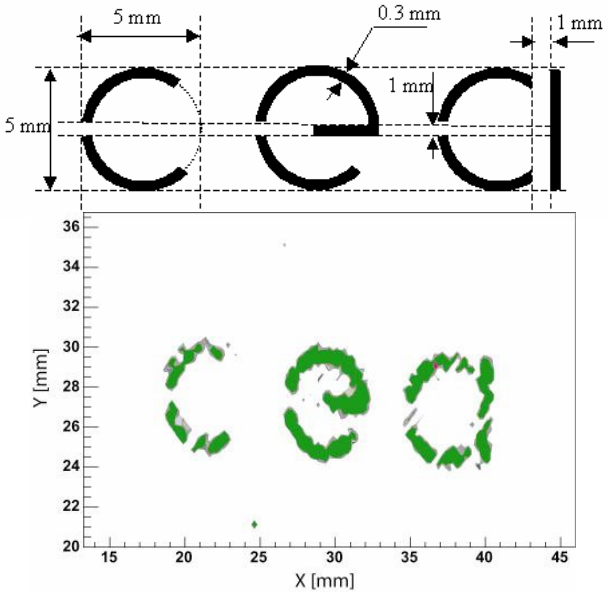


Fig. 5. Scheme of the gadolinium foil (100 µm) etching and image obtained with the detector.

GKSS FORSCHUNGSZENTRUM in der HELMHOLTZ-GEMEINSCHAFT	**EXPERIMENTAL REPORT**	**GeNF POLDI**

Determination of personal dosemeter responses within the EC project EVIDOS

Proposer:	**Marlies Luszik-Bhadra,** PTB, Braunschweig, Germany
Co-Proposers:	**Reinhard Böttger, Hans Friedrich, Marcel Reginatto,** PTB Braunschweig **Francesco d'Errico**, DIMNP Italy **Quang Chau, Thierry Lahye**, IRSN France **Annette Fiechtner**, PSI Switzerland **Rick Tanner**, NRPB UK **Filip Vanhavere**, SCK-CEN Belgium
Experimental Team:	**Marlies Luszik-Bhadra, Reinhard Böttger, Sebastian Fässer, Stefan Löb, Adalbert Reiske,** PTB, Braunschweig
User Group Leader:	**Reinhard Böttger,** PTB, Braunschweig
Date(s) of Experiment:	April 2003, December 2003, April 2004, November 2004

Objectives

Within its 5th Framework Programme, the EC is funding the project EVIDOS ("Evaluation of Individual Dosimetry in Mixed Neutron and Photon Radiation Fields", Contract No FIKR-CT-2001-00175). A series of measurements with spectrometers and dosemeters are being made in selected workplace fields in nuclear installations throughout Europe. Dosemeters – especially new electronic devices – are being tested in these fields by comparing their readings to reference values of personal dose equivalent determined by spectrometers, and over- and underreadings are being interpreted in relation to their responses as a function of neutron energy. Data at thermal energies were determined at GeNF.

Experiment

The PTB thermal neutron reference field at GeNF, which has a well characterized and monitored fluence and energy distribution[1], has been used. The dosemeters were irradiated uniformly on a special ISO slab phantom (30 cm x 30 cm x 15 cm) by means of a scanning machine. For a field size of 30 cm x 30 cm, the fluence rate obtained at full beam intensity was about 10^3 cm^{-2} s^{-1}.

A simple evaluation of the personal dose equivalent response was done by dividing the reading of the dosemeters by the corresponding personal dose equivalent. The latter value was obtained by folding the fluence spectral distribution with the respective energy dependent fluence-to-dose conversion coefficients as given by the International Commission on Radiological Protection (ICRP). For the GKSS spectrum (close to Maxwellian distribution, peaked at about 25 meV, mean fluence weighted energy 45 meV), a mean conversion factor (11.6 ± 0.2) pSv cm^2 was obtained. In this way, a mean response in the quasi-mono-energetic field was determined.

A more complex evaluation aims at determining the neutron energy response in the thermal and intermediate regions. Since no mono-energetic reference fields are available in these regions, measurements in fields with broad energy distribution (GKSS thermal beam, radionuclide sources) with known spectral distributions and in mono-energetic fields in the region from 24 keV to 15 MeV were combined and the response determined using Bayesian data analysis methods.

Achievements and Main Results

Table 1 shows some results obtained with various types of DIS-N dosemeters by A. Fiechtner et al.[2] This dosemeter is still under development. Within the EVIDOS project, four dosemeter types with different converters and shieldings – as indicated in the table heading - are being used. The personal dose equivalent responses show particularly large variations at thermal neutron energies (indicated as 2.53E-08 MeV).

Table 1: $H_p(10)$ response of four different dosemeter types, normalized to ^{241}Am-Be.

Neutron Energy / MeV Neutron Source Field Spectra	PE (4% $LiNO_3$)	PE (4% $LiNO_3$) (1 mm B_4C)	A-150 (1.25% BN)	A-150 (1.25% BN) (2 mm B_4C)
2.53E-08	12	1.00	50	2.3
0.070	0.45	0.17	1.75	0.14
0.144	0.26	0.14	0.74	0.19
0.565	0.48	0.36	0.63	0.47
14.8	0.78	0.78	0.75	0.76
^{252}Cf (D_2O)	0.92	0.70	2.2	0.97
^{252}Cf (D_2O), Cd	0.89	0.71	1.6	0.85
^{252}Cf	0.88	0.70	0.90	0.83
AmBe	1.00	1.00	1.00	1.00
Sigma (IRSN)	5.0	1.2	25	1.3
Canel (IRSN)	2.5	0.54	7.9	0.64

Results of full energy responses were presented at the 11th International Congress of the International Radiation Protection Association in Madrid by M. Reginatto et al.[3]. The data analysis was done with a Bayesian parameter estimation program written specifically for this purpose using the software package WinBUGS. Personal dose equivalent responses were determined for the commercially available dosemeters ALOKA PDM-313, Thermo Electron EPD-N2 and Saphydose-n and the laboratory prototypes PSI DIS-N (4% $LiNO_3$, 1 mm B_4C), PTB DOS-2002 and DIMNP HpSLAB. The final results will be published at the “European workshop on individual monitoring of ionizing radiation” in Vienna (2005).

References

1) R. Böttger, H. Friedrich, H. Janßen. THE PTB THERMAL NEUTRON REFERENCE FIELD AT GENF. PTB report PTB-N-47 (2004).
2) A. Fiechtner, M. Boschung and C. Wernli. PRESENT STATUS OF THE PERSONAL NEUTRON DOSEMETER BASED ON DIRECT ION STORAGE. Radiat. Prot. Dosim. 110, 213-217 (2004).
3) M. Reginatto, R. Böttger, F. d’Errico, A. Fiechtner, H. Friedrich, V. Lacoste, T. Lahaye, M. Luszik-Bhadra and F. Vanhavere. DOSE EQUIVALENT RESPONSE OF NEUTRON DOSEMETERS USING UNFOLDING METHODS. Contribution to IRPA 11, 23-28. May 2004, Madrid, Spain.

GKSS FORSCHUNGSZENTRUM in der HELMHOLTZ-GEMEINSCHAFT	**EXPERIMENTAL REPORT**	**GeNF POLDI**
Neutron diffraction study on EuSe		
Principal Proposer:	**M. Bode,[2] D. Lott[1], A. Schreyer[1]** [1] GKSS Forschungszentrum GmbH,Institut for Material Science, [2] Institut für Angewandte Physik, Universität Hamburg, Jungiusstr. 11, 20355 Hamburg, GERMANY	
Experimental Team: **User group leader:**	**D. Lott[1], S. Krause, [2] T. Hänke, [2] V. Wagner[3], S. Braun[3]** [3] PTB, Braunschweig, Germany **D. Lott[1]**	
Date(s) of Experiment:	April 2004	

Introduction

Since the discovery of an incommensurate spin density wave (I-SDW) in 1959 [1], the complex magnetic structure of Cr raised a lot of interest, mainly arising from its role in exchange-coupled Fe/Cr bilayers and superlattices [2,3], which feature interesting magnetic effects such as giant magneto-resistance [4,5]. Proximity effects of Cr with ferromagnetic layers, thin Cr films, and the Cr surface itself were intensively studied [6]. Nevertheless, it is still an open question how the magnetic structure of the Cr(001) surface behaves when crossing the spin-flip temperature. Fig. 1 shows spin-polarized scanning tunneling microscopy (SP-STM) measurements of the Cr(001) surface taken at temperatures between room temperature (T = 200 K) and 23 K, thereby crossing the spin-flip temperature at T_{SF} = 123 K (left: topography; right: left and spin-resolved dI/dU map right). Surprisingly, the dI/dU map in Fig. 1(c) exhibits the same magnetic structure as the images (a)-(b), even though it was measured at 23K which is far below T_{SF}.

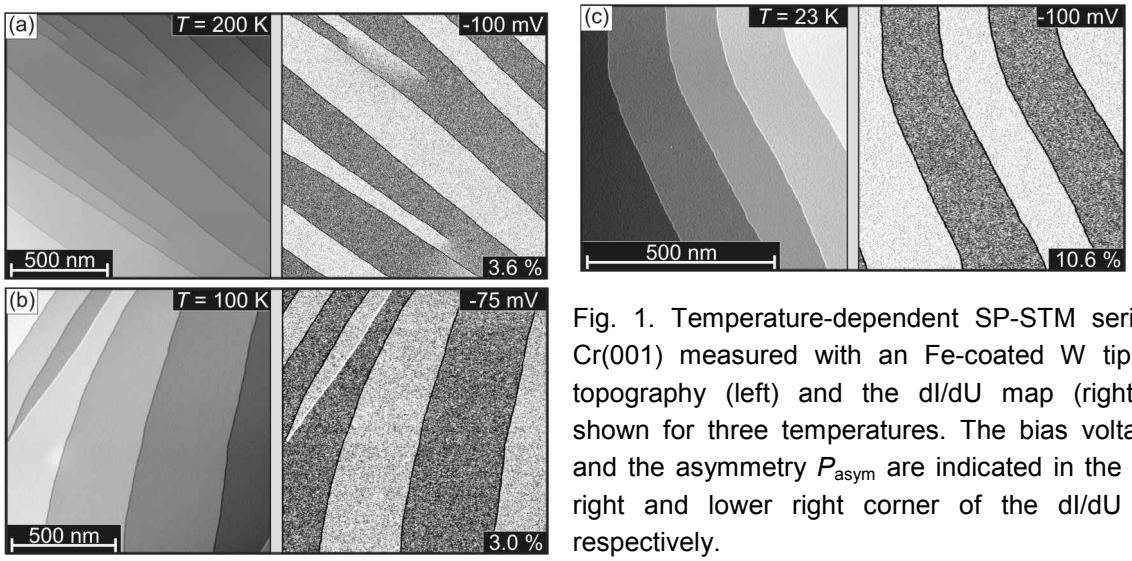


Fig. 1. Temperature-dependent SP-STM series of Cr(001) measured with an Fe-coated W tip. The topography (left) and the dI/dU map (right) are shown for three temperatures. The bias voltage *U* and the asymmetry P_{asym} are indicated in the upper right and lower right corner of the dI/dU map, respectively.

Experiment

In order to examine the SDW bulk behaviour of our Cr crystal and to identify possible stress-induced changes of T_{SF}, neutron scattering experiments were carried out at POLDI. In the case of the Cr crystal examined here mechanical strain may result from the mounting procedure. In particular, locations, where our Cr sample and the tantalum foil touch, exhibit crystalline imperfections (ripples) which are visible to the naked eye.

In the first experiments, we have illuminated the entire crystal with the neutron beam, including some of the surrounding Ta frame. The resulting scans are shown in Fig. 2(a)-(d). At 200 K, well above the spin-flip temperature T_{SF}, satellite reflections are observed along the K and L direction in the vicinity of the (010) and the (001) forbidden Bragg positions for the structural reflections, being characteristic for a transverse I-SDW as expected above T_{SF}. At 20 K, far below the spin- flip temperature, the satellites in the vicinity of the (001) position along the K direction in Fig. 2(b) and the satellites along the L direction next to the (010) position in Fig. 2(c) remain present, but the satellites in the proximity of the (001) and (010) positions along the L- and K direction, respectively, in Fig. 2(a) and (d) disappear. This is the expected behavior for a longitudinal I-SDW in the K and L direction.

Along with the satellite peaks in Fig. 2 peaks owed to magnetic scattering also appear directly at the (010) and the (001) Bragg positions. These peaks arise from magnetic scattering from a commensurate SDW (AF_0 phase). The appearance of the AF_0 phase can be attributed to the mechanical strain which is expected to be present at the crystal edges where the Ta foil presses onto the Cr surface. In order to check whether the AF_0 phase pervades the whole sample or is only restricted to the edges of the sample, the beam size of the neutron beam was confined by a Lithium plated aperture to an area of $(2\times2)mm^2$ to the center of the Cr crystal (see hatched area in the sketch of Fig. 3). Fig. 3 shows the corresponding neutron scattering scans. Qualitatively, the satellite reflections exhibit the same behavior as without an aperture, i.e., the existence of a transverse I-SDW above and a longitudinal I-SDW below T_{SF}. In contrast to the previous data taken by averaging over the entire crystal, however, the intensities of the commensurate SDW's are now dramatically reduced relative to the incommensurate satellites. Obviously, the incommensurate SDW phase is dominant in the center of the Cr crystal, the same position at which the SP-STS measurements were carried out later.

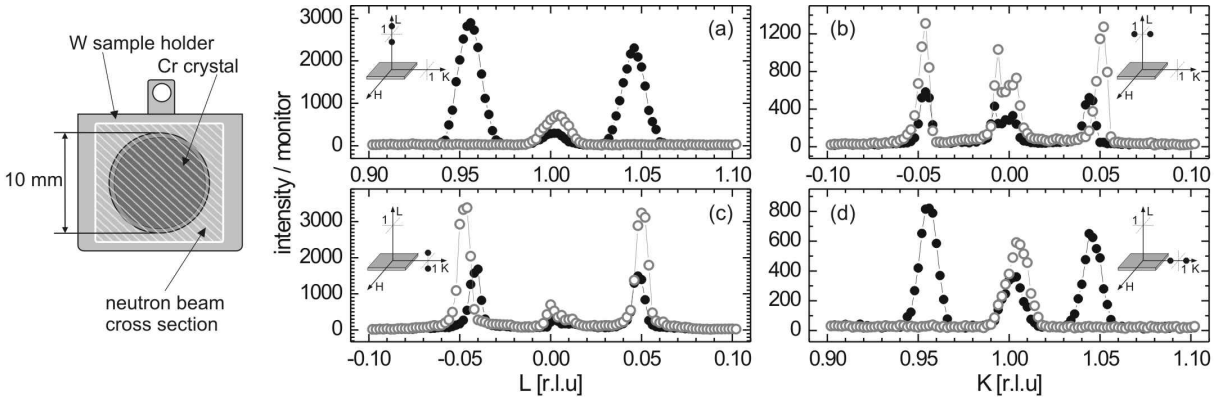


FIG. 2: Neutron scattering data of Cr(001) measured with neutrons illuminating the entire crystal (see hatched area in drawing on the left). Measurement temperatures are $T_{SF} < T = 200$ K (filled circles) and $T_{SF} > T = 20$ K (open circles) to explore the propagation directions and polarizations of the spin-density waves. The scattering geometries are sketched as insets.

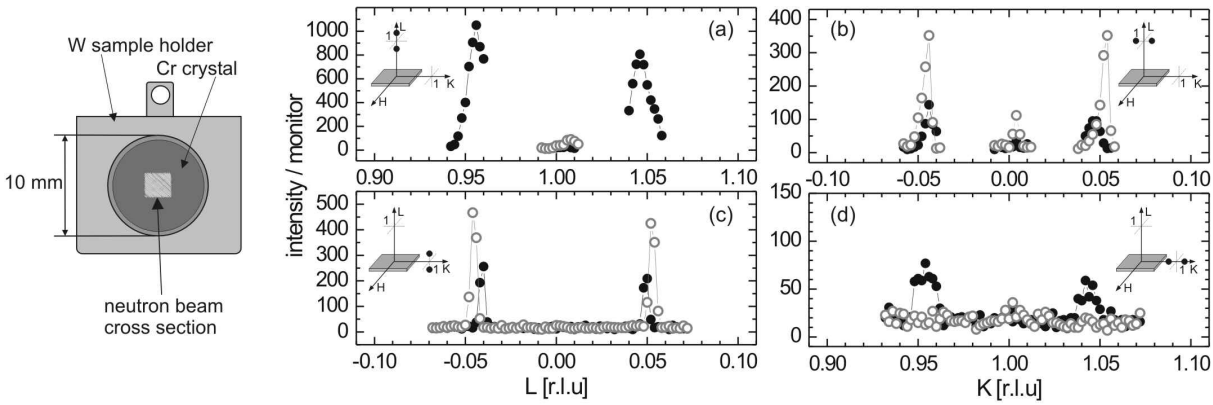


FIG. 5: Neutron scattering data of Cr(001) measured with the neutron beam confined to the central region of the Cr crystal (see hatched area in drawing on the left). Measurement temperatures are $T_{SF} < T = 200$ K (filled circles) and $T_{SF} > T = 20$ K (open circles) to explore the propagation directions and polarizations of the spin-density waves. The scattering geometries are as sketched as insets.

Conclusion

The experimental data show that the Cr(001) surface exhibits an in-plane magnetization even far below the spin-flip temperature T_{SF}. Obviously, the surface magnetic structure cannot be described appropriately by a simple continuation of the bulk SDW. Probably, the Cr surface exhibits the same magnetic structure as for $T > T_{SF}$, i.e., a T-SDW a propagation direction perpendicular to the surface plane. A continuous connection of the surface T-SDW to the L-SDW is accomplished by the formation of a 90° domain wall. The origin of the in-plane pinning of the surface magnetization may arise from a strong in-plane surface anisotropy.

References

[1] L. M. Corliss, J. M. Hastings, and R. J. Weiss, Phys. Rev. Lett. **3**, 211 (1959).

[2] P. Bödeker, A. Hucht, A. Schreyer, J. Borchers, F. Güthoff, and H. Zabel, Phys. Rev. Lett. **81**, 914 (1998).

[3] E. J. Escorcia-Aparicio, H. J. Choi, W. L. Ling, R. K. Kawakami, and Z. Q. Qiu, Phys. Rev. Lett. **81**, 2144 (1998).

[4] G. Binasch, P. Grünberg, F. Saurenbach, and W. Zinn, Phys. Rev. B **39**, 4828 (1989).

[5] M. N. Baibich, J. M. Broto, A. Fert, F. NguyenVanDau, F. Petroff, P. Eitenne, G. Creuzet, A. Friederich, and J. Chazelas, Phys. Rev. Lett. **61**, 2472 (1988).

[6] H. Zabel, J. Phys.: Condens. Matter **11**, 9303 (1999).

GKSS FORSCHUNGSZENTRUM in der HELMHOLTZ-GEMEINSCHAFT	**EXPERIMENTAL REPORT**	**GeNF POLDI**

Polarized Neutron Diffraction on a Dy/Y Superlattice

Principal Proposer:	**Andreas Schreyer[1], Dieter Lott[1]** [1]GKSS-Forschungszentrum, Geesthacht
Experimental Team:	**Dieter Lott[1], Volker Wagner[2]** [2]Physik. Tech. Bundesanstalt, 38116 Braunschweig
User group leader:	**Dieter Lott[1]**
Date(s) of Experiment:	Dezember 2004

Introduction

The first sucessful inelastic neutron scattering on an thin-film sample was performed on a Dy/Y supperlattice only a few years ago. The experiment, performed at the IN12 inelastic neutron diffractometer at the ILL in Grenoble, gave access to a wide portion of the Brilliouin zone which before had not been accessible. [1]. The layer sequence of the here investigated superlattice is $Y_{500Å}[Dy_{43Å}/Y_{28Å}]_{350}/Y_{2340Å}/Nb_{2000Å}$,prepared on an Al_2O_3 substrate by MBE methods. Below the Neél temperature of 179K, Dy exhibits a helical phase along the Dy c-axis in the Dy/Y supperlattice while the ferromagnetic structure below 89 K, present in bulk Dy, is here supressed. The objective of this experiment, performed at POLDI at the GKSS in Geesthacht, was to examine the rotational direction of the helix, i.e. to probe if any preference concerning the direction of the rotation exists.

Experiment

The magnetic structure of Dy in Dy/Y superlattices can be studied by neutron diffraction measuring around the Dy/Y(0002) Bragg reflection. Below the Neél temperature, magnetic satellites appear in the vicinity of the 0002-Peak which arise from the helimagnetical structure of the Dy, propagating through the Y spacer layer. To retrieve information about the direction of the rotation, the polarization of the scattered neutrons need to be analyzed. At the POLDI diffractometer, the incoming neutrons were polarized by a Heusler monochromator and after scattering analyzed by using a Co/Ti supermirror. The scattering amplitude for the different polarization channels can be written as

$$A(\vec{Q}) \propto \begin{cases} M_{\perp z}(\vec{Q}) & + \rightarrow + \quad NSF \\ -M_{\perp z}(\vec{Q}) & - \rightarrow - \quad NSF \\ M_{\perp x}(\vec{Q}) - iM_{\perp y}(\vec{Q}) & + \rightarrow - \quad SF \\ M_{\perp x}(\vec{Q}) + iM_{\perp y}(\vec{Q}) & - \rightarrow + \quad SF \end{cases} \tag{1}$$

with $M_{\perp i}(\vec{Q})$ as the i-th (i=x,y,z) component of magnetization with respect to the polarization vector and perpendicular to the scattering vector Q ; + and – denote the spin up and down of the polarized or analyzed neutron state, respectively, and NSF indicate the non spin flip and SF the spin flip channels, respectively. Figure 1 shows the polarization-analyzed diffraction data around the Dy/Y(0002)-peak for an incoming polarization vector P perpendicular to Q. The measurement was carried out at two temperatures, far below (at T=11.3K) and above

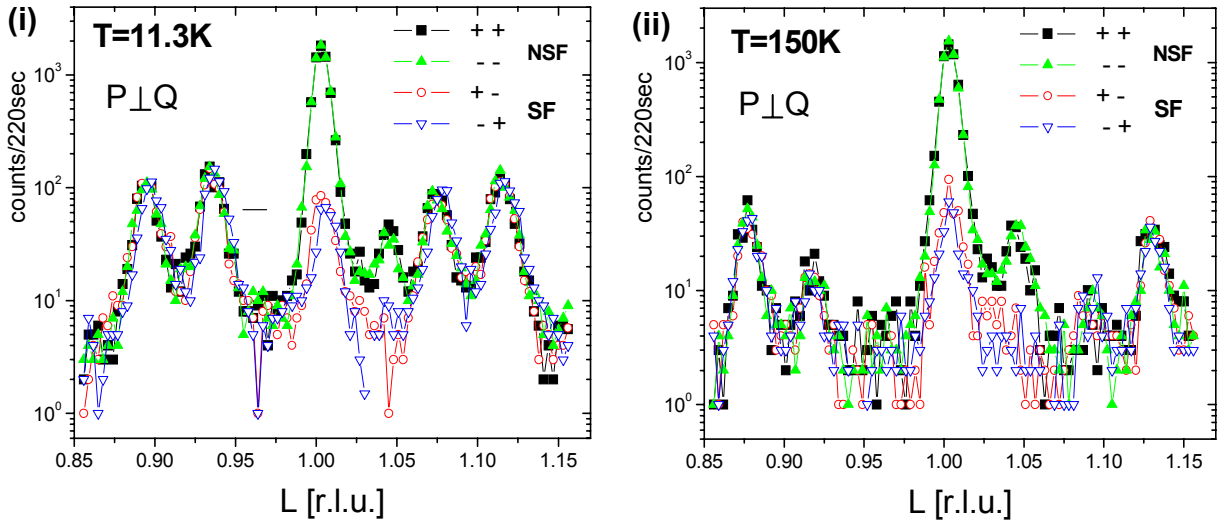


Figure 1: Polarized Neutron Diffraction around the Dy/Y(0002) superlattice peak with polarization analysis at (i) T=11.3K and at (ii) T=150K . Polarization vector of incoming neutrons is **perpendicular** to the scattering.

the Neél temperature at T=150 K. At 11.3 K, both the NSF and SF channels show coinciding distribution of the scattering intensity at the satellite reflections, indicating that both components of the in-plane magnetization are equally present, as expected for the helimagnetical phase of Dy in the Dy/Y superlattice.

By arranging the magnetic guiding fields in such a way that the polarization vector P of the incoming neutrons is parallel to the scattering vector Q at the sample position, intensity due to magnetic scattering is only expected in the SF channel. If one handiness of the magnetic spiral in the Dy/Y superlattice is preferred, the intensities for both SF channel would differ, as indicated in (1).

Figure 2 presents the four cross sections for the polarization vector parallel to the scattering vector at the temperatures T=11.3 K and T=150 K. In both cases, no difference in the intensities of the magnetic satellites can be observed in both spin flip intensities indicating that no direction of rotation preferred, i.e. that as many domains with helicities of right as with left direction coexist in the sample.

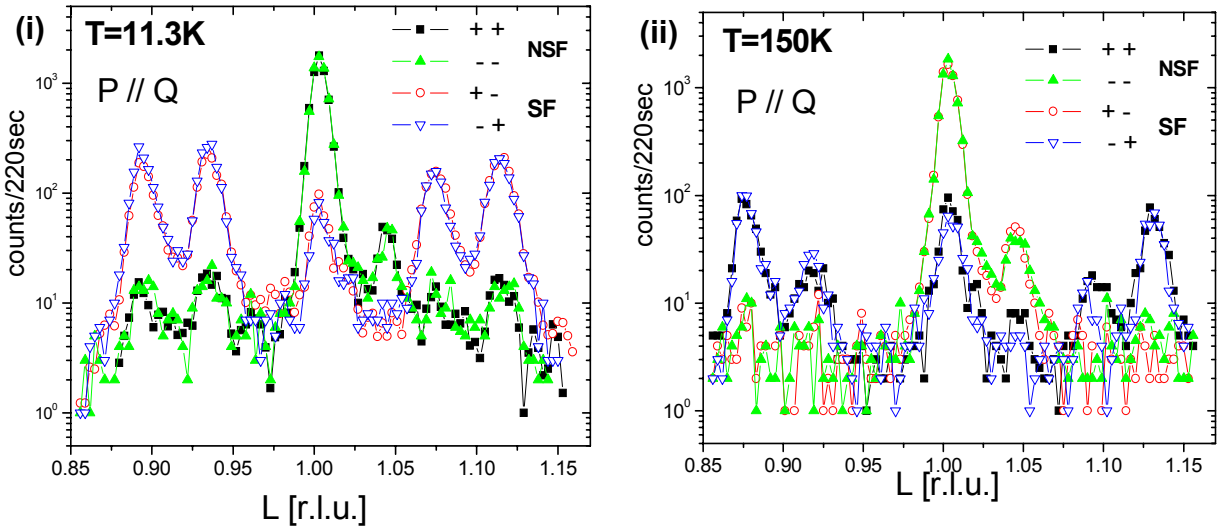


Figure 2: Polarized Neutron Diffraction around the Dy/Y(0002) superlattice peak with polarization analysis at (i) T=11.3K and at (ii) T=150K . Polarization vector of incoming neutrons is **parallel** to the scattering

[1] A. Schreyer et al., J. Appl.Phys. 87, 5443 (2000)

GKSS FORSCHUNGSZENTRUM in der HELMHOLTZ-GEMEINSCHAFT	EXPERIMENTAL REPORT	GeNF GENRA-3
Geesthacht neutron radiography facility GENRA-3		

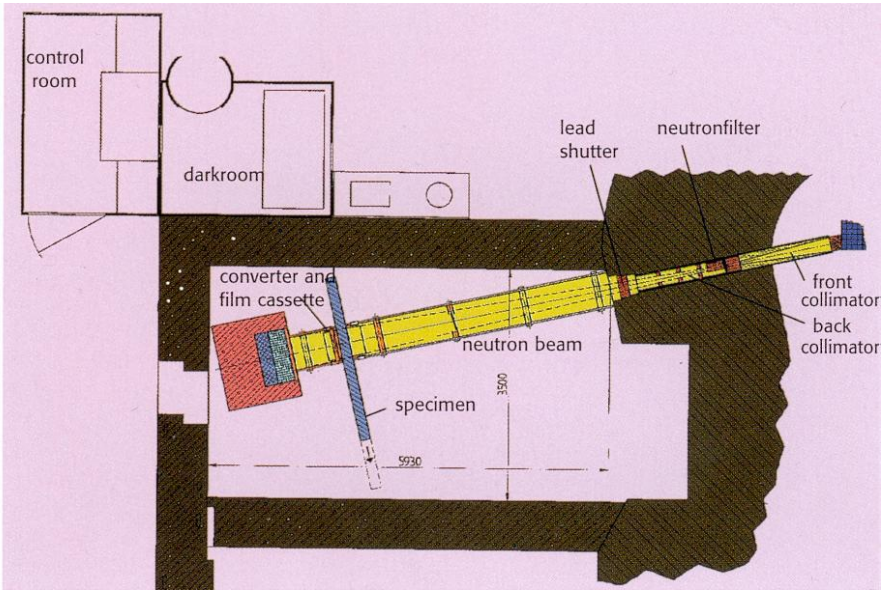
Short Instrument Description

The Geesthacht neutron radiography facility serves as an instrument for non-destructive testing and damage analysis of materials and technical structures by static and dynamic imaging. The ability of light elements, e.g. hydrogen or boron, to absorb neutrons allows unique analysis possibilities.

Local Contact:

Jürgen Vollbrandt
Phone/Fax : +49 (0)4152 87 – 1268 / +49 (0)4152 87 – 1338
e-mail: juergen.vollbrandt@gkss.de

Schematic View of GENRA-3:



Instrument Details:

Location at FRG-1:	beamline 13, thermal neutrons
Collimation ratio:	100 to 300
Flux at sample position:	$\Phi_{therm} = 1.4 \cdot 10^6$ cm^{-2} s^{-1} $\Phi_{epi} = 8 \cdot 10^3$ cm^{-2} s^{-1} with 4 cm Bi-filter at position: 2 m from beam exit available filters: 9 cm Bi-filter combined with 10 cm Be 0.2 cm Cd
max. size of specimen:	100 x 200 cm^2
Image:	15 x 15 cm^2 to 45 x 45 cm^2
Detecting: direct imaging	Gadolinium foil: max 14 x 17 inch Gd-scintillation screen connected to an image intensifier video camera
indirect imaging	transfer material: Indium, Dysprosium
Sample handling	Remote control of specimen, e.g. for scan purposes

Note:

The following research projects have been supported by the European Commission under the 6th Framework Programme through the Key Action: Strengthening the European Research Area, Research Infrastructures. Contract n°: RII3-CT-2003-505925':

M. V. Avdeev, L. Vekas:

Nuclear and magnetic structures of ferrofluids on organic non-polar carriers by small-angle scattering of polarized neutrons

M. Almgren:
Demixing in Micellar Solutions Containing CTAC and a Partially Fluorinated Cationic Surfactant

A. Dedinaite, M. Bergström, J. S. Pedersen:
Association between chitosan and oppositely charged surfactants

P. Claesson, A. Dedinaite, R. Makuska:
Association between a graft comb polyelectrolyte and oppositely charged surfactants

A. Triolo, C. M. Gordon:
Aggregative behaviour of Room Temperature Ionic Liquids in Water

E. Grossman, R. Verker, N. Eliaz:
Characterisation of the Effect of Space Debris Impact on Polymer Foils by SANS and USANS

M. Bischof:
Precipitation kinetics of a tool steel containing carbides and intermetallic phases

A. Michels, O. Moze, K. Suzuki:
Dipole-field controlled spin disorder in a nanocomposite ferromagnet

M. Bischof:
Characterisation of particles in dispersoide strengthened tantalum

U. Cihak, W.Marketz:
Residual Stress in IN718 Turbine Discs

Appendix I

Progress Report 2004
of the REFSANS Project

GKSS FORSCHUNGSZENTRUM in der HELMHOLTZ-GEMEINSCHAFT	**PROGRESS REPORT**	**GeNF REFSANS/FRM-II**

Status of the Horizontal Reflectometer REFSANS at FRM-II

Principal Proposer: **R. Kampmann[1], M. Haese-Seiller[1], V. Kudryashov[1,4], C. Daniel[2], B. Nickel[3], J. Rädler[3], A. Schreyer[1], E. Sackmann[2]**

[1] GKSS Forschungszentrum, Institut für Werkstoffforschung, D-21502 Geesthacht,
[2] Technische Universität München, Physik Department, E22, D-85747 Garching,
[3] Ludwig-Maximilians-Universität, Geschwister-Scholl-Platz 1, D-80539 München,
[4] Petersburg Nuclear Physics Institute, Gatchina, 188350, Russian Federation

Experimental Team: **R. Kampmann, M. Haese-Seiller, V. Kudryashov, C. Daniel, B. Nickel**

Date: 2004

INTRODUCTION

The horizontal reflectometer REFSANS is dedicated to the comprehensive analysis of the air/water interface by means of specular and off-specular reflectivity as well as GISANS measurements [1, 2, 3]. In parts, novel components concerning the chopper system, the neutron optics, the detector and the data acquisition system have been developed to meet the requirements of the different operation modi. An overview of the status of REFSANS as achieved in 2004 is presented in this report.

REFSANS AND ITS MAIN COMPONENTS

The design of REFSANS reflects the requirements of the different operation modi. Its total length of ~ 26 m fits to demands on the neutron optics for GISANS applications (Fig. 2). In the chopper chamber the slave chopper (SC) can be positioned in neutron guide gaps at distances between ~ 5 cm and 2.1 m from the master chopper (MC) for setting the wavelength resolution in the broad range of 0.25 % < $\Delta\lambda/\lambda$ < 15 % (Fig. 1 and 2). Double disc choppers allow adjusting the transmission window between 0° and 120° (Fig. 1 and 4) in accordance with the wavelength resolution.

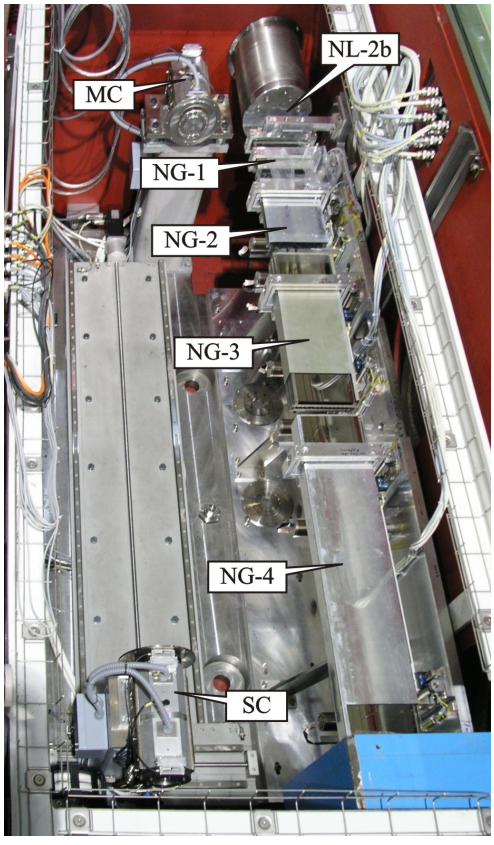


Figure 1: View of neutron optics, master chopper (MC) and slave chopper (SC) without disks in the chopper chamber (NL-2b: end of neutron guide NL-2b at the entrance of the chopper housing; NG-1, NG-2, NG-3, and NG-4: neutron guide elements.

Neutron guide elements as well as their mechanical support in the chopper and in the beam guide chamber are designed for realizing very different beam geometries (Fig. 1 to 5). Standard reflectivity measurements are performed with a horizontally slit height-smeared beam and incidence angles of the primary beam of ± 3, 12 and 48 mrad (main beam settings; Fig. 2). The beam may be guided towards the sample surface from the air or through the substrate [1, 2, 3].

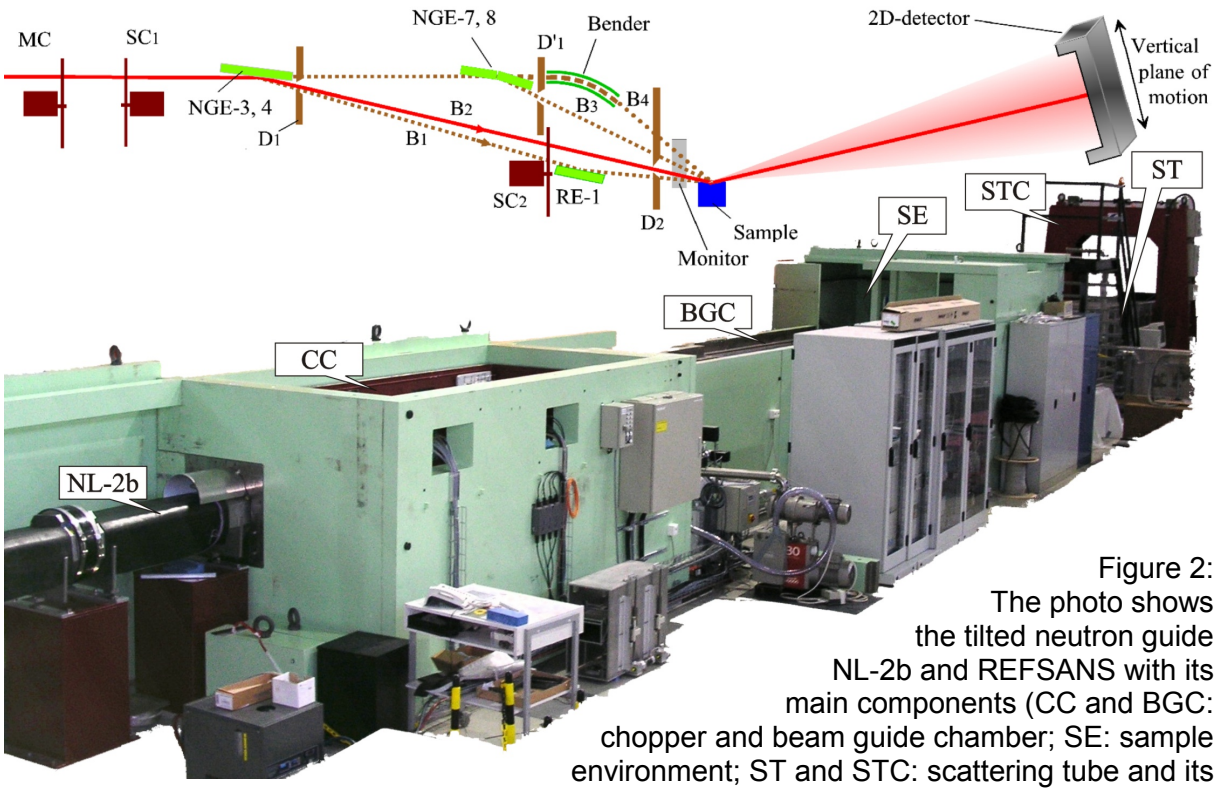


Figure 2: The photo shows the tilted neutron guide NL-2b and REFSANS with its main components (CC and BGC: chopper and beam guide chamber; SE: sample environment; ST and STC: scattering tube and its crane). Covers and upper shieldings of the CC and the BGC are dismounted. Schematics of the chopper and main beam guides of REFSANS are shown in the upper chart.

GISANS geometry is achieved by means of collimating the beam horizontally and vertically. In this geometry the intensity is increased by more than one order of magnitude by means of focussing 13 partial beams in the detector plane at a distance of ~ 10 m from the sample. The latter is performed by means of pre-collimating the beams in radially collimating neutron guide channels in the chopper chamber (Fig. 5) and by comb-like apertures in the beam guide chamber (between neutron optical bodies; Fig. 3) preventing mixing of neutrons in different partial beams [1, 3, 4].

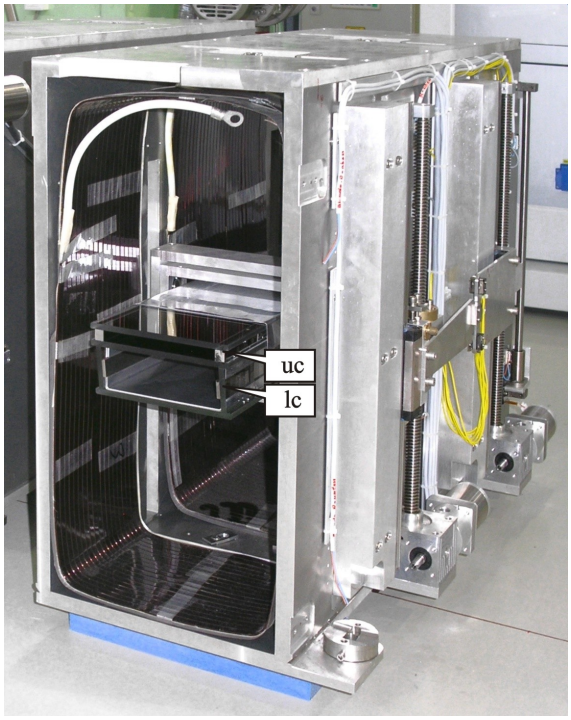


Figure 3: View of a neutron optical body of the beam guide chamber with the mechanics for vertically aligning a NGE. The NGE consists of an upper channel (uc) for continuing NL-2b (height: 12 mm; width: 170 mm) and a lower channel (lc) designed for vertically collimating and keeping the large horizontal beam divergence.

A 2D-position sensitive area detector with an active area of 500 mm × 500 mm and a position resolution of ~ 2 mm × 3 mm has successfully been put into operation. With its high quantum efficiency for neutrons (~ 80% for λ ~ 0.8 nm) and a very low one for gammas (< 10^{-6} for E ~ 660 keV) the detector meets all requirements for measuring low reflectivity and weak GISANS contributions [5, 6]. A new data acquisition based on the P7888 card from FAST ComTec GmbH has been developed for the delay-line based 2D-detector. It allows of maximum count

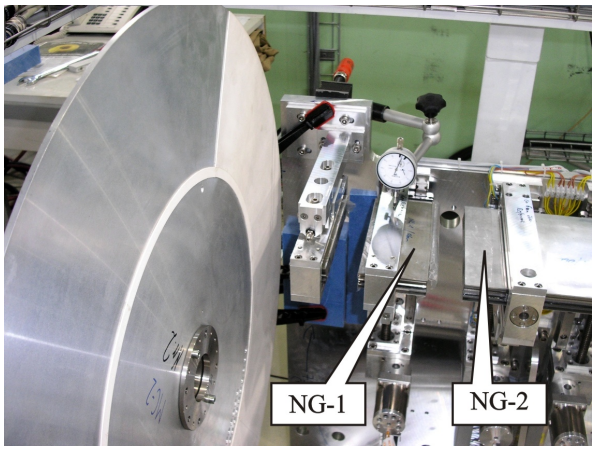


Figure 4: Master chopper with one disc and neutron guide elements NG-1 and NG-2 mounted in the chopper chamber.

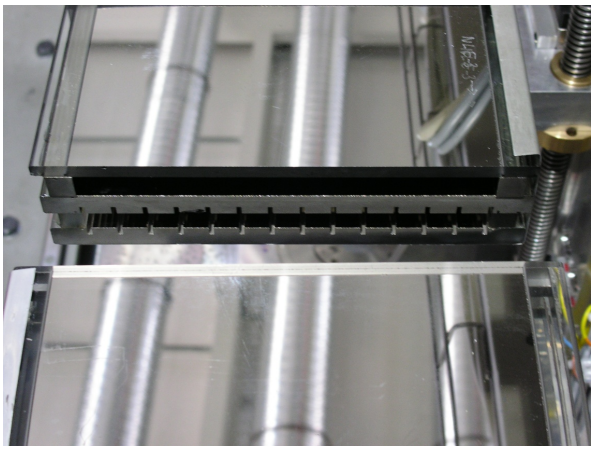


Figure 5: View of neutron guide element 3 with its upper channel used for continuing NL-2b (height: 12 mm; width: 170 mm) and its lower channel designed as a radial pre-collimator.

rates of ~ 10^6 n/s and will significantly improve the performance of REFSANS for the case of fast time dependent reflectivity measurements and special SANS investigations.

In the scattering tube the 2D-detector can be positioned at distances between ~ 2 m and ~12 m from the sample [6]. For positioning the detector at optimum height a special crane has been developed for the scattering tube which allows of aligning the tube such that the specularly reflected beam passes its center for incidence angles between ~ 0 and -100 mrad (Fig. 2).

The sample environment (Fig. 6) is designed for experiments at the air/water interface as well as at the air/solid and liquid/solid interface. In all cases one can make use of a microscope in upright or inverted position either for preparation purposes or as a complementary measuring option (e.g. fluorescence techniques). The further equipment consists of a damping table, a temperature controlled film balance and a set of translational tables (x, y, z) together with a three-axis goniometer (X, Φ, Ω).

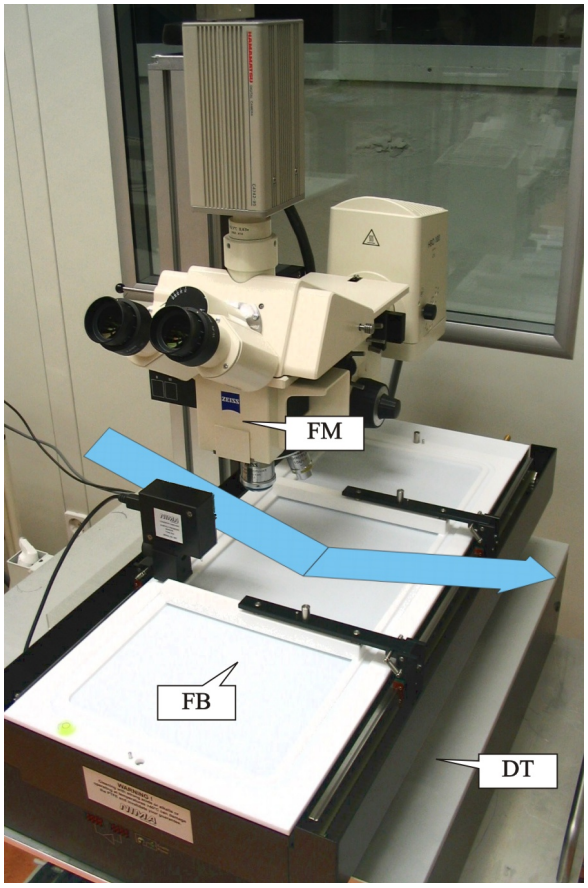


Figure 6: Setup for air-water experiments including damping table (DT), film balance (FB) and fluorescence microscope (FM). The path of the neutron beam is indicated by blue arrows.

Current status

The main components of REFSANS (chopper system, neutron optics, sample environment, 2D-detector, shielding, scattering tube with lifting system and data acquisition system) have successfully been tested and are being put into operation. First measurements will be performed at REFSANS early in 2005.

Acknowledgements

The great contribution of the technical department of GKSS to constructing and manufacturing of REFSANS components is gratefully acknowledged. The development of REFSANS has been supported by the German Federal Ministry of Education, Research and Technology (BMBF) under contracts 03-KA5FRM-1 and 03-KAE8X-3.

Bibliography

[1] Kampmann, R., Haese-Seiller, M., Marmotti, M., Burmester, J., Deriglazov, V., Syromiatnikov, V., Okorokov, A., Frisius, F., Tristl, M., Sackmann, E. *Applied Physics A*, 74, (2002), 249–251.
[2] Kampmann, R., Haese-Seiller, M., Kudryashov, V., Deriglazov, V.,Syromiatnikov, V., Tristl, M., Toperverg, B., Okorokov, A., Schreyer, A., Sackmann, E, Physica B 335 (2003), 274 - 277.
[3] Kampmann, R., Haese-Seiller, M., Kudryashov, V., Deriglazov, V., Tristl, M., Toperverg, B., Schreyer, A., Sackmann, E. *Nuclear Instruments and Methods A*. Submitted.
[4] Kampmann, R., Haese-Seiller, M., Kudryashov, V., Daniel, C., Deriglazov, V., Toperverg, B., Okorokov, A., Schreyer, A., Sackmann, E., TU-Munich, Annual Report 2003, ZWE FRM-II, pp. 30-32.
[5] Kampmann, R., Marmotti, M., Haese-Seiller, M., Kudryashov, V.: *Nuclear Instruments and Methods A* 529 (2004) 342-347.
[6] Kampmann, R., Marmotti, M., Haese-Seiller, M., Kudryashov, V.: in this annual report.

Appendix II

Reports of experiments carried out at HASYLAB / DESY by GKSS personel – GKSS outstation HARWI-II at DESY – as responsible experimenters in support of external users.

These reports have been taken from HASYLAB Annual Report 2004.

(reprints by courtesy of DESY, Hamburg)

HARWI-II Materials Science Beamline

End of 2002 the GKSS-Research Center Geesthacht, Germany, started the construction of the high-energy beamline HARWI-II at HASYLAB / DESY. The beamline is designed to be specialized in texture, strain, and imaging measurements for materials science. The outstanding characteristics of this beamline is the use of X-rays in the energy range from 20 - 250 keV. The project is a collaboration of the HGF centres DESY Hamburg, GKSS Geesthacht, and GFZ Potsdam. While DESY provides the source, the two other HGF laboratories in the collaboration focus on research on engineering (GKSS) and on geological (GFZ) materials, respectively. The beamline HARWI-II will allow to use a small white beam (0.5 mm x 0.5 mm), a large monochromatic X-ray beam (70 mm x 10 mm) in an energy range of 20 to 200 keV, and a monochromatic X-ray beam (10 mm x 10 mm) in an energy range of 50 to 250 keV.

The current status of the project is shown in the viewgraphs below representing the different timesteps in the setup of the X-ray shielding components of the beamline.



January 2004



May 2004



July 2004



August 2004



November 2004



November 2004

Pictures of the HARWI-II beamline starting from January 2004 to the current status in November 2004.

High-energy beamline HARWI-II

F. Beckmann, T. Lippmann, J. Metge, R.V. Martins, T. Dose and A. Schreyer

GKSS-Forschungszentrum Geesthacht, Max-Planck-Str. 1, 21502 Geesthacht, Germany

The new high-energy beamline HARWI-II will be dedicated to texture, strain, and imaging measurements for materials science. The beamline layout including the beamline optics, the experimental stations, and the control hutch are presented in figure 1. The GKSS-Forschungszentrum Geesthacht will operate the monochromator and three permanent experiments. Extra space for temporary setups will be provided. In a separate experimental hutch the high pressure cell MAX200x will be run by the GFZ Potsdam [1].

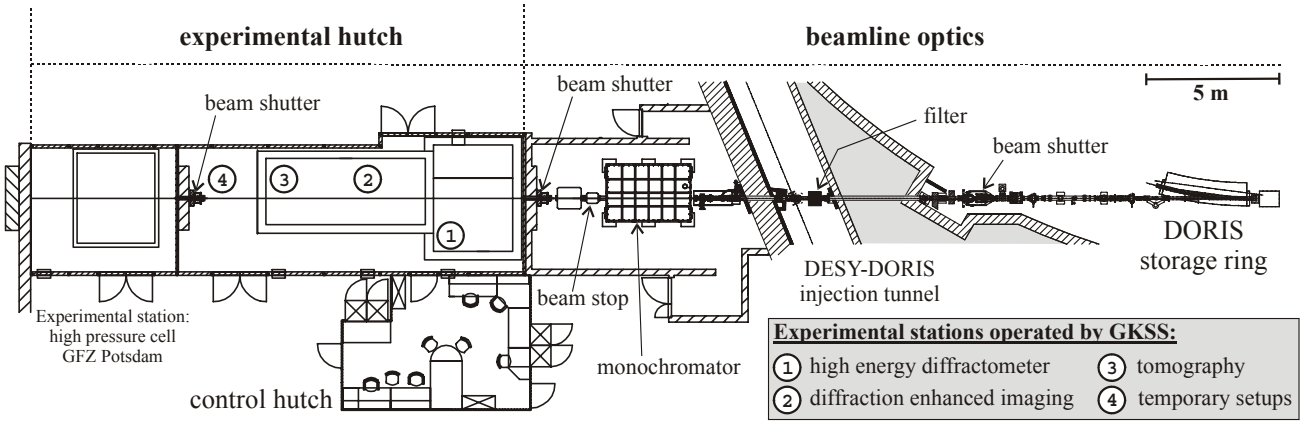


Figure 1: Sketch of the HARWI-II beamline including the beamline optics, the experimental stations and control hutch.

The main components for the beamline optics are the new HARWI-II wiggler [2], the new front-end filter [3], the monochromator setup and the beam stop.

The monochromator tank, shown in figure 3, is located about 39 m downstream of the new HARWI-II wiggler. 3 mm Carbon will be permanently installed as a high pass filter in order to reduce the heat load onto the monochromator. For the use of high photon energies 7 mm Carbon, 1 mm, or 2 mm Copper can additionally be placed into the beam (s. figure 2). The total power of the white beam is about 12.6 kW. Different high pass filters allow to reduce the power of the beam [3].

Two different types of monochromators will be installed in the vacuum tank. The first type will be a double Laue monochromator in horizontal geometry which will deliver beams of up to 10 mm x 10 mm in size optimized for diffraction experiments. The energy range will be 50 to 250 keV. The second monochromator optimized for imaging experiments will produce a beam size of up to 70 mm x 10 mm in a vertical diffraction geometry. The energy range will be 20 to 200 keV. Different pairs of crystals in Laue-Laue and Laue-Bragg geometry will be used. Furthermore a direct white beam of about 0.5 mm x 0.5 mm will be available.

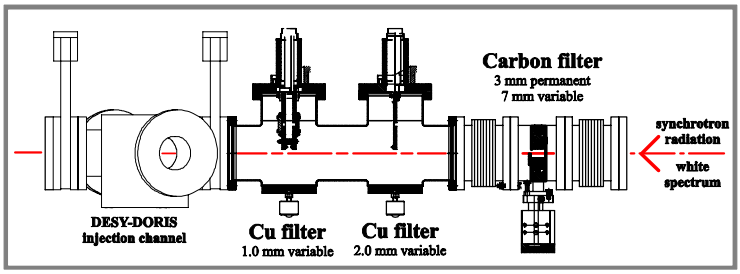


Figure 2: Sketch of the high-pass filter installed in the DORIS-DESY injection tunnel. On the right the permanent 3 mm Carbon filter and, by changing the height, the 7 mm optional Carbon filter is shown. Copper filters of 1 mm or 2 mm thickness can be added.

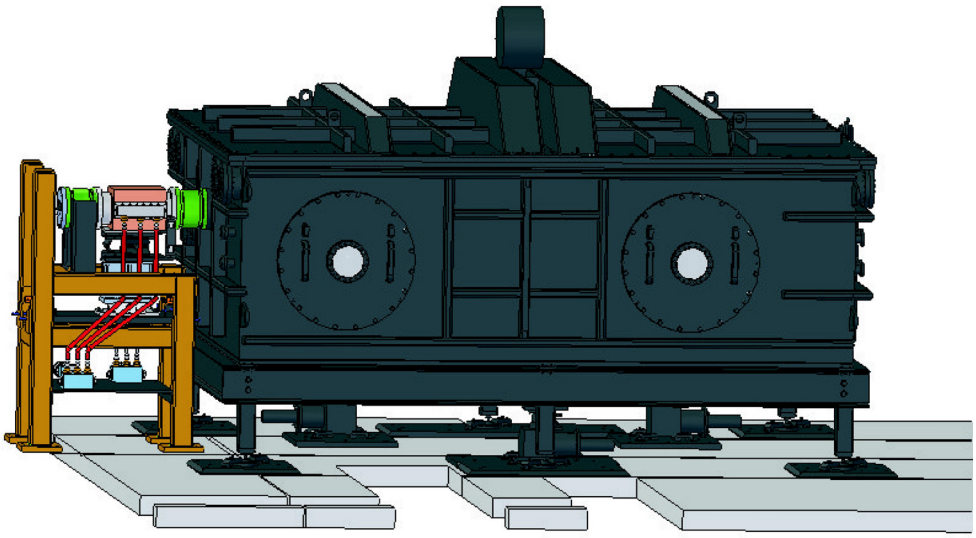


Figure 3: Sketch of the beamstop (left) and monochromator tank (right), the size of the tank is 3m by 2 m by 1 m (L x W x H).

In the experimental hutches three pits will house the different experiments (s. figure 1). One of the experiments operated by the GKSS is a diffractometer specialized for high photon energies and heavy loads. It will be installed in the pit at position 1 (figure 1). The instrument has been ordered from HUBER Diffraktionstechnik GmbH, Rimsting, Germany. It is equipped with various translation, rotation, and tilt stages. The tower will be large enough to carry heavy samples and heavy user environment up to 600 kg as tanks, cryostats, stress riggs, or superconducting magnets. It is planned to offer different kinds of area detectors: A CCD with a small active area and a large area detector (e.g. flat panel detector). The sample detector distance can be up to 9 m (for high angular resolution) by the use of a large movable frame in the experimental hutch.

The setups for Diffraction Enhanced Imaging DEI (figure 1 position 2) and tomography (figure 1 position 3) will be installed onto separated lift tables. Figure 4 gives an impression of the concept of the lift tables. On the left the fully extende table for the tomography setup is shown. The table for the DEI setup is in its rest position, i.e. not intercepting the beam. To allow for the operation of other experiments at the beamline the apparatuses will be moved out of the beam. In the rest position of the tables the pit will be covered by an accessible roof

The different components for the beamline optics will be installed in the beginning of 2005. First operation of the beamline is planned for March 2005. Beamtime for users will be available in the second half of 2005.

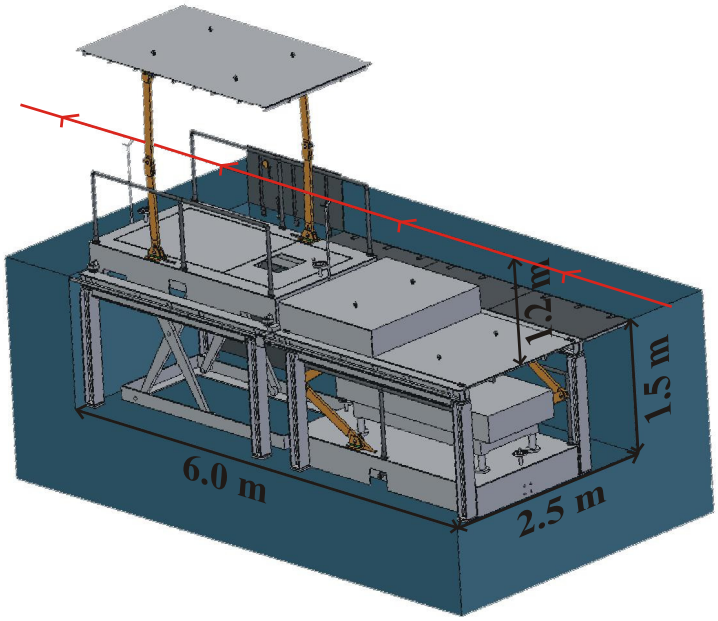


Figure 2: Design of the lift tables for the microtomography setup (left) and the DEI setup (right).

References

[1] C. Lathe, F.R. Schilling, J. Lauterjung. "Triple H experiments - MAX200x", this volume.

[2] M. Tischer, J. Pflüger, L. Gumprecht, T. Vielitz. "A new wiggler for the HARWI-II beamline", this volume.

[3] H. Schulte-Schrepping, U. Hahn. "HARWI-II front-end filter design", this volume.

Analysis of the material behaviour of the MMC Al/TiN by microtomography

H.-A. Crostack, J. Nellesen, H. Blum[1], T. Rauscher[1], F. Beckmann[2], G. Fischer

Lehrstuhl für Qualitätswesen, Fakultät Maschinenbau, Universität Dortmund, D-44221 Dortmund, Germany
[1] Chair X of Scientific Computing, Institute of Applied Mathematics, University of Dortmund, D-44221 Dortmund
[2] GKSS, Max-Planck-Str. 1, D-21502 Geesthacht, Germany

1 Introduction

For the design of tailored materials with certain desired macroscopical mechanical properties materials of different elastic and plastic properties are combined. In metal-matrix composites (MMC) e.g. brittle ceramic particles are dispersed in a ductile metal matrix. The macroscopically observable strain in such materials reflects an average value of local plastic strain distribution due to defects and its two-phase nature. In order to predict the material behaviour and to give hints for optimisation of its design, processes like micro deformation as well as initiation and growth of micro defects, which take place in composite materials under load and which precede the macroscopical fracture of a specimen, have to be understood. In this work this experience and knowledge was deduced from *a* 3D analysis of real microstructure based on X-ray tomographic microscopy (XTM) at different stages of deformation with high spatial resolution. The results of 3D data processing on the tomographic data sets have further been fed into realistic FE-simulations [1].

2 Experimental procedure

Plain dog bone shaped tensile specimens of MMC_p Al/TiN were produced on a powder metallurgic route. CT measurements were carried out at beamline BW2 using monochromatic photons of 24 keV. The projection data set contain radioscopic images consisting of 1536x1024 pixels acquired at 720 rotation angles in the half-circle. At different stages of deformation the microstructure of the tensile specimen was imaged by tomography with a magnification $m \approx 6$. Details can be found elsewhere [1].

3 Analysis procedure and results

The three-dimensional tomograms were processed by two different data analysis methods: For the first approach sub-volumes of tomograms containing 512x512x344 voxels were studied at different deformation stages. To segment both phases of the composite a material label for Al and TiN was assigned to each voxel applying a combination of global and adaptive thresholding to the raw data. The segmented particle phase in the sub-volume was labelled afterwards, i.e. new labels, like 'particle1', 'particle2' were assigned to contiguous voxel regions. The labelling was established by 3D-region growing. Additionally, the center of gravity, the volume and the perimeter of the labelled particles were determined. Due to the deformation and particle cracking the number of identified particles (roughly 200) increases with the deformation level.

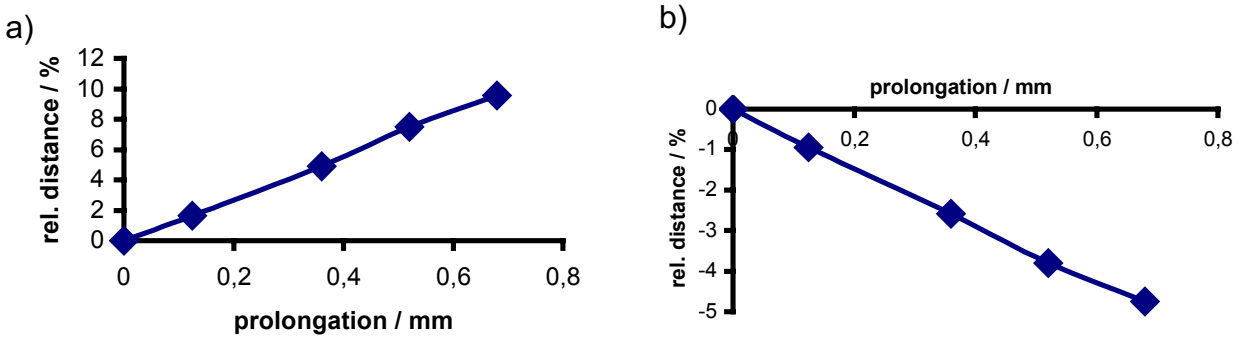


fig. 1: relative distances of particles as a function of the specimen's prolongation a) particles in two different *z*-planes, b) particles in the same *z*-plane

In order to identify pairs of corresponding particles, few particles were chosen and identified interactively for consecutive deformation stages. Secondly, an average 3D-transformation for the centers of gravity was

computed by means of least squares fitting. Thirdly, the mass centers of all particles were transformed from the less to the more deformed stage. By this means, a mapping function could be set up.

The particle distance of pairs were measured on the basis of these mapping functions to verify the increase of particle distances aligned in the loading direction (z) and the decrease of particle distances perpendicular to the loading direction during the tensile experiment.

In the second analysis procedure the displacement field in the studied volume was determined. The tomogram of the undeformed state was subdivided into overlapping cubes of 128^3 voxels therefor. In an iterative process the deformation gradient of each cube is computed by fitting its grey value distributions of the undeformed and the deformed state. The displacement vector and the Lagrangian strain tensor can be calculated from the deformation gradient.

To provide input data for the FE-simulation, the displacement vectors on the surface of the sub-volume, shown in fig. 2a+b, were calculated using the 3D-grey value mapping method mentioned above. Whereas in fig. 2a all TiN particles of the sub-volume are shown, in fig. 2b the measured displacement vectors are visualized using the center particle as reference position. In fig. 2b magnitude and direction of displacement vectors located at the corners, edges' and faces' centers of the sub-volume are coded by volume and orientations of cones, respectively. The displacement vectors reflect material extension in loading direction (z) and a smaller transverse contraction.

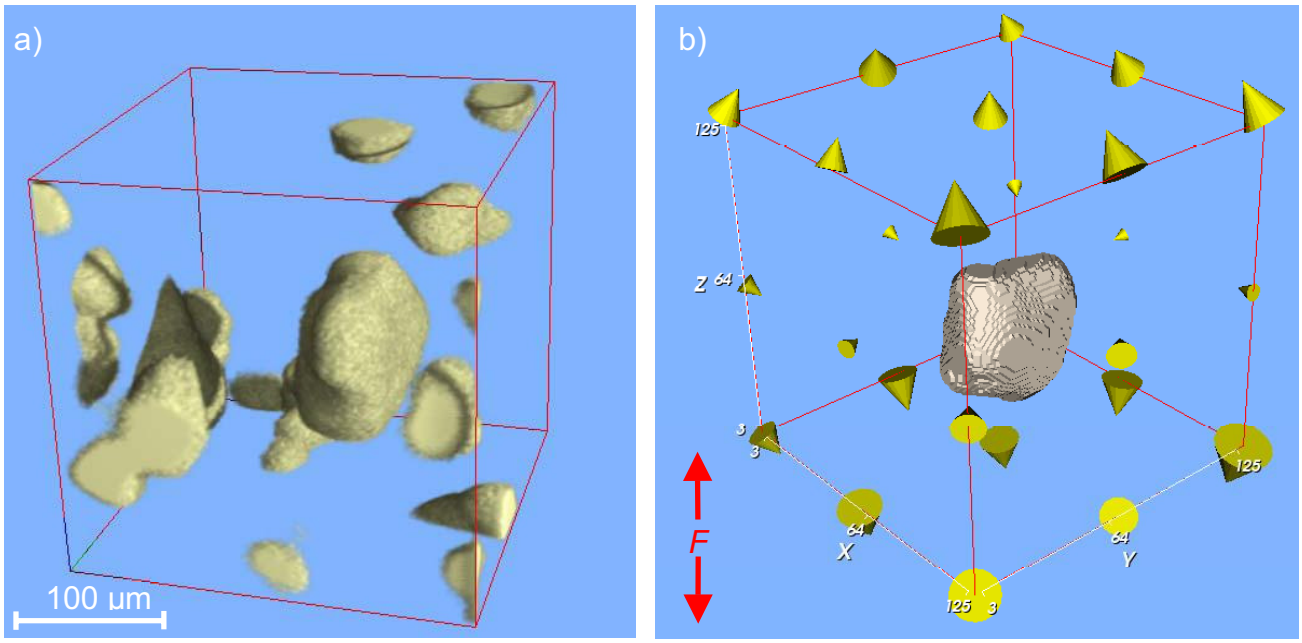


fig. 2: tomogram sub-volume used for strain-mapping and FE-simulation with all particles (a) and with center particle and measured displacement vectors (b)

4 Acknowledgement

The financial support of this work in the scope of the research projects Cr4/100-3,-4 is gratefully acknowledged.

5 Reference

[1] CROSTACK, H.-A.; NELLESEN, J.; BLUM, H.; RAUSCHER, T.; BECKMANN, F.; FISCHER, G.: *Analysis of the material behaviour of metal-matrix composites under tension by synchrotron radiation based microtomography and FE-calculations*, in *Developments in X-ray Tomography IV*, edited by Ulrich Bonse, Proceedings of SPIE Vol. 5535 (SPIE, Bellingham, WA, 2004), 493-504

Characterisation of the Effect of Simulated Space Debris on Polymers Using X-ray Microtomography

R. Verker[1,2], P.K. Pranzas[3], F. Beckmann[3], T. Donath[3], A. Schreyer[3], N. Eliaz[2] and E. Grossman[1]

[1] Space Environment Division, Soreq NRC, Yavne 81800, Israel

[2] Department of Solid Mechanics, Materials and Systems, Tel Aviv University, Ramat Aviv, Tel Aviv 69978, Israel

[3] Institute for Materials Research, GKSS Forschungszentrum, Max-Planck-Str. 1, 21502 Geesthacht, Germany

The aggressive space environment present in Low Earth Orbit (LEO) at altitudes ranging from 200 to 700 km restricts the number of space-qualified materials and reduces the service life of polymers used in space technologies. The predominant environmental species in LEO responsible for polymers degradation are Atomic Oxygen (AO), UV radiation and space debris particles. Hypervelocity space debris impacts can lead to degradation of satellite performance and, in extreme cases, might cause a total loss of a spacecraft. The increase in space debris population provides the motivation for this study, which focuses mainly on the structure and mechanical behaviour of space-qualified polyimide Kapton films impacted by simulated hypervelocity debris. The effect of the simulated debris was studied using X-ray microtomography which provides three-dimensional information of the damaged area by reconstructing a series of two-dimensional absorption images. It allows the characterisation of structures larger than 1 μm.

For the simulation of spacecraft hypervelocity debris with dimensions ranging from 10 to 100's μm and impact velocities of up to 3 km/s, the Laser-Driven Flyer (LDF) method was used. Impact effects on the internal three-dimensional microstructure of Kapton are studied by means of the synchrotron radiation-based X-ray absorption micro computerized tomography (μ-CT) [1]. The measurements were performed at beamline BW2, using a photon energy of 24 keV and an effective pixel size of 1.5 μm.

Figure 1 shows a top-view cut just below the surface of a 125 μm-thick Kapton sample impacted by 2.9 km/s flyers. Figure 2 and 3 show two-dimensional cuts through the three-dimensional image of the impacted Kapton. The white regions are aluminum particles imbedded in the polymer at the displayed depth. The dark areas are holes created by the impacts [2].

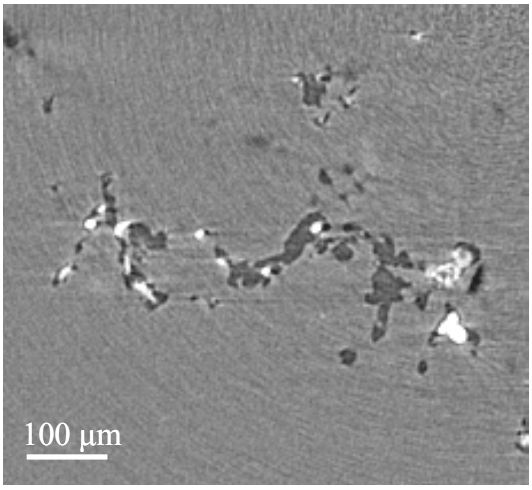


Figure 1: Top-view cut just below the surface of a 125 μm-thick Kapton foil impacted by 2.9 km/s flyers.

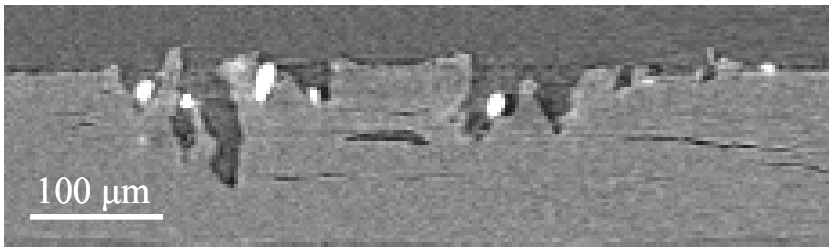


Figure 2: Two-dimensional cut through the three-dimensional μ-CT image of the impacted Kapton.

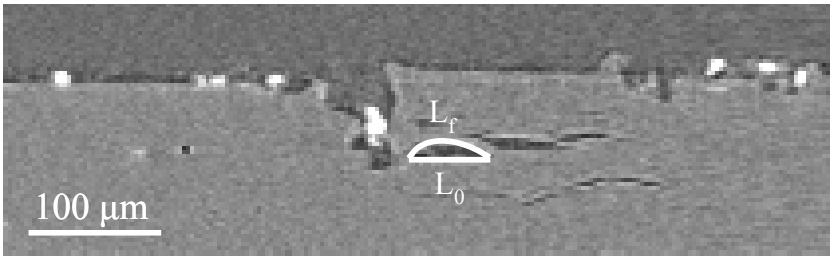


Figure 3: A spall created by the impact is evident and used to estimate the fracture strain.

These results provide information on size and distribution of the flyers. It is evident that the cloud of aluminum flyers created by the LDF system is composed of several small particles, each of the order of few tens of micrometers in size. Figure 3 shows a cross-section of the impacted sample, revealing – besides of the observed holes – also the formation of longitudinal cracks (i.e., spalls). These cracks originate from debris impacts and the related spallation process. Using this image the engineering fracture strain and the strain rate can be calculated.

References

[1] D. Tadic, F. Beckmann, K. Schwarz, and M. Epple, Biomaterials 25, 3335 (2004)
[2] R. Verker, N. Eliaz, I. Gouzman, S. Eliezer, M. Fraenkel, S. Maman, F. Beckmann, K. Pranzas, and E. Grossman, Acta. Mat. 52, 5539 (2004)

Determination of in-vivo corrosion rates of degradable implants by SR-microtomography

J. Fischer[1], J. Nellesen[2], H.-A. Crostack[2], T. Donath[3], F. Beckmann[3] and F. Witte[1]

[1] *Department of Orthopaedic Surgery, Hannover Medical School, Anna-von-Borries-Str. 1-7, 30625 Hannover, Germany*
[2] *Lehrstuhl für Qualitätswesen, Fakultät Maschinenbau, Universität Dortmund, 44221 Dortmund, Germany*
[3] *Institute for Materials Research, GKSS-Research Centre, Max-Planck-Str.1, 21502 Geesthacht, Germany*

In trauma and orthopaedic surgery metal implants are widely used for bone augmentation after bone fracture to provide the fracture site with adequate stabilization to heal. In order to prevent a second operative procedure for implant removal, innovative materials for implants have to be manufactured meeting the requirements for biocompatibility and degradablity while the fracture is healing. Magnesium alloys seems to meet these requirements for degradable biomaterials [1]. For the development of magnesium alloys, that are appropriate for the specific local application in the human organism, the in-vivo corrosion rate has to be measured and the understanding of the corrosion process has to be gained. Both of these aims can be achieved by SR-based microtomography: Within this study the remaining metal implant and the corrosion layer were quantified on the basis of 3D-tomographic datasets of the specimen. Since absorption values in the dataset of the corrosion layer and the remaining metal implant are quite similar, the segmentation of different region of interest (ROI) with 3D data/image processing is still a challenge.
Sample cylinders made of magnesium alloys were implanted into the femur of rabbits and explanted after various time intervals. In the project II-078-001, the specimens were imaged by absorption microtomography utilizing synchrotron radiation. The projection data were aquired at 720 rotation steps equally spaced in the half-circle at beamline W2 using 31 keV photon energy. To obtain a high spatial resolution the specimens were investigated in two different position of the z-axis. Further these two separat datasets were finally stacked to an entire dataset. The voxel size of an unbinned dataset was equal to 10 µm. This voxel size is adequate to detect the corrosion layer of the degrading magnesium implant. In some cases the specimen could be investigated at a higher magnification to obtain better resolution of the corrosion layer.

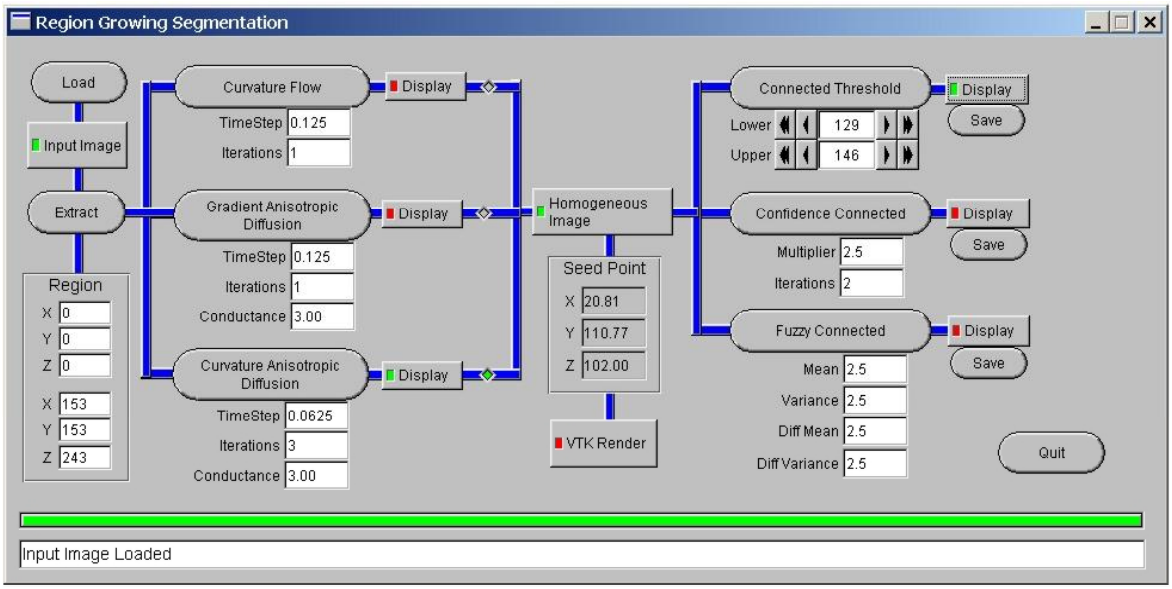


Figure 1: Screenshot of ITK-Tool displaying various filter systems for data pre-processing

For further data processing, the ROI was defined as a reduced cylindrical volume of the entire dataset that enclosed 0.5 mm of surrounding bone of the degrading magnesium implant. Subsequently, the ITK tool "Region Growing Segmentation" was used for further 3D-analysis on the dataset (Fig.1) [2].
The combination of different 3D filter systems shown in figure 1 enabled us to binarize the dataset for segmenting the corrosion layer and to count the corresponding voxel. To minimize the influence of the global threshold on the segmented volume of the corrosion layer, the processing algorithm was set as followed: In a slice of the entire 32-bit floating point dataset an area of voxels representing the corrosion layer was selected. The mean attenuation value of these voxels was calculated. The specimens were imaged by tomography at various magnification, therefore, the size of the voxels were different in many datasets. To standardize the attenuation value per voxel for all datasets, the attenuation value per voxel was adjusted to attenuation value per micrometer. The threshold for the segmented volume of the corrosion layer in each dataset was determined by using an "upper and lower threshold" corresponding to +/- 10 percent of the mean attenuation value per micrometer in the 32-bit float-dataset.
This procedure enabled us to use the corresponding attentuation values in each dataset to determine the corrosion layer in the 8-bit tiff-images calculated from the 32-bit float datasets.
In further research, this technique will allow us to determine in-vivo corrosion rates of various magnesium implants.

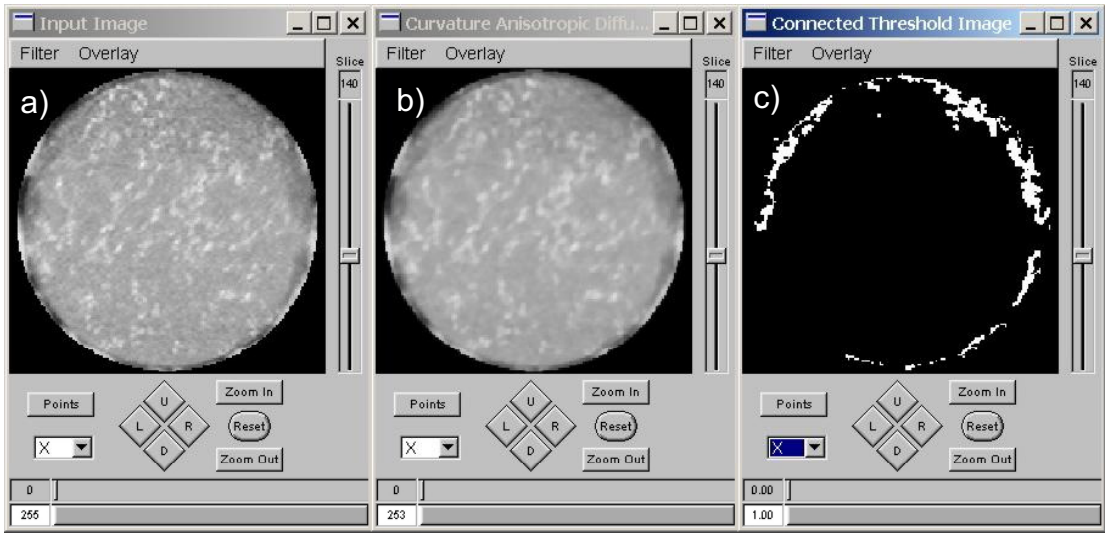


Figure 2: Data processing starting with the original 32-bit dataset (a) followed by using the filter "Curvature Anisotropic Diffusion" (b) and finally binarizing the dataset with the determined threshold (c).

References

[1] F. WITTE ET AL., *In-vivo corrosion of four magnesium alloys and the associated bone response*. Biomaterials, in press

[2] ITK Version 1.6.0 http://www.itk.org

Acknowledgement

The authors acknowledge the financial support of the Colloborative Research Project 599.

Geometric properties of layered sands and their relevance for water distribution

P. Lehmann, A. Kaestner, F. Beckmann[1] and H. Flühler

Institute of Terrestrial Ecology, ETH Zurich, Grabenstrasse 3, 8952 Schlieren, Switzerland
[1]Institute for Materials Research, GKSS-Research Center, Max-Planck Strasse, 21502 Geesthacht, Germany

The solid particles in soils form a complex network of voids that determines the storage and flow of water and the transport of dissolved substances. The larger these voids, in the following denoted as pores, the higher the water flow velocity and the smaller the capillary forces avoiding air entry. In small pores, water flow is slow due to the friction at the solid walls but they remain water filled due to the high capillary forces. So, to predict the flow and the distribution of water, the size of the pores must be known. In soil physics, the size of the pores is determined indirectly by measuring the water volume remaining in the soil, when a pressure is applied to the soil water to overcome the capillary forces. For an applied pressure p , only pores of radius r fulfilling the following condition remain water filled

$$r < \frac{2\sigma}{p} \qquad (1)$$

with the surface tension of water σ [kg s^{-2}]. Such an indirect measurement is flawed by the fact that large pores with weak capillary forces may be surrounded by small pores that prevent the air intrusion. Therefore, we need a method to measure the size of the pores directly. Four different cylindrical samples of 15mm in diameter were prepared containing fine and coarse sand material. The measurement of the pore sizes with a resolution of 11microns was performed at the beamline W2 at HASYLAB. The particle sizes range from 0.1 to 0.5mm for the fine and from 0.3 to 0.9mm for the coarse sand. Natural soils contain different materials that may be arranged in complex patterns. To analyze the geometric properties at the boundary between different materials, two samples were prepared with vertical or horizontal layers, while two samples contained pure material. Vertical cross sections through the four samples are shown in Figure 1.

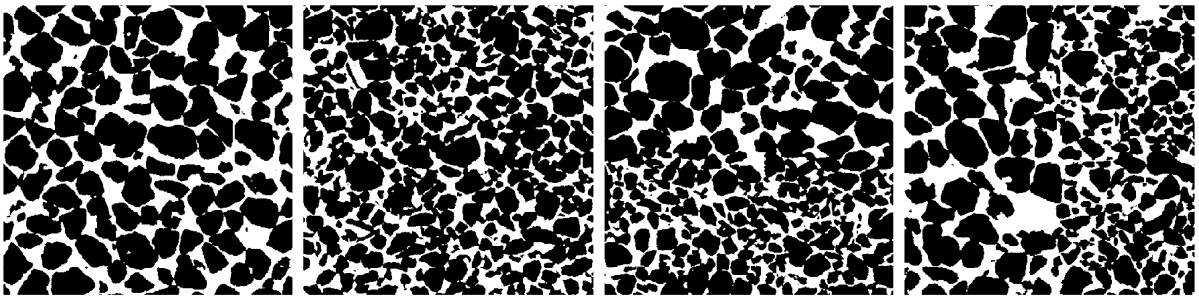


Figure 1: Vertical cross-sections of length 5.5mm through four sand samples. The voxel size is 0.011mm.

After the reconstruction of the data, a cubic section of 500^3 voxels was segmented into pores and grains and the pore sizes were determined. First, the mean pore size of planes parallel to the boundary was computed: Each pixel is assumed to be the centre of a disk touching the closest grain. A pore pixel, denoted as A , may be an element of different disks that are centred at neighboured pixels. The radius of the largest of these disks determines the pore size of pixel A . Then, the mean value of the size of all pore pixels in a plane is calculated. In Figure 2A, the mean pore radius as a function of the distance from the boundary is shown for the layered materials. The thickness of the transition zone between the coarse and the fine material is about 1mm. Within this transition zone, the hydraulic properties may be different and affect flow and transport properties. To compute the water distribution in the layered media, the three dimensional pore sizes must be taken into account. The three dimensional pore radius is determined using a sphere as probe instead of a disk as in the two dimensional case. The result is shown in Figure 2B for the pure and the layered materials. The pore sizes of the layered media are the average of the pure materials.

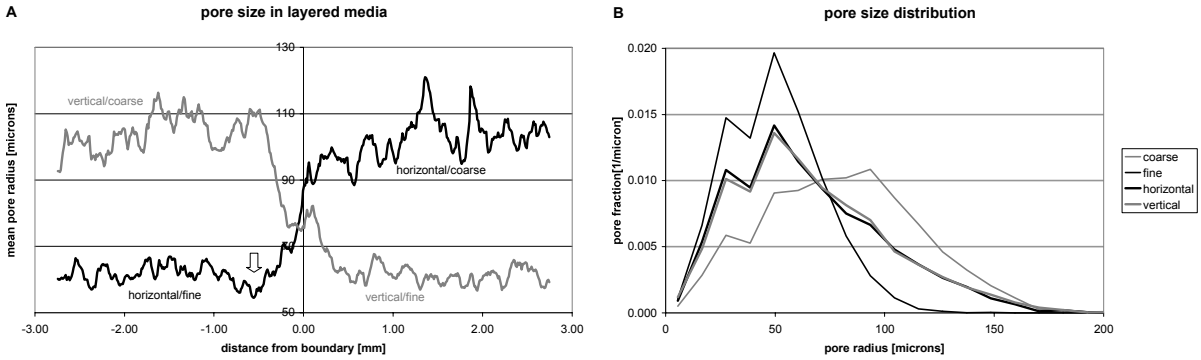


Figure 2: In Figure A, the two dimensional pore sizes are shown. The arrow indicates a layer with minimum porosity. In Figure B, the three dimensional pore size distributions four the four samples are given.

After the determination of the pore size, the drainage of the samples was calculated in a numerical experiment. A pressure p was applied at the lower boundary of the initially water filled cubic sample to drain the sands. At the top, air will enter in pores with size $r \geq 2\,\sigma / p$ according to equation 1. To drain smaller pores, the pressure was increased stepwise. A water filled pore will drain out when the capillary forces are too weak to sustain the applied pressure and when it is not completely surrounded by smaller pores. To quantify this effect of connectivity with smaller pores, the drainage computed with the numerical model is compared to the cumulated pore size distribution. Without connectivity, all pores of size $r \geq 2\,\sigma / p$ would drain out. The comparison is shown in Figure 3.

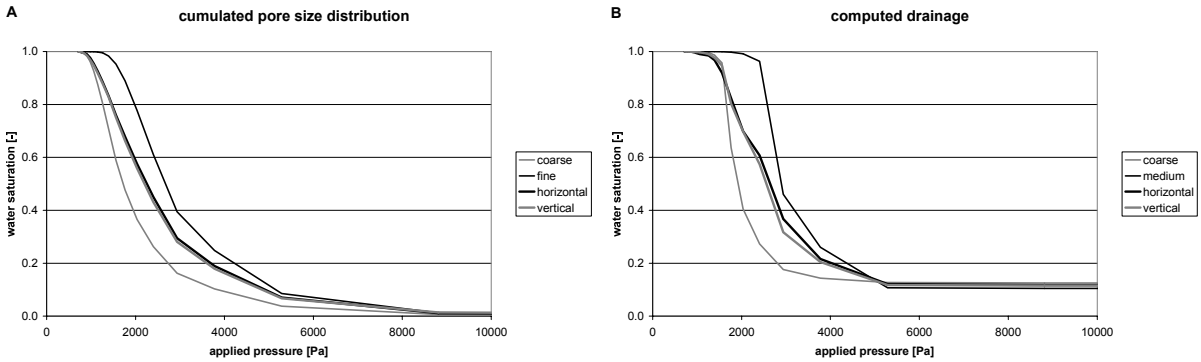


Figure 3: Drainage of sand samples. If the connectivity between pores of different sizes would be neglect able, the water saturation would correspond to the cumulated pore size distribution (A). The computed drainage taking into account the connectivity is shown in Figure B.

Compared to the cumulated pore size distribution, higher pressure values are needed in the numerical model before the samples starts to drain out. According to the cumulated pore size distribution, the samples should start to drain out for pressure values between 1'000 and 1'500 Pa. But in the numerical experiment, the drainage begins for values between 1'500 and 2'500 Pa. In addition, about 10% of the pore space remains water filled in all four samples. This occurs, when large pores surrounding small pores becomes air filled and the water within the small pores is isolated and not connected with the lower boundary, where the force is applied to the soil water. Finally, there is a small difference between the curves for the layered materials. The fine sand in the horizontal arrangement drains out for higher pressure values. This is caused by the existence of layers with small pores and higher capillary forces, as indicated by the arrow in Figure 2A.

We can conclude that due to the synchrotron light technology a new insight into the geometry of the pore space is given. In combination with numerical models, the effect of pore size and pore connectivity on water distribution can be analyzed in more detail.

Microstructure of Medium Density Fiberboard (MDF)

T. Walther[1], H. Thömen[1], T. Donath[2], F. Beckmann[2]

[1]Department of Wood Science, Hamburg University, Leuschnerstrasse 91, 21031 Hamburg, Germany
[2]GKSS-Forschungszentrum, Max-Planck-Strasse 1, 21502 Geesthacht, Germany

Medium or High Density Fiberboard (MDF/HDF) are common wood composite products that are widely used for the furniture industry and for laminate flooring. To produce such composites the wood furnish material consisting of single fibers or fiber bundles is treated with an adhesive and is subsequently consolidated under temperatures of 180 to 220°C to a panel with an average density of 650 to 900 kg/m³. During the hot-pressing process the individual wood fibers undergo significant structural changes. The structure and the mechanical properties of the composite are influenced by the raw material characteristics, moisture of the fibers, type of adhesive, pressing program and pressing temperature [1]. The resulting microstructure of the composite and the effect of the compression process on the individual fibers is usually being studied by scanning electron microscopy. However, the scope of this approach is somehow limited due to surface artefacts and the sensitivity of the sample towards mechanical preparation which prohibits a damage-free surface. Furthermore, only two-dimensional images of the composite structure can be obtained. The use of µCT to record the whole undamaged 3D-structure provides a new opportunity to analyse the alignment of the fibers, the size and number of the voids and the fiber to fiber bonding.

The microstructure of laboratory MDF samples has been examined in preliminary experiments using the synchrotron radiation X-ray µCT-equipment operated by the GKSS at beamline BW2. The photon energy was set to 14.5 keV to match the low absorption of the wood fibers.

Volume renderings of a 2 by 2 mm MDF sample are shown in Figure 1.

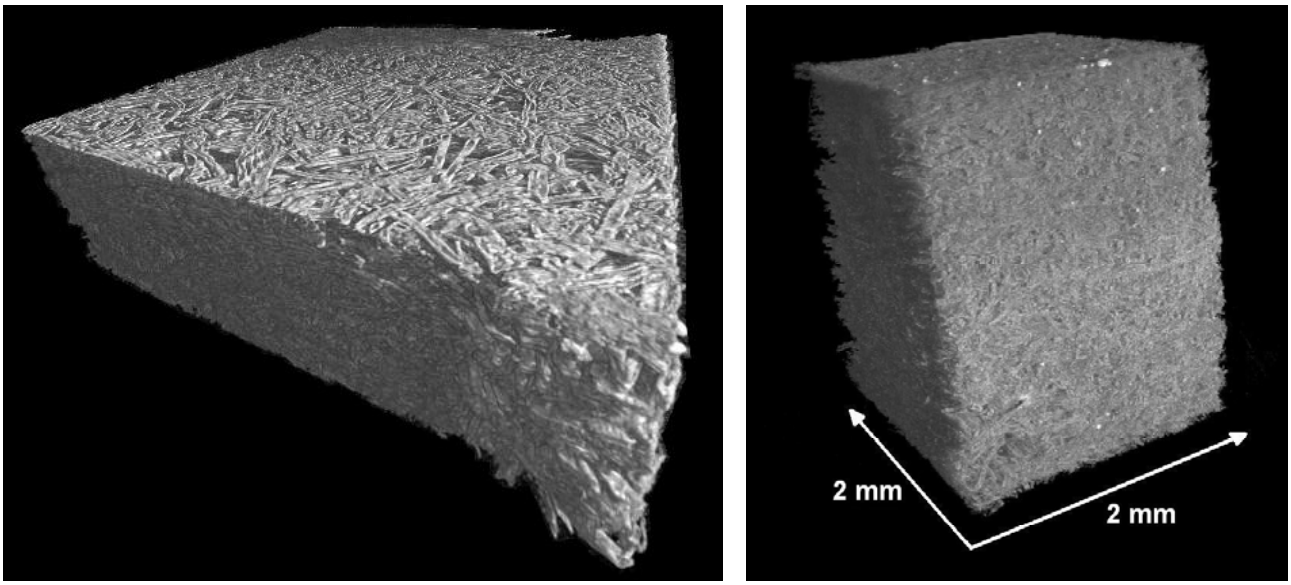


Figure 1: Microtomography of a MDF sample. Volume renderings of a part (left) and of the whole (right) reconstructed volume with a size of 2 x 2 x 3 mm are shown.

The wood fibers that are used for MDF/HDF have a typical length of 3000 µm with an average diameter of 10 to 20 µm. The spatial resolution of the images gained with the tomography equipment was 2 µm so that individual fibers and fiber bundles are clearly visible. The alignment and the distribution of the fibers in the sample are displayed in the cross section shown in Figure 2. The elliptical cross section of the fibers and a few fibers cut in the longitudinal direction are visible. It is possible to determine important geometrical parameters, such as the shape of the fibers, the thickness of the cell walls, and the structure of the interlinked void system by morphometric analysis of the volume data set.

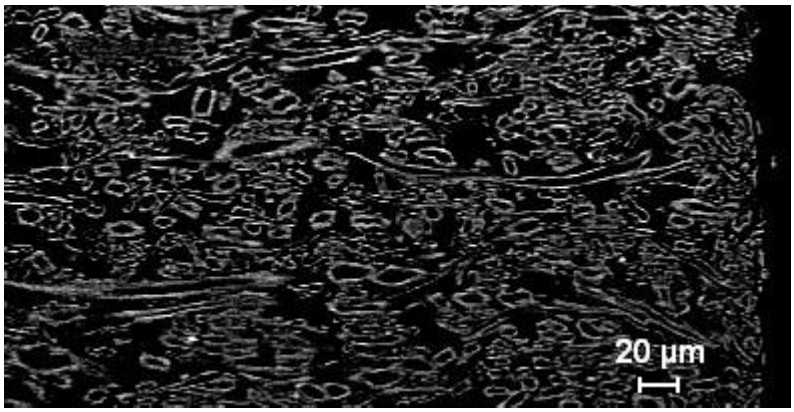


Figure 2: Section of the microtomography of the cross section of a MDF sample.

Further research on the microstructure of natural fiber composites will be done in 2005 within the project I-04-100 “Microstructure of Natural Fiber Composites”. It is planned to investigate different types of fibre panels made out of sisal, flax, hemp and wood fibers. The distribution of the voids, the alignment of the fibers, the fiber deformation and the contact points between the fibers will be subject for evaluation. Additionally, the adhesive distribution in the samples will be investigated by staining the adhesives. Preliminary tests indicated that the distribution of the adhesive on the fibers can be visualized by using high absorbing substances [2].

The project at HASYLAB is embedded in the research project “Natural Fiber Composites – An Alternative?” supported by the Arthur and Aenne Feindt Foundation, Hamburg.

References

[1] G. von Haas, A. Frühwald, Holz- als Roh- und Werkstoff 58, 317-323 (2000)
[2] J. Fischer "Mikrotomographie mit Synchrotronstrahlung: Gefäßdarstellung an biologischen Geweben", Diplomarbeit Fachhochschule Münster, 2003.

Using synchrotron µCT to analyse the development process of metallic foams

O.Brunke, S. Odenbach and F. Beckmann

[1]ZARM Universität Bremen, Am Fallturm, 28359 Bremen, Germany
[2]GKSS, Max-Planck-Str. 1, 21502 Geesthacht, Germany

Aluminium based metallic foams offer a combination of highly interesting properties like a favourable stiffness to weight ratio, excellent energy absorbing capabilities and low flammability which make them an extremely interesting material for many industrial applications, mainly in automotive and aerospace industry. The physical properties of the solid foam which are relevant for most applications are strongly affected by its structure parameters, like for instance pore size and their distribution, pore shape, the relative density distribution, the location of inhomogeneities, the distribution of solid material between films and plateau borders. On the other hand, these parameters directly depend on the temporal development, stability and ageing of the liquid foam system.

A common method for the production of metallic foams is the powder metallurgical route developed by the Fraunhofer Institute IFAM in Bremen [1]. The process is based on the compaction of a mixture of metal powder and a suitable blowing agent. In case of Aluminium based foam alloys, about 0.5 weight percent of TiH2 is used for this purpose. The decomposition of the blowing agent in the melt, i.e. the release of Hydrogen generates the foam. In order to conserve this porous structure the samples are cooled down below their melting point.

Synchrotron micro computed tomography with a spatial resolution between 4 and 10 µm at the HASYLAB beamline W2 has been used to analyse the structure of AlSi7 foams produced by the IFAM route.

Figure 1 shows 2D cross-sectional images taken from the tomographic datasets of the precursor material (a) and 3 different steps of the foaming process (b-e), respectively. All samples have been foamed at a furnace temperature of 750°C. The foams have been solidified immediately (b), 60 s (c), 300 s (d) and 500 s (e) after reaching the solidus temperature of 580°C.

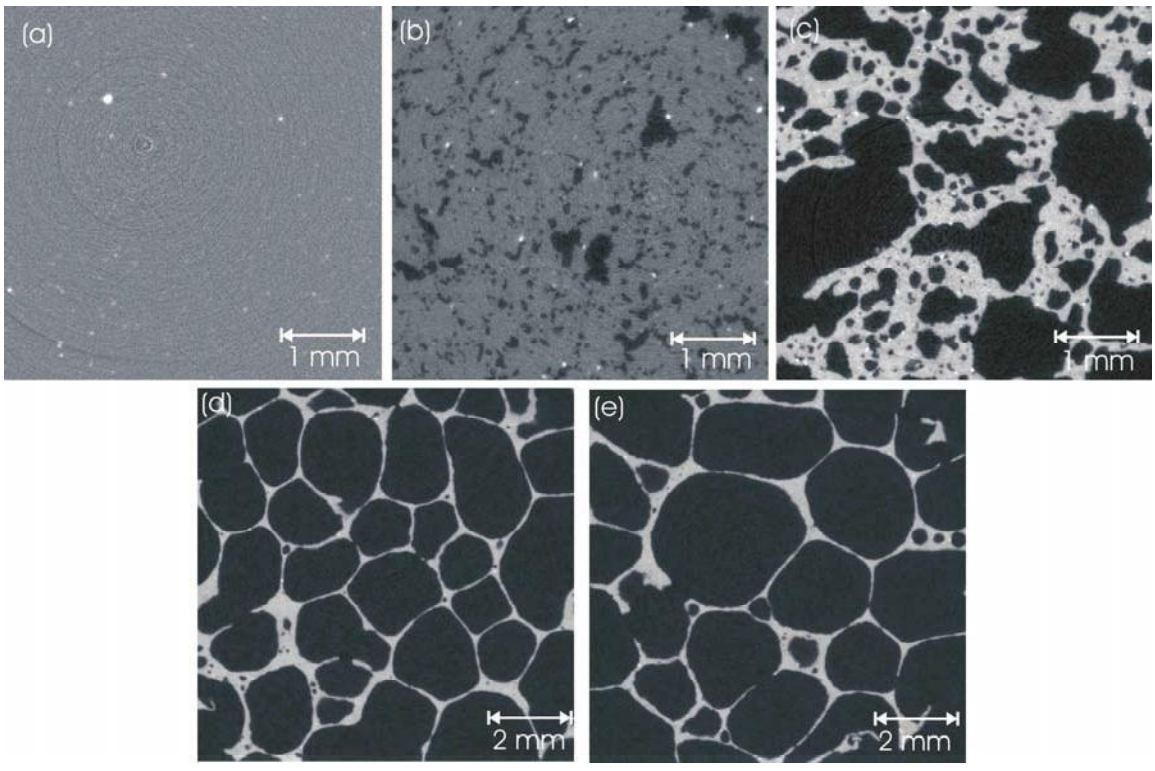


Figure 1: Cross sectional images taken from tomographic datasets of Al-foam samples at different temporal steps of the ageing process

Three dimensional image processing methods can be used to analyse the temporal changes of the foam structure quantitatively [2][3]. As typical result, Figure 2 shows the changes of the 3D pore size distribution of the samples (d) and (e). Due to the coarsening of the foam, the total number of pores decreases from 1631 for the young foam to 583 for the old one. Accordingly, the mean pore size doubles from a mean theoretical value of $\overline{r}_{pore}(300s) = 0.19\,\text{mm}$ to $\overline{r}_{pore}(500s) = 0.37\,\text{mm}$.

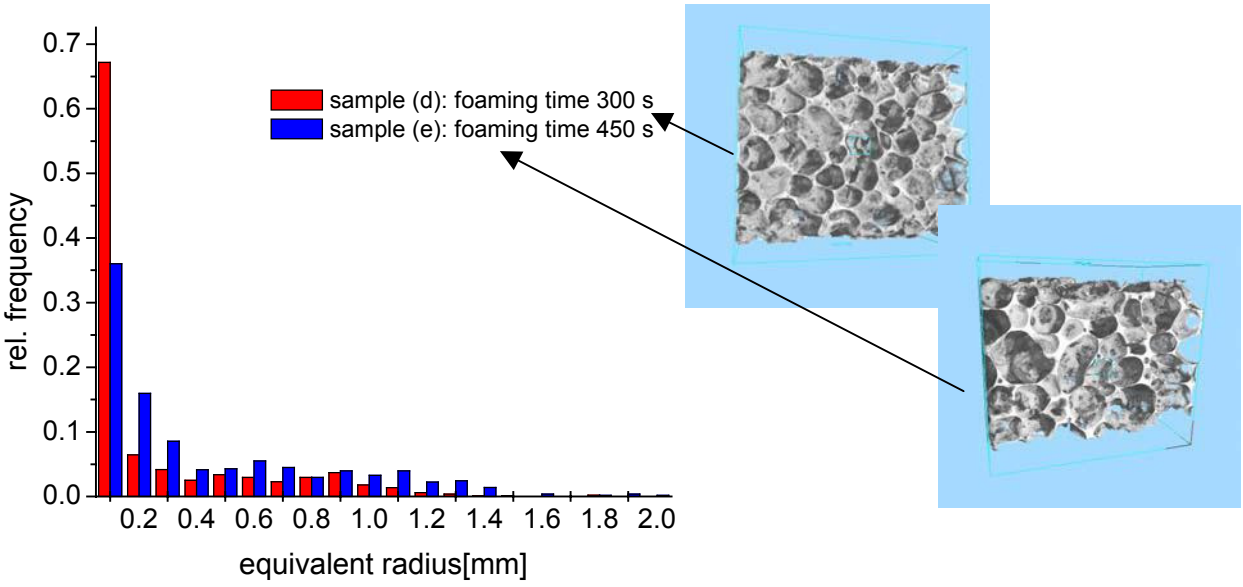


Figure 2 Pore size (a) and solid phase size distribution (b) of the sample shown in

Figure 1

The next steps will be the analysis of the complete datasets taken at different foaming temperatures.

References

[1] F. Baumgärtner, I. Duarte, J. Banhart, Adv. Eng. Mat. 2 (4), 2000

[2] O. Brunke, S. Odenbach, F. Beckmann, "Quantitative methods for the analysis of µCT datasets of metallic foams", DOI: 10.1051/epjap:2004203, Eur. Phys. J. Appl. Phys. (2004)

[3] O. Brunke, S. Odenbach, F. Beckmann, "Structural characterization of aluminium foams by means of micro computed tomography", Proceedings of the SPIE Developments in X-ray tomography IV, in press, 2004

Validation of Marker Material Flow in 4mm Thick Friction Stir Welded Al 2024-T351 as reported by Computed Microtomography using Standard Metallographic Techniques

R. Zettler, J.F. dos Santos, T. Donath, F. Beckmann, T. Lippmann, D. Lohwasser[1] and A. Schreyer

Institute for Materials Research, GKSS Research Centre, Max-Planck-Str. 1, 21502 Geesthacht, Germany
[1]Airbus Deutschland GmbH

Friction Stir Welding (FSW) was invented and patented by The Welding Institute (TWI) of Cambridge, in 1991 [1]. The process is referred to as a solid state joining process where no bulk melting of the base material occurs. In comparison to fusion welds there is no evidence of an as cast structure in the weld nugget. The process essentially relies on frictional heating and plastic deformation brought about by a rotating and non-consumable tool that is plunged into and then traversed along the join line between typically two abutting workpieces. A schematic of the process can be found in Figure 1.



Figure 1: Schematic of FSW process: Left to right: tool rotation, tool plunge, tool traverse, tool exit.

The FSW tool in conjunction with the processing parameters; axial load or downforce, rotation and travel speed provide the necessary energy input required to thermally soften the workpiece material. The joining tool comprises essentially of two parts: a shoulder and a pin. The tool shoulder not only helps to produce heat by means of friction induced rubbing with the surface of the workpiece but also acts as a barrier preventing expulsion of locally plasticised material from the immediate weld zone. The FSW pin then forces this thermally softened material, contained at the underside of the workpieces by a backing bar or anvil, to flow in the direction of rotation where it is transferred from in front of and then to the back of the pin where it cools and consolidates. The residue of this interaction between the welding tool, the workpieces and the clamping system can be evidenced in the microstructure and flow induced patterns of the weld nugget. These flow patterns appear like the layers of an onion prompting the term onion ring structure for the weld nugget, Figure 2.

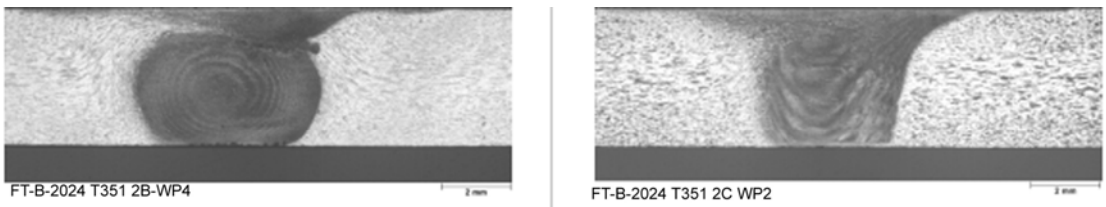


Figure 2: Macrographs of two friction stir welds as seen transverse to weld travel direction produced in 4mm thick Al 2024 T351 using identical tool shoulders but dissimilar tool pins, demonstrating very different flow patterns.

Although many aluminium alloys have proven to be capable of being joined using the FSW process, much conjecture still exists concerning the nature of the deformation process, the bonding mechanisms involved and their influence on subsequent weld properties.

The use of minute embedded marker materials strategically placed in the path of the FSW tool have allowed for much greater insight into material flow resulting from the interaction of the FSW tool with the workpieces. The visualisation and displacement of a Ti powder marker material has here been investigated for friction stir welds produced in a 4 mm thick Al 2024 T351 alloy using X-ray computed microtomography (μCT) [2]. The results from this investigation have demonstrated that marker flow originating from two different locations and for two different tool geometries generates significant differences in the observed flow patterns of the marker material. The accuracy of the μCT technique in validating marker material flow has been assessed using standard metallographic techniques. The results confirm the accuracy of the CT measurements but also highlight advantages and disadvantages associated with each procedure.

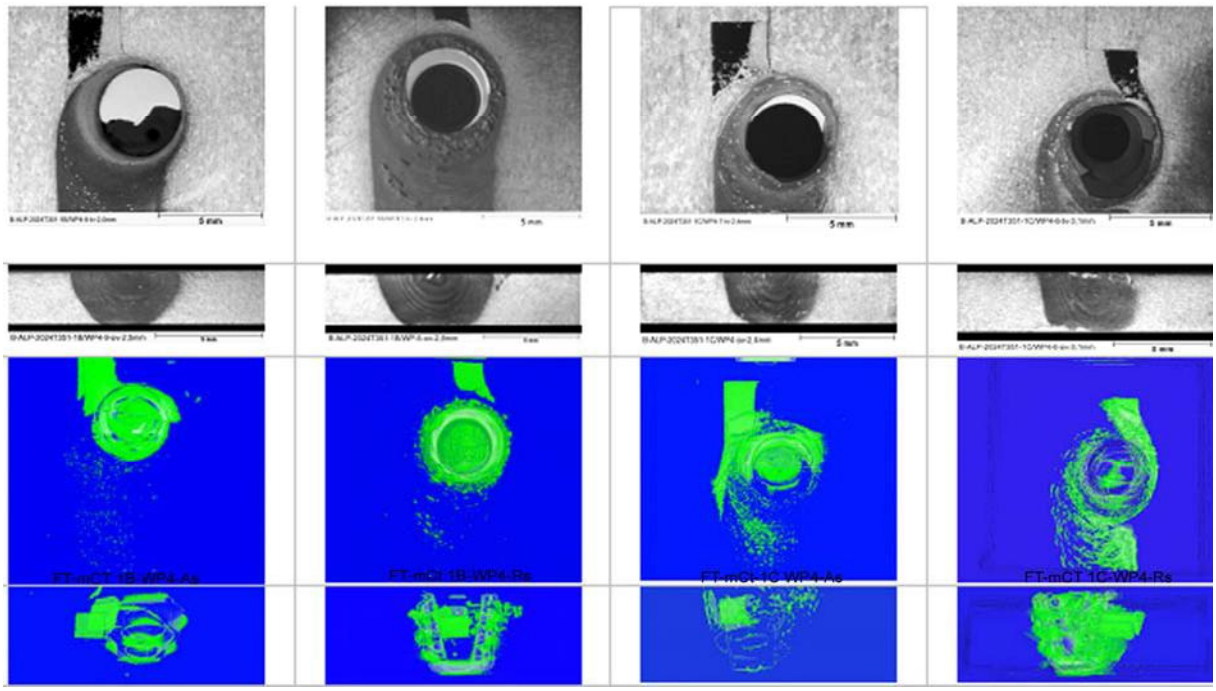


Figure 3: Comparison of metallographic images (top) and renderings from μCT-data (bottom). From left to right: Tool 1B marker placed l.h.s top., Tool 1B marker placed r.h.s top, Tool 1C marker placed l.h.s top, Tool 1C marker placed r.h.s top. Note tool rotation is clockwise and traveling up the page:

Samples were generated by using a stop action technique where the welding tool pin is abruptly halted as it enters the marker embedded region of the workpieces. Figure 3 compares the information obtained by the standard metallographic technique and the μCT data obtained at beamline W2 at a photon energy of 60 keV.

The metallographic technique is capable of defining the location of the marker material in relation to the onion ring or banded structures within the weld nugget. This is important if one wishes to correlate the relationship between material flow or banding with that of crack growth within the weld nugget under cyclic e.g. fatigue loading. Obtaining a 3D marker distribution for flow studies is not possible using standard metallographic techniques where only one surface can be ground, polished and etched at any one time. The metallographic technique thereby requires the ultimate destruction of the specimen. By use of the non-destructive μCT technique the 3D distribution of marker material around the FSW pin could be obtained at 10 μm spatial resolution. From this data set information on the material flow is accessible. The combination of the two techniques will give new insights in the understanding of the welding process.

References

[1] W.M. Thomas, E.D. Nicholas, J.C. Needham, M.G. Church, P. Templesmith, C.J. Dawes: International Patent Application No. PCT/GB92/02203 and GB Patent Application No. 9125978.9, (1991).

[2] T. Donath, F. Beckmann, R. Zettler, J. dos Santos, D. Lohwasser, T. Lippman, H. Clemens, and A. Schreyer, AIP Conf. Proc. 705, 1312, (2004).

Visualization of capillaries in the myocardium using synchrotron radiation based microtomography

J. Fischer[1,2], U. Dietz[3], P. Thurner[1,4], F. Beckmann[5] and B. Müller[1]

[1] Computer Vision Laboratory ETH Zürich, Sternwartstrasse 7, 8092 Zürich, Switzerland
[2] Department of Orthopaedic Surgery, Hannover Medical School, Anna-von-Borries-Str. 1-7, 30625 Hannover, Germany
[3] German Clinic for Diagnostics, Aukammallee 33, 65191 Wiesbaden, Germany
[4] Swiss Federal Institute for Materials Testing and Research, Überlandstr., 8600 Dübendorf, Switzerland
[5] Institute for Materials Research, GKSS-Research Centre, Max-Planck-Str. 1, 21502 Geesthacht, Germany

The result of medical interventions, such as the radiofrequency treatment of the myocardium to induce blood vessel formation has to be verified. In order to visualize the vessel trees down to the smallest blood vessels - the capillaries about 5 µm in diameter – an appropriate 3D imaging method of true micrometer resolution has to be developed. In principle, synchrotron radiation based microtomography (SRµCT) provides the spatial resolution, but since the vessels and the surrounding tissue mainly consist of water the absorption contrast is insufficient to segment the vessels. The incorporation of a suitable contrast agent into the vessels of interest is, therefore, required.

The study is based on heart tissue of pigs (Deutsche Landrasse) with the weight between 92 and 128 kg resulting in hearts of about 335 g. For fixation and conservation of the myocardium the embedding kit JB-4 (Polysciences Inc.) was used. To avoid the formation of bubbles, the monomer solution was cooled down to 4 °C and degased at a pressure of 200 mbar. The most suitable staining agents of our experiments were lyophilic powdered salts: $CaSO_4$, $SrSO_4$, and $BaSO_4$ each with a mean particle diameter of 1.5 µm. These particles suspended in JB-4 were injected into larger arteries. Because the particles are of the

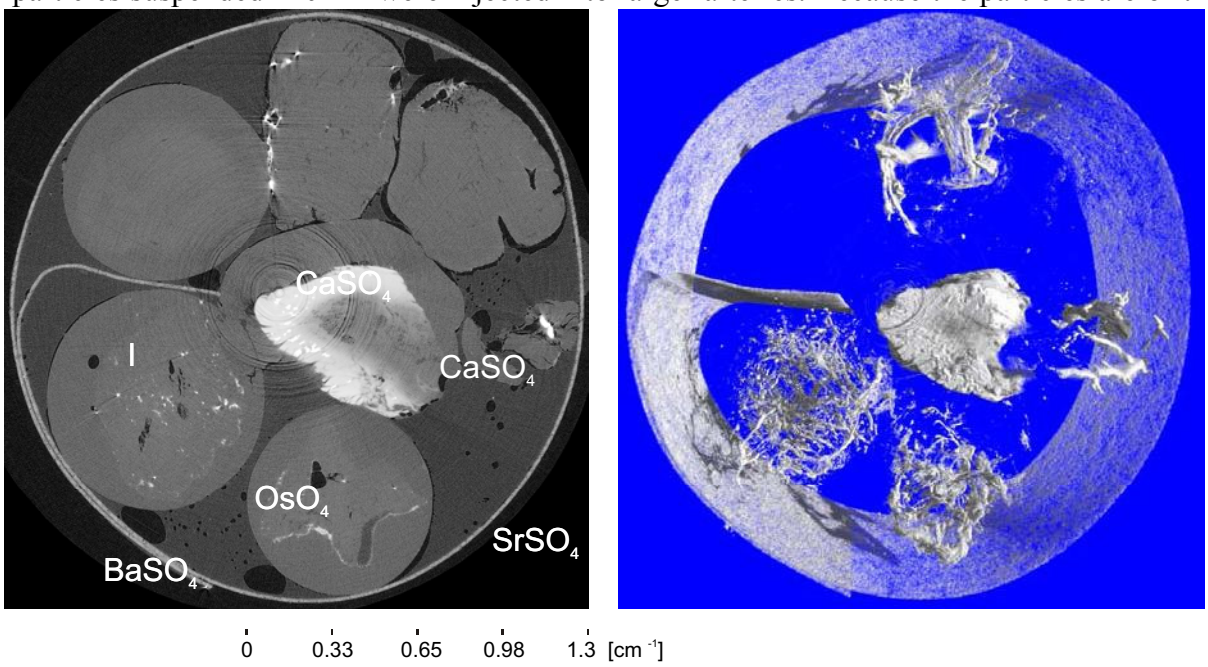


Figure 1. The assembly of 7 myocardium samples filled with different staining agents (as indicated). On the left, a typical slice is represented. On the right the sample is visualized as the 3D-image. This image demonstrates that the sulfates are well suited to stain the blood vessel system. The measurement was carried out at the beamline W2 using the photon energy of 20 keV and the spatial resolution of 5.1 µm.

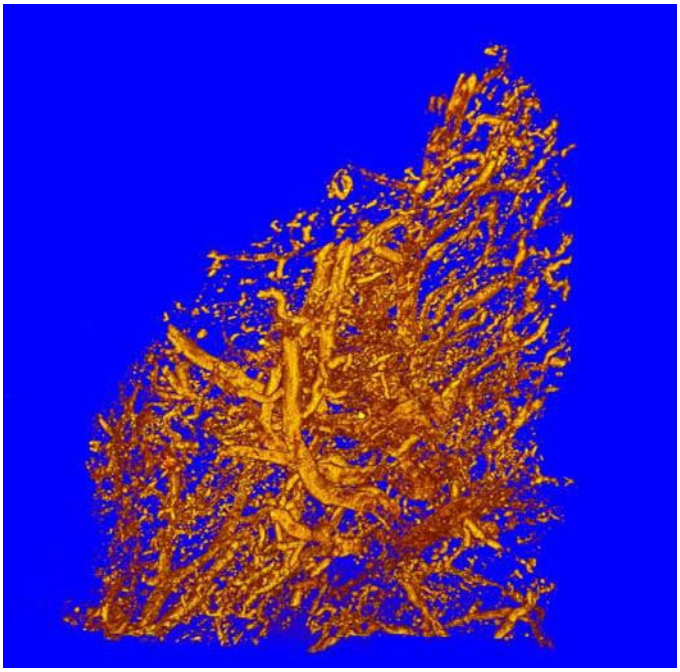


Figure 2. The 3D representation of the blood vessel tree in the myocardium. The image shows that the staining agent is not homogeneously distributed, since many smaller vessels are not connected. The diameter of the piece of myocardium shown corresponds to about 3 mm.

micrometer size they interpenetrate the blood vessel system but do not penetrate the walls of the vessels. Consequently, the difference in X-ray absorption between the vessels and the surrounding myocardium tissue is achieved.

The SRμCT-measurements were carried out at the beamline W2, HASYLAB at DESY. The used monochromator setup (bent Si-crystals in Laue geometry) allows for monochromatic X-rays in the energy range from 20 keV to 60 keV. Below 20 keV the photon flux in the monochromatic X-ray beam decreases, and the exposure time becomes too long for tomographic measurements. From the radiographic imaging at micro-focus sources we know that the optimal photon energy to visualize the stained vessels, i.e. sample diameter (4 mm) times absorption equals two, is about 10 keV. As the lowest possible energy was 20 keV the combined samples, as shown in Figure 1, were investigated. Such an assembly has the advantage that the different specimens are measured simultaneously, and the results are, therefore, directly comparable. Potential influences of individual measurements are definitely excluded. The disadvantage of this kind of experiment is the reduced spatial resolution within the acquired data set. For the 3D visualization of the blood vessel tree the software VG Studio Max (Volume Graphics, Heidelberg, Germany) has been applied (cp. Figures 1 and 2).

The staining method developed is an essential step to verify the neo-vascularization after medical interventions such as radio-frequency treatment in the myocardium. Nevertheless, the staining procedure has to be improved, since the salt particles sediment and the concentration of the particles within the individual vessels varies considerably. Therefore, it is essential to tailor the viscosity of the suspension. On one hand, one has to increase the viscosity to prevent the sedimentation. On the other hand, the viscosity of the suspension has to be high enough to interpenetrate the capillaries.

References

J. FISCHER, *Mikrotomographie mit Synchrotronstrahlung – Gefäßdarstellung an biologischen Geweben, Diploma Thesis FH Münster, 2003.*

Electron Density Distribution in Co-Olivine, Co_2SiO_4, from D3 and BW5 Data

T. Lippmann[1], W. Morgenroth[2], A. Kirfel[3]

[1]GKSS, Max-Planck-Str. 1, 21502 Geesthacht, Germany
[2] DESY/HASYLAB, Notkestr. 85, 22603 Hamburg, Germany
[3]Mineralogisch-Petrologisches Institut, Poppelsdorfer Schloss, 53115, Germany

Co-olivine belongs to the group of synthetic olivines and is isotypic to forsterite and fayalite, the Mg and Fe-end members, respectively of the (Mg, Fe) solid solution series. Thus, it crystallizes in the olivine structure, space group Pbnm, a_0 = 4.778(1) Å, b_0 = 10.293(3) Å, c_0 = 5.996(2) Å, Z = 4. In continuation of our earlier forsterite [1], fayalite [2] and tephroite [3] studies we have now carried out room temperature single-crystal diffraction experiments with the aim to complement the earlier results by adding material for a transition element with a $3d^7$ electron configuration. The comparison of the chemical bonding in forsterite on one hand and the transition metal olivines on the other hand is expected to shed more light on the role of the cation exchange in the isotypic structures as well as on the transferability of the isolated SiO_4 group.

Simultaneously, it was intended to further explore for accurate electron density determinations the feasibility of combining data recorded from the same crystal, but on different diffraction instruments and with different synchrotron radiation energies.

For the Low-Order reflections, which carry most of the information concerning bond induced charge redistributions, but are notoriously affected by absorption and extinction effects, we have chosen synchrotron radiation of 100.78 keV in order to obtain essentially absorption and extinction free data for the electron density modelling and ensuing topological analysis. The experiment on a sample produced by the Czrochalski technique and ground to an approximate sphere of 150 µm diameter was performed on the Triple-Crystal-Diffractometer (BW5, [4]).

For a half sphere up to $\sin\theta/\lambda$ = 0.848 $Å^{-1}$, 3987 reflections (including standards) were recorded in the conventional bisecting mode using ω−scans. After data merging and careful elimination of outliers deviating more than 3σ from the mean intensity the data reduction without absorption correction resulted in a set of 748 unique observed reflections (I > 3σ) with an internal agreement factor $R(F^2)$ = 0.0118.

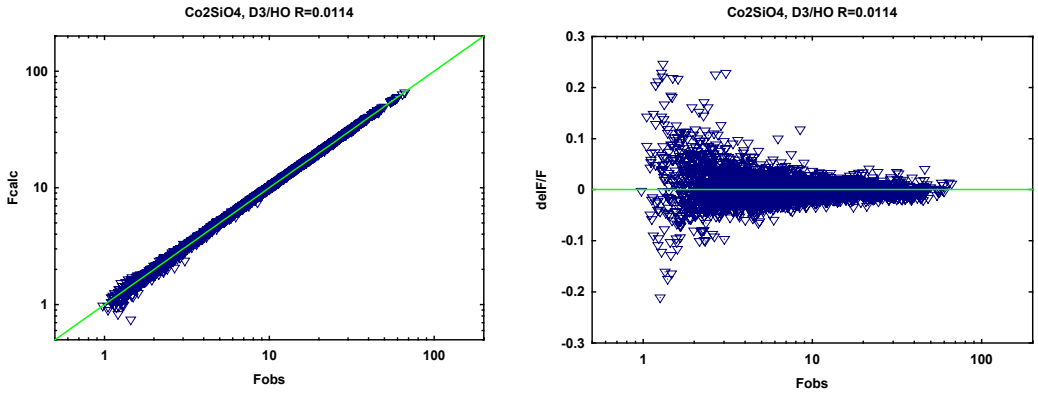


Figure 1: HO-data collected on D3 after IAM-refinement. Left: logarithmic F(obs) vs. F(calc); right: relative differences between observed and calculated structure amplitudes.

High-Order reflections, which are generally hardly affected by extinction and are dominated by the atomic core electrons, can be used to determine unbiased crystallographic standard parameters. To this purpose, additional data where collected at the Four-Circle-Diffractometer (D3) at a beam energy of 27.62 keV corresponding to a wavelength of 0.4488 Å. Exploring a half shell between 0.73 $Å^{-1}$ and 1.49 $Å^{-1}$, 14716 reflections were recorded in the bisecting mode yielding a set of 3148 unique reflections ($2825 > 3\sigma$) with an internal agreement factor $R(F^2) = 0.0122$.

So far, structure refinements were only carried out with the independent atom model (IAM). Applied to the High-Order reflections convergence was reached at R(F) = 0.0114, wR = 0.0212, GoF = 1.13. No significant extinction effects were detected. Fig. 1 illustrates the quality of these data by a logarithmic F(calc) vs. F(obs) plot.

In the next step, a refinement was carried out with the Low-Order reflections alone. Fixing the previously refined atomic standard parameters considered as free from chemical bias, this refinement is expected to show the charge redistribution in terms of dynamic deformation density maps. Thus, the only variables to be adjusted are the scale factor and extinction coefficient. This refinement converged at R(F) = 0.0150, wR = 0.039, GoF = 1.68. The largest extinction correction factor amounted to 3.7% for the 004 reflection. Fig. 2 shows as a preliminary result the deformation density distribution in the mirror plane accommodating Si, O_1, O_2 and Co in the centre of the M2-coordination octahedron. The positive deformation density features indicate non-negligible shared interaction components in the Co-O bonds.

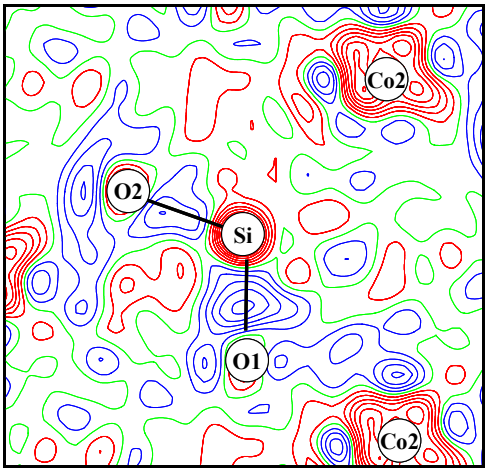


Figure 2: Dynamic deformation density distribution in the mirror plane normal [001] calculated from BW5 data and structure parameters obtained from refinement of HO-data recorded on D3. Contours at 0.1 e/ $Å^3$.

The full refinement of the LO-data alone yielded R(F) = 0.012, GoF = 1.38, and partially significant deviations from the HO-thermal displacement parameters. These differences are most likely due to the still missing absorption treatment of the D3 data. First refinements with Generalized Scattering Factors indicate a significantly improved agreement index below R(F) = 0.008.

References

[1] A. Kirfel, T. Lippmann, Acta Cryst., **A58** (Suppl.), C165 (2002)
[2] A. Kirfel, T. Lippmann, HASYLAB Jahresbericht, 515 (2002)
[3] A. Kirfel, T. Lippmann, W. Morgenroth, HASYLAB Jahresbericht, 601 (2003)
[4] R. Bouchard et al., J. Synchrotron Rad. **5**, 90 (1998)

Functional Micromorphology of Sponges (Porifera)

M. Nickel, E. Bullinger[1], H.M. Reiswig[2], T. Donath[3] and F. Beckmann[3]

Department of Zoology, Biological Institute, University of Stuttgart, Pfaffenwaldring 57, 70550 Stuttgart, Germany

[1]Institute for Systems Theory in Engineering, University of Stuttgart, 70550 Stuttgart, Germany

[2]Biology Department, University of Victoria, P.O. Box 3020 Stn. CSC, Victoria V8W 3N5, B.C. Canada

[3]GKSS Forschungszentrum, Max-Planck-Str. 1, 21502 Geesthacht, Germany.

Sponges (Porifera) are sessile, filter-feeding animals. They live mainly in the sea, but some groups also inhabit freshwater environment. In recent years interest in sponges rose due to their high diversity of secondary metabolites of pharmaceutical value. Therefore, sponges became interesting for pharmacology and biotechnology, aiming production of sponge biomass and metabolites. Soon it became evident that a more detailed knowledge on the general biology of sponges is a prerequisite for successful cultivation. Cellular growth and synthesis of skeletal elements are connected in sponges. The skeletons consist of organic substances, like collagen and its derivative spongin, in conjunction with mineral sclera (spicules) in most groups of the phylum Porifera [1, 2]. The main function is to stabilise the bodies of sponges. On the other hand the skeletal elements possess a variety of other functions in contraction and locomotion of sponges. Since these processes are slow and inconspicuous they are not well investigated. Nevertheless, they are very important in the life of sponges, since they are linked to the nutrition (filter feeding activity) and the response to short-term and long-term environmental changes. A wide variety of spicule forms can be found, which reflects their various physical functions. This variety of functions is neither well investigated, nor well understood. Our project aims to understand the functional micromorphology of sponges, by applying synchrotron radiation based micro computed tomography SR-µCT. We performed experiments at HASYLAB beamline BW2 on dead, preserved sponges as well as on living material. In 2004 we mainly focused on two sponge species.

***Tethya* spp.**

The demosponge sister species *T. wilhelma* and *T. minuta* display conspicuous body contractions, which have recently been characterized [3]. The structure of the skeleton of *T. minuta* has been imaged by SR-µCT and visualized in preliminary experiments in 2002 [4]. Meanwhile we have developed a Matlab-based software tool, to quantitatively analyze the sponge spicules in the 3D-dataset. We were able to automatically detect and measure all 16.900 megaster-type (oxyaster) spicules to create an extensive morphometric dataset, representing the first quantitative analysis of a complete set of a single spicule within a sponge. We were able to show that >98.5 % of all megasters are arranged within a distinct sphere, supporting the filtering core unit during contraction of the outer cortex, by deflecting contraction forces from the sponge core (Nickel, Bullinger & Beckmann, submitted).

In 2004, we extended our work on *T. wilhelma*. Using the same experimental set-up than before [4], we imaged the complete skeletal structures of a contracted and a non-contracted adult specimen and an asexual reproduction body (bud), which was amputated from an adult sponge at an early stage, just several days after

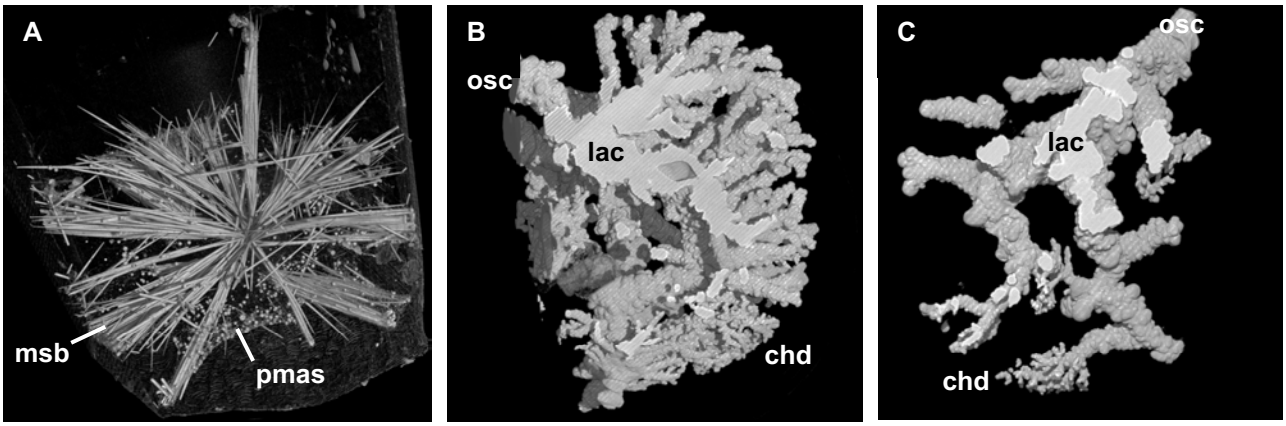


Figure 1 A. The skeletal morphology of a *T. wilhelma* bud, visualised by SR-µCT. msb, macrosclere bundles; pmas, primordial megaster sphere. **B – C.** 3D-reconstruction of a corrosion cast of a part of the *T. wilhelma* aquiferous system; osc; osculum region; lac; cortex-lacunae region; chd, choanoderm.

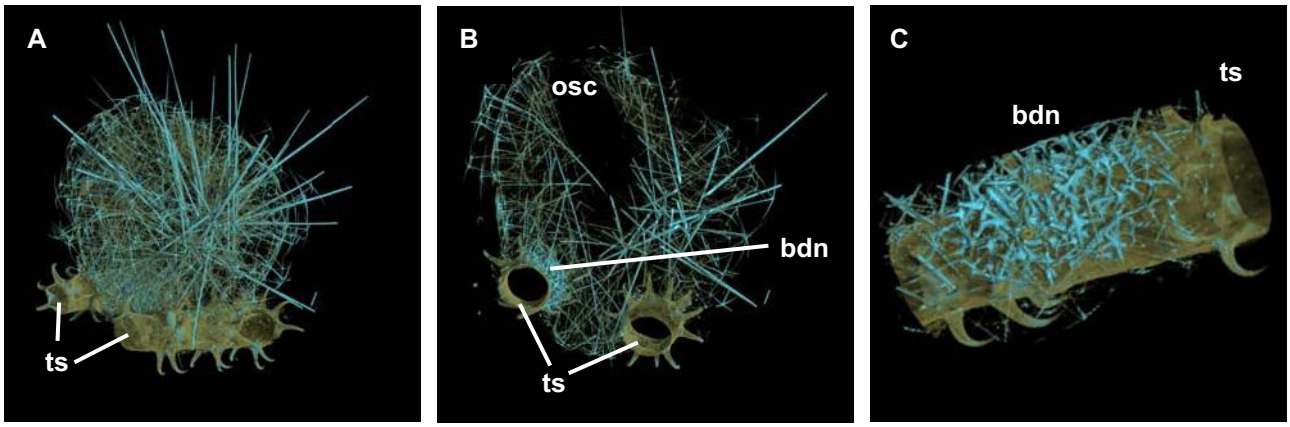


Figure 2 A. The skeletal morphology of a juvenile *R. dawsonii*, attached to two tunicate spines, visualised by SR-µCT; ts, tunicate spines. **B.** 740 µm thick virtual section through the sponge; osc, oscule; ts, tunicate spines; dbn, basidyctional network. **C.** One of the basidyctional networks, firmly attached to the spine. bdn, basidyctional network; ts, tunicate spine.

initiation of formation. In addition a small part of the cortex region of an adult sponge was scanned at high resolution, in order to resolve the microsclere layer supporting the sponge surface. The quantitative analysis of the contraction states is not yet completed, but it shows that *T. wilhelma* has a slightly modified skeleton structure in comparison to *T. minuta*. The megaster sphere is not as prominent and the density of megasters is reduced. The bud displays the same principal skeletal arrangement like the adult sponge, with megasclere bundles originating from the center (Fig. 1A). A primordial megaster sphere is already present. A micraster layer covers the surface of the sponge. There seems to be no cortex present in this stage of budding, which corresponds to observations that early buds do not contract.
In addition we scanned a corrosion cast [5] of the aquiferous system of a non-contracted sponge, demonstrating that the major part of the cortex consists of lacunar structures of the aquiferous system (Fig. 1B,C). The data analysis of this experiment was not completed at the time of writing.
At last, we tried to image the skeletal dynamics during contraction in a living sponge. A specimen of T. wilhelma was mounted in a 5 ml experimental chamber, filled with seawater, on beamline BW2. Though we were able to visualize the megasclere bundles on the radiograms, we were not able to follow any contraction event, most likely due to the fact that the sponge was in a contracted state before we intended to induce it. The experiment will be repeated under optimised conditions.

Rhabdocalyptus dawsoni
We scanned a complete juvenile glass sponge of R. dawsoni. The overall 3D-visualization of the complete sponge confirmed observations done by dissecting microscope (Fig 2 A), but virtual sectioning of the reconstructed sponge allowed to visualise internal structures of the skeleton in its natural confirmation. For the first time the basidyctional network, the main anchoring structure of the skeleton, could be addressed in undisturbed conditions (Fig 2 B, C). Conventional microscopic preparation techniques at least partially disrupt this fragile structure. For the first time we showed that two independent basidyctional networks where built by the sponge. A detailed analysis of the data was in progress at time of writing.

References

[1] P. Bergquist, Sponges. University of California Press, Los Angeles, 268 pp. (1978)
[2] T.L. Simpson, The cell biology of sponges. Springer Verlag, New York, 662 pp (1984)
[3] M. Nickel, J. Exp. Biol. 207 (26), in press (2004)
[4] M. Nickel and F. Beckmann, Hasylab Anual Reports 2002 Part I, 919-920 (2002)
[5] G. Bavestrello, B. Burlando and M. Sarà, Zoomorphol. 108, 161-166 (1988)

High Resolution 3D-Analysis of the Middle Ear Stapes with Footplate using Synchrotron Radiation Microcomputed Tomography (SRμCT)

R. Bernhardt, T. Douglas, T. Beleites[1], M.Neudert[1], M. Ney[1], D. Scharnweber, F. Beckmann[2], Th. Zahnert[1], H. Worch

Max Bergmann Center for Biomaterials, University of Technology, Dresden, Germany
[1]Faculty of Medicine, University of Technology, Dresden, Germany
[2]GKSS-Research Center, Geesthacht, Germany

Introduction

Destruction of ossicular chain components necessitates their replacement with a middle ear prosthesis in order to restore hearing. Anchoring of the prosthesis is particularly difficult when the posterior crus and anterior crus of the stapes have been destroyed by inflammatory processes (e.g. choleasteoma), so that only the base or footplate remains. Previous prostheses have proved unsatisfactory due to the unstable connection between prosthesis and footplate, which often led to slipping and renewed deafness. This new approach involves the fixation of a titanium middle ear implant through osseointegration, which is induced by a biomimetic implant coating containing extra-cellular matrix components. SRμCT enables the precise determination of stapes dimensions and topography. These factors have implications for the design and geometry of the prosthesis and the nature of the surgical intervention, which in turn influence the production method of the prosthesis and the choice of animal model for in vivo tests. In addition, using the SRμCT data and stereolithography, 3D models of the stapes can be created, which are useful as visualisation aids and in devising and practising the implantation procedure.

Materials and Methods

A rabbit stape with footplate was extracted from temporal bone specimens. After wax-embedding the sample were measured with a SRμCT device at HASYLAB (BW2). Using an x-ray energy of 13 keV, 720 x-ray attenuation projections with a local resolution of about 12 μm were acquired. The reconstruction of the radiographs was performed with a filtered backprojection algorithm. Reconstructed 3D-information was prepared for stereolithography. Values below the threshold for bone were filtered out. RPCure 100 HC Epoxy resin was hardened with a He/Cd-Laser. A local resolution of 30 μm was achieved.

Results and Discussion

SRμCT allows a full visualisation of stapes geometry (Fig. 1). In particular, variation in the thickness of the footplate was observed (50-200 μm, Fig. 3A) and new insights into the footplate substructure were gained (Fig. 3B). SRμCT data was successfully converted for the stereolithographal production of life-size models (Fig. 2), despite the reduction in resolution. SRμCT data has assisted prosthesis design and influenced the choice of animal for in vivo experiments. It is conceivable that stereolithographic models made using SRμCT data could be used as templates for prosthesis production through titanium casting. Stereolithographic models made using SRμCT data have been of use in devising and practising the implantation procedure prior to actual animal experiments.

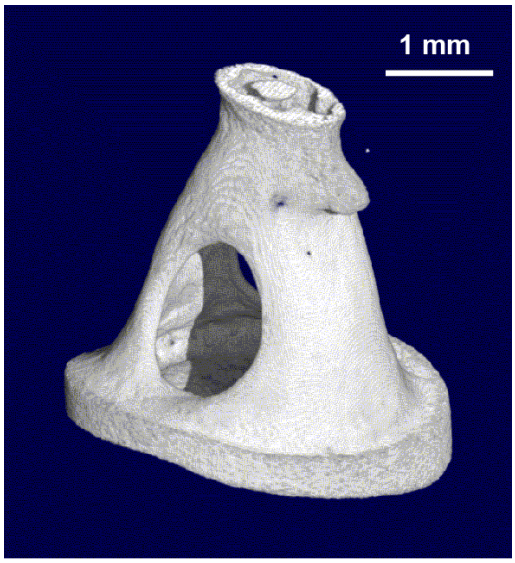


Figure 1: Reconstruction of the stapes with footplate using filtered 3D-data from the SRμCT measurement at HASYLAB (BW2).

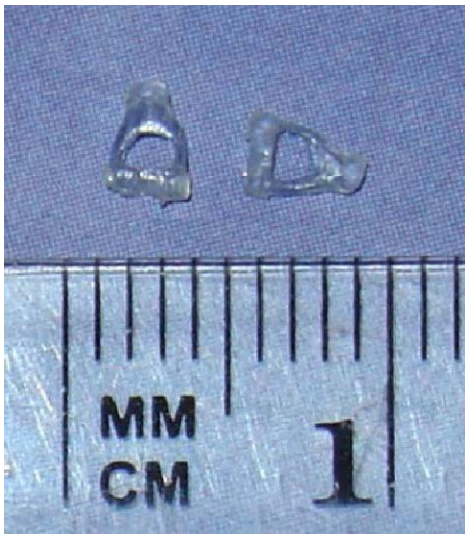


Figure 2: Reproduction of the middle ear stapes with footplate using filtered 3D-data from the SRμCT measurement at HASYLAB as the input for a stereolithographic technique.

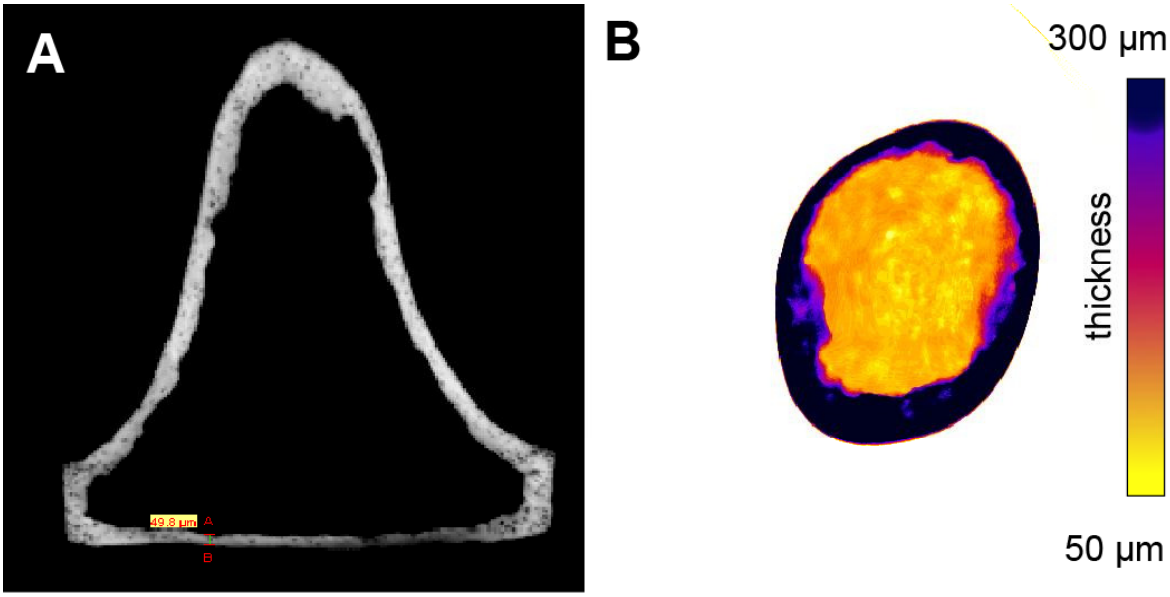


Figure 3: (A) Slice from the SRμCT measurement to obtain the thickness of the footplate. (B) thickness profile of footplate.

Acknowledgements

The authors are grateful to NRU GmbH, Neukirchen near Chemnitz, for producing the stereolithographic models, and to DFG and BMBF for their financial support.